# FERROELECTRIC PROPERTIES OF ORGANIC CROCONIC ACID

Doctoral Thesis submitted at the
École Doctorale physique et chimie-physique - ED 182,
University of Strasbourg,
in partial fulfilment of the requirements for
Doctor of Philosophy in Physics

by

**Sambit Mohapatra**
Department of Magnetic Objects On the Nano Scale (DMONS),
Institut de Physique et Chimie des Matériaux de Strasbourg (IPCMS),
CNRS-UMR 7504
University of Strasbourg
France

Defended on 10 November, 2020

**Jury:**

| | |
|---|---|
| **Director of the thesis:** | Dr. Samy Boukari |
| | The late Dr. Eric Beaurepaire |
| **External Reporters:** | Dr. Patrycja Paruch |
| | Prof. Dr. Rachel Desfeux |
| **Examiners:** | Dr. Victor Da Costa |
| **Invited Guests:** | Dr. Salia Cherifi-Hertel |

ERIC BEAUREPAIRE (1959-2018)

Dedicated to the late Dr Eric Beaurepaire...

*There are things, I think I know, that I know.*

*There are things, I think I know, that I do not know.*

*There are things, I do not think I know, if I know.*

*There are things, I do not think I know, if I can know.*

*And what it means to know, I do not think I know, if I know.*

# Acknowledgements

A doctoral thesis is the first step towards the world of research. Irrespective of the subject, a doctoral thesis brings specialization and greater insight for the student to the understanding, significance and the broader aspect of the subject. It brings up newer questions and perspective while also solving older problems and answering older questions in the subject of study at the same time. Starting from the birth of the idea and its shaping up to its execution, interpretation, inference and more importantly, the bigger perspective that a doctoral thesis brings, the entire process may not be within the mere abilities of a student. Especially, in science and more specifically, in experimental science, when the student is supposed to learn newer techniques and operate delicate and complex instruments, a lot of assistance from experienced superiors may be indispensable. Further, a lot of indirect support and assistance that come from the non-scientific members in the workplace and elsewhere makes the journey smooth and fruitful. Thus, acknowledging the direct and indirect support from innumerably many entities seems to be a challenging task, perhaps more challenging than conducting the doctoral research and writing the doctoral thesis itself. It is my immature attempt to write an acknowledgement with the hope that it appropriately acknowledges all the support without which this thesis would have merely been an imagination. Moreover, there is always a lot of support and courage that come from the personal social domain of the person conducting the thesis. Although, in my understanding, it may not be very professional to acknowledge those while acknowledging the professional support for the thesis, they can never be ignored in any way, nonetheless.

I begin by acknowledging the support for funding the entire project from ANR-DFG funding agencies: Project ORINSPIN (ANR-16-CE92-005-01). I would also like to thank the jury members, Prof. Dr Rachel Desfeux from UCCS Artois - Université d'Artois, France and Dr Patrycja Paruch from Université de Genève, Switzerland and the invited guest, Dr Salia Cherifi-Hertel from IPCMS, CNRS, Université de Strasbourg for participating and successfully conducting the process

of thesis defense.

First of all, my gratitude to the late Dr Eric Beaurepaire, one of my supervisors, who was one of the designers and architects of the project. While I was very fortunate to have the opportunity to work under a great mind and one of the pioneers of the field of study, it is a misfortune that I could not spend sufficient time under his supervision; his departure is a great loss to the scientific community. Nevertheless, the several meetings that I had the fortune of having with him were quite influential. I am sure his influence will go a long way in shaping up the future directions and decisions, both scientific and non-scientific, of my life. I would like to dedicate my doctoral research and this thesis to the late Dr Eric Beaurepaire.

I would take this opportunity to thank my supervisor Dr Samy Boukari who has been an integral part of the entire thesis work including all the ups and the downs of it, taking charge of supervising the thesis. His quick response and advice to all the academic and non-academic situations and issues have been a great support throughout. I thank him for listening patiently through all my recurring and invasive ideas and directions on exploring the research while pacifying them with logic and rationale and putting them into the perspective of practicality.

The name of Dr Victor Da Costa needs a special mention. Apart from being the project coordinator of the ANR thesis project, due to his complete involvement in all the aspects of the thesis, it is equally his thesis as it is mine. I thank him for training me on the several sensitive instruments techniques used during the process of the thesis work. His belief of doing great science without great noise has always appealed a lot to me.

Similarly, I owe sincere thanks and obligations to Mr Jacek Arabski. While his vast experience with several aspects of instrumentation has ignited my previous inspiration for proceeding towards my dream of achieving engineering prowess, his scientific ideas has introduced me to new and unexplored directions in the field of spintronics. I must also acknowledge his exhaustive training on the operation of the UHV cluster assembly which has played an essential role for the execution of the thesis. Further, I must not forget all the generous non-academic assistance that I, and any newcomer for that matter, receives from Mr Arabski that helps one immediately settle down in a new city. He has been my go-to person for a lot of issues that came up during the entire course of the thesis. I wish him a good post retirement time.

Another very important person whose assistance has been crucial for exploring the directions of the thesis is Mr Guy Schmerber. Any PhD thesis looks clean on

the surface, however, a lot of complicated and untidy work stay at the background without which the work of the thesis cannot even begin. Mr. Schmerber has been the person who took the entire load of doing this background work, even before the beginning of the thesis work, supporting the thesis throughout. It is still a mystery to me how my question to Mr Schmerber asking whether we could do some particular measurement always came up with an immediate schedule and not just a 'yes' as an answer, ofcourse, a 'no' was something that I have never heard from him.

I also thank the support and assistance from Dr Salia Cherifi-Hertel from the DSI department of IPCMS. Other than offering her ideas to explore various directions of the work, her generous offer to utilize the equipment at her laboratory has certainly made it possible to explore some very challenging aspects and directions of the work. Optimistically, her support with the research goes beyond the scope of the thesis work and hopefully, science will benefit from the wonderful collaboration between the DMONS-hybrid spintronics group and Dr Cherifi-Hertel's work.

It is imperative to acknowledge the assistance, advice and guidance from Dr Senthil Kumar Kuppusamy of IPCMS (currently at KIT, Karlshruhe) whose innovative ideas have always been a motivation for me to explore the possibilities of organic materials to do science. Other than all of his proposed directions of work that could not be pursued properly due to technical difficulties, his assistance with crystallography has been essential with the execution of certain section of the thesis. Especially, with the work done on Croconic Acid crystals, a major assistance from Dr Kuppusamy is sincerely acknowledged.

I also thank Dr Martin Bowen and Dr Wolfgang Weber who have always been at the backend of the support chain of the entire research group. Their advice and suggestions have been of paramount importance for the thesis work, especially, for the drafting of several manuscripts of publications that resulted from this work. Additionally, I must sincerely thank Dr Bowen for providing me with the numerous opportunities to be a part of the experimental team at the synchrotron beamline and always encouraging to be a part of the larger working group of the hybrid spintronics team. With his insights, I would love to carry forward the work of this thesis towards the interface spintronics aspect, bringing a broder impact to the subject.

Prof. Dr Wulf Wulfheckel from KIT, Karlshruhe whose involvement and support has been essential for the design of the project, also needs a special mention of acknowledgement. His advice on certain aspects of the work has been crucial to explore possible directions of the research.

I thank the DEIMOS beamline team, especially Dr Philippe Ohresser at the Soleil

synchrotron facility for kindly assisting me to learn synchrotron grade measurement techniques that had a broader impact on the overall perspective of the thesis. A special thanks to Dr Loic Joly who has been a great inspiration for large scale industrial instrumentation and I also acknowledge his assistance for my experience at the Soleil synchrotron.

I acknowledge the assistance from all other members of the DMONS-hybrid spintronics group and members of DMONS department; Mr Christophe Kieber, Mr Manual Acosta, Mr Daniel Spor, Mr Jeremy Thoraval, Mr Romain Bernard, Dr Benoît Gobaut, Dr Christian Meny, Dr Matthieu Bailleul, Dr Ricardo Hertel, Dr Mebarek Alouani, Dr Bodan Kundys, Dr David Halley, Dr Hicham Majjad and members of other departments of the institute; Dr Mircea Rastei, Mr Emmanuel Sternitzky, Dr Silviu Colis, Dr Guillaume Rogez, Dr Fabrice Scheurer.

I acknowledge the support from all the administrative and other technical staffs at IPCMS and at the University of Strasbourg. Especially, I would like to name Mme Veronique Wernher and Mme Catherine Bonin for all their continuous assistance with the entire non-scientific part of the work without which the entire process of doctoral research would not have been possible.

Finally, I would like to thank all my colleagues at IPCMS who have been a great support system throughout and also for all the scientific discussions. A special thanks goes to Mr Swapneel Pathak and Mr Suvidyakumar Homkar who have been a great support system for me. I thank Mr Garen Avedissian, Dr Kostantin Katcko, Ms Bhavishya Chowrira and Dr Filippe Schleicher for all the assistance with the operation of the systems in the lab and for all the scientific discussions. I also thank Mr Khaled Rassoul, Mr Matias Grassi, Ms Gladice Magnifouet and Mr Corentin Roumegou for their support.

I must also thank Mr Lalit M. Kandpal for his assistance with the research as a colleague. I must acknowledge his innovative ways of solving my problems that required special access to the clean room and in some cases at the multifunctional magneto-transport bench. Apart from the professional help, his informal guidance on Indian classical music has been a precious experience for me, the impact of which goes beyond the span of the thesis.

Also, to briefly mention some names whose support outside the academic boundaries was encouraging, I would go on as Smruti, Satya, Sanjeev, Shilpa, Vishnu, Thomas, Priyanka, Ayushi, Christian, Rashi, Arshdeep, Anu and Abhipsha.

Another name outside the academic circle that needs a special mention because of the contributions to the rigorous discussions on the ideas and the basics, espe-

cially in electronics and electrodynamics, that helped shape the thesis would be of Mr Soumyashree Sahoo. His strong grasp of the basics and engineering expertise along with my interpersonal comfort with his explanations made it easier to discuss complicated scenarios.

I would like to end by saying that the period of my doctoral research work for the thesis has not only been academically and scientifically an interesting one but also, from a philosophical point of view, has been a great journey for me and I thank everyone, with utmost sincerity, all who have been a part of the ride.

# Contents

# Résumé en français

**Introduction:**

L'histoire moderne de l'humanité a connu plusieurs révolutions industrielles dans le passé lorsque les trois secteurs clés du progrès de la société humaine, à savoir l'énergie, les transports et la communication, ont été révolutionnés par de nouvelles inventions alimentées par des découvertes scientifiques. Aujourd'hui, nous sommes au début d'une autre révolution industrielle avec des progrès sans précédent ces dernières décennies dans les technologies numériques et les industries du logiciel. Au cœur de cette révolution se trouvent les composants électroniques numériques modernes, qu'il s'agisse des dispositifs de stockage de mémoire ou des puces de traitement de l'information. Cependant, les plates-formes de fabrication des dispositifs et composants électroniques sont encore majoritairement tournées vers des architectures de conception classiques basées sur les semi-conducteurs. La demande sans cesse croissante de miniaturisation des appareils électroniques a poussé les dimensions des composants électroniques à atteindre un niveau nanoscopique où une réduction supplémentaire des dimensions semble être une tâche difficile à la fois en termes de faisabilité et de viabilité. Plus important encore, la génération de chaleur dans les composants électroniques avec la réduction des dimensions est un problème important pour le fonctionnement efficace des composants. D'une part nous recherchons des sources d'énergie alternatives pour alimenter notre avenir et nous utilisons la technologie numérique moderne pour rechercher des solutions alternatives aux problèmes liés à l'énergie et à l'environnement, d'autre part une partie importante de l'énergie disponible est simplement gaspillée. Avec la numérisation des activités économiques, commerciales et de toutes les autres activités humaines, l'augmentation stupéfiante des appareils électroniques est éminente, ce qui soulève des inquiétudes pour la consommation d'énergie et la perte d'énergie thermique dans l'utilisation future des appareils électroniques. Cela a nécessité des actions dans la recherche de plates-formes alternatives pour la conception de composants et

de dispositifs électroniques qui peuvent être plus économes en énergie.

La recherche de technologies alternatives a conduit à la recherche et à l'exploration dans plusieurs domaines. Par exemple, l'exploitation du spin des électrons pour construire l'électronique est devenue le domaine de l'électronique de spin ou communément appelé spintronique, alors que toute l'électronique conventionnelle utilise la charge d'électrons pour effectuer des tâches. L'émergence de la spintronique a révolutionné les systèmes de stockage de données numériques qui ont jusqu'à présent été le terrain sur lequel se déroule la prochaine révolution industrielle. De même, l'utilisation de complexes organiques pour réaliser l'électronique et concevoir des composants électroniques a indépendamment donné naissance au domaine de l'électronique organique. Sur une voie parallèle, l'utilisation de molécules organiques ou de matériaux à base de carbone en spintronique est appelée le domaine de la spintronique organique. Qu'il s'agisse de l'électronique conventionnelle ou de la spintronique, l'utilisation de molécules organiques fournit une voie pour réaliser des dispositifs électroniques écoénergétiques à faible consommation d'énergie.

Un autre aspect des dispositifs électroniques à base de matériaux organiques qui est intéressant du point de vue applicatif est leur multifonctionnalité. Lorsque plusieurs propriétés des composants de l'appareil peuvent être modulées via différents mécanismes de détection, les opérations de l'appareil peuvent être rendues plus faciles et plus efficaces. Par exemple, les complexes organiques à transition de spin offrent une réponse à de multiples signaux de stimulation et peuvent être utilisés dans des dispositifs multifonctionnels qui peuvent avoir des caractéristiques d'entrée/sortie distinctes et multiples.

De même, la possibilité de concevoir chimiquement un complexe moléculaire pour cibler des propriétés moléculaires et massives spécifiques et ainsi créer des dispositifs électroniques spécifiques avec des matériaux organiques offre des possibilités abondantes au-delà des limites de l'électronique traditionnelle conventionnelle.

Semblable au domaine de la spintronique organique où les aimants moléculaires et d'autres molécules organiques à proximité de matériaux magnétiques inorganiques sont étudiés, les matériaux ferroélectriques organiques émergent également pour trouver des applications potentielles. Les matériaux ferroélectriques organiques combinent les avantages de la présence de molécule organique avec l'applicabilité de la ferroélectricité, de la piézoélectricité et de la pyroélectricité présentes dans ces matériaux pour fournir des applications multifonctionnelles. Bien que ces matériaux avec des valeurs élevées de polarisation spontanée n'aient pas été abondants, les découvertes récentes de molécules ferroélectriques organiques stables à température

ambiante ont propulsé la motivation des chercheurs pour découvrir et concevoir de tels nouveaux matériaux.

Parmi tous les ferroélectriques organiques nouvellement découverts, l'acide croconique (AC) (4,5-dihydroxy-4-cyclopentène-1,2,3-trione, $H_2C_5O_5$) se distingue comme un système moléculaire unique dans lequel l'inversion de polarisation se produit par résonance tautomérie protonique produisant une valeur de polarisation très élevée, la plus élevée parmi tous les matériaux ferroélectriques organiques.[1, 2] Grâce à la valeur élevée de polarisation, il devient naturellement un candidat souhaitable pour les applications de dispositifs à base de ferroélectrique organique. Cependant, pour la réalisation du potentiel de ce ferroélectrique dans de telles applications, des études sur la croissance et les propriétés ferroélectriques sous forme de couches minces sont une condition préalable. Avec la motivation ci-dessus, nous avons étudié la croissance, l'optimisation de la croissance et les propriétés ferroélectriques des couches minces d'acide croconique au cours de cette thèse.

Dans le premier chapitre, nous décrivons brièvement les aspects généraux de la ferroélectricité. Après quoi, nous passons brièvement en revue le spectre des systèmes ferroélectriques organiques qui ont été étudiés jusqu'à présent. La section suivante est consacrée à l'acide croconique où nous discutons de la compréhension actuelle de l'origine et de la nature de la ferroélectricité qu'il contient. Nous terminons la section par de brèves discussions sur les études menées dans la perspective des applications de ce ferroélectrique organique.

Dans le troisième chapitre, nous décrivons les dispositifs de fabrication et de caractérisation utilisés pour les travaux de cette thèse. Outre les dispositifs de dépôts sous ultra-vide (UHV), une brève description des principes de fonctionnement de base des méthodes de caractérisation telles que la microscopie à force atomique (MFA) et la microscopie à force piézoélectrique (MFP) est également présentée.

Les chapitres suivants sont consacrés aux résultats obtenus à partir des expériences. Dans le chapitre 4, nous étudions l'aspect croissance des couches minces d'acide croconique sur des substrats spintroniquement pertinents tels que l'Au et le Co. Les efforts pour optimiser la croissance à température ambiante et leur impact sur les propriétés ferroélectriques des films moléculaires sont étudiés ex-situ par MFP.

Dans le chapitre 5, nous nous concentrons sur les propriétés ferroélectriques locales in situ détaillées des couches minces ci-dessus. En utilisant des pointes MFP standard, nous tentons de caractériser localement les films à des échelles nanoscopiques. Les caractéristiques ferroélectriques nanoscopiques locales telles que

la cartographie locale des domaines, la cartographie de l'orientation du vecteur de polarisation, l'étude des cycles d'hystérésis locales, etc. sont les points clés de ce chapitre.

Dans le chapitre 6, nous présentons des études sur des cristaux macroscopiques d'acide croconique fabriqués par voie physico-chimique. À l'aide de la microscopie en lumière polarisée, des études de diffraction des rayons X et de la MFA, nous tentons de caractériser les structures de surface particulières observées sur ces cristaux.

Enfin, dans le chapitre de conclusion, nous discutons des perspectives et des avantages des matériaux ferroélectriques organiques et nous discutons de la manière dont les travaux de cette thèse peuvent être utiles pour une exploration plus approfondie des nouveaux systèmes ferroélectriques organiques comme l'acide croconique et de leurs applications futures possibles en nanoélectronique et spintronique dispositifs.

## Résultats:

### 1- Propriétés ferroélectriques de l'acide croconique déposé sur des substrats pertinents pour la spintronique:

La conception de tout appareil électronique implique l'étape cruciale de fabrication des électrodes. Le choix du matériau d'électrode dépend du type d'applications pour lesquelles le dispositif est conçu. Habituellement, des films minces métalliques sont utilisés comme électrodes dans la plupart des appareils électroniques. Les métaux hautement conducteurs comme l'or, l'argent et le cuivre sont des exemples courants de matériaux d'électrode. Dans des domaines spécialisés comme la spintronique, d'autres types d'électrodes comme les électrodes en métal ferromagnétique trouvent une application substantielle.

Dans un dispositif nanoélectronique à structure verticale, les électrodes métalliques sont fabriquées à proximité directe du dispositif. En raison de la proximité étroite des films métalliques d'électrode avec le noyau du dispositif, le choix du matériau de l'électrode et la méthode de son intégration avec le système de noyau jouent un rôle crucial dans la définition des caractéristiques générales du dispositif. Par exemple, la résistance d'électrode, la qualité et les propriétés électroniques au niveau de la jonction électrode-noyau et les propriétés des matériaux d'électrode contribuent majoritairement aux propriétés du dispositif. Par conséquent, une étude approfondie du choix des bons matériaux d'électrode en termes de procédure de fabrication et l'étude des caractéristiques réelles du dispositif en présence des électrodes sont nécessaires avant toute fabrication de dispositif à grande échelle.

Dans cette section, nous explorons la croissance et les propriétés ferroélectriques de l'acide croconique dans des conditions ambiantes sur des films métalliques d'or et de cobalt qui sont couramment utilisés comme matériaux d'électrode dans le domaine de la nanoélectronique et de la spintronique. Une analyse comparative des propriétés sur les deux surfaces métalliques révèle qualitativement le degré d'aptitude des deux métaux en tant qu'électrodes tout en conservant les propriétés natives de l'AC.

Lorsqu'un film mince d'un matériau quelconque est déposé sur la surface d'un substrat, il existe diverses propriétés du substrat telles que la cristallinité, la rugosité, les défauts cristallins présents sur la surface et la réactivité de la surface qui affectent de manière significative la croissance et les propriétés du matériau déposé. Parmi ces propriétés de substrat, la plupart sont réglables, ce qui signifie, par exemple, que le type requis de cristallinité, le degré de rugosité de surface, etc. peuvent être obtenus par un réglage approprié des paramètres de fabrication et de post-fabrication. Cependant, des propriétés telles que la réactivité d'une surface de substrat sont intrinsèques au matériau du substrat et ne peuvent pas être modifiées sans utiliser des mesures drastiques telles que le traitement au plasma d'oxygène, la métallisation de surface avec des métaux de réactivité différente, etc., qui nécessitent souvent des arrangements techniques sophistiqués et beaucoup d'optimisation.

La réactivité chimique de surface d'un matériau de substrat peut être définie comme la tendance à interagir chimiquement et à former des liaisons chimiques avec les matériaux du dépôt. En particulier, lorsque des molécules organiques sont déposées sur des substrats métalliques, la réactivité de surface du substrat joue un rôle important dans la détermination de la croissance et des propriétés du système moléculaire. Les métaux comme l'Au fournissent des surfaces relativement inertes sur lesquelles l'interaction molécule-substrat est souvent régie par les forces de Van der Waal.[3, 4, 5] Ce type d'interaction moléculaire est appelé physisorption où les propriétés électroniques et géométriques des molécules déposées ne sont pas affectées par la surface du substrat inerte. Au contraire, les surfaces plus réactives comme celle des matériaux ferromagnétiques ont tendance à former des liaisons chimiques fortes avec les molécules organiques. Ce type d'interaction est appelé chimisorption. Sur le plan énergétique, la force de l'interaction substrat-molécule est déterminée par la différence entre l'énergie des molécules séparées et de métaux combinés et l'énergie du système hybride substrat-molécule. Une différence d'énergie au-delà de 1 eV est généralement considérée comme de la chimisorption. Cependant, en fonction de la réactivité de surface et du type de molécules, la gamme d'énergétique d'interface peut être bien plus grande que 1 eV, des énergies plus élevées correspondant à une

forte chimisorption se produisant au niveau de la première couche moléculaire près de l'interface et des énergies plus faibles correspondant à une faible chimisorption ou physisorption pour la deuxième couche moléculaire et au-delà. En raison de la large gamme d'échelle d'énergie, des propriétés physiques intrigantes peuvent émerger à l'interface substrat-molécule métallique, ce qui rend ce type d'interface différent de toutes les interfaces inorganiques.

Dans le domaine de la nanoélectronique et de la spintronique, l'interface entre l'électrode métallique et l'appareil joue un rôle essentiel dans la génération de la réponse électronique de l'appareil. Surtout, avec la réduction de taille, les appareils électroniques deviennent de plus en plus sensibles aux propriétés physiques qui émergent à l'interface. Compte tenu des effets intrigants qui peuvent se produire à l'interface de l'électrode métallique dans un dispositif organique électronique ou spintronique, il est essentiel d'étudier l'effet de l'électrode sur les propriétés moléculaires interfaciales. En outre, bien que les exemples ci-dessus d'effet induit par le substrat sur les propriétés de la couche moléculaire soient limités à quelques monocouches en dehors de l'interface, ces variations dépendantes du substrat des propriétés d'interface peuvent également avoir un impact substantiel sur les propriétés de couches épaisses de matériau organique qui sont couramment utilisées dans les appareils électroniques commerciaux. Par conséquent, il est de la plus haute importance d'étudier également l'effet induit par le substrat sur les propriétés des films organiques dans la limite d'encombrement.

Au vu de la discussion ci-dessus, avant la réalisation d'applications électroniques ou spintroniques de films minces d'AC, il devient nécessaire d'étudier les propriétés ferroélectriques d'AC sur des surfaces de substrat métalliques pertinentes dans des conditions ambiantes, en particulier sur des substrats à réactivité de surface élevée. Dans cet esprit, nous avons étudié la stabilité des propriétés des films d'AC déposés sur deux électrodes spintroniques couramment utilisées avec une nature cristalline similaire mais avec une réactivité de surface différente à température ambiante et sous pression atmosphérique.

Pour étudier l'effet des conditions de croissance sur les propriétés ferroélectriques des films d'AC sur la surface Au, deux paramètres de croissance, (i) le flux du dépôt et (ii) l'épaisseur du film, ont été modifiés. A partir de la caractérisation ferroélectrique ex-situ par Microscopie à Force de Piézoréponse (MFP), il a été observé que ces deux paramètres ont un effet significatif non seulement sur la morphologie de croissance mais également sur les structures de domaine ferroélectrique des couches minces d'AC. Comme le montre la fig. 1, en augmentant le flux du dépôt de 0,9

nm/min (panneau supérieur) à 1,6 nm/min (panneau inférieur), on observe une réduction de la distribution granulométrique avec la rugosité RMS diminuant de 12,8 nm à 8,7 nm. Pour une vitesse de 0,9 nm/min, le contraste similaire entre les cartes VMFP (MFP verticale) et LMFP (MFP latérale) (fig. 1 (b) et (c) respectivement) indique que la polarisation est inclinée par rapport à la surface du substrat. Cependant, pour une vitesse de 1,6 nm/min, le contraste de phase LMFP est facilement visible (fig. 1 (f)), le contraste de phase VMFP étant grandement minimisé (fig. 1 (e)), indiquant que la polarisation est maintenant principalement parallèle à la surface. Cela suggère que le taux de flux influence non seulement la morphologie du film, mais également l'ordre structurel de ces molécules polaires.

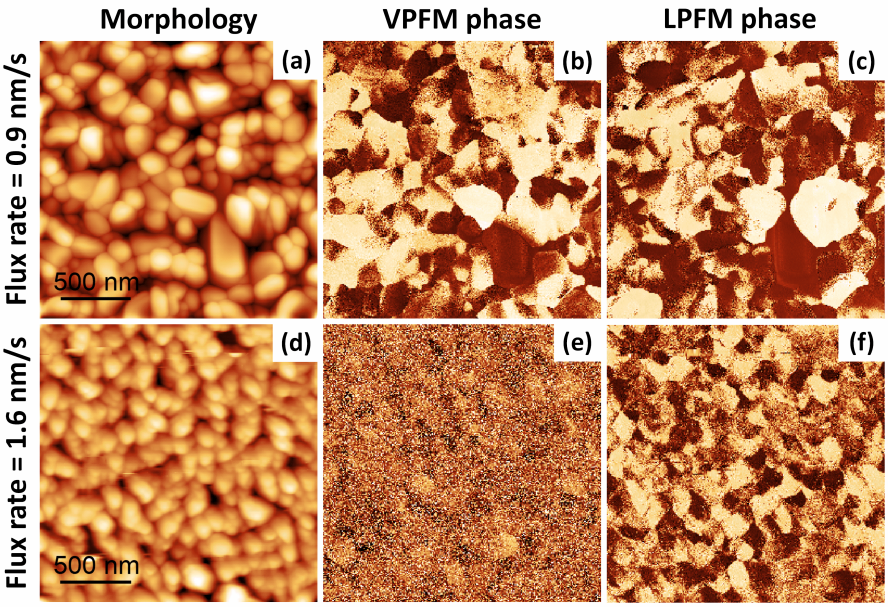


Figure 1: Dépendance au flux de la morphologie et de la structure des domaines ferroélectriques pour mica//Au/AC (50 nm). (a, d) Morphologie de la surface, (b, e) phase PFM hors plan, et (c, f) phase PFM dans le plan de la même région de l'échantillon de 2 × 2 $\mu m^2$. Les flux étaient de 0,9 nm/min (panneaux a-b-c) et 1,6 nm/min (panneaux d-e-f). La mise à l'échelle est normalisée aux valeurs minimale et maximale: (a) = (0 nm, 98 nm), (b) = (0 °, 252 °), (c) = (0 °, 326 °), (d) = ( 0 nm, 61 nm), (e) = (0 °, 241 °), (f) = (0 °, 249 °).

Nous avons également étudié les propriétés en faisant varier l'épaisseur du film d'AC déposé à un flux de 1,6 nm/min. Pour des épaisseurs de film de 50 nm, 100 nm et 200 nm, le contraste VMFP ne s'améliore pas, indiquant que la polarisation ferroélectrique a tendance à être dans le plan avec l'augmentation de l'épaisseur du film pour cette vitesse de dépôt de flux. Cependant, les grains d'AC ont tendance à atteindre une morphologie légèrement allongée qui est suivie par des structures

de domaine LMFP allongées. De plus, nous observons également une variation de contraste cohérente dans les cartes d'amplitude MFP pour les variations d'épaisseur et de flux des cas ci-dessus.

Les spectroscopies de commutation sur des régions granulaires spécifiques ont été réalisées avec une vitesse d'incrémentation des pas de tension de 0,1 Hz, c'est-à-dire à une vitesse de 0,2 V/s. À notre grande surprise, aucun des échantillons de films d'AC sur la surface d'Au n'a montré une inversion de polarisation robuste. Ceci a été confirmé en balayant la région avant et après les spectroscopies : il n'y a aucun changement dans les structures de domaine, que ce soit dans les cartes de phase VMFP ou LMFP. Lors d'une tentative, nous avons obtenu un cycle qui ressemblait à une inversion ferroélectrique se produisant uniquement dans une direction, mais un tel résultat n'était pas reproductible. Nous avons souvent observé qu'avec l'application de la tension de commutation, les grains de la région se déformaient et des trous morphologiques apparaissaient par la suite. Dans certains cas, la distorsion était si forte qu'elle pouvait être capturée avec la caméra optique du MFA.

Contrairement au cas de l'absence de commutation de polarisation des grains d'AC sur la surface d'Au, nous avons observé une commutation de polarisation réussie et robuste à partir de grains uniques sur la surface de Co. Nous présentons, sur la fig. 2 (a), (b) et (c), des cycles d'hystérésis de trois grandeurs MFP différentes, à savoir VMFP, LMFP et l'amplitude relative de la déformation du levier de la pointe. Ces données montrent qu'une commutation de polarisation est possible à une tension modérée. On observe que la courbe d'inversion / hystérésis de la phase LMFP (fig. 2 (b)) est beaucoup plus nette que celle de la phase VMFP (fig. 2 (a)), comme prévu puisque l'état de polarisation est dans le plan. Néanmoins, de minuscules caractéristiques de commutation peuvent également être remarquées dans la courbe d'inversion de phase VMFP (flèches grises de la fig. 2 (a)) qui apparaissent exactement aux mêmes valeurs de tension que celles de la courbe d'inversion de phase LMFP. L'inversion de phase réussie des phases verticales et latérales confirme la ferroélectricité d'AC sur Co.

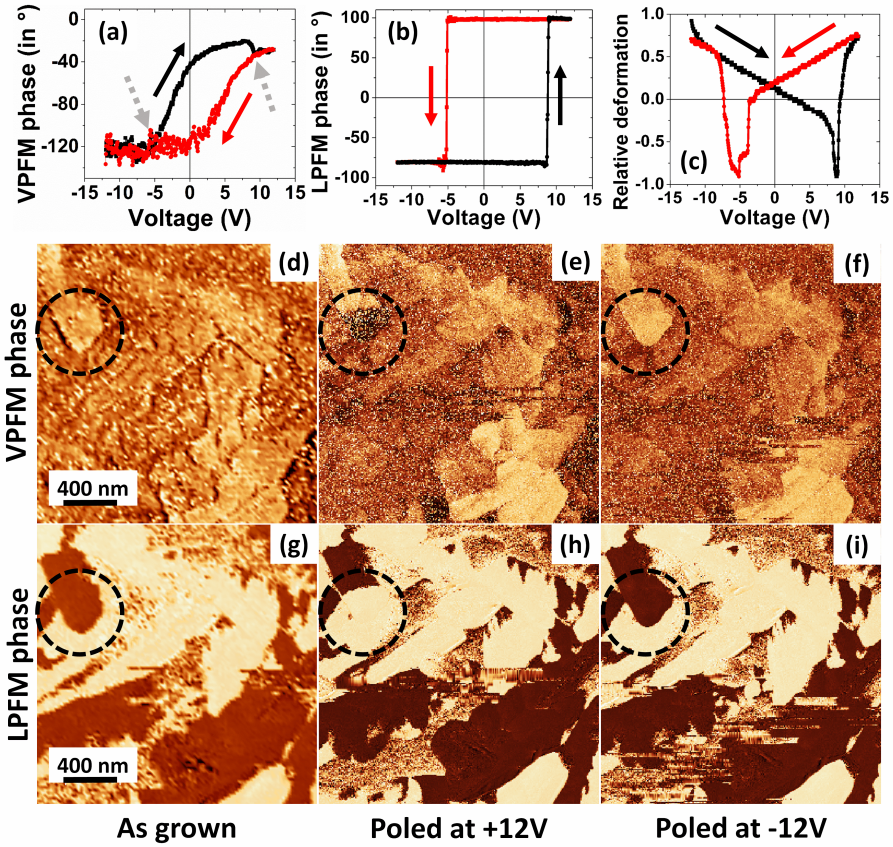


Figure 2: Cycles d'hystérésis d'inversion de polarisation et cartes de phase des états polarisés d'un domaine dans un film de mica // Au / Co / CA (50 nm). Le panneau supérieur montre les courbes d'inversion de polarisation en termes de phase VMFP (a), phase LMFP (b) et déformation relative des grains (c). Les flèches en pointillé en (a) indiquent les caractéristiques d'inversion faiblement visibles. Les courbes rouges et noires représentent les directions de la rampe de tension, rouges pour +12 V à -12 V et noires pour -12 V à + 12 V. Le panneau du milieu montre les cartes de phase VMFP à l'état de croissance (d), après polarisation avec +12 V (e) et après polarisation avec -12 V (f). Les panneaux inférieurs montrent les cartes de phase LMFP sur la même zone que (d), (e) et (f). Les états tels que développés du domaine sont indiqués en (d) et (g) où les cercles en pointillés encerclent le grain d'intérêt.

Les panneaux inférieurs de la fig. 2 démontrent un processus d'inversion de polarisation réussi. Fig.2 (c) et fig. 2 (g) montrent l'état ferroélectrique initial tel qu'imagé en utilisant respectivement VMFP et LMFP. Les images de phase après polarisation du domaine avec +12 V et -12 V sont montrées sur la fig. 2 (e) et 2 (f), respectivement, pour la phase VMFP et sur la fig. 2 (h) et 2 (i), respectivement, pour la phase LMFP. Un changement clair de contraste de phase entre les deux états de polarisation opposée est évident dans les phases VMFP et LMFP pour le grain d'intérêt (cercles en pointillés). L'inversion de polarisation observée sur la fig. 2

se passe principalement dans la direction dans le plan. Mais les caractéristiques de commutation mineures de la courbe d'inversion de phase VMFP et un changement clair du contraste VMFP du domaine indiquent la présence d'une composante non nulle d'inversion de polarisation se produisant également dans la direction hors plan. En outre, on peut noter qu'un champ appliqué perpendiculairement à la surface est capable d'inverser la polarisation dans le plan ce qui indique un couplage entre les deux composantes de polarisation. Ces deux faits indiquent que l'axe de polarisation net est incliné par rapport au plan du film à un petit angle.

De plus, pour vérifier la robustesse d'un processus d'écriture, nous écrivons à plusieurs reprises un domaine de polarité opposée (+12 V et -12 V) et capturons une image du domaine après chaque processus d'écriture. Une carte LMFP spatialement détaillée acquise après une telle expérience consécutive d'inversion de polarisation sur un film d'AC de 50 nm d'épaisseur sur Co est représentée sur la fig. 3. Le grain (cercle blanc) a survécu avec succès à des tentatives de polarisation répétées qui ont abouti à l'inversion systématique de l'état de polarisation d'une partie du grain, la polarité de tension déterminant l'état de polarisation résultant.

Les calculs de la théorie fonctionnelle de la densité et de la dynamique moléculaire prédisent qu'il devrait être possible de commuter la polarisation dans une couche 2D d'AC sur les surfaces d'Au et aussi sur une surface plus réactive d'Ag.[6, 7] Cependant, la confirmation expérimentale d'une telle commutation au niveau de quelques monocouches n'est pas facile et a fait défaut jusqu'à présent. Dans les couches 2D, la polarisation du réseau d'AC est essentiellement dans le plan du film nécessitant un champ électrique dans le plan pour la commutation, alors que dans un film polycristallin massif, l'axe de polarisation peut être à un angle par rapport au plan du film. Ainsi, même avec un champ électrique hors plan comme celui émanant d'une pointe MFP, on s'attend à ce que l'inversion de polarisation puisse avoir lieu à la fois dans et hors des directions du plan. Ainsi, on ne sait pas pourquoi sur la surface d'Au les propriétés ferroélectriques réversibles de films d'AC ne sont pas robustes alors que sur la surface du Co elles le sont. En l'absence de toute information structurelle des grains d'AC sur les deux surfaces, nous essayons d'expliquer qualitativement l'anomalie comme suit.

Des études STM récentes sur la croissance de couche 2D d'AC sur les surfaces d'Au et d'Ag montrent que les molécules d'AC forment différents types de réseaux en fonction du substrat, principalement en raison de différentes interactions entre les molécules du substrat.[6, 7] Les calculs montrent que l'interaction d'AC avec l'Au est plus faible que celle avec l'Ag, qui est un substrat plus réactif. En outre, les

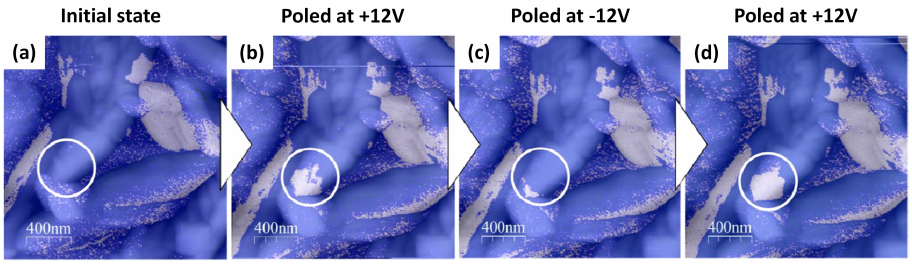


Figure 3: Réversibilité de polarisation d'un domaine d'AC sur la surface de Co. Le contraste gris-bleu montre les domaines dans le plan dans les cartes de phase LMFP d'une région de 2×2 µm$^2$ dans l'état initial (a), après polarisation consécutive à + 12 V (b), -12 V (c) et à + 12 V (d).

études STM révèlent une mobilité de surface élevée et une faible barrière de diffusion des couches d'AC sur la surface d'Au. Des réseaux d'AC hautement instables pour une épaisseur de couverture inférieure à 1 monocouche ont également été observés sur la surface d'Au.[7] Des études similaires d'AC sur la surface du Co n'ont pas été rapportées jusqu'à présent, mais grâce à une réactivité de surface plus élevée ou à une interaction Co-molécule sur la surface du Co, des réseaux de couches d'AC stables peuvent être attendus.

Ceci est cohérent avec notre observation des propriétés robustes d'AC sur la surface du Co. Nous pensons que l'interaction molécule substrat plus faible lors de la croissance initiale d'AC sur la surface d'Au est à l'origine du manque de robustesse observé dans les propriétés ferroélectriques sur la surface d'Au. Cela peut également expliquer la distorsion observée de la topographie du film après des tentatives de commutation de polarisation dans le cas d'un substrat Au. Ainsi, nous observons que des substrats métalliques comme le Co avec une réactivité de surface relativement plus élevée contribuent à stabiliser les propriétés ferroélectriques d'AC. Ceci, cependant, contraste avec le scénario habituellement observé où la réduction de la réactivité de surface stabilise les propriétés moléculaires.

Sur la surface d'Au, la présence de plusieurs domaines dans un seul grain d'AC est un signe d'ordre ferroélectrique mais le manque d'inversion de polarisation robuste soulève des doutes sur la facilité de commutation des grains d'AC sur la surface d'Au. Comme la preuve de la ferroélectricité nécessite nécessairement l'observation de l'inversion de polarisation, il est difficile de conclure sur la réponse ferroélectrique d'AC sur la surface d'Au, cependant, la réponse piézoélectrique est évidente à travers la présence d'un contraste net dans les images de phase verticale et latérale. Sur la surface Co, la commutation se produit principalement le long du plan du film avec

une petite composante le long de sa normale.

En conclusion, il apparaît qu'il est possible de fabriquer des couches minces d'acide croconique ferroélectrique commutables et robustes sur Co, alors que sur des substrats moins réactifs comme l'Au, ce n'est pas si évident. Contrairement aux tentatives faites dans le domaine de la spintronique organique où l'objectif est d'atténuer la force d'hybridation substrat-molécule pour stabiliser les propriétés moléculaires, nous observons un impact positif de l'interaction substrat-molécule ou de la réactivité de surface sur les propriétés moléculaires. Nos observations pourraient servir de guide pour le développement de dispositifs multifonctionnels basés sur des films composites d'acide croconique ferroélectrique. La stabilité des propriétés ferroélectriques sur la surface du Co combinée à la densité de charge de polarisation élevée du AC devrait encourager la fabrication de dispositifs pour des applications de spintronique; par exemple, des dispositifs multiferroïques artificiels hybrides organiques (ferroélectriques) -inorganiques (ferromagnétiques), des jonctions tunnel ferroélectriques organiques (O-FTJ), etc. Enfin, nous pensons que des études supplémentaires sur une variété de surfaces métalliques ainsi que des simulations détaillées sur les interfaces surface-molécule et également des études dans des conditions in-situ sont nécessaires pour explorer attentivement la relation entre la stabilité des couches massives d'AC et la réactivité de surface du métal.

**2- Etude du renversement de la polarisation d'un matériau ferroélectrique à l'échelle nanométrique:**

La découverte récente d'une ferroélectricité stable à température ambiante dans l'acide croconique organique avec des valeurs de polarisation équivalentes à celles trouvées dans les matériaux ferroélectriques inorganiques et les plus élevées parmi les matériaux ferroélectriques organiques[1], a ouvert des possibilités de réaliser des myriades de dispositifs nanoélectroniques et spintroniques à base de ferroélectriques organiques qui combinent les avantages de la présence d'un matériau organique et d'une valeur de polarisation ferroélectrique élevée. De telles possibilités nécessitent une compréhension adéquate des propriétés ferroélectriques des films d'acide croconique déposés sur des surfaces qui sont couramment utilisées dans la fabrication de dispositifs. Outre la grande valeur de polarisation de l'acide croconique, le fait que la polarisation puisse être inversée avec de petits champs électriques à des fréquences aussi élevées que 1 kHz[1] en fait un candidat potentiel pour le fonctionnement des dispositifs à basse tension. En outre, l'observation d'une grande susceptibilité non

linéaire du second ordre[8] et la commutation ferroélectrique photoinduite[9] suggèrent que l'acide croconique peut être potentiellement utile pour les dispositifs optiques ou optoélectroniques non linéaires.

Pour explorer le potentiel de ce candidat ferroélectrique prometteur du point de vue des applications de dispositifs nanoélectroniques, des études substantielles des propriétés ferroélectriques dans des dispositifs microscopiques et nanoscopiques basés sur des films minces d'acide croconique sont nécessaires. Alors que plusieurs types d'études macroscopiques sur des cristaux relativement grands et sur la croissance de films ultra-minces sur des surfaces métalliques ont été réalisées,[6] les études sur la ferroélectricité, la croissance de couches minces ne sont qu'à leurs premiers stades.[10] Par conséquent, les études sur l'aspect applicatif des dispositifs microscopiques de l'acide croconique sont sévèrement limitées.

En outre, un dispositif ferroélectrique microscopique peut contenir plusieurs grains d'un espaceur ferroélectrique polycristallin à l'intérieur de chaque dispositif. Mais à mesure que les dimensions latérales des dispositifs nanoélectroniques diminuent, le dispositif typique se rapproche des dimensions latérales des grains, constitués de seulement quelques grains ou éventuellement d'un seul grain. Dans un dispositif microscopique, les propriétés ferroélectriques des grains individuels peuvent être moyennées tout en définissant la réponse globale du dispositif. Cependant, à l'échelle nanoscopique des dispositifs, en raison des orientations cristallographiques aléatoires et, par conséquent, des propriétés ferroélectriques des grains individuels, des différences significatives entre les performances du dispositif fabriqué à partir de la même couche ferroélectrique peuvent apparaître. Dans le contexte ci-dessus, d'une part, il devient indispensable d'optimiser la croissance pour rendre les grains aussi identiques que possible et d'autre part, il devient important de descendre l'échelle des caractérisations ferroélectriques détaillées jusqu'au domaine nanoscopique.

Ainsi, alors que les futurs dispositifs ferroélectriques organiques semblent posséder un potentiel pour les futurs dispositifs électroniques en raison de plusieurs avantages significatifs par rapport à leurs homologues inorganiques et que la taille latérale des dispositifs électroniques tend vers le régime nano, l'analyse à l'échelle nanoscopique des propriétés ferroélectriques des matériaux organiques devient naturellement une direction essentielle. Par conséquent, pour explorer les véritables potentiels de l'AC dans les futurs dispositifs électroniques nanoscopiques ferroélectriques organiques, il est d'une importance cruciale d'étudier ses propriétés ferroélectriques nanoscopiques. En raison du type particulier de l'origine ferroélectrique de l'AC[2], il peut être encore plus intéressant de voir comment ses propriétés fer-

roélectriques évoluent au fur et à mesure que les dimensions latérales se réduiront progressivement aux dimensions moléculaires. En outre, la physique fondamentale associée à la cinétique et à la dynamique de commutation, aux parois de domaine et à leur mouvement etc. peut être explorée à l'échelle nanoscopique.[11, 12]

Une technique courante pour caractériser un matériau ferroélectrique consiste à mesurer le cycle d'hystérésis de la polarisation en fonction de la tension appliquée, ceci dans une géométrie où le matériau à étudier est placé entre les armatures d'un condensateur. Les courants qui apparaissent dans ces expériences en raison du renversement de polarisation sont de nature purement macroscopique car la dimension latérale des condensateurs est généralement de l'ordre de plusieurs dizaines de micromètres. Le mécanisme de commutation de polarisation d'un ensemble de grains dans de telles géométries est un processus statistique, entravant l'accès aux propriétés ferroélectriques dans des régions nanométriques telles que des grains individuels. De plus le courant de renversement est fréquemment parasité par un courant de fuite dû aux points chauds de conduction ainsi qu'aux charges piégées dans le matériau ou aux interfaces.[13, 14]

Nous introduisons la technique de caractérisation nanoscopique appelée spectroscopie de courant de commutation nanoscopique pour étudier les propriétés nanoscopiques des couches minces polycristallines d'AC. Cette méthode est basée sur la détection et la mesure de faibles courants de commutation provenant de l'inversion de polarisation de régions nanoscopiques formées d'un seul grain du matériau ferroélectrique. En capturant simultanément la réponse électromécanique de la région nanoscopique, la véracité des mesures de courant de commutation obtenues est également établie. De plus, en analysant cette réponse électromécanique, on obtient des informations plus approfondies sur la cinétique des processus d'inversion de polarisation se produisant à l'échelle nanométrique. De plus, en effectuant plusieurs mesures sur une même région nanoscopique, nous étudions l'aspect statistique de la commutation de polarisation nanoscopique.

Le courant de commutation apparaît sous forme de pics nets en spectroscopie I-V. La forme du courant de commutation contient des informations non seulement sur la dynamique et la cinétique de la commutation, mais également sur le mécanisme de commutation sous-jacent dans le matériau particulier. Par exemple, des études menées dans les années 1960 montrent que la symétrie du pic de commutation peut être associée à la force de l'interaction domaine-noyau qui détermine la vitesse de déplacement de la paroi du domaine. Les études sur la dépendance de la forme du pic de commutation sur l'intensité du champ électrique, la tem-

pérature et l'épaisseur du film fournissent des informations encore plus détaillées et fondamentales telles que le temps de mouvement de la paroi de domaine, le temps de nucléation et l'interaction domaine-noyau.[11, 12, 15] Ces études fondamentales sur les propriétés de commutation étaient de nature macroscopique impliquant les courants de commutation d'un grand nombre de grains individuels ou de cristaux ferroélectriques macroscopiques. Notre approche d'observation des courants de commutation des régions nanoscopiques apportera des informations plus approfondies et récentes à notre compréhension des propriétés fondamentales ci-dessus associées à un événement de commutation ferroélectrique, en particulier la nature stochastique de la commutation de polarisation se produisant à l'échelle nanométrique. En outre, des études détaillées des pics de courant de commutation soutenues par une modélisation appropriée des interfaces peuvent fournir une image des interfaces métal/ferroélectrique en termes de nature des charges de blindage et d'aspect électrochimique de l'interface.

Du point de vue de l'application également, la détection de courants de commutation à partir d'une région ferroélectrique nanoscopique peut être d'une importance significative car presque toutes les applications commerciales utilisent des films minces ferroélectriques polycristallins. Par exemple, il y a eu des tentatives d'employer une limitation électronique des courants de commutation ferroélectriques pour contrôler de manière déterministe la zone commutée dans une région commutable macroscopique et ainsi articuler un mécanisme de commutation ferroélectrique à plusieurs étages de la région particulière. Cela fournit un moyen contrôlable de matérialiser le concept de stockage de données à plusieurs niveaux dans le même volume de matière, chaque état ferroélectrique intermédiaire fonctionnant comme un niveau, multipliant ainsi la densité de bits dans les systèmes de stockage de données à base ferroélectrique sans avoir besoin de réduire la taille physique des bits . En suivant le concept ci-dessus, Lee et al[16] pourraient en effet démontrer l'écriture de 8 états logiques bien définis d'un élément FErroelectric Random Access Memory (FERAM) et improviser un élément de mémoire à un bit pour former un système en trois parties. Comprendre les propriétés des courants de commutation à l'échelle nanométrique ou granulaire est au cœur de ces idées et s'avérera utile pour l'ingénierie d'une large gamme de dispositifs électroniques. En outre, l'extension directe d'une telle mise en œuvre aux régions nanoscopiques pourrait ouvrir des possibilités d'augmenter la densité de stockage des FERAM disponibles dans le commerce.

La spectroscopie de courant de commutation a été réalisée à l'échelle nanoscopique

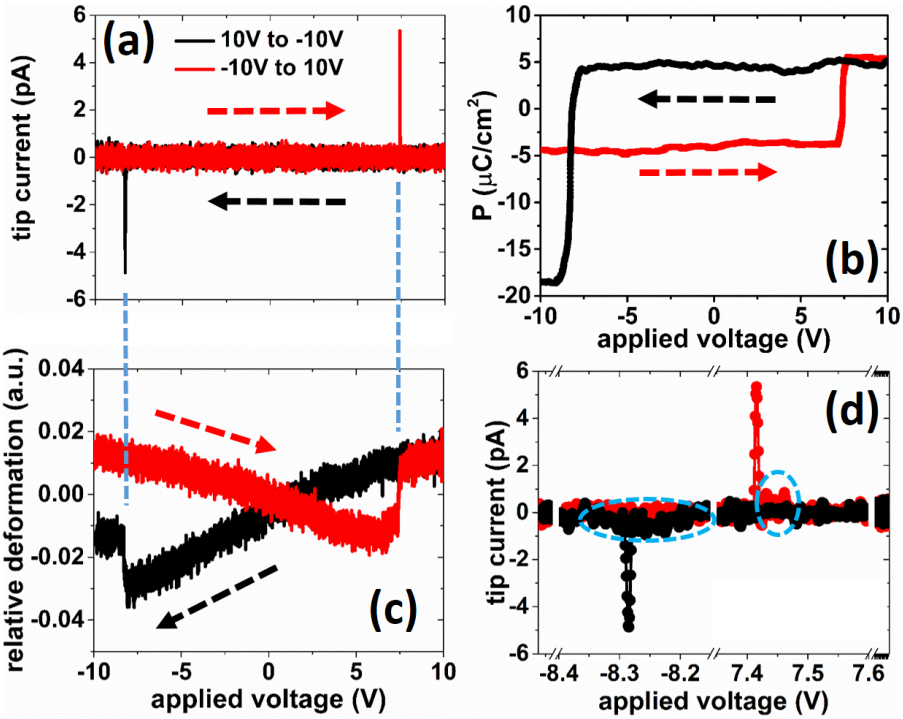


Figure 4: Courant de renversement, polarisation et déformation sur les domaines d'AC nanoscopiques. (a) montre la courbe I-V observée avec les pics de courant caractéristiques correspondant au renversement de la polarisation. (b) montre la courbe P-V calculée à partir de (a), où P est la polarisation en $\mu C/cm^2$. La déformation du grain lors du renversement est indiquée en (c). La coïncidence entre les pics de courant en (a) et les sauts en (c) prouve que les pics de courant en (a) sont bien dus au renversement de la polarisation. (d) montre un zoom de (a) autour des pics. Les courbes en pointillés montrent la présence de faibles courants de renversement autour des pics principaux. Ces faibles courants montrent que le renversement peut se faire en plusieurs étapes, progressives et plus rapides. Aucun signal d'excitation alternatif n'a été appliqué pendant la mesure.

sur les films d'AC d'épaisseur 50 nm déposés sur une surface de 4 nm de Co en utilisant la MFP in situ. Comme nous l'avons vu au chapitre précédent, la croissance à température ambiante de couches minces d'AC sur des surfaces de Co résulte en des films quasi-continus avec des grains généralement aussi grands que ∼300 nm de diamètre. Habituellement, la région nanoscopique sondée est constituée d'un seul grain. Parfois, il peut inclure des régions de plusieurs domaines voisins.

Les caractérisations MFP ont été réalisées sous UHV à température ambiante en mode contact. L'environnement ultra-vide et les mesures de MFP in situ minimisent la présence d'impuretés qui autrement parasiteraient les analyses des courants de commutation mesurés. Le courant de commutation de polarisation, la visualisation du domaine et les mesures de cycle d'hystérésis ont été obtenus en utilisant le mode MFP standard, équipé d'un étage amplificateur de courant à gain élevé. L'inversion de polarisation a été déclenchée en appliquant une rampe de tension à la pointe conductrice MFP en contact avec la région nanoscopique. Les courants de commutation provenant de l'inversion de polarisation dans la région nanoscopique de l'échantillon ont été mesurés avec succès sous forme de pics nets dans les courbes I-V. Nous avons également mesuré simultanément la réponse à la déformation par la déviation de l'assemblage pointe-levier causée par la déformation du grain lors de l'inversion de polarisation.

Pour faciliter l'observation des courants de commutation, nous avons désactivé le signal d'excitation alternatif du MFP pour éviter les bruits périodiques indésirables et appliqué uniquement la rampe de tension continue à la pointe et mesuré le courant de pointe à l'aide de l'amplificateur de courant en fonction de la tension appliquée.

La figure 4 (a) montre un tel tracé caractéristique I-V obtenu à partir de la région nanoscopique susmentionnée après soustraction d'un fond linéaire (courbe I-V mesurée en l'absence de tout échantillon). Comme on peut le voir sur la figure, le bruit dans notre mesure I-V se situe dans la gamme sub-pA (niveau de bruit $\sim 2\times10^{-13}$ A rms). Cela nous a aidé à détecter proprement de très petites valeurs de courants de commutation provenant de régions nanoscopiques du matériau. Deux pics de courant de commutation nets peuvent être clairement vus lorsque la tension de polarisation est balayée vers le haut, puis vers le bas. Bien que ces pics aient une amplitude similaire, leur position est différente. Hormis ces pics de courant de commutation, nous n'avons observé aucun courant de conduction mesurable d'aucune sorte (tunnel, fuite, charges piégées...).

Lors de la mesure I-V, nous avons également mesuré simultanément la composante verticale (normale au plan du film) de la force relative qui s'exerce sur la

pointe en contact avec le grain. Cela nous a donné une mesure directe de la déformation du grain (réponse à la déformation) qui se produit en synchronisation avec le processus d'inversion de polarisation via l'effet piézoélectrique inverse (fig. 4 (c)). Il est évident que le principal saut dans la déformation du grain (fig. 4 (c)) et les pics de courant sur la figure 4 (a) se produisent à la même tension, confirmant une véritable inversion de polarisation.

De la fig. 4 (a) on conclurait que l'inversion se produit en un seul saut brusque aux positions données par les pics du courant de commutation. Cependant, si l'on agrandit l'échelle pour se concentrer sur la base des pics comme sur la fig. 4 (d), nous voyons que l'inversion commence brusquement à ∼7,42 V produisant un pic principal dans le courant de commutation, mais n'est complète qu'à ∼7,47 V. De même, le pic à ∼ -8,28 V n'est ni une indication pour le début ni l'achèvement de l'inversion. Ces caractéristiques sont dues au caractère aléatoire de l'inversion, qui est un processus activé thermiquement au-dessus des barrières énergétiques. Comme le courant de commutation est proportionnel à la vitesse des changements de polarisation, une inversion en plusieurs étapes conduit à des pics dont la hauteur dépend des taux d'inversion. Ce caractère aléatoire est moyenné au niveau macroscopique mais particulièrement important ici à l'échelle nanométrique.

Le courant de commutation peut être utilisé pour déduire la polarisation P du matériau. La dépendance de la polarisation P est obtenue en intégrant le courant de la fig. 4 (d) dans le temps (chaque point de tension correspond à 100 µs), divisé par la zone commutée. La cycle P-V calculé est représentée sur la fig. 4 (b). On peut voir que même si la hauteur des pics de courant de commutation sur la fig. 4 (a) sont presque les mêmes dans les deux sens de la tension appliquée, il existe une différence significative dans les valeurs calculées de polarisation pour les deux sens de l'application de la tension.

Cet écart peut s'expliquer par le fait que la valeur du courant de commutation mesuré ne dépend pas seulement de la zone de la région commutée mais également de la cinétique du processus de commutation dans cette région. La polarisation étant une intégration temporelle du courant instantané, la cinétique de commutation affecte grandement l'estimation de son amplitude. Sur la fig. 4 (d), nous voyons que les pics ne sont pas symétriques: leurs formes sont différentes et le pic du côté des tensions positives s'étend sur une durée de ∼900 µs alors que le pic du côté des tensions négatives a un plus grand étalement dans le temps avec une durée de ∼1200 µs.

Nous pensons qu'une partie importante du courant de commutation lié à l'inversion

de polarisation n'est pas détectée car elle est inférieure aux possibilités de détection de notre instrument; une inversion progressive peut produire un courant de commutation enfoui dans le niveau de bruit basse fréquence. Dans ce cas, il y aura une perte de polarisation lors de l'intégration temporelle qui aboutira à une perte apparente de polarisation de saturation. Ainsi, l'asymétrie de la cinétique de commutation se traduit par une asymétrie des densités de polarisation dans les cycles P-V. Kwon et al. ont également observé une densité de charge de polarisation légèrement asymétrique attribuée à l'asymétrie de la jonction[17]. Nous montrons qu'une telle asymétrie peut également résulter de problèmes liés aux mesures de courant. La valeur maximale de $\sim$12 µC / cm$^2$ que nous avons obtenue pour la polarisation de saturation est donc une limite inférieure de la valeur réelle. Cette valeur est 60% inférieure à la valeur de 30 µC / cm$^2$ rapportée pour les cristaux d'AC [2]. Si nous supposons que nos grains ont la même structure et donc la même polarisation que les cristaux massifs, la sous-estimation de la polarisation de saturation laisse entrevoir les difficultés à capter la totalité du courant de commutation à l'échelle nanométrique.

Pour approfondir la nature stochastique de l'inversion, nous avons répété les mêmes mesures onze fois sur la même région, en gardant tous les paramètres inchangés. Les courbes courant (I) - voltage (V) correspondantes sont représentées sur la fig. 5. On voit que les pics apparaissent à des positions de tension aléatoires (fig. 5 (a)). Leur hauteur et leur position sont asymétriques par rapport à la direction du champ électrique appliqué pour toutes les inversions (fig. 5 (a), (b)). Il est évident qu'une propriété spécifique d'un matériau ne peut être déduite d'une seule mesure; un traitement statistique est nécessaire. La hauteur et les positions des pics de courant visibles sur la fig. 5 (a) sont rapportés sur la fig. 5 b). Deux groupes de points sont visibles, un pour les tensions négatives et un pour les tensions positives. Les moyennes et écarts types correspondants sont (-8,3 $\pm$ 0,3 V; -3,7 $\pm$ 0,9 pA) et (7,0 $\pm$ 0,7 V; 4,2 $\pm$ 1,6 pA). Il n'y a pas de différence significative dans la hauteur moyenne des deux groupes, mais la hauteur du pic actuel n'a pas de signification évidente: seule l'intégration temporelle actuelle sur le pic exprimant la polarisation en a une. Les valeurs de tension auxquelles les inversions ont lieu ne sont pas symétriques; elles sont plutôt polarisé vers les tensions négatives. Ce décalage est probablement dû à un champ de polarisation interne dont l'ampleur et la distribution dépendent de la composition, de la microstructure et de l'histoire thermique et électrique du système.[18] Lorsqu'il s'agit du fonctionnement d'un dispositif nanoscopique, la distribution statistique de la tension d'inversion doit être considéré.

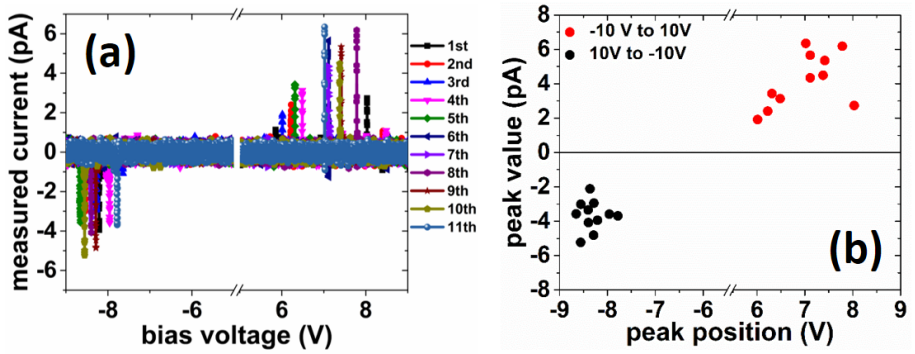


Figure 5: Nature stochastique de la commutation de polarisation. (a) montre l'ensemble des spectroscopies I-V répétées sur la même région avec des paramètres expérimentaux inchangés avec un intervalle de temps de 100 µs entre chaque deux mesures successives. Les étiquettes de tracé montrent la séquence de chaque mesure. (b) montre un diagramme de dispersion des maximums de courant de commutation des courbes I-V représentées en (a) par rapport à la tension appliquée. La nature aléatoire de la distribution décrit le comportement stochastique du processus de commutation de polarisation.

Pour une mémoire ferroélectrique par exemple, un nombre élevé d'expériences doit être fait pour trouver la probabilité requise d'inverser la polarisation à une tension donnée.

Comme perspectives, compte tenu de l'importance d'accéder aux courants de commutation de petits grains ferroélectriques, nous proposons la méthode de mesure suivante. Les deux aspects les plus importants d'une telle mesure délicate sont (i) une pointe fine et (ii) un amplificateur de courant à gain élevé à faible bruit. Une pointe fine réduit concentre le champ électrique sur une petite région. Une pointe conductrice atomiquement finee peut être utilisée pour balayer la morphologie de la surface en mode sans contact, après quoi la pointe peut être mise en contact avec un grain spécifique et des mesures spectroscopiques peuvent être effectuées. Le balayage de la surface en mode sans contact causera un minimum de dommages à la pointe avant que la spectroscopie du courant de commutation ne soit effectuée. De plus, la tension de rampe peut être remplacée par des impulsions de tension électrique avec une largeur d'impulsion et une hauteur d'impulsion appropriées. Cela réduira l'impact des effets électrostatiques présents pendant les mesures en raison de la tension continue appliquée en facilitant une mesure de champ-off DC chaque fois que nécessaire.

En conclusion de cette partie, nous avons sondé les propriétés ferroélectriques nanoscopiques d'un nouveau matériau ferroélectrique organique, l'acide croconique sous forme de film mince sous ultra-vide et dans des conditions de mesure in situ à

l'aide de spectroscopie MFP et de courant de commutation. Nous avons pu détecter les minuscules courants de commutation de polarisation nanoscopiques, de l'ordre de quelques pico ampères, à partir de la surface du film d'acide croconique en utilisant directement la pointe de la sonde comme électrode supérieure. Ce travail est la toute première démonstration de détection de courants de commutation nanoscopiques à partir de la surface d'un matériau ferroélectrique organique. À partir des courants de commutation mesurés, nous avons estimé les valeurs de polarisation nanoscopique d'un film mince d'acide croconique. La valeur de polarisation de l'acide croconique n'était auparavant connue que sous sa forme cristalline et nos travaux ont révélé que la valeur de polarisation reste du même ordre de grandeur dans les régions nanoscopiques d'un film mince que celle des cristaux. Bien que notre valeur observée de polarisation de 12 µC / $cm^2$ soit presque ∼60% plus petite que celle rapportée pour les cristaux d'AC qui est de 30 µC / $cm^2$, cela nous a conduit à réaliser la cinétique d'inversion de polarisation asymétrique à l'échelle nanométrique qui peut être en partie à l'origine de cette perte de polarisation estimée.

## Conclusion

Pour conclure, cette thèse se prépare à un moment où, d'un côté, en raison de la demande croissante de systèmes ferroélectriques organiques, la recherche s'intensifie sur la recherche de nouveaux matériaux ferroélectriques organiques et de l'autre, des études sur des candidats déjà disponibles.  avec une polarisation spontanée élevée comme l'acide croconique ne sont pas abondants. Nous pensons que ce travail apportera un aperçu de la possibilité d'envisager ce nouveau système organique pour d'éventuelles applications futures et encourageons les chercheurs travaillant sur des sujets liés aux couches minces ferroélectriques à attirer leur attention vers les perspectives de l'acide croconique et des ferroélectriques organiques en général. De plus, avec l'expertise de notre groupe en spintronique organique, en science des interfaces et en systèmes moléculaires déposés sur des surfaces, nous prévoyons d'explorer l'aspect multifonctionnel de ce ferroélectrique organique pour réaliser des spinterfaces moléculaires actives contrôlables électriquement.

# Motivation and organization of the thesis

Modern history of mankind has seen several industrial revolutions in the past when the three key sectors for progress of human society, namely, energy, transportation and communication have been revolutionized by new inventions fueled by scientific discoveries. Today, we are in the beginning of another industrial revolution when the unprecedented progress over the last few decades in the digital technologies and software industries is beginning to emerge revolutionary in all the aforementioned sectors of human progress. At the heart of this revolution stays the hardware of all the modern digital electronic components, be it the memory storage devices or the information processing chips. However, the manufacturing platforms for the electronic devices and components are still majorly stuck with the conventional semiconductors based design architectures. The continuously increasing demand for miniaturization of electronic devices has pushed the dimensions of electronic components to reach nanoscopic level where further reduction in dimensions seems like a challenging task both in terms of feasibility and viability. More importantly, the heat generation in electronic components with the reduction of dimensions has been devastating for the efficient functioning of the components. Further, when on one hand, we are looking for alternative energy sources to fuel our future and employing the modern digital technology to look for alternative solutions to energy and environment related problems, on the other hand, a significant portion of available energy being wasted merely as heat that is generated in all these electronic activities has been the bottleneck issue of energy saving. With the digitalization of economic, commercial and all other human activities, the astounding increase in electronic devices is eminent which raises concern for the power consumption and thermal energy loss in future usage of electronic devices. This has called for actions in looking for alternative platforms for the design of electronic components and devices which can be more energy efficient.

The search for alternative technologies has led to research and exploration in several fields. For example, exploiting the spin attribute of electrons to build electronics has emerged as the field of spin-electronics or commonly known as spintronics, whereas, all the conventional electronics utilize the charge of electrons to perform tasks. The emergence of spintronics has revolutionized the digital data storage systems which has so far been the ground on which the upcoming industrial revolution is staged. Similarly, the use of organic complexes to perform electronics and design electronic components has independently given birth to the field of organic electronics. On a parallel track, the use of organic molecules or carbon based materials in spintronics is being termed as the field of organic spintronics. Be it the conventional electronics or spintronics, the use of organic molecules provides a pathway to realize low power consuming energy efficient electronic devices.

Another aspect of organic materials based electronic devices which is interesting from application point of view is their multifunctionality. When multiple properties of the device components can be modulated via different probing mechanisms, device operations can be made easier and more efficient. For example, spin-crossover organic complexes offer response to multiple stimulus signals and can be used in multifunctional devices that can have distinct and multiple input/output characteristics.

Similarly, the possibility to chemically engineer the molecular complex to target specific molecular and bulk properties and thereby create specific electronic devices with organic materials offers abundant possibilities beyond the limits of conventional mainstream electronics.

In the field of organic spintronics where molecular magnets and other organic molecules in proximity to inorganic magnetic materials are explored, organic ferroelectric materials are also emerging to find potential applications. Organic ferroelectric materials combine the advantages of the presence of organic molecule with the applicability of ferroelectricity, piezoelectricity and pyroelectricity present in such materials to provide multifunctional applications. Although such materials with high values of spontaneous polarization have not been abundant, recent discoveries of stable room temperature organic ferroelectric molecules have propelled the motivation of researchers to discover and design such new materials.

Out of all the newly discovered organic ferroelectrics, Croconic Acid (4,5-dihydroxy-4-cyclopentene-1,2,3-trione, $H_2C_5O_5$) stands out as a unique molecular system where the polarization reversal takes place via resonance assisted concerted intermolecular proton tautomerism reuslting in a very high value for polarization which is the

highest among all organic ferroelectric materials. Thanks to the high value of polarization, it naturally becomes a desirable candidate for organic ferroelectric based device applications. However, for the realization of the potential of this novel organic ferroelectric in such applications, studies on growth and ferroelectric properties in its thin film forms are a prerequisite. Further, ultra high vacuum evaporation of this organic molecule makes it possible to fabricate its thin films which then allows to integrate its fabrication with other ultra high vacuum fabrication processes leading to the fabrication of a broad range of organic inorganic systems based on this organic ferroelectric With the above motivation, we have studied the growth, growth optimization and ferroelectric properties of Croconic Acid thin films on surfaces of commonly used electrode materials in the course of this thesis. We have also studied the macroscopic crystals of it in an attempt to gain deeper insight into the fundamental aspects of the ferroelectricity present in such crystals.

In the first chapter, we briefly describe the general aspects of ferroelectricity. After which we move on to summarizing briefly the spectrum of organic ferroelectric systems that have been studied so far. The following section is devoted to Croconic Acid where we discuss about the current understanding of the origin and nature of ferroelectricity in it. We end the section with brief discussions on the studies carried out along the applications perspective of this organic ferroelectric.

In the second chapter, we describe the fabrication and the characterization setups used for the work of this thesis. Along with the Ultra-High Vacuum (UHV) fabrication assemblies and multiple probe based characterization setup, a brief description of the basic working principles of the characterization methods such as Atomic Force Microscopy (AFM) and Piezoresponse Force Microscopy (PFM) is also presented.
The following chapters are dedicated to the results obtained from the experiments. In chapter 3, we investigate the growth aspect of the thin films of Croconic Acid on spintronically relevant substrates such as Au and Co. The efforts to optimize the room temperature growth and their impact on the ferroelectric properties of the molecular films are studied using PFM.

In chapter 4, we focus on the detailed in-situ local ferroelectric properties of the above thin films. Using the standard PFM probe tips, we attempt to locally characterize the films at nanoscopic scales. Local nanoscopic ferroelectric features like local domain mapping, polarization vector orientation mapping, study of local hysteresis loops etc. are the key points of this chapter.

In chapter 5, we present the studies on the home-grown macroscopic crystals of Croconic Acid. With the help of Polarized Light Microscopy, X-ray Diffraction stud-

ies and AFM, we attempt to characterize the peculiar surface structures observed on these crystals.

Finally, in the concluding chapter, we discuss the prospects and advantages of organic ferroelectric materials and shed light on how the work of this thesis may be useful for deeper exploration on novel organic ferroelectric systems like Croconic Acid and their possible future applications in nanoelectronic and spintronic devices.

# Chapter 1

# A brief introduction to organic ferroelectrics

## 1.1 General concepts in ferroelectricity

Electric charge is a fundamental entity in nature. In ordinary non sub-atomic objects, charge is defined by the presence of either electrons for negative or protons for positive charge. An isolated atom is electrically neutral. However, when atoms constitute to form matter, the interatomic electrostatic interactions can favour an asymmetric charge distribution that form electric dipoles.

An electric dipole can be seen as a set of two oppositely charged centers separated by some distance and quantitatively defined with dipole moment, where dipole moment is a scalar product of the common charge of the distribution and the distance of separation. When such a dipole exists permanently in a molecule, the molecule is called as a polar molecule. Water is a very simple example of a polar molecular system. The electric dipoles in a material respond to the presence of external electric field by aligning themselves along the direction of the field so that the electrostatic energy associated with them is minimized. Also, when a neutral insulating material without any intrinsic dipoles is placed inside an external electric field, the positive and negative charges constituting the neutral material experience opposite electric field environments and can lead to the creation of induced dipoles in the material aligning along the direction of the external electric field.

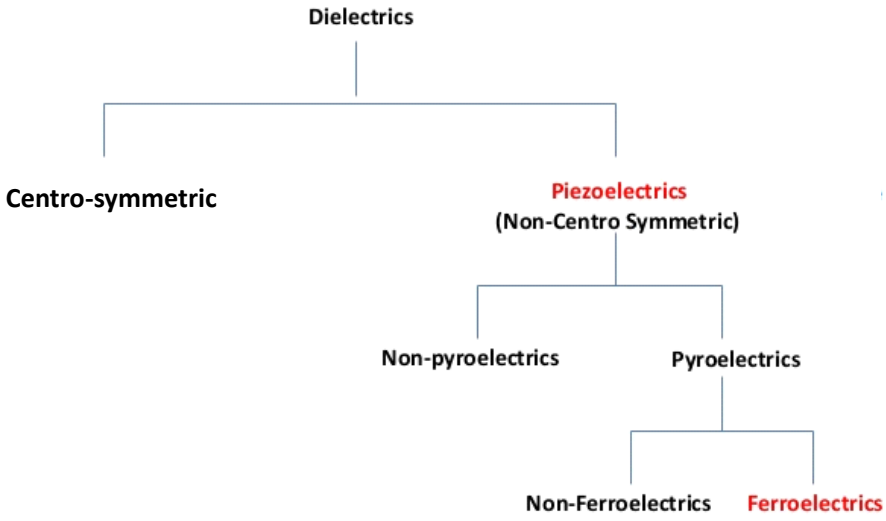


Figure 1.1: Classification of materials in terms of electrical properties.

Quantitatively, the dipole moment formed in a unit of volume is called as the polarization of the material. The ease with which a material forms these dipoles is what defines the polarizability of the material. Based on the polarizability, a particular class of materials, which are more susceptible to forming dipoles under

external field, are known as dielectric materials. In dielectric materials, the dipoles are either induced by electric field or the already present disordered molecular dipoles are arranged by the field, however, with the withdrawal of the field, they tend to randomize again. Thus, no net spontaneous polarization is present in such materials in the absence of external electric field.

Then, there comes another class of materials which is a subset of dielectric materials with reduced symmetry among the constituent atoms or the crystal system, for example, non-centrosymmetric systems. These type of materials are electromechanically active; electrical polarization can be generated by mechanical force. This property is called as piezoelectricity and the materials are called as piezoelectric materials. In an inverse way, electric field when applied to these materials can generate mechanical deformation via inverse piezoelectric effect. The magnitude and direction of deformation upon application of electric field are dependent on the piezoelectric tensor which is specific to the piezoelectric material.

Further, a subset of piezoelectric materials comprises of a certain type of materials for which the polarization generation may not necessarily be dependent on external electric field, the polarization along certain polar axis can be spontaneous and is dependent on temperature. Such class of materials are called as pyroelectric materials. Now, the subset of pyroelectric materials for which the spontaneous polarization direction can be reversed by external electric field care called as ferroelectric materials. A typical feature of ferroelectric materials is the polarization (P) versus external electric field (E) behavior which forms a hysteresis loop characterized mainly by (a) saturation polarization, $P_s$, (b) remanent polarization, $P_r$ and (c) coercive field, $E_c$. The standard P-E hysteresis loop (figure 1.2 (c)) is formed by increasing the magnitude of electric field along certain direction until the polarization is saturated at a particular value, the saturation polarization, and then when the electric field is reduced to zero, the polarization retains a particular value, the remanent polarization. Upon increasing the electric field along the opposite direction, the polarization decreases and at a particular value of electric field, the coercive field, it becomes zero. Further increase in the electric field magnitude reverses the polarization and thus polarization becomes negative and gets saturated at a value of $-P_s$. Similarly, when the electric field magnitude is now again reversed and slowly increased till the maximum positive value of E, the polarization hysteresis loop forms. The shape of the hysteresis loop is dependent on various material specific parameters. For example, if the polarization reversal is a sharp process, the hysteresis loop becomes more rectangular and if it is more gradual, the loop becomes

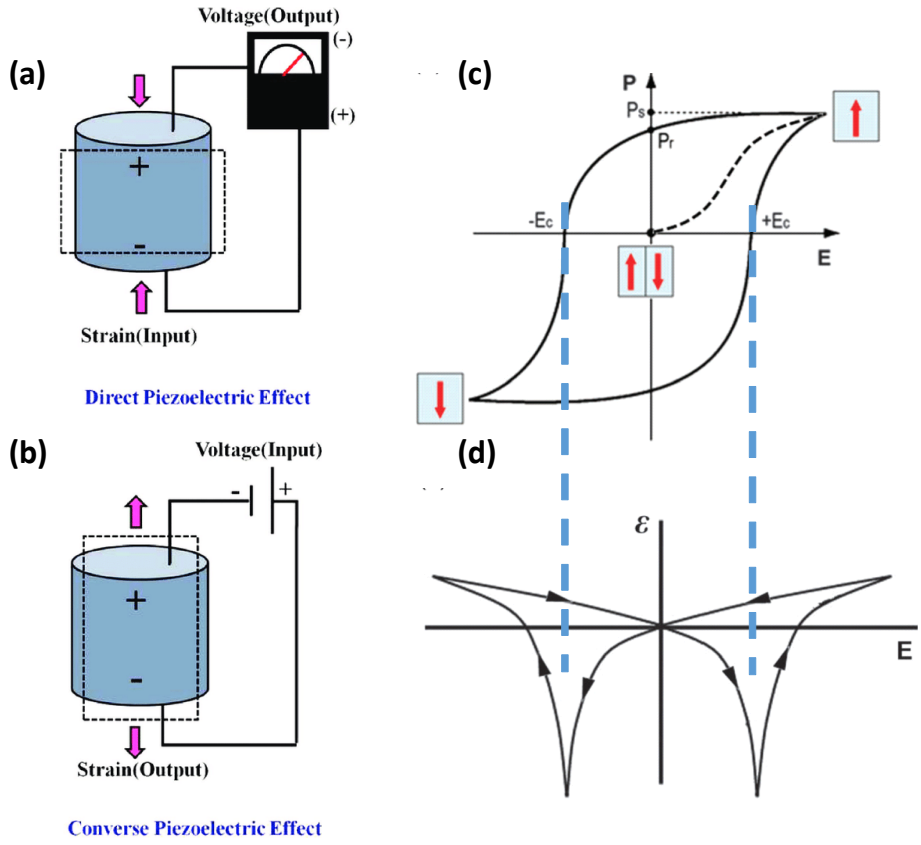


Figure 1.2: Schematics of a standard piezoelectric (a), inverse-piezoelectric response (b), ferroelectric hysteresis loop (c) and strain response curve (d) of a macroscopic ferroelectric material. Red arrows in (c) show the direction of the ferroelectric polarization. Blue dashed lines indicate that the ferroelectric reversals and the dips in the strain response curve occur synchronously. Figures are taken from references [19, 20].

more curved and non-linear.

As ferroelectric materials are by default piezoelectric, application of electric field across them generates the inverse-piezoelectric strain in the material. This results in the elongation or contraction of volume of the ferroelectric along the direction of the applied field when the field is parallel or antiparallel to the polarization direction respectively. Thus, when the applied voltage opposite to the direction of polarization approaches the coercive field during a hysteresis loop measurement and the polarization of the ferroelectric is reversed, the polarization direction becomes parallel to that of the electric field and this results in the sudden change, forming a dip, in the otherwise linear response of the strain across the ferroelectric. The strain versus electric field loop is called as the strain response curve of the ferroelectric. Such a curve is schematically shown in figure 1.2 (d).

The above features are the general macroscopic properties of any ferroelectric

materials. However, the origin of ferroelectricity in any material has to do with the crystalline arrangement of the constituent atoms. Ferroelectricity cannot originate in amorphous materials as the random orientation of electric dipoles will cancel each other out, unlike the case of amorphous magnetic systems where magnetic exchange interactions pave the way for magnetic ordering even without the absence of structural crystallographic ordering of magnetic dipoles.

Conventionally, the origin of ferroelectricity is classified into two types, (i) displacive type and (ii) order-disorder type. In the case of (i), polarization is created by the relative displaced position of the atoms/ions. In the ferroelectric state, the ions are positioned in a displaced manner from the non-polar symmetric state and this generates net local dipole moment giving rise to a net polarization in a finite volume of material. Barium Titanate ($BaTiO_3$) is an example of such a system. On the other hand, (ii) order-disorder type ferroelectricity originates from the rotation of ions or polar molecules in the material system where below a certain temperature, the otherwise disordered individual dipoles undergo a phase transition to order up and give rise to ferroelectricity. $NaNO_2$ can be considered to be partly an example of such a ferroelectric system.[21]

Another type of classification of ferroelectric materials can be done based on the nature of constituent atoms. For example, commonly known ferroelectric materials such as $BaTiO_3$ and $BiFeO_3$ that are composed of inorganic atoms are classified as inorganic ferroelectric materials, whereas, organic molecules and polymeric materials showing ferroelectricity are categorized as organic ferroelectric materials.

## 1.2 Organic ferroelectrics

It is imperative to note that the first ever discovered material to show ferroelectricity, Rochelle salt ($KNaC_4H_4O_6{\cdot}4H_2O$) was an inorganic salt of an organic compound.[22, 23] Even after several decades of its discovery, organic ferroelectric materials have been rare. Only recently different types of organic ferroelectrics were discovered and due to their certain advantages over inorganic ferroelectric materials, the efforts to search for newer organic ferroelectrics is booming. A lot of research is also being carried out to explore their potential for their future applications in a variety of fields. Further, a significant amount of effort is towards the design and discovery of new materials with high spontaneous polarization value. For example, metal free all organic perovskite structures are being explored which resulted in the discovery of MDABCO (N-methyl-N'-diazabicyclo[2.2.2]octonium)-ammonium tri-iodide

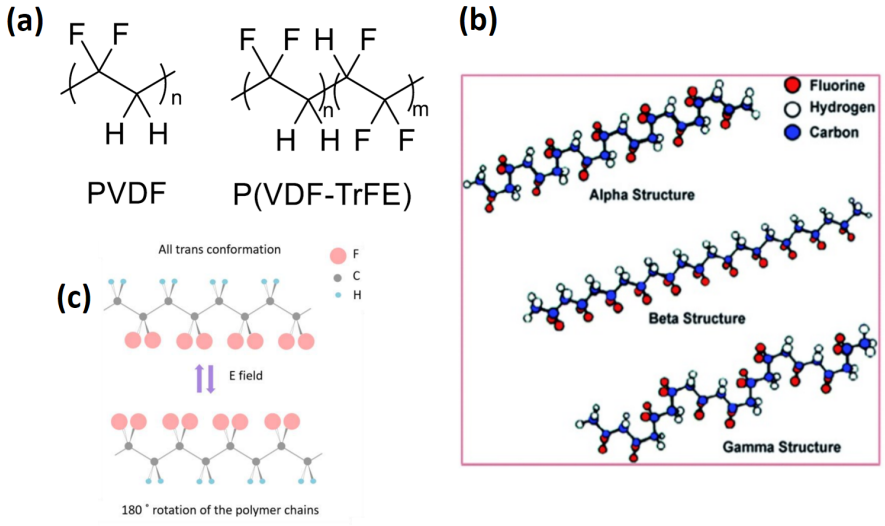


Figure 1.3: Molecular structure of polymeric PVDF. (a) shows the molecular structure for PVDF and the co-polymer PVDF-TrFE. (b) shows the linear chain structures for three different phases of PVDF. (c) shows the structures corresponding to the two ferroelectric states for a $\beta$-phase PVDF demonstrating the molecular rotation being at the origin of polarization reversal. The figures are taken from references [30][31].

which is a high temperature ferroelectric with a spontaneous polarization value of 23 $\mu C/cm^2$.[24] A brief discussion on some organic ferroelectric materials is presented below.

### 1.2.1 Polymer based ferroelectrics

Ferroelectricity has been shown to exist in many polymeric materials such as polyureas, polyurethanes, nylons, polyvinylidene fluoride (PVDF) and co-polymers of PVDF.[25, 26, 27, 28, 29] Of all the polymer based ferroelectric materials, PVDF and its co-polymer such as PVDF-TrFE (PVDF-trifluoroethylene) have received the maximum attention mainly due to their large remanent polarization, short switching time and thermal stability. The ferroelectricity in PVDF originates from the individual polar VDF molecules which carry the electronegative fluorine and electropositive protons at opposite ends of it. The application of electric field results in the rotation of the molecules which results in the reversal of molecular dipole moment and hence the net polarization reversal in the molecular system. In the co-polymer PVDF-TrFE, the presence of trifluoroethylene group helps in the molecular rotation. The molecular arrangement and the schematics for molecular rotation for the co-polymer PVDF-TrFE are shown in figure 1.3.

As it can be seen in figure 1.3 (a), the molecular structure of PVDF and PVDF-TrFE can allow for several possible structural conformations. Thus, depending on which conformation the polymer crystallizes in during growth, different phases of PVDF or PVDF-TrFE may be obtained. Out of all possible phases, the $\beta$-phase shows the maximum value of polarization as in this phase, the Chlorine atoms and the Hydrogen atoms of all the molecules in a polymer chain are positioned opposite to each other. All the molecular dipole moments are oriented along a direction perpendicular to the chain axis. The individual molecules in the chain rotate upon the application of electric field perpendicular to the chain direction, thereby rotating the polarization of the entire chain. In this phase, the remanent polarization is approximately 7 $\mu C/cm^2$ with a coercive field of around 90 V/m.[32, 33, 34] PVDF based ferroelectric films have been a favourite for the commercial sector as a ferroelectric material due to its abrasion resistance, durability, non-flammability and radiation tolerance. In the field of nanoelectronic devices as well, PVDF has received substantial attention. Detailed discussion of applications of PVDF can be found in the review articles in the references [35, 36].

### 1.2.2 Charge transfer complexes

If a multi-component molecular material is composed of one electron rich donor type unit and another electron poor acceptor type unit and the neutral pairs of these two types are stacked together, then it is possible that there could be an intermolecular/inter-unit charge transfer within the donor-acceptor systems. The charge transfer can break the symmetry of an otherwise regular donor-acceptor type neutral arrangement to form a polar chai arrangement with polarity being mediated via electrostatic interactions. The two energetically degenerate polar arrangements, $A^-D^+A^-D^+$ and $D^+A^-D^+A^-$ can represent the two states of ferroelectricity. Clearly, the occurrence of such a possibility will be possible only if it is favoured by the energetics which is governed by the energy cost in creating charged species and the energy reduction due to the consequent attractive electrostatic interactions among them.[37, 38, 39] A schematic diagram of a general picture of charge transfer complex molrcular structure is illustrated in figure 1.4.

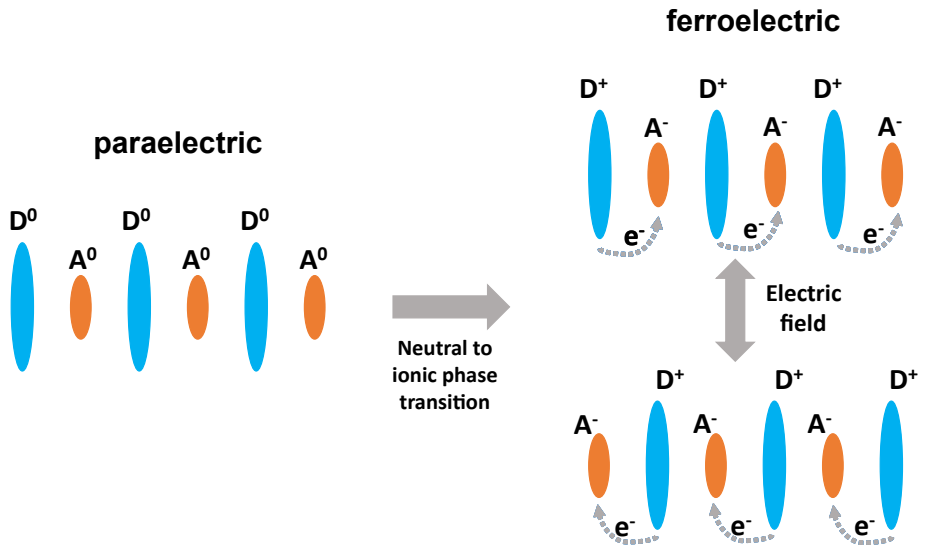


Figure 1.4: Structural schematic diagram of a typical charge transfer type ferroelectric system. D and A represent the charge donor and acceptor component in the donor-acceptor system respectively.

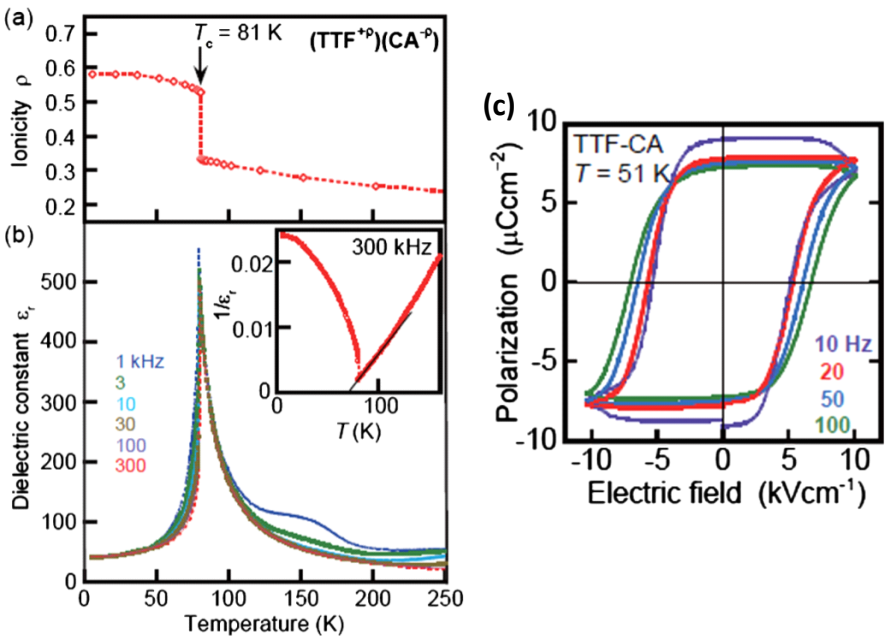


Figure 1.5: Electric characterization on TTF-CA charge transfer ferroelectric complex. (a) and (b) show the sudden change in iconicity and dielectric constant at a temperature of 81 K corresponding to the neutral to ionic ferroelectric phase transition. (c) shows the measured polarization hysteresis loops obtained at a temperature of 51 K. The figures are taken from reference [40].

Charge transfer complexes such as tetrathiafulvalene(D) – quinone(A) type systems are well studied.[41, 42, 43] Tetrathiafulvalene–p-chloranil (TTF–CA) complex,

where TTF serves as the electron donor and CA as an acceptor, is a typical example of such a system where the non-polar centrosymmetric neutral structure undergoes a peculiar neutral to ionic phase transition to create a polar ionic structure below 81 K.[44, 45, 46] This polar structure is ferroelectric with a remanent polarization of $\sim$6.3 $\mu C/cm^2$ and a coercive field of $\sim$5.4 kV/cm at a temperature of 51 K.[40] The ferroelectric phase transition is accompanied by sharp change of the dielectric constant and an indication of first order phase transition as shown in figure 1.5.

### 1.2.3 Hydrogen bonded systems:

A hydrogen bond is an attractive electrostatic bond between one electronegative atom and a hydrogen atom which is connected to an electronegative atom. Thus, in a hydrogen bonded system, dipoles are generated due to the presence of electronegative atoms and the electropositive protons or Hydrogen atoms/ions. For example, water molecules are hydrogen bonded to each other where Oxygen atom is electronegative and is hydrogen bonded to the Hydrogen atom of another water molecule. A hydrogen bonded system need not necessarily be composed of similar molecules as in the case of water. It can also be of multi-component nature, for example, acid-base systems can also be hydrogen bonded where the acid component works as the H/proton donor and the base component works as the acceptor. If a donor-acceptor system can crystallize into a linear chain of alternating hydrogen bonded donor-acceptor pairs, it is possible that the dipoles in the acid-base pairs can be ordered and ferroelectricity may emerge.

There are two possible ways in which a ferroelectric ordering can be generated in the donor-acceptor hydrogen bonded chains of a bi-component system, (i) both the donor and acceptor molecular units in the chain are individually neutral and ferroelectricity is originated due to the displacive behavior of H atoms in a charge neutral chain and (ii) there is an actual proton transfer between the donor and acceptor molecular units giving rise to an ionic hydrogen bonded chain system where the ferroelectricity is originated due to ordering of dipoles created by non-centrosymmetric arrangement of transferred H atoms or protons.[39]

A good example of type (i) is the supramolecular chain assembly of two $\pi$-conjugated molecular systems, one being the phenazine (Phz) as H-acceptor (base component) and the other is the Chloranilic acid ($H_2ca$) as the H-donor (acid component). $H_2ca$ possesses two proton donating O-H groups and Phz possesses proton accepting N atoms on both side of the molecules. Thus, these two components co-

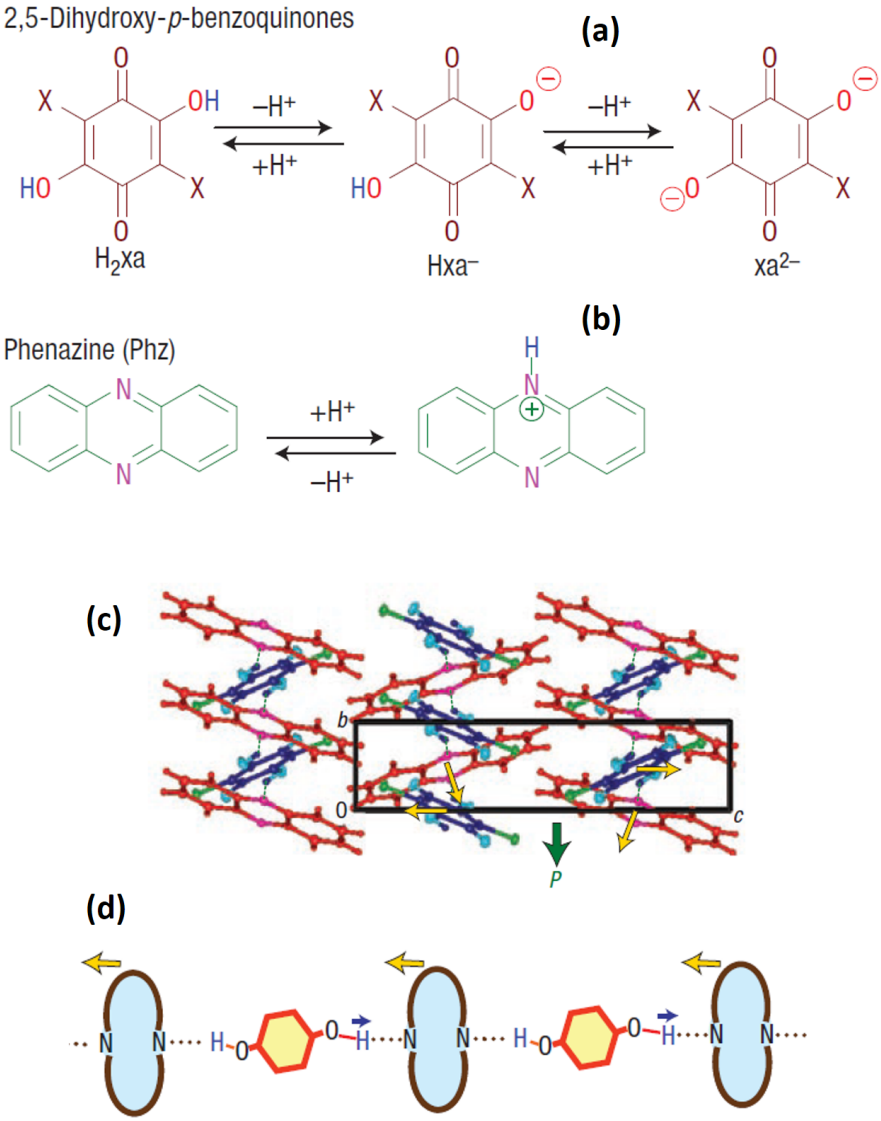


Figure 1.6: Structure of a displacive type (type i) bi-component hydrogen bonded ferroelectric system (Phz-$H_2Xa$). (a) and (b) show the chemical structure of the acid component (D) $H_2Xa$ (X=Cl, Br, I) and the base component (A) phenazine respectively of the acid-base or donor-acceptor system. (c) shows the crystal structure of the Phz-$H_2Xa$ system with yellow arrows showing the molecular displacement. (d) shows the schematics of the same system where yellow rings blue ellipses represent the $H_2Xa$ and Phz units respectively and blue and yellow arrows showing the displacement of the H-atoms and the Phz molecules respectively. Figures are taken from reference [39].

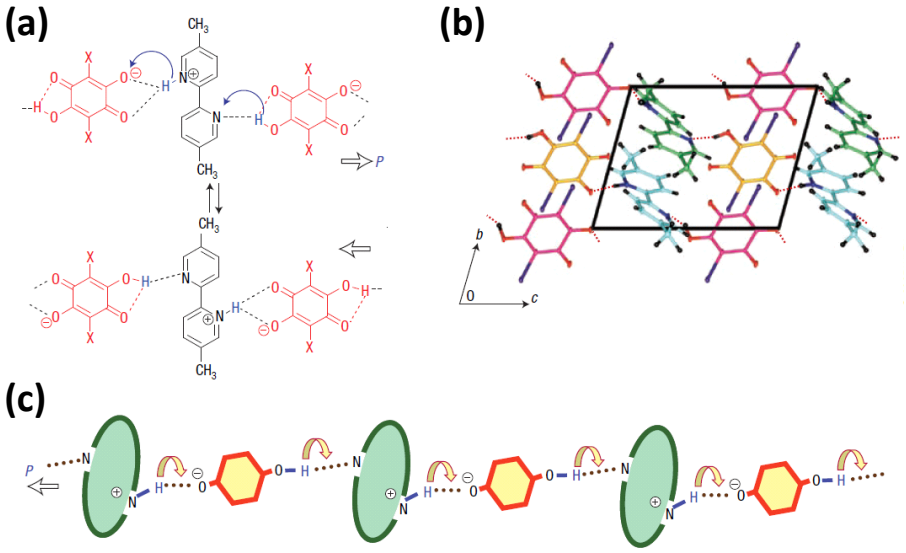


Figure 1.7: Structure of a proton transfer type (type ii) bi-component hydrogen bonded ferroelectric system ($H_2$Xa-55DMBP). (a) shows the two ferroelectric states with net system polarization oriented along opposite directions where blue curved arrows show the direction of collective proton/H-atom transfer. (b) shows the crystal structure of the system. (c) shows the structural schematics of the ferroelectric system where yellow rings and green ellipses represent $H_2$Xa and 55DMBP units respectively and the yellow curved arrows showing the direction of intermolecular proton transfer. Figures are taken from reference [39].

crystallize to form alternating hydrogen bonded acid-base pairs. At room temperature, the H atoms are positioned centrosymmetrically and the charge distribution in the entire chain is neutral. Below a certain temperature, the H atoms of all the $H_2$ca molecules gets displaced towards the neighbouring Phz molecules and the Phz molecules get displaced towards the neighbouring $H_2$ca molecules, thereby breaking the inversion symmetry and giving rise to a net polarization of the supramolecular chain. The spontaneous polarization of Phz-$H_2$ca system is $\sim$1.2 $\mu C/cm^2$ at 160 K.[47, 48, 49, 50] The schematics of the system is shown in figure 1.6. It must be noted that there is no intermolecular transfer of proton in such a supramolecular system.

Type (ii) on the other hand represents the systems where, unlike in the case of type (i), the H-atom/proton of the hydrogen bond gets transferred from one molecular unit to another neighbouring one during the ferroelectric reversal process (figure 1.7). This transfer can take place in a concerted way, thereby without changing the chemical structure of any components. A nice example of such a system could be the supramolecular system of the acid named iodianilic acid ($H_2$ia) and the base named 5,5´-dimethyl-2,2´-bipyridine (55DMBP). In this system, in the ferroelectric

state, the O-H bonds of $H_2$ia and the $N^-H^+$ bonds of 55DMBP are aligned in the same direction. Ferroelectricity is originated due to the alternative polar ordering of O-H---N and N-$H^+$---O bonds. During the polarization reversal, the H-atom undergoes intermolecular transfer between the N-atom of 55DMBP and the O atom of $H_2$ia. For all the H-atoms to undergo a concerted transfer, the $\pi$-electron system of both the base and acid unit also participate in the transfer process.[51, 52]

Interestingly, hydrogen bonded ferroelectric systems need not necessarily be of multi-component nature. Single component systems can also show ferroelectricity. Several examples exist, such as 2-phenylmalondialdehyde (PhMDA), 3-hydroxyphenalenone (3-HPLN), and cyclobutene-1,2-dicarboxylic acid (CBDC) and 2-methylbenzimidazole (MBI) are proton transfer based (type ii) single component hydrogen bonded ferroelectric systems.[53, 54, 2] However, the most remarkable example of a similar system would be the hydrogen bonded system named 4,5-dihydroxycyclopentenetrione (Croconic Acid) which was shown to be ferroelectric only rather recently.[1] What makes this particular system interesting is its high value of above room temperature polarization ($\sim$30 $\mu C/cm^2$) which reaches to the level of polarization offered by inorganic ferroelectrics.[2] Clearly, Croconic Acid has the highest room temperature polarization among organic ferroelectric materials. Large value of polarization makes this organic ferroelectric a prominent candidate for possible applications. A dedicated section discussing the work done so far on Croconic Acid to understand the origin and nature of ferroelectricity and to explore the possibility of its future applications is presented in one of the upcoming subsections.

### 1.2.4 Ferroelectric liquid crystals

Liquid crystals are ordered anisotropic materials which are thermodynamically somewhere in between the crystalline solid and liquid phase. Ferroelectric liquid crystals are special ferroelectric or special liquid crystals which possess the unique combinatorial feature of dipolar reversal and fluidity. This makes such materials very useful for application. Various types of ferroelectric liquid crystals have been discovered and studied such as 2-methylbutyl 4-(4-decyloxybenzylideneamino)-cinnamate (DOBAMBC), surface-stabilized systems, dibenzopyrene molecule type discotic systems, cone shaped, columnar and bent core type ferroelectric liquid crystals are to name a few. Detailed information on ferroelectric liquid crystals may be found in the references [55, 56, 57, 58].

### 1.2.5 Advanced supramolecular ferroelectric systems

Supramolecular design of molecular system deals with forming ordered molecular assemblies using non-covalent interactions. Some of the types of organic ferroelectric materials discussed above can be considered as supramolecular systems. However, the quest for developing newer robust above room temperature ferroelectric materials have led ways to some advanced supramolecular systems where different mechanisms such as charge transfer mechanism and hydrogen bonding mechanism are synergistically combined to design advanced organic ferroelectric materials with the help of chemical functionalization. For example, Tayi et al. have designed charge transfer complexes based on pyromellitic diimide (PMI)-based electron acceptor and TTF based donor units which encompasses four different types of non-covalent bonding interactions, namely, hydrogen bonding, charge transfer, $\pi$-$\pi$ stacking and Van der Waals type interactions and is ferroelectric at room temperature.[59]

## 1.3 Applications of organic ferroelectrics

Organic ferroelectric materials find applications in a variety of fields due to their beneficial features such as the ease in the fabrication and processing, environmentally sustainability, low cost etc. Apart from various fields of application such as optoelectronics, flexible electronics and bio-compatible electronics, one main area where they find promising applications is the field of nanoelectronic and spintronic devices. Combining the possibility of two stable memory states of a ferroelectric working as binary memory component with the advantages of an organic material, organic memory devices are being studies for future memory device applications. A concise review on the applications of organic ferroelectrics in memory applications can be found in reference [60, 61, 62]. Similarly, combining the ferroic properties of organic ferroelectrics with other ferroic materials via various types of mechanism, new multiferroic materials are being designed which possess great potential for applications in future nanoelectronic devices sector. These two aspects of the applications of organic ferroelectric materials with examples of studied systems are briefly discussed as below.

### 1.3.1 Applications in memory devices

The simplest memory device with any ferroelectric materials would be the ferroelectric capacitor with the ferroelectric as the dielectric sandwiched between two

metallic electrodes. The two ferroelectric states working as the two binary memory states can be written electrically with the application of electric voltage across the capacitor and can be read by detecting the hysteretic charges appearing after the application of a switching bias. This method of reading, however, alters the original memory states of the ferroelectric capacitors and requires reprogramming the capacitor after every read operation.

A lot of research have been conducted to study organic ferroelectric based capacitors. While most of the work have focused on the use of polymeric PVDF or co-crystals of PVDF as the ferroelectric[63, 64, 65], some applications have also utilized the recently discovered proton transfer based single component hydrogen bonded organic ferroelectric such as 2-methylbenzimidazole (MBI) as the ferroelectric.[66] Ferroelectric capacitors are used as memory elements in Ferroelectric Random Access Memory (FERAM) elements and PVDF based FERAM designs are also being explored.[67]

Another direction of memory application of organic ferroelectrics involves their usage in Ferroelectric Field Effect Transistors (FEFET). In an FEFET, the ferroelectric material is used as the gate of the FET device. Due to the polarization charges that appear at the surface of the ferroelectric gate when the ferroelectric is polarized in one polarization state, compensating charges get generated in the neighbouring semiconducting channel, thereby, creating a conduction channel between the source and the drain of the FET. The properties of this channel is modulated between two states according to the two states of the ferroelectric gate which does not require continuous application of external voltage. Thus, a use of ferroelectric gate in a standard FET helps create a non-volatile memory element. Organic ferroelectrics have been used as the ferroelectric component in FEFET devices which are then called, organic FEFET or OFEFET devices.[68, 69, 70]

Similarly, Ferroelectric Tunnel Junctions (FTJ) have been another type of heavily studied ferroelectric based memory device where organic ferroelectrics have found applications. An FTJ memory element is basically a thin ferroelectric film sandwiched between metal electrodes, allowing quantum mechanical tunneling of electrons through itself. The resistance of an FTJ is dependent on the polarization state of the ferroelectric, known as the Tunnel Electro Resistance (TER) effect which originates due to the dependence of tunnel barrier height on the ferroelectric polarization. Thus, the two resistance states of an FTJ depending on the two polarization states of the ferroelectric are used as the memory states in an FTJ memory element. PVDF based organic ferroelectric thin films have been used as the ferroelectric in FTJ due

to the possibility ultra-thin film growth for such polymeric ferroelectrics.[71, 72, 73]

### 1.3.2 Organic multiferroic systems

Multiferroic systems are essentially systems with multiple ferroic orders, such as magnetic, elastic or electric orders. Depending on the design, there are two types of multiferroic systems, artificial/composite multiferroic systems and intrinsic multiferroic systems. In an artificial multiferroic system, two ferroic systems such as thin films are extrinsically combined together to form the multiferroic whereas in an intrinsic multiferoic system, multiple ferroic orders are intrinsically present and coupled with each other. Restricting the discussion only to the magnetic and electric ferroic orders which are otherwise called as the magnetoelectric multiferroics, multiferroic systems with inorganic materials are a heavily studied and researched topic and detailed information can be found in the review articles given in references [74, 75, 76]. However, organic multiferroic systems and organic-inorganic hybrid multiferroic systems are in the nascent stage of investigation.

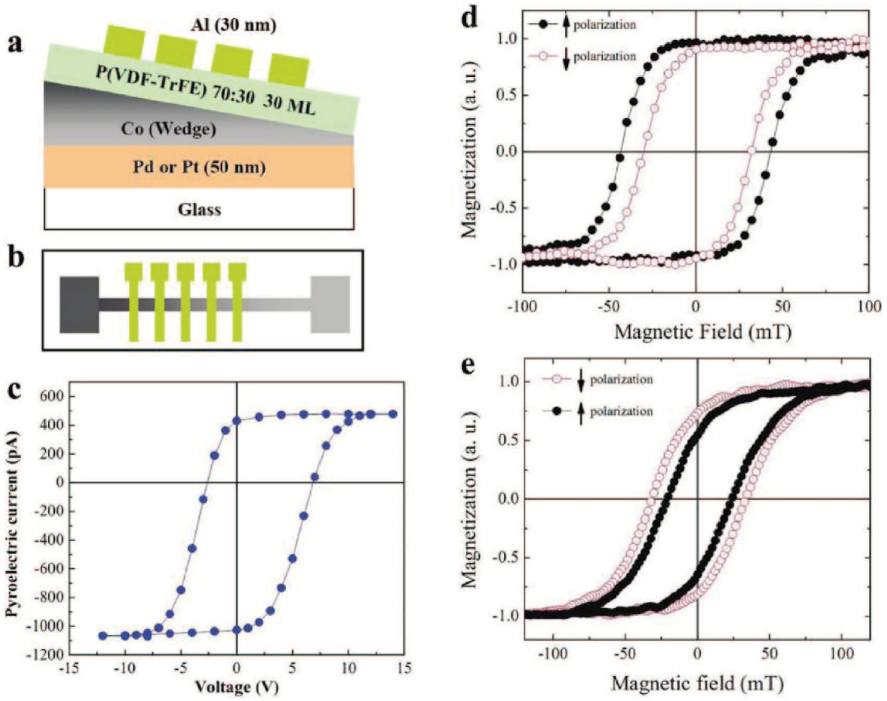


Figure 1.8: Electric control of magnetism in PVDF-TrFE/Co artificial multiferroic system. (a) and (b) show the device schematics of the system. (c) shows the pyroelectric hysteresis loop of the ferroelectric component. (d) and (e) show the magnetic hysteresis loop shapes getting affected by the reversal of ferroelectric polarization. Figures are taken from reference [77].

Organic-inorganic hybrid system is a particular way of designing multiferroics where the ferroelectric component can be organic and the ferromagnetic component can be any regular ferromagnetic material. There have been efforts to utilize polymeric PVDF co-polymer based organic ferroelectrics to create artificial organic-inorganic hybrid multiferroic systems. Mardana et al have been able to control the magnetic properties of Co films using the polarization of PVDF-TrFE films grown in the proximity of the Co film in the PVDF-TrFE/Co artificial multiferroic system (figure 1.8). They show the polarization reversal of the ferroelectric results in the change of magnetic anisotropy of Co with the change reaching as large as 50%. Further, they show that the polarization reversal can also modify the out-of-plane or in-plane anisotropy for ultra-thin Co films.[77]

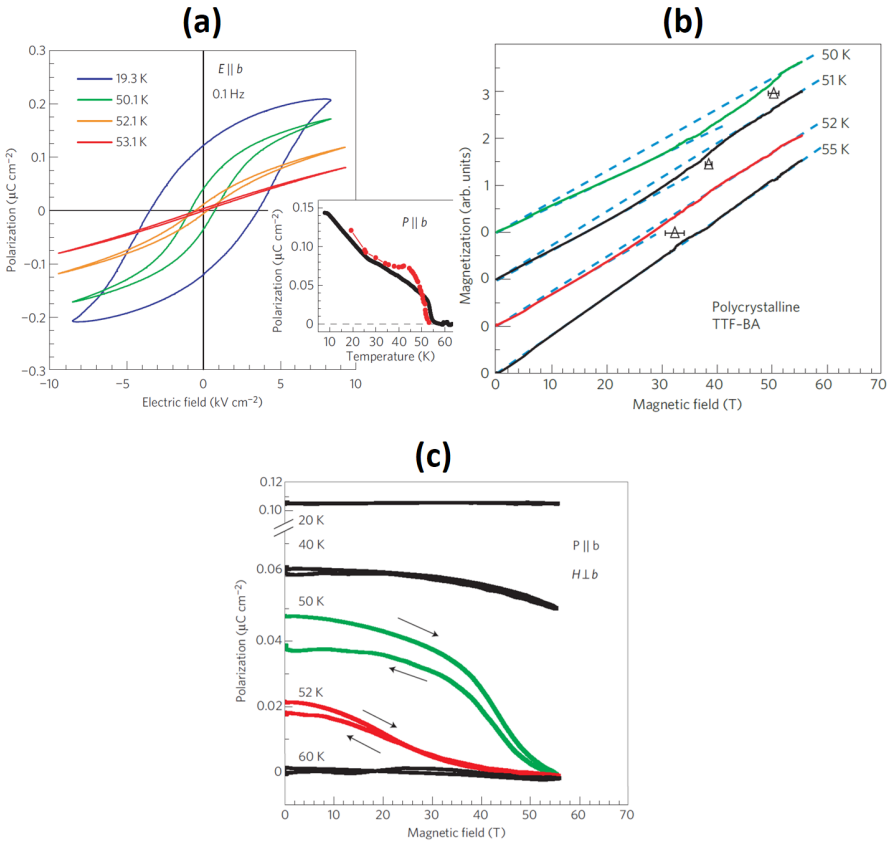


Figure 1.9: Electric and magnetic measurements on TTF-BA crystals showing the magnetic order driven ferroelectricity in a bi-component organic intrinsic multiferroic system. (a) shows the ferroelectric hysteresis loop, (b) shows the magnetization versus applied magnetic field (M-H) curves of randomly oriented small crystals at different temperatures and (c) shows the magnetic field dependence of the electric polarization in TTF-BA. Figures are taken from reference [78].

Taking the concept of organic artificial multiferroics one step further, PVDF co-

crystal based Magnetic Tunnel Junctions (MTJ) (can also be called as FTJ) have been designed which show a tunnel electromagnetoresistance of 1000% and electroresistance of 30% at a temperature of 200 K. Apart from the electrical tuning of the interfacial spin polarization, this work also indicates the possibility of designing room temperature 4-bit memory elements for increased data storage density.[79]

However, all organic multiferroic systems can perhaps only be realized by designing all organic intrinsic multiferroic complexes having both ferroic orders coupled to each other. As the interface between two organic materials such as one ferroelectric and the other ferromagnetic may be a very complicated system, designing all organic artificial multiferroic will require the undestanding of such interfaces. Thus, extrinsically combining organic ferroelectrics with organic ferromagnets to form all organic artificial multiferroics may be technically a very challenging path. On the other hand, interestingly, all organic intrinsic multiferroics such as organic charge transfer based complexes and metal organic frameworks with recently discovered magnetoelectric mechanisms such as spin-ordering-induced electric polarization[78] and ferroelectricity-induced spin alignment[80] are being heavily investigated.

Organic charge transfer complex tetrathiafulvalene-p-bromanil (TTF–BA) have been shown to have magnetic order driven ferroelectricity (figure 1.9) where the tuning of ferroelectric polarization is possible by application of external magnetic field.[78] Similarly, another all organic charge transfer complex with crystalline thiophene as the electron donor and $C_{60}$ as the acceptor has been found to possess coupled intrinsic ferromagnetism and ferroelectricity.[81, 82] For both these examples, ferroelectricity is induced by the charge distribution that takes place in the system to minimize the magnetic order energy.

Similarly, in charge transfer multiferroic systems like $\kappa$-(BEDT-TTF)$_2$-Cu[N(CN)$_2$]-Cl (where BEDT-TTF bis(ethylenedithio)-tetrathiafulvalene), the magnetic order is believed to be originating from the long range ferroelectric ordering.[80]

Additionally, single phase metal-organic frameworks with both ferroelectric and ferromagnetic ordering have been shown to exist[83, 84] with some systems offering high values of magnetoelectric coupling.[85, 86]

# Chapter 2

# Croconic Acid: an organic ferroelectric

The work done in this thesis is concerned with the study of properties the novel single compnoent organic ferroelectric, Croconic Acid. In this chapter, we have briefly summarized most of the research already carried out on various aspects of this ferroelectric material.

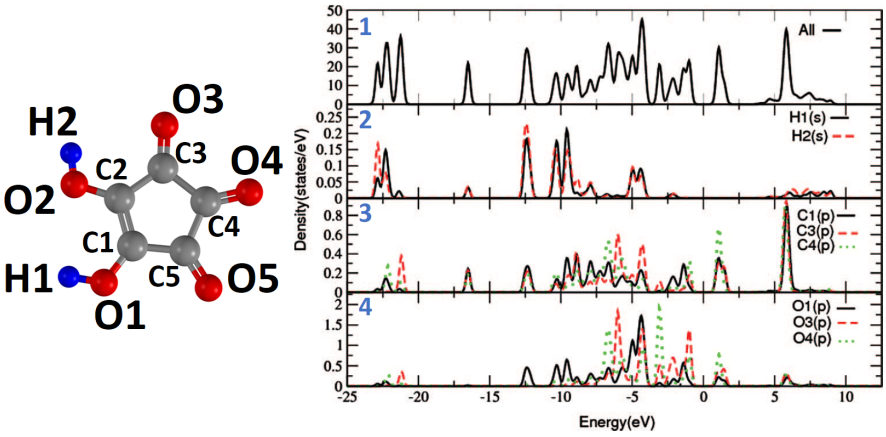


Figure 2.1: DFT calculated DOS: total DOS (upper most panel) and PDOS (panel 2, 3 and 4) of a single CA molecule. A CA molecule with all the atoms labelled is shown on the left for reference. Figure is taken from reference [87].

Croconic Acid (CA) (4,5-dihydroxy-4-cyclopentene-1,2,3-trione, $H_2C_5O_5$) is an oxocarbon ($C_nO_n^{2-}$) based acid with fine carbon atoms (n=5). It is a fairly simple organic molecule composed only of carbon, hydrogen and oxygen atoms. Two hydroxyl and three ketone groups sticking to the 5 carbon atoms of a cyclopentene base forms the structure of the molecule. The hydrogen ions/protons in the hydroxyl groups are strongly coupled to the central delocalised $\pi$-electron system of the oxocarbon via the $\pi$-electron system of the ketone groups. A single Croconic acid molecule is electrically polar with a dipole moment of 7-7.5 D (1 D = 3.336 $\times$ $10^{-30}$ Cm) or 9-10 D.[88, 89] Due to the pentagonal symmetry, 5 polar ketone (C=O) units should not produce a net dipole moment in a single molecule. Clearly, then, the dipole moment is due to the two Hydrogen atoms present in the hydroxyl groups at the two opposite ends of the C=C unit. Further, the relative orientations of the H atoms in the hydroxyl groups define different isomeric forms with different dipole moments. For example, the two H atoms may symmetrically point outward or inward giving rise to an achiral isomer and a chiral isomer (as shown in figure 2.1) develops when one of the H atoms point inwards while the other points outwards.

The total density of states (DOS) (panel 1) and partial DOS (PDOS) of constituent atoms (panel 2 for H, panel 3 for C and panel 4 for O) obtained from by Density Functional Theory (DFT) calculations are shown in figure 2.1. The strong

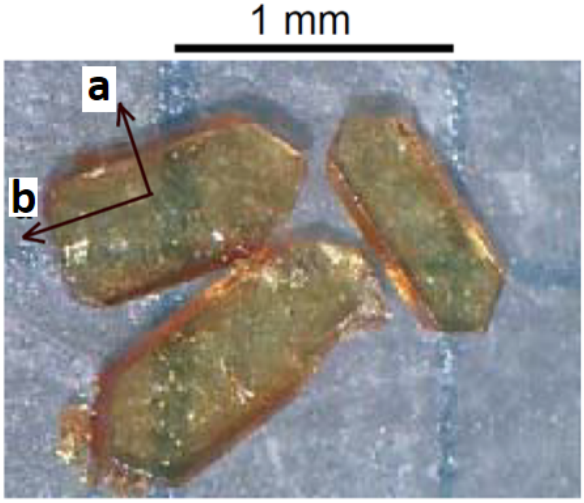


Figure 2.2: Optical image of solution grown typical crystals of Croconic Acid. Figure is taken from reference [1].

overlapping between the PDOS peaks in the valence band corresponding to 'p' orbitals of C and O atoms at the third and fourth panels is indicative of electron delocalization or a covalent bonding between the C and O atoms. Further, the absence of any PDOS corresponding to the 's' orbitals of H atoms at the bottom of conduction band signifies the ionic nature of the O-H bonds.

## 2.1 The solid state bulk crystal form of Croconic Acid

Croconic acid was known to exist for a long time, however, its crystallization was successfully carried out very lately.[90] Slow evaporation of the acqueous solution of Croconic acid in 1N Hydrochloric acid resuts in the crystallization, forming semi-transparent yellow crystals that take up elongated slab like shapes with several 100s of micrometer in length and several 10s of micrometers in thickness (figure 2.2).

### 2.1.1 Molecular structure in the crystal form

In the solid state crystal form, Croconic Acid molecules take up interesting structure forming patterns of hydrogen bonded networks. The structural information in the crystal form has been obtained from detailed structural characterizations including X-ray diffraction, neutron scattering and ab-initio studies on CA crystals.[91, 92, 93, 94, 95, 96, 97] As shown in figure 2.3, in a CA crystal, infinite zigzag layers

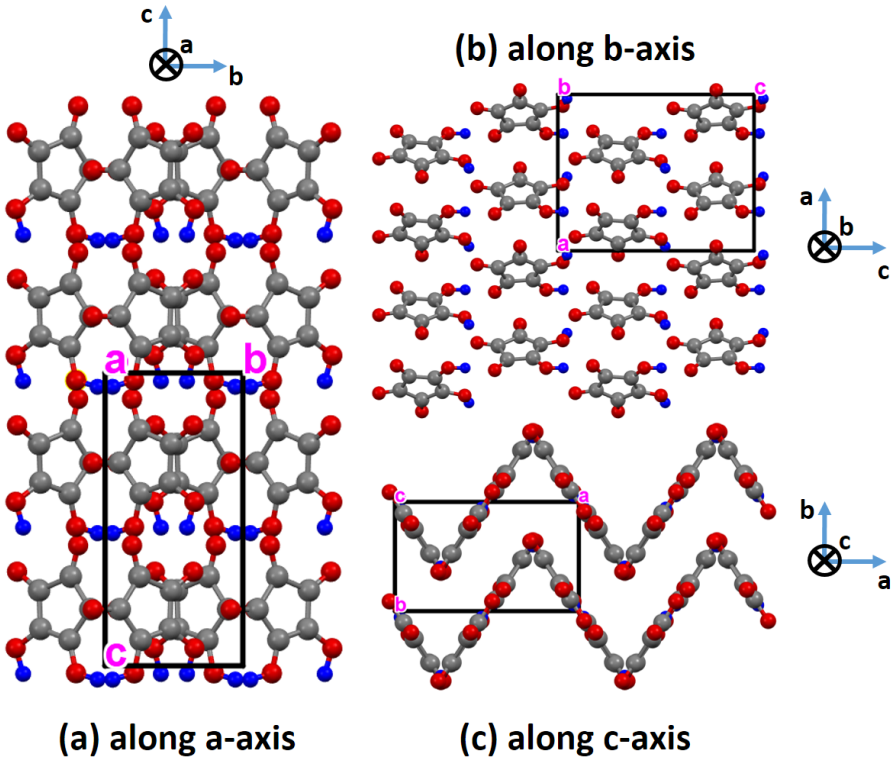


Figure 2.3: Views of CA crystal structure with two stacked layers along three orthogonal axes. The axes mentioned in the subtitles represent directions into the plane of paper. Black boxes represent unit cells. Red, blue and grey balls represent the Oxygen, Hydrogen and Carbon atoms respectively. The structures are generated using the $Pca2_1$ structure (identifier number=753043) of the Cambridge structural database.

are stacked on top of each other and shifted in order to avoid overlap of molecules across the layers with an angle of 69.9° between the CA planes in each layer. Within each plane, CA molecules are again arranged in a zigzag manner, forming hydrogen bonded linear chains along the crystallographic c-axis (figure 2.4). Each CA molecule has a chiral form and is hydrogen bonded to four neighbouring molecules, two in one plane and the remaining two in the adjacent plane forming tetrameric rings (unit cell) as shown within the rectangular box in figure 2.3 (b).

The formation of these hydrogen bonds are facilitated by the presence of oppositely positioned electron-releasing (H1-O1 and H2-O2 in figure 2.1) and electron-attracting (C4=O4 and C5=O5 in figure 2.1) groups in the CA molecules. The view of the structure along an arbitrary direction is presented in figure 2.5 for a clearer understanding of the molecular arrangements in the CA crystal.

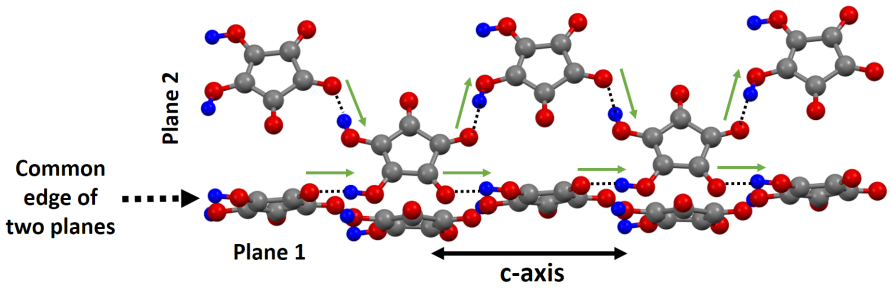


Figure 2.4: Two adjacent planes of CA crystal structure are shown with 5 molecules in each plane. The dashed lines indicate the intermolecular hydrogen bonds and the green arrows show the dipole moments arising out of the asymmetry in the O-H---O bonds. The dipole moments along the common edge of two planes point in the same direction. It should be noted that the net polarization of the network is directed to the right whereas the hydrogen atoms of all individual molecules are towards the left of the molecules. The structures are generated using the $Pca2_1$ space group structure (identifier number=753043) from the Cambridge structural database.

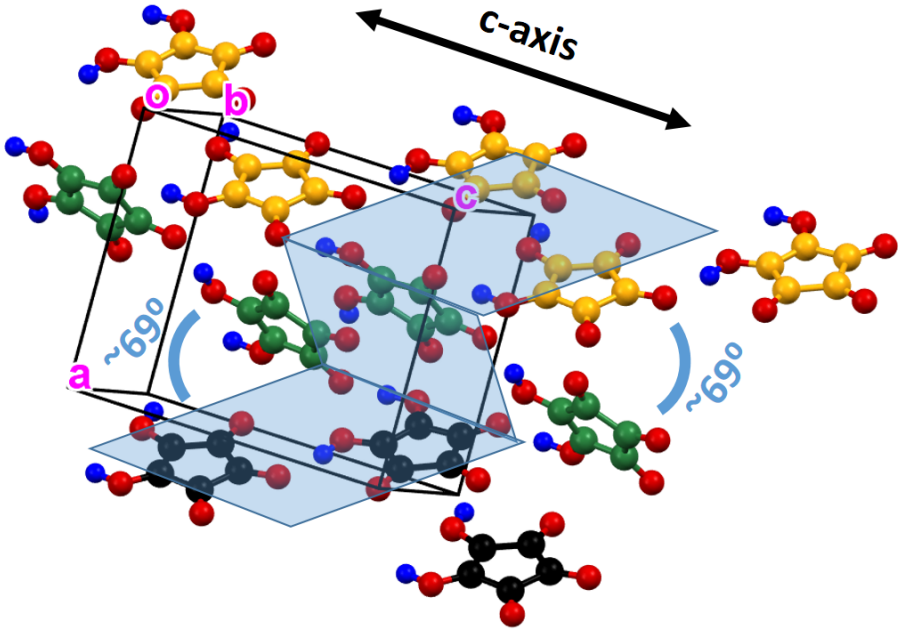


Figure 2.5: Three zig zag planes of one molecular layer (sheet) viewed along an arbitrary direction. For ease of distinction, 3 molecules in the lowest plane are shown with black carbon atoms. Similarly, 4 and 5 molecules with green and orange carbon atoms are shown for the middle and the top planes respectively. The blue shaded regions help identify the individual planes. 'O' stands for the origin of the co-ordinate system. Oa, Ob and Oc indicate the direction of a, b and c axes respectively. An angle of $69^0$ between two consecutive planes is indicated. The structures are generated using the $Pca2_1$ space group structure (identifier number=753043) from the Cambridge structural database.

### 2.1.2 Origin of ferroelectric order

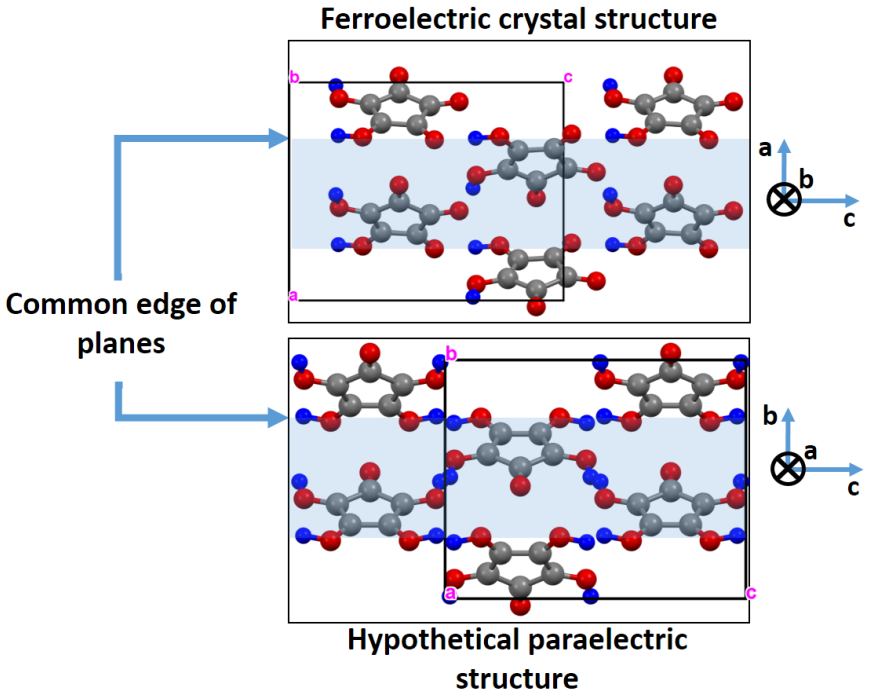


Figure 2.6: Structural comparison between the non-centrosymmetric actual ferroelectric crystal structure and the hypothetical centrosymmetric paraelectric structure. The blue shaded region indicates one plane of the zigzag sheets along the c-axis in a 2-dimensional way. Note the difference in the axes directions for both cases. The structures are generated using the $Pca2_1$ space group structure (identifier number=753043) for ferroelectric structure and Pbcm space group structure (identifier number=753044) from the Cambridge structural database.

Although a CA molecule itself is polar, thanks to the presence of electropositive H atoms, the polar nature of a bulk crystal of CA with hydrogen bonded networks has a more interesting origin which has contributions from both ionic and electronic characters of the molecular system. The ionic characteristic of the polar ordering in the crystal is due to the non centrosymmetric positioning of the Hydrogen atoms of the molecules with respect to the hypothetical centrosymmetric paraelectric structure (figure 2.6). As shown in figure 2.4 and and upper panel of figure 2.6, out of the four intermolecular hydrogen bonds that each molecule takes part in, two lie along the common edge of the two adjacent planes of the zigzag layer and are parallel to the c-axis. The asymmetry in the position of the H atoms in these hydrogen bonds (O---H-O) is additive along the c-axis, thus, it is expected that major component of the net polarization due to the non centrosymmetric network of the structure is also

along the c-axis. The dipole moments arising due to the asymmetric intermolecular Hydrogen bonds are shown in green arrows in figure 2.4.

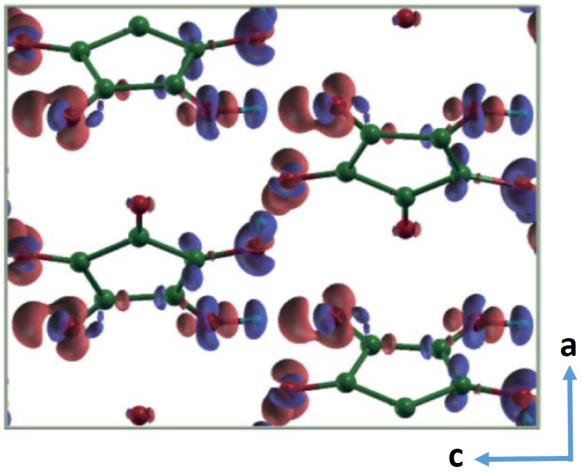


Figure 2.7: Charge density difference between a crystalline molecular network and individual molecules with all atomic positions being the same. Red and blue correspond to positive and negative charge density respectively. A significant shift of positive charge density towards the left is evident. Figure is taken from reference [1].

Detailed Berry phase calculations based on the non centrosymmetric positioning of Hydrogen atoms suggest that the ferroelectric structure is energetically more stable than the paraelectric one resulting in a polarization of 26 $\mu C/cm^2$ directed along the c-axis which is more than the sum of all the individual molecular dipole moments ($\sim$21 $\mu C/cm^2$).[1] The calculated polarization value can go upto $\sim$32 $\mu C/cm^2$ depending on the exchange correlation function used during the calculation.[98] The fact that the net polarization of the network is more than the sum of molecular dipole moments is indicative of the contribution of intermolecular interactions to the net polarization of the structure. Indeed, the charge-density difference between the actual network of the crystal structure and that of individual molecules with all the atoms at respective positions reveal substantial intermolecular charge rearrangements that take place in the crystal network (figure 2.7). Bader charges on each of the atoms of a molecule in a crystalline CA network as calculated by Density Functional Theory as shown in table 2.1 is also suggestive of the partial positive charge on electron-releasing and negative charge on electron-attracting groups.

The electronic contribution to the polar ordering is expected to have its origin in the non-centrosymmetric positioning of the $\pi$-electron unit and the associated electronic charge density in a CA molecule. Theoretical calculation suggests that a

| Atom number | C | O | H |
|---|---|---|---|
| 1 | 0.724 | -1.139 | 0.675 |
| 2 | 0.646 | -1.144 | 0.689 |
| 3 | 0.965 | -1.054 | |
| 4 | 0.9132 | -1.08 | |
| 5 | 0.869 | -1.074 | |

Table 2.1: Calculated Bader charges on individual atoms of a CA molecule in a crystalline molecular network. Data is reproduced from reference [87].

significant contribution (∼80%) to the polarization of the crystalline CA structure is of electronic origin.[2] The electronic nature of the polarization has been probed experimentally by a combination of various ultrafast probing techniques targetting different mecahanisms that take place in a CA molecule when the crystal is excited with ultrafast terahertz electric field pulses.[99]

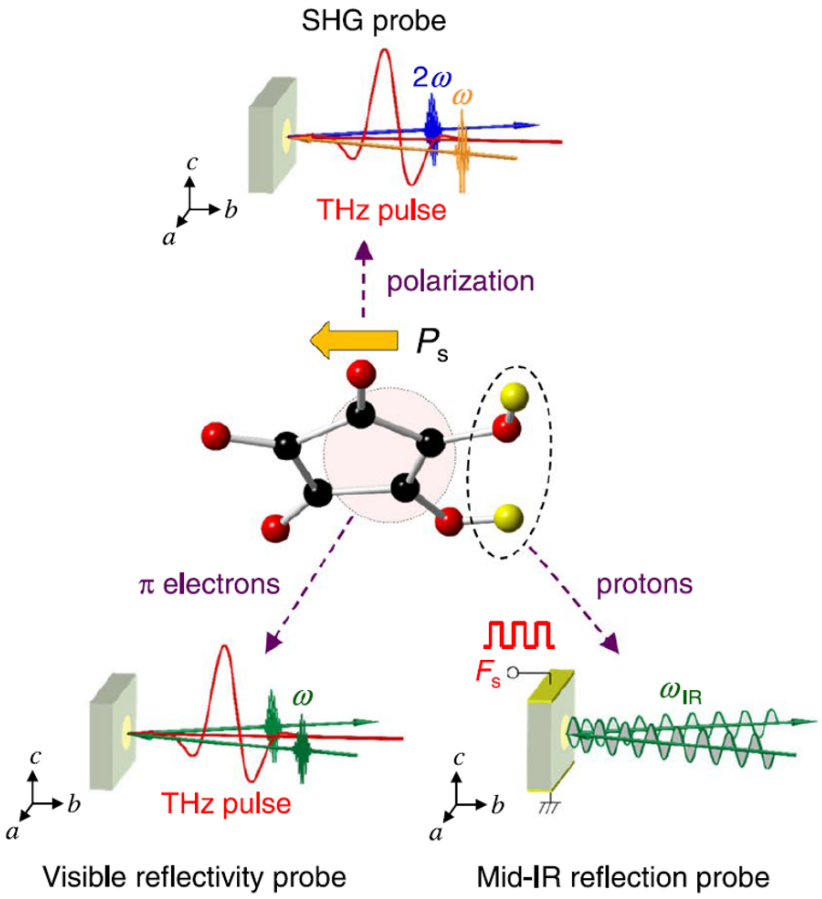


Figure 2.8: The schematics for a combined ultra-fast IR-SHG-visible spectroscopy of a CA crystal. Figure is taken from reference [99].

The ultrafast electric field is able to induce the polarization modulations as probed by the ultrafast modulations of the observed Second Harmonic Generation (SHG) intensities. As the domain wall motions, that can cause the polarization modulation due to the ionic/protonic motions, occur in a much slower time scale (ms) compared to the ultra fast scale (ps), the observed ultrafast polarization modulation should have some type of electronic origin which can be responsive at the ultrafast scale. The exact electronic origin is probed by using an ultrafast optical reflectivity probe which detects the intramolecular transfer of $\pi$-electron density. The electric field induced electron density transfer from C=C unit to the oppositely positioned C-C unit corresponds to the transition between the simulated HOMO and LUMO states of a molecule in a 5 molecule network. Experimentally, this transition gives rise to a peak in optical reflectivity plot at a photon energy of $\sim$3.1 eV.[8]

Further, DFT calculations show that the dipole moment of an individual molecule in the lowest photoexcited state of a CA molecule is opposite to that in the ground state. This results in large values of second order optical non linearity in CA crystals which have been experimentally observed by Sawada et al.[8] The fact that the dipole moment of individual molecules can be tuned optically by photoexcitation of the energy states of the molecule in the crystal strongly advocates for the electronic nature of the polarization in CA crystals. Further, the negligible contribution of the protonic displacements to the polarization modulation is experimentally verified by a combination of ultra fast IR+SHG+visible spectroscopy. These observations suggest that the observed polarization modulation upon ultrafast electric field excitation is due not to the motion of ions or H atoms but to the modulation in the $\pi$-electron density of the molecular system which indicates that in the steady state too, the net polarization of a crystal has significant contribution from the electronic properties of the molecular system.[99] The fact that the polarization in CA can be modulated at ultra fast speeds, may open up possible ultra fast applications of this organic ferroeelctric.

### 2.1.3 Polarization reversal mechanism

In conventional organic ferroelectrics, electric field induced polarization reversal occurs via bulk molecular rotation. Even for the dimethyl substitued compound of Croconic acid, dimethyl croconate follows the above mechanism for reversal of molecular dipoles. In contrast, no molecular rotation takes place in CA, rather the polarization reversal takes place via a coherent proton tautomerization. While molecular

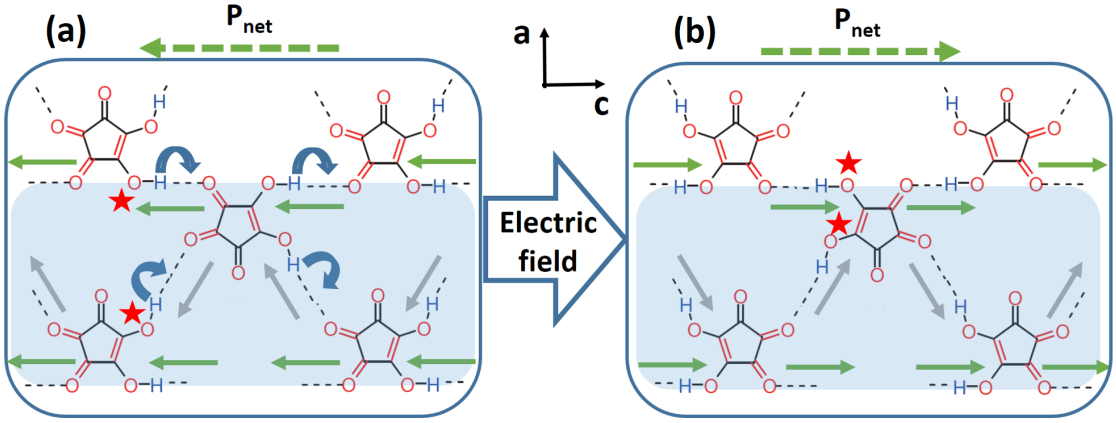


Figure 2.9: Schematics of proton tautomerism process in a hydrogen bonded network of CA molecules. (a) and (b) show the molecular network in opposite states of polarization orientation along c-axis. Blue curved arrows indicate the proton tautomerism processes involving the central CA molecule. The red stars indicate the enol forms of the O-H group of the central CA molecule. Green and grey arrows represent the intermolecular hydrogen bond dipole moments parallel and canted with respect to the c-axis respectively. The blue shade represents one plane along c-axis in one zig zag sheet of CA.

rotation may be energetically not favorable due to steric hinderance in the molecular system, proton tautomerism on the other hand can be achieved/triggered at lower energies.

Synchronized polarization reversal of the non-centrosymmetrically ordered intermolecular dipole moments occur through a co-operative keto-enol tautomerism within an entire network of hydrogen bonded molecules. Each molecule simultaneously works as a donor and acceptor of pairs of protons with the two electron-releasing (hydroxyl) and two electron-attracting (ketone) groups each working as acceptor and donor of a proton respectively; the two keto groups tautomerizing to two enol groups and the two enol groups to keto groups. In this way, the protons of the entire network co-operatively move along the c-axis and thus the net polar arrangement of the network and the net polarization of the crystal is reversed. This process is facilitated by the proper relocation of the delocalised $\pi$-bond in the central oxocarbon system and the $5^{th}$ keto group of each molecule stays neutral without participating in the intermolecular H-transfer phenomena.

Such a coherent tautomeric proton transfer in a molecular network is schematically shown in figure 2.9. which shows a portion of the hydrogen bonded network. The central CA molecule is hydrogen bonded to four neighbouring molecules. The network shown on the left has a net polarization towards the right and after polar-

ization reversal it takes a $180^0$ turn to align towards the left hand side. The pair of hydrogen ions/protons of the enol groups (as indicated by the red stars on fig. (a)) from two neighbouring molecules on the left of the central molecule gets synchronizingly transferred to the central molecule tautomerizing two of its keto groups into their enol forms (red stars on fig (b)). Similarly, the two protons/hydrogen ions of the central molecules gets transferred to two different molecules on the right hand side tautomerizing their keto groups into enol forms. It must be noted that these processes are not sequential, rather, synchronized throughout the network. This is how each molecule in the network participate in a collaborative process of synchronized proton transfer to reverse the polarization axis of the network.

As a significant contribution to the steady state polarization of the CA network is of electronic origin, this electronic contribution must reverse its directionality in synchronization with the proton transfer upon the net polarization reversal of a crystal. This occurs by virtue of switching of the $\pi$-bond of the central ring and the associated electronic charge density that acompanies the tautomeric proton transfer.

Along with the ionic and electronic mechanism behind the existence and reversal of steady state polarization, it is important also to recognize the inter co-operative and additive relation between these two mechanisms which is the main reason behind large polarization values in CA. In the steady state, the $\pi$-electron density in each molecule is asymmetrized in a direction opposite to that of the protonic asymmetry in the intermolecular hydrogen bonds associated with the molecules. The dipole moment generated due to the electronic asymmetry gets added to that due to the protonic one and results in the enhanced net polarization. Similarly, during the polarization reversal, the electronic displacement occurs in the opposite direction to that of the protonic displacement and this aids the polarization reversal process. It is clear that the addition of the electronic contribution to the protonic one is maximum when the relative angles between the directions/axes of the two asymmetries is exactly $180^0$. Any inclination between these two direction will reduce the electronic contribution to the net polarization with minimum contribution in the case of orthogonal directions. Indeed, there are examples of organic ferroelectric molecules, such as 3-anilinoacrolein anil, where the direction of electronic asymmetry is inclined at an angle ($90^0$ in this particular case) to the protonic displacement direction. In such molecules, the electronic and protonic contributions to the net polarization do not add up completely and hence resulting in reduced polarization values.[2]

An interesting question that may arise regarding the electronic origin of the polarization in CA crystal structure is the following. As the electronic density in

each molecule in a hydrogen bonded network is coupled to that of the neighbouring molecules via the resonance assisted hydrogen bonds, could it be possible to realize stable protonic displacement of molecules in a macroscopic region reversing the net crystal polarization by optically exciting the electronic density of the molecules in that region? Iwano et al[9] have tried to experimentally investigate this aspect by optical pulse pump and SHG probe based measurements and their calculations suggest the existence of possible energy pathways for optically triggered polarization reversal by optical excitation in a one dimensional domain.

Lastly, the moderate nature of the hydrogen bond strength in CA structures plays a crucial role in allowing the polarization reversal to occur via proton transfer. Too weak hydrogen bonds would not be able to sustain the non centrosymmetric positioning of the protons/hydrogen atoms, and on the other hand, too strong bonds will not allow for the proton transfer to occur, thereby causing hindrance to the polarization reversal process.

### 2.1.4 Ferroelectric characterizations

Polarization hysteresis loops with triangularly waveformed alternating electric fields applied along the c-axis of a CA crystal is shown in figure 2.10 (a). It can be observed that the remanent polarization value decreases with increase in the frequency of the electric field. The remanent polarization values of crystals were optimized by repeated poling and thermal treatments and the maximum optimized remanent polarization obtained was 21 $\mu C/cm^2$; the coercive field was $\sim$14 kV/cm. The effect of poling on a crystal is optically investigated and shown in figure 2.10 (b). The upper panel shows the linear image of the (100) plane of the crystal, showing the positions of the electrodes used to apply the electric field. The middle panel show the second harmonic generation signal (SHG) intensity measured in the absence of electric field in reflection geometry along the c-axis of the crystal in its virgin state in the absence of electric field. Randomly distributed anti parallel domains can be observed. The increase in SHG intensity after poling the crystal along c-axis (lower panel) signifies ferroelectric activity.[1] Similarly, SHG intensities have also been quantitatively measured both in reflection and transmission mode with fs laser sources. In the reflection mode, the SHG intensity is found to be highly dependent on the quality of crystal surface.[99, 8]

Usually, during the growth of crystal from the solution, multidomain structures form with ferroelectric domain walls separating the domains. The polarization

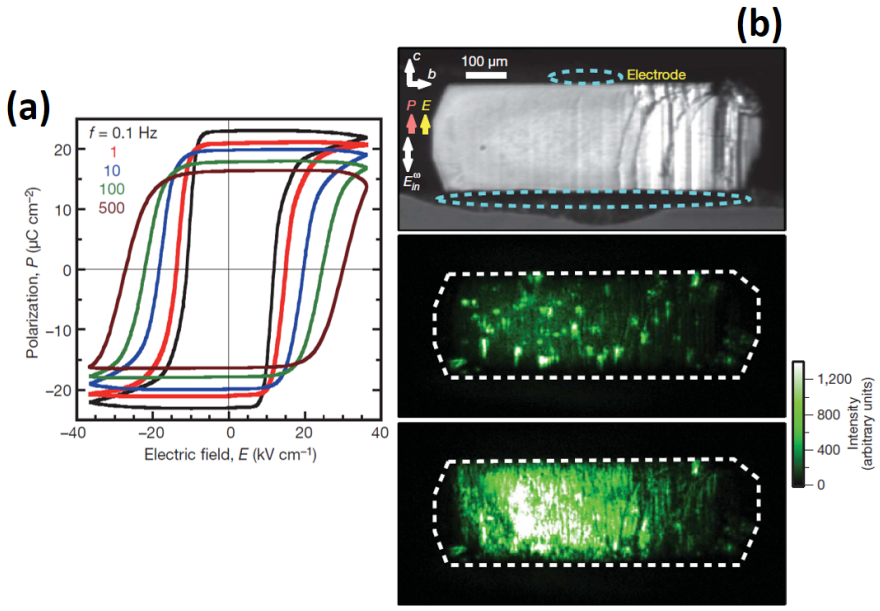


Figure 2.10: Ferroelectric characterizations of CA crystal. (a) shows the ferroelectric hysteresis loops measured on a crystal using an AC electric field, E with triangular waveform. (b) shows the optical microscope image of CA crystal surface with top panel showing a linear image and middle and bottom panels show second harmonic image before and after the poling with an electric field of 24 kV/cm respectively. Image is taken from reference [1].

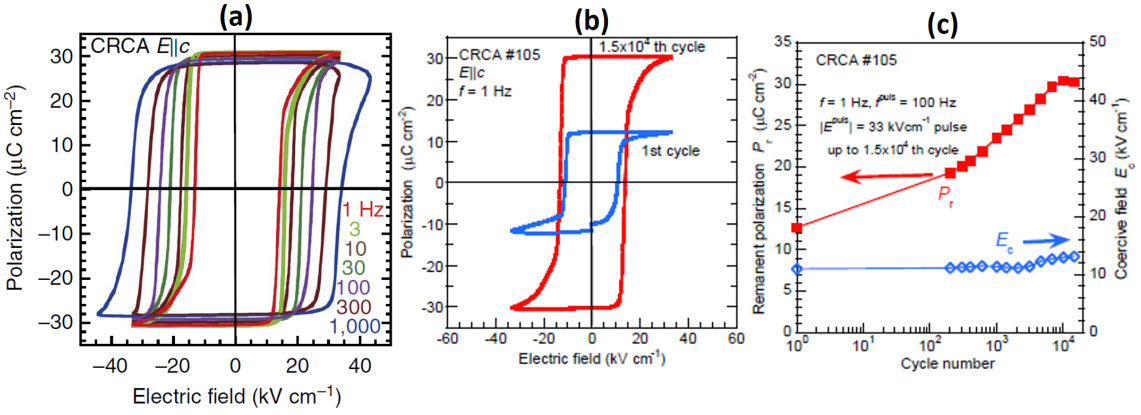


Figure 2.11: Optimization improvements of CA ferroelectric properties. (a) shows the polarization hysteresis loops of CA crystal after proper optimization through thermal and electrical treatment. Remanent polarization reaching upto 30 $\mu C/cm^2$ and its reduced frequency dependence is evident. (b) shows the improvement of remanent polarization of another crystal after repeated polarization procedures. (c) shows how the remanent polarization and coercive field values evolve with repeated cycles of polarization reversals. Figures are taken from reference 14.

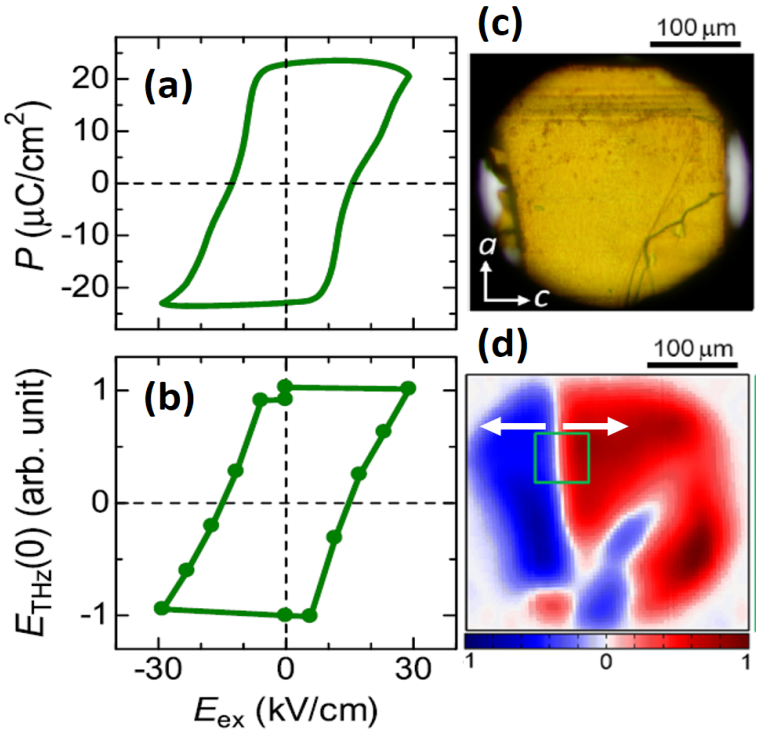


Figure 2.12: Terahertz radiation imaging of CA crystal. (a) and (b) show the hysteresis loop of the crystal polarization and the tera hertz field amplitude respectively with respect to the applied external electric field. (c) and (d) show the optical and tera hertz phase images of the crystal respectively. Images taken from reference [101].

charges on domain walls create huge depolarizing fields, to compensate which, dense mobile charges and charged mobile or immobile defects get embedded in the crystal growing at room temperature. These pinned defects and charged domain walls result in imperfect and incomplete switching of bulk polarization due to relatively slower motion of the charged domain walls which may result in the suppressed values of observed remanent polarization.[100] However, by thermal annealing and repeated poling procedure these defects can be removed, thus, the remanent polarization can be improved and faster switching can be obtained. Such an effort on CA crystals by Hirouchi et al[2] have improved the remanent polarization of CA crystals to reach $\sim$30 µC/cm$^2$, increased the switching frequency without significant loss of polarization and reduce the frequency dependence of remanent polarization and improved rectangularity of hysteresis loops. (figure 2.11).

The multidomain structures of the as grown crystals and the domain propagation under applied electric field have been imaged with terahertz radiation imaging by Sotome et al.[101] Femto second laser pulses in tera hertz (THz) frequency range

are irradiated onto the crystal and the radiated tera hertz electric fields, originated by virture of the non-centrosymmetric ordering in CA crystals, parallel to the c-axis of the crystal are measured in transmission mode. The magnitude and direction of the polarization of the crystal is locally mapped by measuring respectively the amplitude and phase of the radiated signal.

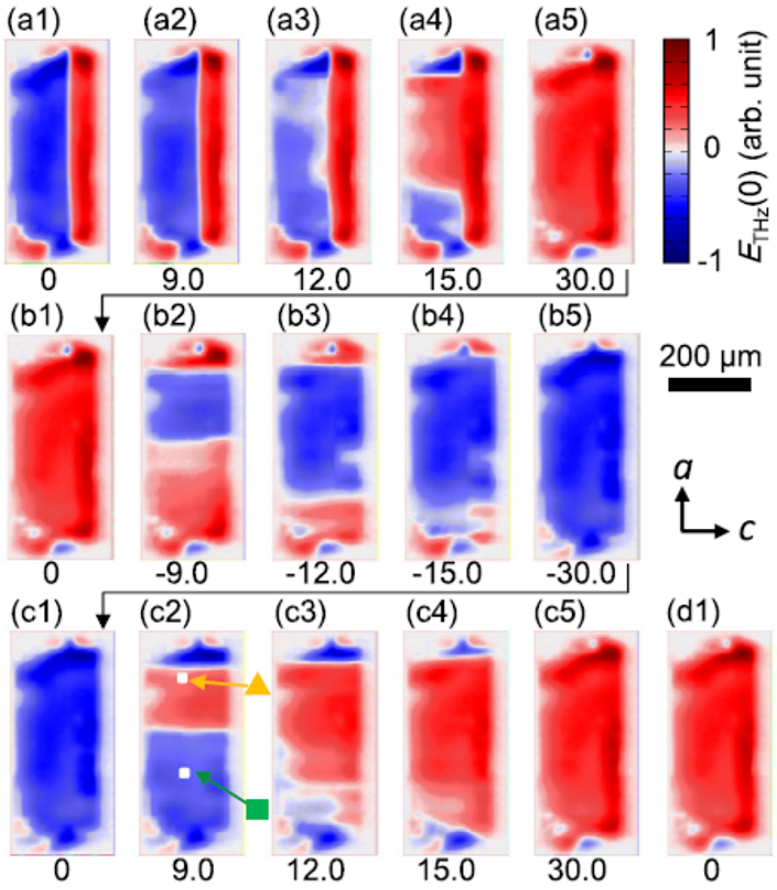


Figure 2.13: Domain dynamics of a CA crystal as imaged by tera-hertz radiation imaging. (a1) shows the tera hertz map of the virgin domain structure of the crystal. (a2)-(a5) show the domain maps after application of different values of external poling electric field as indicated below each corresponding image in the units of kV/cm. (a5) and (b5) show the completely poled state of opposite polarization. It can be seen that the domain maps of virgin states are different from the completely poled states. Image is taken from reference [101].

The $180^0$ phase reversal of the tera hertz electric field upon polarization reversal of the crystal obtained by applying external electric field to the cystal along the c-axis signifies the coupling between the polarization and the radiated tera hertz electric field. The spatial map of the phase of the radiated tera hertz field reveals the ferroelectric domain structure of the crystal. Such a map is shown in figure 2.12,

where (a), (b) show the polarization reversal hysteresis loops of crystal polarization and the initial tera hertz electric field amplitude with respect to the applied external electric field strength respectively and (c), (d) show the optical image of the crystal and the corresponding tera hertz phase map respectively.

Further, the domain wall propagation dynamics is captured by tera hertz mapping the crystal by increasing external electric field mangitude. It is observed that even for a virgin crystal with a domain wall perpendicular to the c-axis, domain wall propagation does not occur along c-axis, rather, a pair of domain walls propagate along a-axis as shown in figure 2.13. This is indicative of the strong anisotropy of the hydrogen bonded dipolar arrangement in CA crystals along the c-axis which makes it difficult for the co-operative bond switching to occur along that axis during domain wall propagation.

## 2.2 Thin films of Croconic Acid

One of the practical advantages that CA offers is its vacuum sublimability which allows the high vacuum or ultra high vacuum frabrication of thin films and integration of the process with the state of the art ultra high vacuum fabrication systems. When almost all organic ferrelectrics are usually grown using ex-situ techniques such as drop casting or spin coating, vacuum integration of CA deposition makes it a suitable material for device fabrication for large scale commercial applications. Especially, fabrication of CA based devices which includes the growth of reactive materials such as reactive ferromagnetic metals would be possible without exposing the reactive materials to degraded environment.

Several groups have utilized this vacuum sublimability aspect to grow and study the properties of CA in thin film form. Studies carried out so far on thin films of CA can be categorized into two sections, (i) ultra thin films and (ii) bulk thin films of several 10s of nanometers. The former type of study deals with the growth of sub monolayer thick films of CA investigating the growth and structural properties of the layers probed by Scanning Tunneling Microscopy (STM) and supported by Density Fuctional Theory (DFT) calculations. The later type of study involves mainly the fabrication of thicker polycrystalline films to optimize the growth conditions and to study the ferroelectric properties of CA films for possible device applications.

### 2.2.1 Ultra thin films

#### 2.2.1.1 Molecular structure

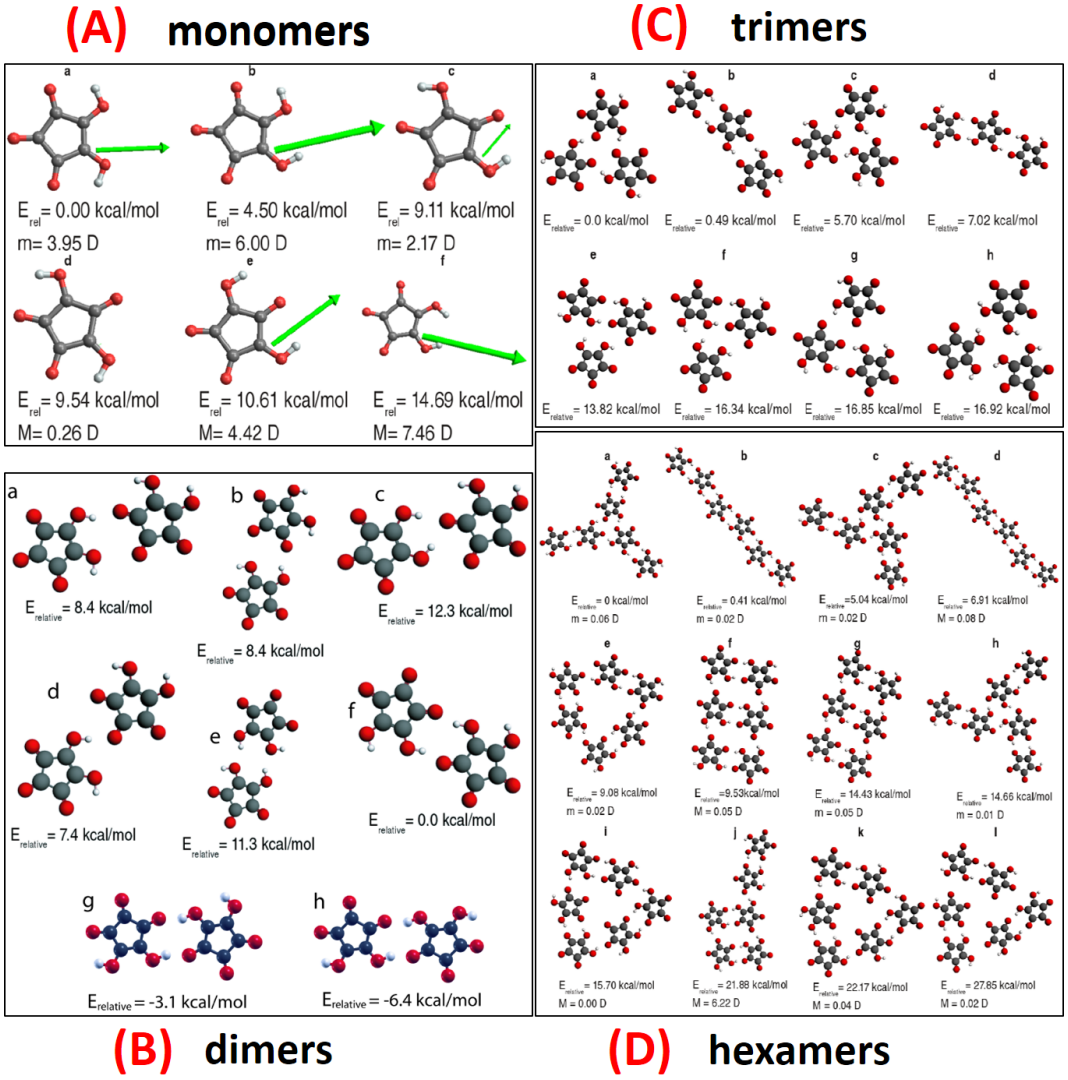


Figure 2.14: Possible molecular configurations of CA units with their corresponding relative enrgies as optimized by DFT calculations. The green arrows in panel A represent the dipole moment vectors of individual monomers of CA. Images taken from the supplemetary information of the reference [6].

When molecules are vacuum evaporated onto metal substrates, the crystallization process that occurs on the substrate surfaces can be very different from what occurs when the molecules are crystallized from a liquid solution. The structure of individual molecules and the entire network or layer of molecules that can form on a substrate surface are determined by several factors such as the energy of evap-

orated molecules in gas phase, surface chemical reactivity and temperature of the substrate surface. Further, the molecular arrangement may have dependence on the particular material surface, thickness of the substrate surface in case of ultra thin substrates and thickness of the molecular layer. Thus, for CA molecules also it is expected that the structural arrangements on substrate surfaces can be different from that in solution grown bulk crystals. Especially, when the thickness of the molecular layer is increased from very low sub monolayer regime to a few monolayers, interesting structural features may appear owing to the increase in the complexity of all the interaction forces. For example, for absolutely low thickness of sub-monolayer regime, individual CA molecules may get adsorbed on the surface and upon increasing the thickness, several molecules may develop intermolecular hydrogen bonds to form dimers, trimers or extended networks on the surface. As CA is a planar molecule, it may be expected that the planar structure retains when the molecules are contrained to be adsorbed on a flat surface. However, the exact details of the molecular orientation may depend on the particular type of monomer or molecular networks getting adsorbed and the type of interaction that takes place at the substrate-molecule interface.

Depending on the relative positions of the two hydrogen atoms of a molecule, a total of 6 monomer conformations of CA are possible for planar orientation (figure 2.14 (A)). It is evident from the figure that out of all six monomer conformations only A.b and A.c are achiral and the minimum energy configuration (A.a) is achiral, where chirality of an individual molecule is related to the molecular conformation and is defined by the relative positions of H atoms in the individual isomers of the molecule. The asymmetric positioning of H atoms with respect to the central pentagon consitute the chiral conformation and symmetric positioning constitue the achiral one. Various possible types of low energy dimers, trimers and hexamers formed from the chiral and achiral monomer conformations as optimized by first principle calculations to lie in one plane are shown in figure 2.14 (B), (C) and (D) respectively. (with first principles program ADF and contraints on molecules to lie in one plane). In the case of trimers, some configurations can be seen preserve the overall chirality of the entire trimer-unit.[6]

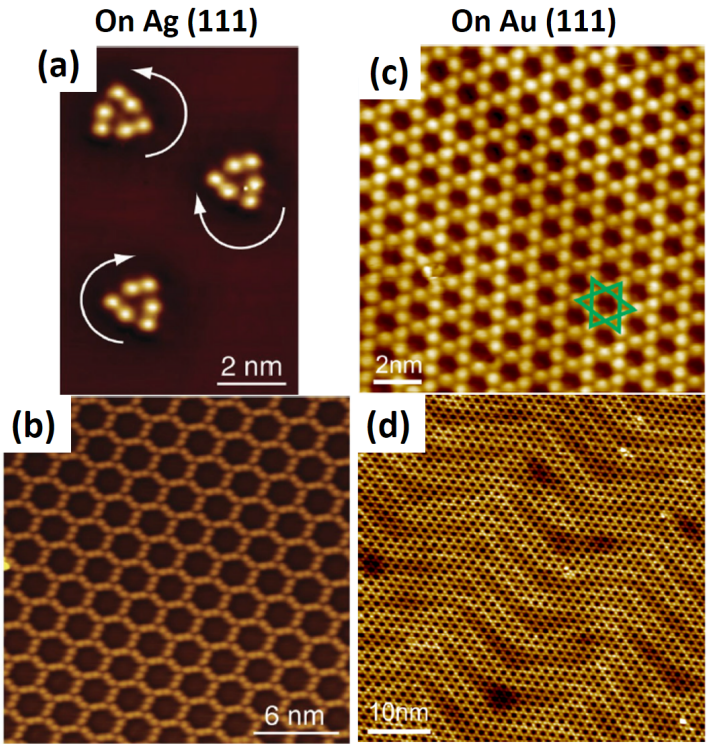


Figure 2.15: Substrate supported two dimensional growth of CA networks as probed by STM imaging. (a), (b) present the growth structures for very low submonolayer and one monolayer thickness of CA films respectively on Ag(111) surface. Circular arrows in (a) represent the direction of chirality of the molecular clusters. (c), (d) present small and large scale surface morphology on Au(111) surface. Figures taken from references [6, 7].

Experimentally, growth of two dimensional sheets of chiral and achiral networks supported by metallic substrate surfaces has been observed contrary to the densely packed zigzag sheets of molecular networks in three dimensional crystals. Such networks are shown in figure 2.15 for sub monolayer growth of CA films on the surface of Ag(111)[6] in which (a) shows the isolated triangular clusters of chiral CA dimers for very low sub monolayer coverage and (b)-(d) show the extended honeycomb network for one monolayer coverage (post annealing at 350 K). The dimer structures are the fundamental building blocks of all the observed porous network structures on Ag(111) surface. Similarly, on Au(111) surface, 2-dimensional sheets with Kagome lattice structures of CA molecules, as opposed to the observed honeycomb structures on Ag(111) surface, have been observed.[7]

A close analysis of figure 2.15 reveals that the molecules on Ag(111) surface in the extended networks are in the chiral form and correspond to the dimer configuration of B.f. However, extended networks with achiral conformation of constituting

molecules were also observed but with very low frequency. On the other hand, the extended structure on Au(111) for one monolayer thickness is achiral, composed of CA trimers as building blocks which are fundamentally different to that on Ag(111) and correspond to the trimer configuration of C.a. It can be noted, in the case of trimers, that the basic monomer units of the networks on Ag and on Au surfaces are different; the one on Ag is chiral (figure 2.14 A.b) and on Au it is achiral (figure 2.14 A.a).

Experimental and computational analyses suggest that the observed structural difference is due to weaker influence of Au(111) surface on the molecules with respect to the intermolecular interaction strength. DFT calculations of modeled planar networks in vacuum (constrained to lie in a plane without any metal substrate) suggest that there is an energy difference of 0.2 eV between the two monomers (2.14 A.a for Au and 2.14 A.b for Ag) used to build the networks corresponding to the observed structures on both surfaces with the monomer for Ag surface being on the higher energy side. The stability of the lowest energy monomer based network on Au surface reveals the weak influence of Au surface on the network formation of CA molecules. Whereas, the observed networks with higher energy monomers on Ag surface are indicative of stronger intermolecular interactions and the effect of substrate surface on the molecular networks that could be playing a vital role in stabilizing such higher energy monomer based networks on a more reactive Ag surface.[7]

#### 2.2.1.2 Ferroelectric Polarization and its reversal

An individual CA molecule is expected to have a dipole moment of approximately 7 D in gas phase. However, this value depends on the particular monomer conformation of the molecule. As shown in figure 2.14 (A), the two monomer conformations with the lowest energy (figure 2.14 A.a and A.b) have significant calculated dipole moment values, although the second lowest energy monomer (figure 2.14 A.b) has a larger dipole moment. It is interesting to note that A.b is the same achiral monomer whose extended networks are dominantly stabilized on Ag surface. It is even more interesting that the individual chiral dimer units on Ag and achiral trimer units on Au surface are non polar as the dipole moments of the constituent monomers cancel out, thereby making the entire networks formed from these dimer and trimer units non-polar. These stable non polar structural arrangements can possibly not exist in the solution grown crystal forms and form only in films grown on certain substrate

surfaces.

Nevertheless, detailed simulations including molecular dynamics and DFT have been performed to explore whether polar 2D networks on these metallic surfaces exist that can host a proton transfer mechanism and give rise to a net polarization. Interestingly, Kunkel et al[6] have observed, in molecular dynamics simulations of CA layers constrained to lie in a plane without any substrate surface, that the experimentally observed non polar networks on Ag surface can undergo spontaneous dynamical structural changes and stabilize a polar network after co-operative hydrogen atom transfers and rearrangements in the absence of any electric field. Such stabilization of polar networks have also been observed in the CA layer when the simulation is performed with two monolayers of Ag as substrate surface in proximity to the CA layer. However, these spontaneous co-operative hydrogen atom transfers need not necessarily be concerted; rather it could be step wise, as suggested by the detailed MD simulations tracking all the hyrogen bond lengths in a network similar to that found on Ag surface as a function of simulation time.[102] In the presence of an in-plane electric field, however, the collective proton tranfers may partially become concerted.

Similarly, for the non polar networks observed on Au(111) surface, calculations show that collective hydrogen transfer can result in a polar network composed of both chiral (figure 2.14 A.a) and achiral (2.14 A.b) monomers. However, detailed MD simulations concerning the energetics of the hydrogen transfer are yet to be performed.

No matter how interesting the feasibility of ferroelectricity in substrate supported ultra thin films of Croconic Acid may sound, its experimental verification poses astounding challenges. The elecromechanical method of characterizing local ferroelectric properties of thin films, where a local tip generated vertical electric field is employed to create a mechanical deformation of the local region in a thin film via the inverse piezoelectric effect which is then detected via photosensitive detection of the tip-hosting cantilever, may not be effective for studying atomic layer ferroelectricity. Especially, when the net polarization of the planar sheet type molecular network structures, as found on Au and Ag surfaces, is expected to lie in the plane of film due to the planar orientation of dipole moments of the constituent monomers, dimers or trimers, it is even more difficult to employ the scanning probe technique. For the same reason, it also becomes challenging to probe the ferroelectric reversal properties of the ultra thin films using a Scanning Tunneling Microscopy (STM) which is otherwise a very effective technique for probing atomic scale dimensions. It

must be noted, nevertheless, both for a single molecule and a dimer based network adsorbed on Ag surface, the DFT optimized orientations seem to be slightly tilted with respect to the film plane[6] with a non-zero out of plane component of polarization. This can be used to the advantage of probing the ferroelectric poralization with the surface probe techniques, provided detailed theoretical understanding of the polarization components and their impact on a possible planar and an out of plane component of hydrogen transfer can be obtained a priori. Moreover, as STM is evolving to be a very effective tool for characterizing 2D ferroelectric materials[103], even with in-plane ferroelectric polarization, similar ideas can be employed to probe ferroelectricity in ultra thin films of CA.

## 2.2.2 Polycrystalline thin films

### 2.2.2.1 Growth optimization studies

Studies on growth and ferroelectric properties of polycrystalline thin films of thickness in the range of several 10s of nanometers have been performed by several groups. These attempts are directed towards the optimization of growth conditions of CA films with the ferroelectric properties unaffected so as to realize the fabrication of nanoelectronic and spintronic devices based on this organic ferroelectric. Usually, when organic materials are vacuum evaporated onto substrates, two parameters, namely, the molecule-molecule interaction and the substrate-molecule interaction, determine the growth behaviour of the molecular layer. The molecule-molecule interaction tends to coaggulate the molecules together and encourage three dimensional growth of the layer, whereas, stronger substrate-molecule interaction encourages two dimensional growth behaviour. The three dimensional growth mode may result in a relatively rougher surface which impedes the growth of high quality interface in vertical devices, resulting in reduced device performance. Thus, the soul motivation behind the growth optimization studies for any organic material is to optimize the growth conditions to obtain thin two dimensional layers with minimum surface roughness.

As an example, Croconic Acid was grown by Jiang et al on $Al_2O_3$ surface by high vacuum physical vapour deposition methods at optimized substrate temperatures and thickness ranges to obtain continuous two dimensional films of several 10s of nanometers. The surface coverage of films grown are highly dependent on the above two parameters and there exists a sweet spot between both the parameters where continuous films can be obtained. Such films grown on $Al_2O_3$ surface are shown in

figure 2.16. These films are grown at specified substrate temperatures to limit the surface diffusion to obtain quasi continuous films and slowly annealed up to room temperature to allow the crystallization to take place.[10] It is clear that films are continuous only above certain film thickness (nominal thickness of 20 nm) and for a particular range of substrate temperature (around -33$^0$ C). However, the surface of the continuous films are not very smooth; with a RMS roughness reaching 3.5 nm for a 5×5 µm$^2$ area. Such a roughness may be acceptable while fabricating thick films of thickness reaching 100s of nanometers but for thinner films, it will result in poor quality interfaces and greatly hamper the device characteristics when used to fabricate vertical devices.

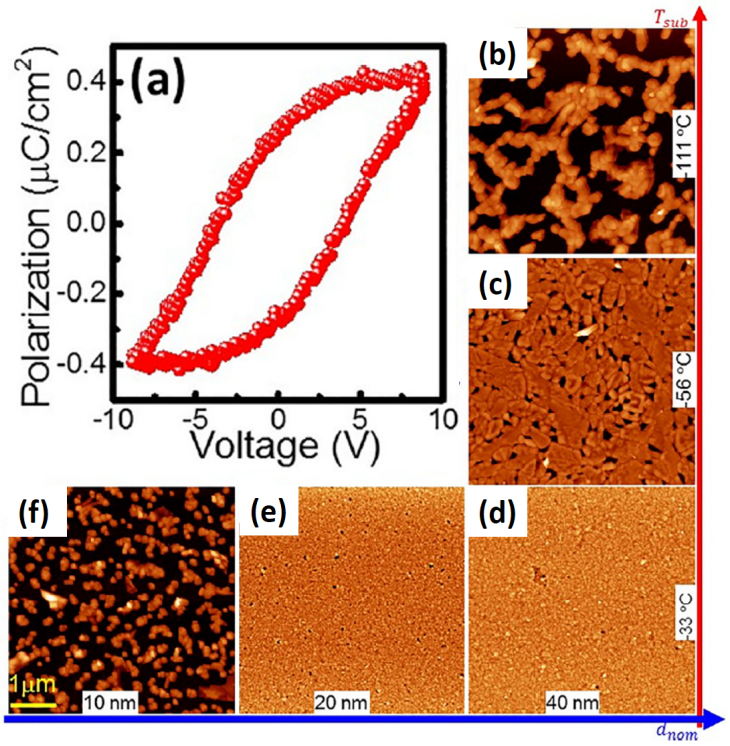


Figure 2.16: Growth optimization of bulk thin films of CA. (a) shows the measured polarization loop of CA used as dielectric in a capacitor device. (b)-(f) collectively show the surface morphology of CA films grown on $Al_2O_3$ substrates at various substrate temperatures ($T_{sub}$) and for various film thicknesses ($d_{nom}$). Images taken from reference [10].

Local imaging of ferroelectric domains on the aforementioned CA films were carried out by room temperature Piezoelectric Force Microscopy which revealed the polydomain structure of the samples. The PFM phase images of a 35 nm sample grown on conducting $NiCo_2O_4$ surface are shown in figure 2.17. The grain to domain correspondence indicate that each grain could be a single crystalline domain of CA.

Further, local polarization reversal attempts by applying electric field with the PFM tip results in polarization hysteresis loops (figure 2.17 (d)) with a coercive field of ∼7V, thereby, confirming ferroelectricity in these films. Besides, macroscopic polarization hysteresis loops obtained from capacitor devices with Al electrodes and 185 nm CA layer results in a macroscopic polarization value of ∼0.4 µC/cm$^2$ (figure 2.16 (a)) which is much lower than that observed in CA crystals.

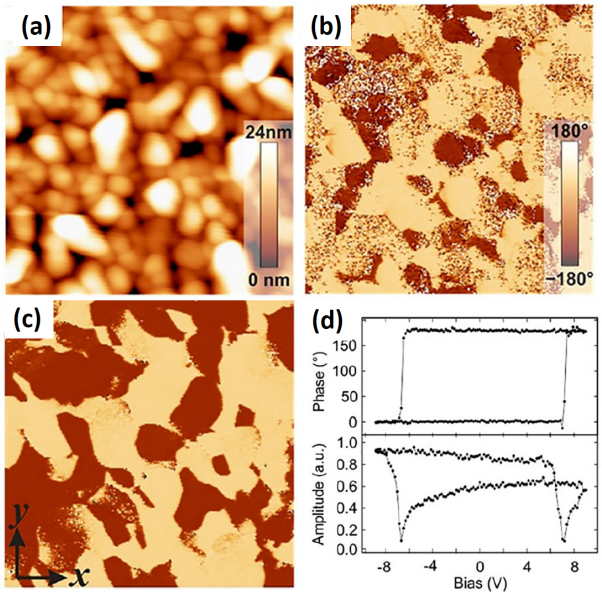


Figure 2.17: Local PFM measurements on CA thin films. (a)-(c) show the morphology, vertical PFM phase and lateral PFM phase respectively. (d) shows the local hysteresis loops of vertical PFM phase and amplitude measured with the PFM tip on a grain. Images taken from reference [10].

From the point of view of fabricating nanoelectronic devices with thin films of CA, the fact that the polarization in ultra thin films of CA grown on metal substrates are in the plane of the film stands as a major obstacle, as this might make it difficult to control the ferroelectric polarization state with an out of plane electric field in a vertically structured electronic device, the most widely used scheme of device fabrication. On the other hand, the high surface roughness of bulk thin films, even after substantial optimization efforts to obtain continuous films, stands in the way of fabricating high quality thin film devices with CA. Further, the highly anisotropic polarization in polydomain-polycrystalline bulk CA films may not allow the entire polarization within the vertical device to orient in the out of plane direction, thereby, reducing the effective macroscopic polarization. This calls for advanced growth methods based on physical vapor deposition which are compatible with large scale device manufacturing setups and can ensure smoother surface, better

surface coverage for ultra thin films, robust ferroelectric properties of the deposited molecules and control over the polarization axis of the organic ferroelectric.[104]

One attempt is to apply strong in-situ electric field during the growth of these polar molecules. This can be done by applying high voltage to a conducting mesh that covers the substrate at a certain distance from it and is placed on the source-substrate path. With the substrate connected to ground, the high voltage will create strong electric field near the substrate surface. Parameters such as the magnitude and direction of applied electric field, distance between the substrate and the mesh, porosity of the mesh etc can be tuned to control the growth behaviour of the films (figure 2.18).

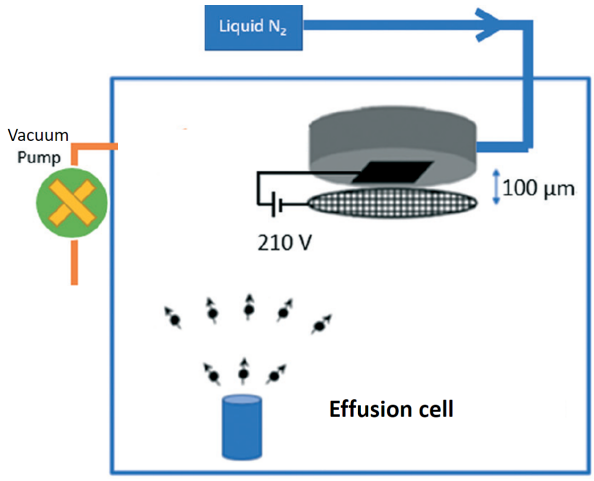


Figure 2.18: Schematics of mesh arrangement for electric field guided growth optimization of CA thin films. Figure is taken from reference [105].

Attempts along the above direction have been taken by several groups. For example, by applying an electric field of 4 kV/cm to the mesh, Costa et al were able to reduce the surface roughness of a 22 nm CA film grown on $Si/SiO_2$ substrate to merely 1 nm (full width half maximum in height distribution). More importantly, the ferroelectric properties of films grown in such a way were shown to be retained.[105] Similarly, Yuan et al studied the temperature dependence of nucleation rate of CA films with and without electric field assisted growth and observed that the maxima of grain density shifts in temperature when electric field is applied during the growth.[106]

# Chapter 3

# Experimental Methods

In this chapter, we describe the experimental techniques, methods and instruments that have been employed for fabrication, processing and characterization in the entire course of the thesis work. Starting with the description of ultra-high vacuum environment for sample fabrication, we proceed to describe the technique of Piezoresponse Force Microscopy (PFM), a widely used technique to characterize ferroelectric materials. This chapter will also include a brief description on some of the instrument automation that was carried out during the characterization process. We will also discuss about the optical methods that were employed to characterize some crystals of Croconic Acid.

## 3.1 Ultra-high vacuum environment

### 3.1.1 Brief introduction to vacuum science

The atmosphere of the earth is full of gaseous particles. Gas molecules of several compounds such as Oxygen, Nitrogen, Carbon monoxide, Sulphur dioxide etc. constitute the atmosphere. The presence of all the molecules exert pressure on any object present in the atmosphere which is known as the atmospheric pressure. The atmospheric pressure at the sea level is 760 mm of mercury. From thermodynamics it follows that the mean free path of the gas particles in a system, defined as the average distance that the molecule traverses between two collisions, varies inversely with the pressure inside the system. At atmospheric pressure, this mean free path is so short and the number density of molecules is so large that, statistically, an enormous amount of molecules is inevitably present near the surface of any object present in the atmosphere. Naturally, fabrication of any form of any material for technological and research purposes under such a condition exposes the material to atmospheric impurities. Especially, in the field of nanoscience, the presence of atmospheric impurities brings major degradation of properties of the fabricated devices. This gives rise to the need of vacuum technologies.

Creating vacuum by pumping out the gaseous molecules from an enclosed environment lowers the pressure inside the system. Decrease in pressure results in decrease in the number density and increase in the mean free path of the molecules inside. With decrease in system pressure, the time required for the formation of impurity adsorbate layer on the substrate surface increases, hence, the reduction in impurity contamination and the improvement of sample quality. The time required for the formation of one monolayer of impurity adsorbates on the substrate surface,

| Vacuum range | Pressure range (mbar) |
|---|---|
| Rough vacuum | $>10^{-4}$ |
| High vacuum | $<10^{-4}$, $>10^{-8}$ |
| Ultra high vacuum | $<10^{-8}$, $>10^{-11}$ |
| Extreme high vacuum | $<10^{-11}$ |

Table 3.1: Pressure range for different vacuum levels

t, is roughly defined as $10^{-6}$ s/pressure (second/millibar). Using this formula, it can be seen that the time for the formation of one adsorbate layer increases from a few nano seconds at atmospheric pressure to approximately 8 hours at a pressure of $10^{-10}$ mbar. This signifies that the higher the vacuum, the cleaner the fabrication process.

Based on the values of pressure, the range of vacuum can be divided into the categories shown in table 3.1. Different applications require different categories of vacuum. For example, certain deposition techniques work fine in HV range whereas for surface sensitive measurements such as Scanning Tunneling Microscopy (STM) on ultra-clean surfaces necessarily requires UHV. Similarly, different techniques are employed to create vacuum in different ranges. For example, a simple rotary pump can be sufficient to create vacuum in Rough Vacuum range, whereas, an efficient Turbo Molecular Pump (TMP) is necessary to create a good level of UHV. Brief description of working principle of various pumps and their range of operation are presented in figure 3.1.

Another factor that plays a significant role in determining the overall pumping efficiency is the quality of steel that is used to design the vacuum chambers. In a standard laboratory grade vacuum system, high quality stainless steel of grade SS-304 or SS-304 L is employed. In special cases, where the measurement and fabrication are sensitive to stray magnetic fields, SS-316 or SS-316 L grade of steel is employed which is the least magnetic grade of steel available. The usage of good quality steel and the smoothness in internal surface finish (smaller surface roughness average) reduces the time needed by a vacuum system to reach its ultimate pressure.

As the vacuum range goes higher into UHV, the system becomes more sensitive to leaks. In UHV range, a small mistake during system integration can cause a vacuum leak. Usually, it is easier to detect a big leak and it can be a real pain at times to detect a very small leak in the range of $1 \times 10^{-9}$ mbar. Such leaks are detected by the use of calibrated leak detectors which employ the He gas to detect small leaks.

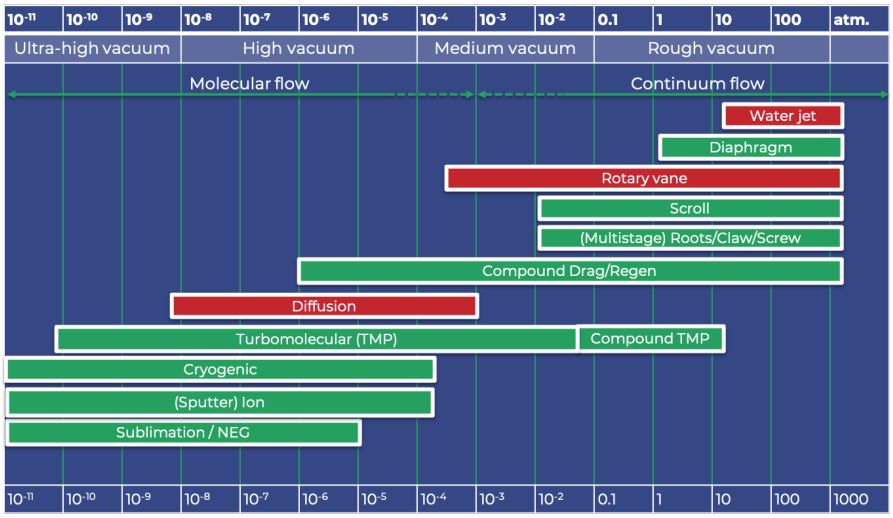


Figure 3.1: Vacuum range for operation of various vacuum pumps. Figure is taken from reference [107].

### 3.1.2 The hybrid fabrication cluster assembly

The hybrid fabrication cluster system is a world class thin film deposition facility situated in the hybrid spintronics laboratory of IPCMS. This facility is a cluster of UHV connected isolated vacuum chambers dedicated for growth of thin films of different types of materials. The sophisticated and careful design and multiple stages of pumping of the chambers provide ultra-high vacuum reaching to a level of $2 \times 10^{-10}$ mbar in some of the growth chambers. Each chamber has its dedicated pumping system and an isolated pumping system provides easier isolation of other chambers during the vacuum breakdown of one. The UHV transfer facility, facilitated by the robotic transfer arms in the central radial transfer chamber and robotic towers in individual growth chambers, makes it possible for a user to fabricate a wide varieties of multilayer thin film heterostructures. Large sized substrate holder enables a user to prepare multiple samples in one go without breaking of chamber vacuum. Robotized towers in individual growth chambers enable the rotation and height adjustment of the sample during fabrication. Resistive heaters embedded in these robotic towers allow the user to perform sample fabrication at elevated substrate temperatures and perform post fabrication annealing of samples at temperatures reaching as high as 700 $^0$C. Further, Reflection high energy electron diffraction (RHEED) available in individual growth chambers allow for the in-situ observation of crystallinity features from the sample surface during the growth of thin films. More importantly, shadow masks connected to high precision position manipulator allows for the fabrication a vertical heterostructure devices.

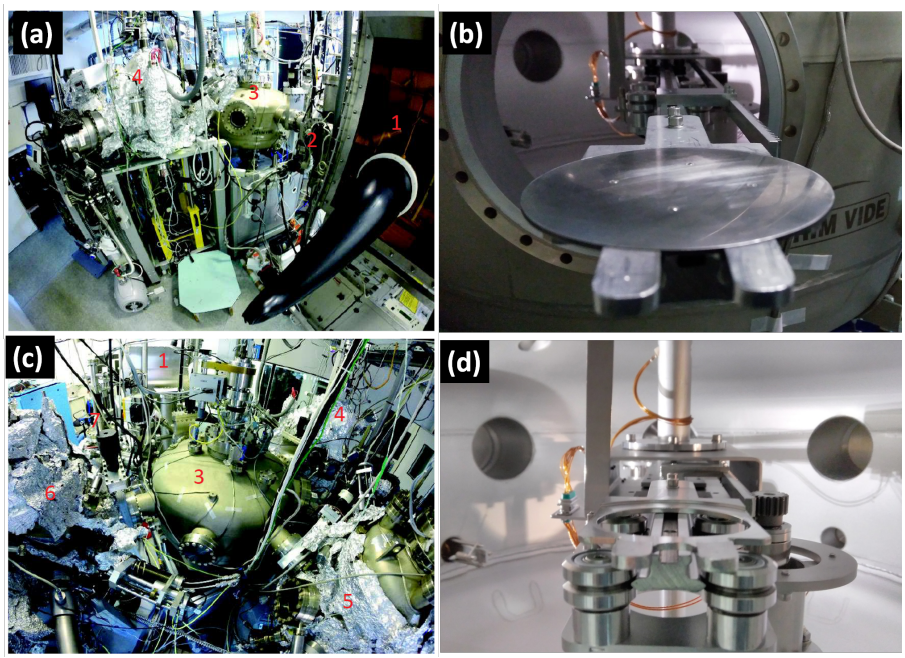


Figure 3.2: Photographs of the hybrid cluster UHV system. (a) and (c) show the entire system from different viewing angles. (b) and (d) show the robotic transfer arm with (outside the radial transfer chamber) and without (inside the radial transfer chamber) the substrate plate respectively. 1- glove box, 2- load lock, 3- robot chamber, 4- sputtering chamber, 5- thermal evaporation chamber, 6- organic MBE chamber, 7- annealing chamber. (a) and (c) are taken from the reference [108].

Figure 3.2 shows the growth and preparation chambers of the hybrid cluster system. The substrates are introduced to the loadlock chamber which can harbor multiple sample holding plates. The loadlock chamber is connected to the central radial transfer chamber and to the glove box. The glove box provides neutral Nitrogen environment for sample or substrate manipulation, spin coating etc. The radial transfer chamber hosts a radial robotic transfer arm that takes the sample from the loadlock and transfers it to other growth chambers. A huge ionic pump supports the pumping of this transfer chamber, maintaining its pressure at $\sim 1 \times 10^{-9}$ mbar.

The Sputtering chamber is dedicated to sample fabrication by DC and RF magnetron sputtering method. Fabrication of three different metals and one oxide material can be performed from these magnetrons by providing optimized conditions of Argon gas flow to the chamber and optimized power wattage to the magnetron power supply. The whole sputtering system is controlled from a computer interface which makes it easier for the user to operate the system. Further, computerized control over the operation of the shutter for each magnetron brings precision to the thickness of deposition.

The Evap chamber is dedicated to deposition of metals by thermal evaporation. This chamber is supported by an efficient Turbomolecular pump, an ionic pump, a titanium sublimation pump and a liquid nitrogen cryo pump which ensure very low working pressure during the growth of materials. Three high temperature Knudsen cells are housed in this chamber, evaporating metals like gold, cobalt and platinum. These cells are water cooled for their proper functioning. Further, substrate cooling upto a temperature of 100 K is possible which is useful in reducing interdiffusion of depositing metals into the previously prepared stacks of sample. The manipulation of cell current is fully automated via PID temperature controller with respect to the cell temperature. For the work of the thesis, this chamber was primarily used to prepare cobalt films with the substrate at room temperature.

The OMBE (Organic Molecular Beam Epitaxy) chamber is the dedicated part of the cluster assembly where organic molecules are grown by molecular beam epitaxy. Four water cooled effusion cells with maximum working temperature reaching ∼700 $^0$C all equipped with individual thermocouples for the temperature measurement enable the deposition of a variety of organic molecules.

All the above functionalities make the hybrid fabrication cluster assembly a highly efficient fabrication facility capable of easy sample fabrication of a variety of complex heterostructures and nanodevices.

### 3.1.3 The metal MBE fabrication setup

The metal MBE setup (figure 3.3) is a dedicated setup for Molecular Beam Epitaxy growth of metallic samples, separated from the hybrid fabrication cluster but housed in the IPCMS laboratory. This system consists of 8 water cooled crucibles having different metallic slugs. By means of applied electric field and a strong magnetic field coming out a specially designed permanent magnet, electron beams emanating from a thermionic filament are focused onto these metallic slugs. The temperature on these slugs locally rise until metal atoms start to evaporate onto a substrate which can be heated to ∼900 $^0$C during growth. This chamber has dedicated pumping system and a dedicated loadlock. Attached RHEED system allows for the in-situ crystalline characterization during growth. A special geometry of available crucibles allows for simultaneous deposition of 2 different metals, allowing for fast and efficient fabrication of multilayer and alloy fims of a range of different metals. This chamber is known to have produced metallic films of highest quality. Also, the MBE growth of high quality insulating materials is possible with a minimum modification to the

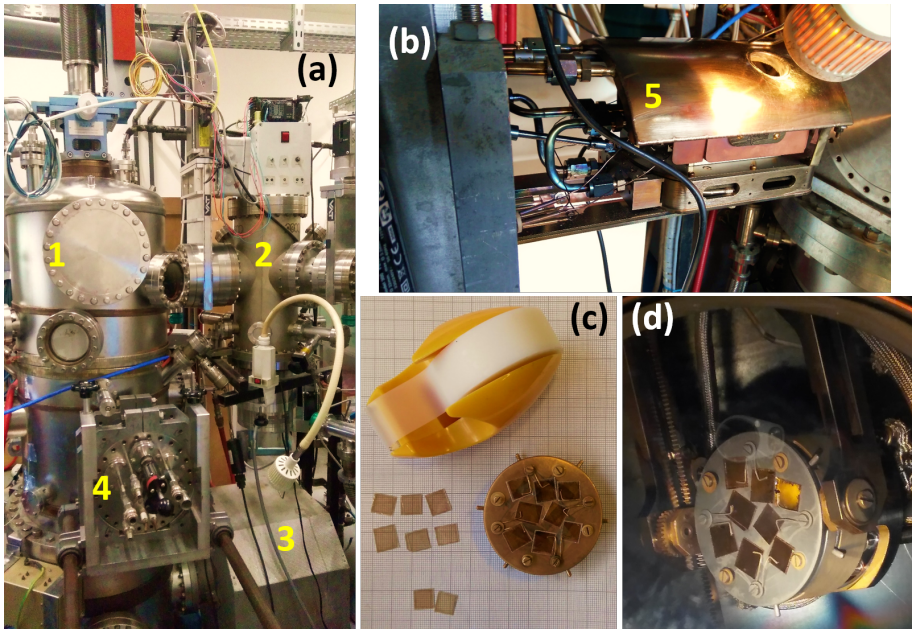


Figure 3.3: Metal MBE system for Au substrate preparation. (a) and (b)show the UHV metal MBE system. (c) and (d) show the freshly cleaved mica on substrate plate (c) and Au film deposited on mica substrates (d). 1- MBE chamber, 2- load lock, 3- ionic pump, 4- MBE target assembly, 5-inside view of MBE target assembly.

setup. For the work of the thesis, Au films on cleaved mica surfaces were prepared using this chamber.

### 3.1.4 The multi-probe setup

The multi-probe setup is an all in-situ fabrication and surface probe microscopy measurement system housed in the hybrid spintronics laboratory of IPCMS. It is dedicated to metal/organic heterostructure fabrication and the in-situ surface characterization studies. This setup was designed and setup by the hybrid spintronics team at IPCMS to integrate high quality surface preparation and thin film growth with a range of surface characterization techniques provided by the the commercial Omicron VT-microscope setup. Major part of the work for the thesis, the work concerning in-situ ferroelectric characterizations was performed in this setup.

The multi-probe setup (figures 3.4, 3.5, 3.6) consists of two assemblies, (i) growth and surface preparation (ii) SPM characterization. Both the assemblies have their dedicated pumping systems (Turbomolecular pump, ionic pump and titanium sublimation pump) and are separated by a manually operated UHV valve. The base pressure in both chambers reach to a level of $2 \times 10^{-10}$ mbar. The entire setup is supported by four air springs that can lift the setup isolating it from mechanical

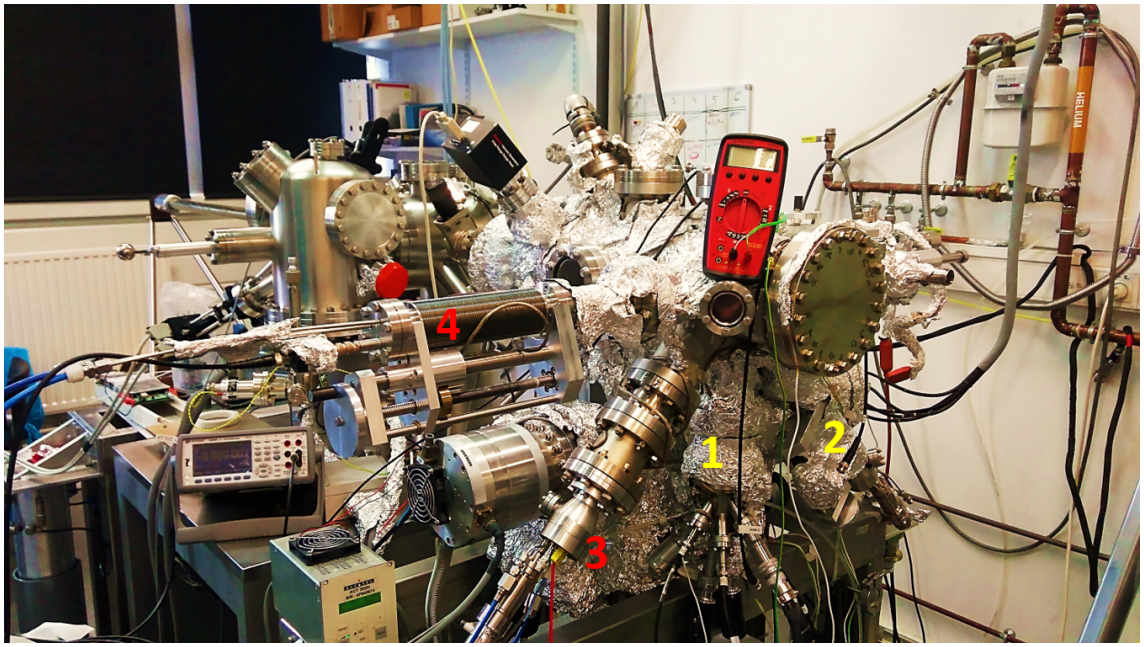


Figure 3.4: Side view of the multi-probe setup. 1- dual MBE cell, 2-Croconic Acid cell, 3- metal thermal evaporation cell, 4- quartz crystal thickness monitor.

vibrations coming from the ground. This helps reduce noise during SPM characterizations. Multiple UHV magnetic transfer arms with Omicron type transfer system help the users transfer the samples between different stations in both the assemblies.

The growth and surface preparation assembly is equipped with one Knudsen cell for Au evaporation, one effusion cell for the sublimation of organic molecules and one dual e-beam based evaporation cell for evaporation of Fe and Co. Additionally, it is equipped with an $Ar^+$ ion gun for ion etching and an e-beam based heater for annealing. These arrangements allow for repeated cycles of substrate etching and annealing which is crucial to prepare a clean substrate surface prior to performing any deposition of ultra-thin films which is important for sensitive SPM characterization experiments like STM measurements. The sample holder also hosts an e-beam based heater enabling high temperature deposition of samples. Further, the residual gas analyzer and the Auger electron spectroscopy setup allow for detailed surface preparations. The surface preparation section of the multiprobe system is entirely an in-house design of the hybrid spintronics group. Similarly, the efficient functioning of the multiprobe system is ensured due to a straightforward UVH transfer system facilitated by magnetic transfer arms that has been integrated into the assembly also by the group.

The SPM characterization assembly hosts a commercial Omicron variable temperature microscopy setup capable of working in a temperature range of 50 K to 650

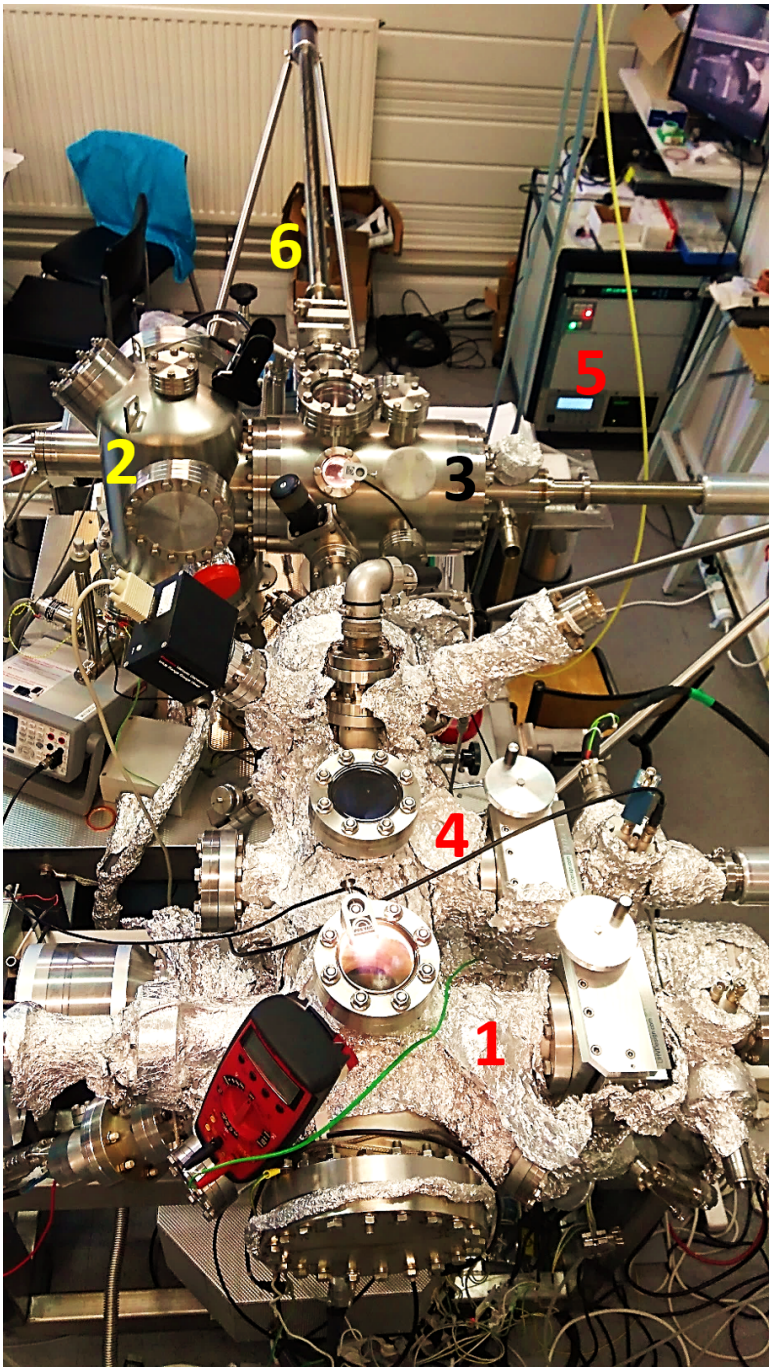


Figure 3.5: Top view of the multi-probe system. 1- thin film growth section, 2- surface characterization section, 3- sample storage region, 4- surface preparation region, 5- system operation control system, 6- magnetic transfer arm

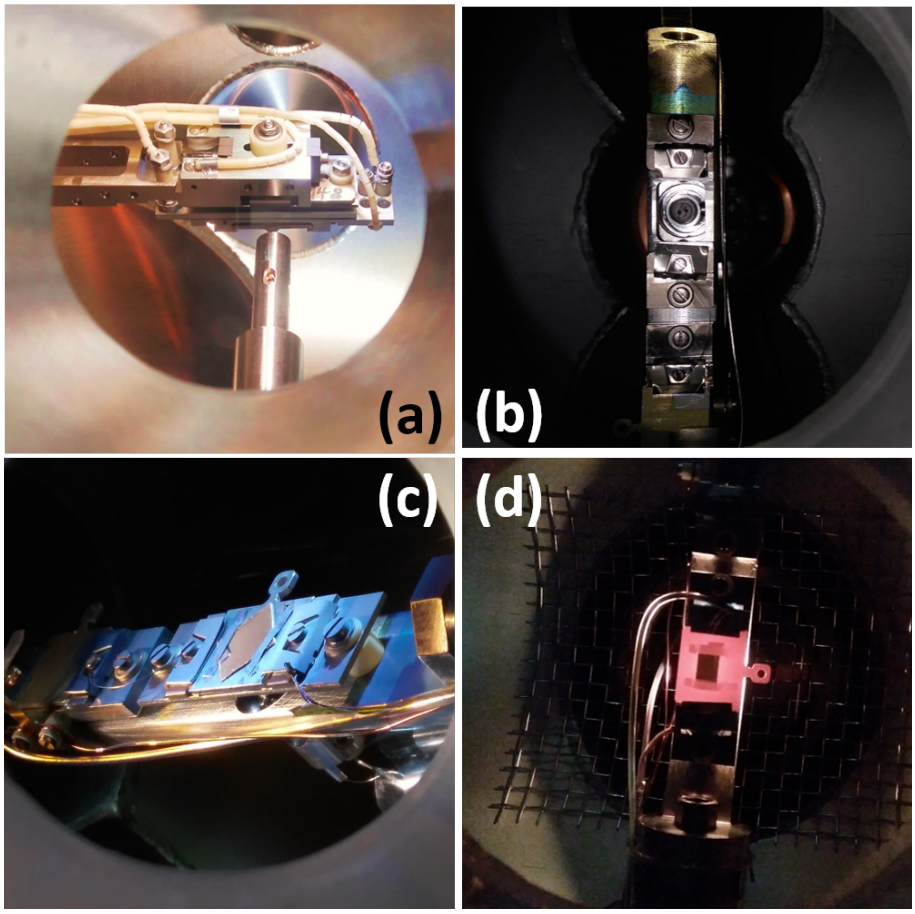


Figure 3.6: Some photographs of the interior of the multi-probe system.(a) shows an ongoing sample transfer process from the magnetic transfer arm to an intermediate transfer arm. (b) shows an UHV e-beam sample heater for surface preparation. (c) shows a mica//Au/CA sample just after deposition of Croconic Acid. (d) shows a Cu single crystal being heated by the e-beam heater. The above facilities have been designed in-house by the hybrid spintronics group to facilitate a wide range of sample and substrate preparation techniques.

K. This setup allows for various types of surface microscopy such as Scanning Tunneling Microcopy (STM), Piezoresponse Force Microscopy (PFM), Magnetic Force Microscopy (MFM), Atomic Force Microscopy (AFM) and Kelvin Probe Force Microscopy (KPFM). To perform the microscopy experiments, the setup is supported by a set of 2 electronic signal generators, two lock-in amplifiers (one dual channel and other single channel), a digital multimeter and a digital oscilloscope.

### 3.1.5 Instrument automation

The electronic apparatus available for the SPM characterization of the multi-probe setup were all manually operated. Under normal experimental conditions, manual

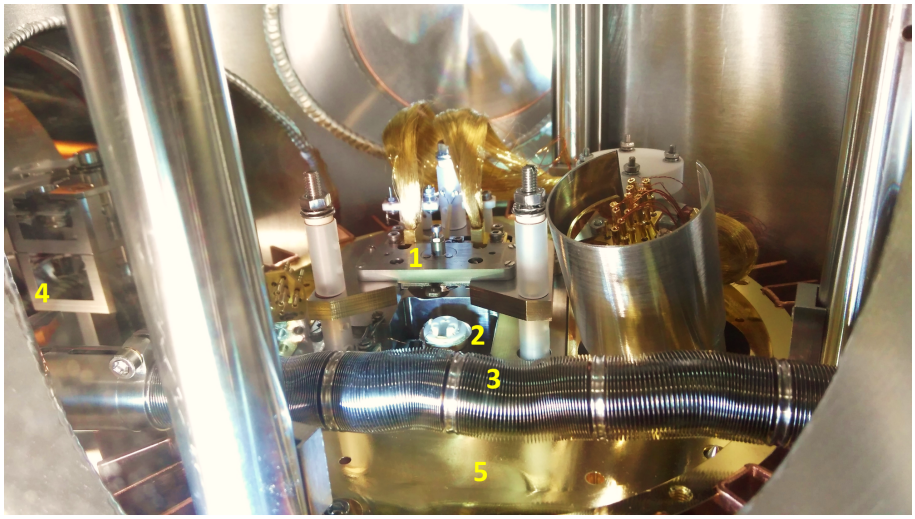


Figure 3.7: Inside view of the surface characterization unit of the multi-probe setup. 1- sample stage, 2- tip holder, 3-UHV wobble stick for sample transfer, 4- sample storage rack, 5- platform for temperature variation

operation worked just fine, however, performing custom experiments requiring custom designed signal waveforms and data acquisition was cumbersome. This resulted in the need to automate the electronic equipment such as the signal generators, oscilloscope and the lock-in amplifiers.

We automated the operation of the above electronic equipment via computer programming with python. First, all the equipment was LAN connected to a LAN Hub which was LAN connected to the operating computer. The operation of the signal generators and the oscilloscope from Agilent Keysight were programmed by VISA and the lock-in amplifier from Anfatec eLockin was programmed using Command Gateway Interface (CGI) commands. Subroutine scripts to program different functions of the equipment were written in python. A main python script was used to call these subroutines according to the required function of the equipment. The programming of the functions allowed us to automate the operation of the electronic equipment for various measurements.

## 3.2 Atomic Force Microscopy (AFM)

Atomic Force Microscopy (AFM) is a scanning probe microscopy technique where the atomic force between a probe tip and the sample surface is utilized to characterize a broad range of properties starting from topography to electrical and magnetic properties. AFM finds application in a wide range of fields including material sci-

ence, chemistry and nanoscience.

### 3.2.1 General working principle of AFM

During the operation of an AFM, a probe tip is brought to the proximity of the sample surface. The probe tip is usually very sharp with a typical lateral size of 15-20 nm and is fixed on a cantilever. When in contact with the sample, Van der Waal forces between the atoms of the tip and the surface become dominant. This results in the deflection of the free cantilever which follows Hooke's law. The deflection of the cantilever is detected optically with the help of a laser light being reflected from the back of the cantilever onto a position sensitive photodetector. Usually, the photodetector is a quadrupole photodiode system. The output of the photodiodes is obtained through a differential amplifier which captures the difference in the light intensity falling on different quadrants of the detector. This enables the extraction of the vertical and horizontal component of the cantilever deflection from the main optical signal. The difference between the top and bottom photodiode signals represents the vertical motion of the cantilever whereas the difference between the left and right photodiode signals represents the horizontal motion.

To obtain a topography image of a surface, the tip is scanned over the surface continuously over a particular region in a raster format along X and Y direction with the cantilever deflection signal constantly monitored at each point of the scanned region. A height feedback loop is employed with the help of a piezoelectric scanner to maintain a particular parameter, e.g. the amplitude of tip deflection or the relative position of the tip with respect to the sample surface, depending on the mode of operation.

### 3.2.2 AFM Operating modes

#### 3.2.2.1 Contact mode

In contact mode operation, scanning of the sample surface is performed with the tip in contact with it while the cantilever deflection is monitored by the photodetector. As the cantilever deflection depends on the force between the tip and the sample surface, depending on the surface features, the cantilever deflection changes while the tip scans over the surface. The feedback circuit ensures the stability of the value of this deflection (setpoint deflection) by moving the tip-cantilever assembly with the help of the piezoelectric scanner. The force between the tip and sample

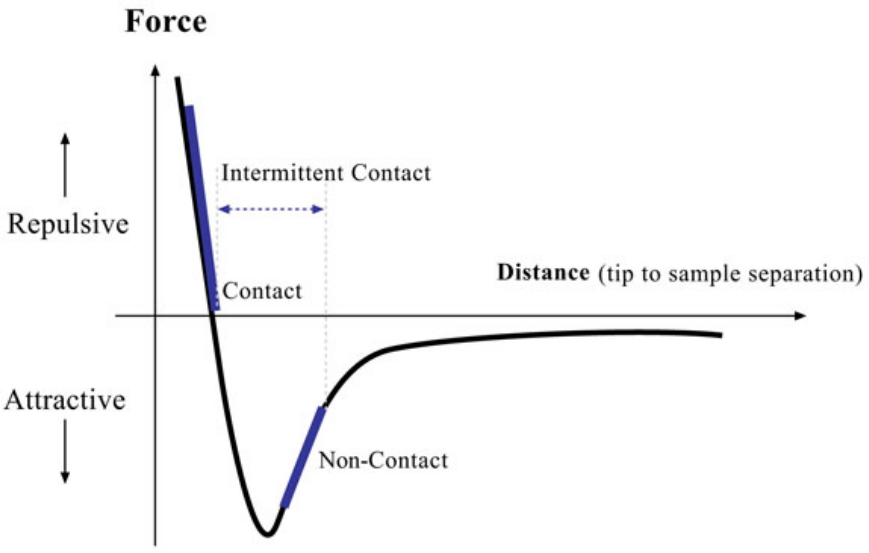


Figure 3.8: Force versus tip-sample separation. Figure is taken from reference [109].

surface remains constant as the cantilever deflection is maintained to be constant. This scanner movement contains the topographic information of the surface which is potted to create the surface topography image.

#### 3.2.2.2 Non-contact mode

In the non-contact mode, the tip is kept a certain distance away from the sample surface. To obtain an AC signal from the cantilever, it is oscillated at a frequency slightly above or below the cantilever resonance frequency. Depending on the force between the tip and the sample surface, the frequency of oscillation is changed when the tip is scanned over the sample surface which makes the amplitude of oscillation to change as well. The feedback circuit ensures a constant amplitude of oscillation by vertically moving the piezoscanner. This distance of movement is recorded for every point on the scanned surface which gives the topographic information of the surface. The non-contact mode is employed when there is a risk of damage to the tip due to the scanning of sample. This method is really useful for imaging of semi solid materials, polymers and other biological materials.

When this method is used to perform microscopy in air, the adsorbed moisture stand in the way of imaging an accurate surface. To overcome this problem, a modified version of non-contact mode is emplyed where the cantilever is oscillated at a much higher amplitude and is allowed to contact the sample surface momentarily within every cycle of cantilever oscillation. As the cantilever pierces through the soft

moisture layer, it is able to map the topography of the surface more accurately without modifying the sample surface due to the tapping behaviour. Due to this tapping behaviour of the cantilever, this mode is called the tapping mode. (TradeMark of Bruker)

## 3.3 Piezoresponse Force Microscopy (PFM)

Piezoresponse Force Microscopy (PFM) is a scanning probe microscopy technique based on AFM that utilizes the inverse piezoelectric effect of ferroelectric and piezoelectric materials to locally probe these electric properties with a conductive tip. Especially for ferroelectric materials, the non-destructive way of PFM to electrically write ferroelectric domains and to characterize local nanoscale ferroelectric properties such as polarization reversal, nucleation bias, piezoelectric co-efficients, domain wall properties makes it a very useful and necessary tool for nanoscale characterization of ferroelectric materials.

### 3.3.1 PFM working principle

The working principle of PFM is based on the electromechanical response of a conducting probe in contact with electromechanically active materials such as ferroelectric or piezoelectric material. When an electrical excitation stimulus is applied to a ferroelectric or piezoelectric sample through a conductive tip in contact with the sample surface, local deformation of the sample takes place due to inverse piezoelectric effect. The magnitude and nature of this deformation is dependent on the local piezoelectric or ferroelectric properties of the sample. The deformation gets electromechanically translated to the cantilever of the probe causing the deflection of the tip. This tip deflection is sensitively detected with the help of a photodetector and analyzed to extract characteristic information on the material properties. As all the ferroelectric materials are piezoelectric by nature, such a technique is applicable to all ferroelectric materials.

The deformation or strain developed in the sample due to application of tip bias is related to the electric field via a tensor of rank 3, called the piezoelectric strain tensor, by the matrix equation, $S_j = d_{ij}E_i$, where $d_{ij}$ is the piezoelectric matrix form of the strain tensor or piezoelectric coefficient tensor with the SI units of m/V. The index i varies from 1 to 3 and j from 1 to 6. Indices 1, 2 and 3 correspond to the orthogonal x, y and z co-ordinates respectively and indices 4, 5 and 6 correspond to

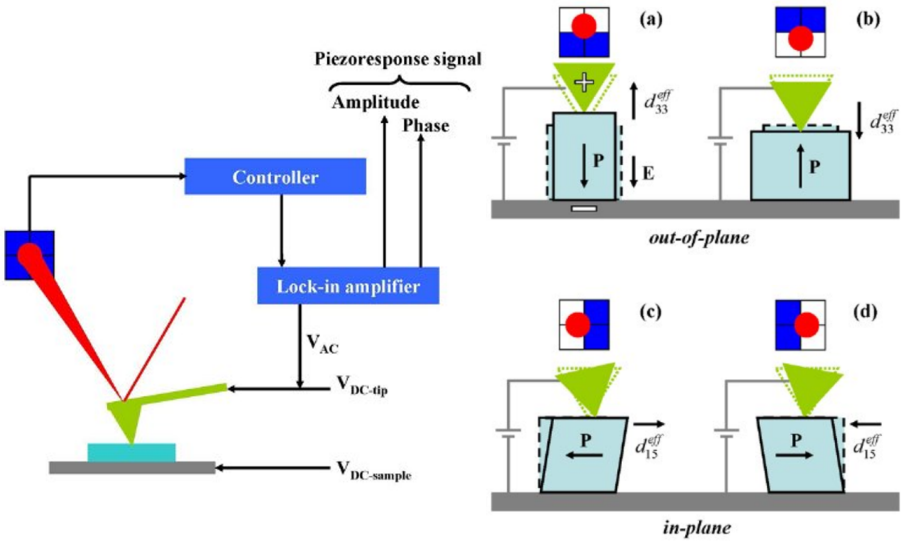


Figure 3.9: Working principle of Piezoresponse Force Microscopy. (a)-(d) show the possible sample deformation scenarios under the application of a vertical electric field and its effect on the tip in contact. Figures are taken from reference [110].

the shear component of the strain tensor. In the strain tensor, the coefficient $d_{33}$ is one of the most important coefficients as it couples directly with the vertical motion of the deformation. For example, if a voltage V is applied with the probe onto a sample of thickness t, assuming a uniform vertical electric field distribution, $S_3 = \Delta z/t$ and $E_3 = V/t$, where $\Delta z$ is the relative grain deformation. The deformation is positive or negative i.e. the sample expands or contracts if the applied electric field is respectively parallel or anti parallel to the direction of polarization. The illustration of this inverse piezoelectric effect is presented in figure 3.9.

As the magnitude of the deformation is proportional to the value of the $d_{33}$ coefficient, which is typically very small, the deformation is also usually very small. For instance, the $d_{33}$ coefficient of a micron thick PZT film is $\sim 3 \times 10^{-10}$ m/V. So a voltage of magnitude 1 V will result in a vertical deformation of just $\sim$0.3 nm which is really close to the limit of sensitivity of probe based measurement techniques. Further, the topographic height variations in a sample is usually in the same order of magnitude, thereby, bringing difficulties to the detection of the piezoelectric deformation. Moreover, due to very high sensitivity of the cantilever to acoustic noise, the detection process would get even more erroneous due to the surrounding noise. This challenge is tackled by employing lock-in amplifier (LiA) based detection techniques. Due to very low bandwidth noise filtering of lock-in amplifiers, sensitive detection of small sample deformation can be successfully

performed.

In the LiA based technique, the sample is subjected to an oscillating electric field at a frequency away from the cantilever resonance frequency. This electric signal is called the modulation/excitation signal. This makes the sample vibrate at the same frequency as that of the modulation signal and with a phase dependent on the polarization direction of the sample relative to the direction of the applied field. If the relative orientations are parallel, the vibration is in phase (phase=$0^0$) and for an antiparallel orientation it is out of phase (phase=$180^0$). The tip deflection signal is fed to the input of the LiA operating at a reference frequency equal to that of the modulating signal. The LiA then extracts the piezoresponse information from the tip deflection signal from where the magnitude and relative direction of sample deformation can be obtained.

If a sinusoidal modulation signal of angular frequency $\omega$ and amplitude V, $V_{ac}$ = Vcos($\omega$t) is applied to the tip then the vertical electromechanical vibration of the tip can be expressed as $\Delta z = d_{33}$ Vcos($\omega t + \phi$). The piezoresponse signal extracted from the LiA is a phasor sum of an amplitude (PRamplitude) and a phase (PRphase) and is represented as, PR= $d_{33}$ Vcos($\phi$), where PRphase = $\phi$ and PRamplitude= $d_{33}$ V. PRphase and PRamplitude are related to the direction and magnitude of the out of plane component of the polarization vector of the sample respectively. As PRamplitude is directly proportional to the applied voltage amplitude, increasing the amplitude of the modulation signal results in higher values of PRamplitude and brings contrast improvement to the domain imaging. Such a contrast improvement in PRamplitude images is shown in figure 3.10. Similarly, by using a quadrupole photodiode, the lateral component of the tip deflection signal can be obtained to be analyzed with the LiA to get the piezoresponse related to the in-plane component of the polarization vector.

### 3.3.2 PFM Imaging modes

Imaging of ferroelectric domains in PFM is carried out by scanning a particular region of the surface of a sample in contact mode with the modulation signal being applied to the tip and the bottom electrode connected to the ground. The PRphase and PRamplitude LiA outputs are captured during the scanning which are used to create the phase and amplitude maps of the scanned region. Detailed descriptions of domain imaging methods can be found in references [111, 112, 113].

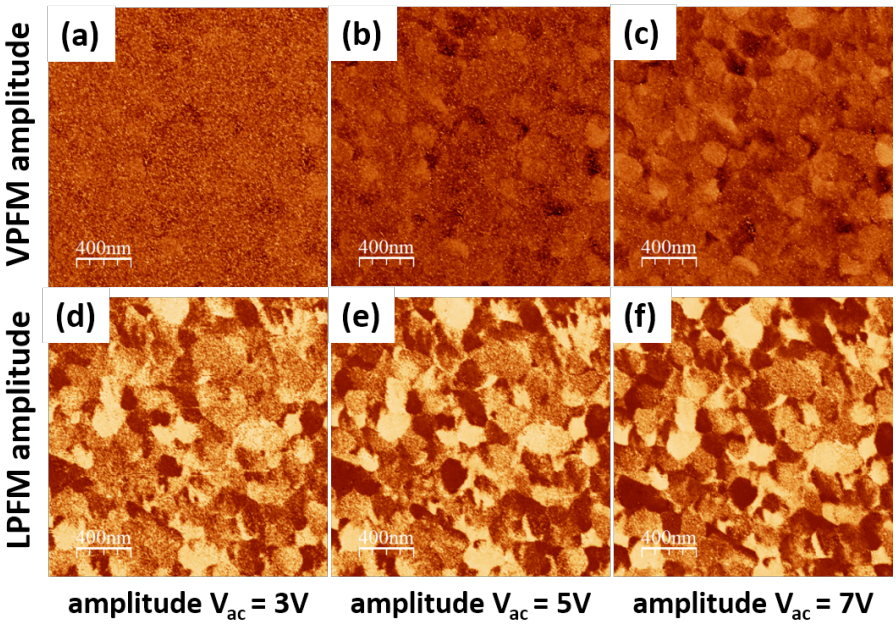


Figure 3.10: Contrast improvement in the PRamplitude signal with increase in the amplitude of PFM modulation signal for Croconic Acid films.

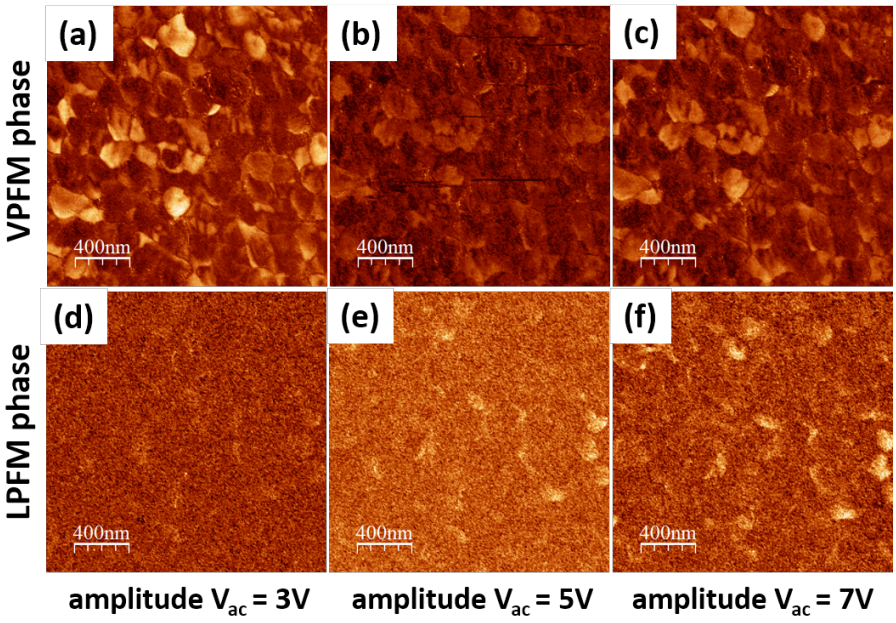


Figure 3.11: Poor contrast improvement in PRphase signal with increase in amplitude of PFM modulation signal for Croconic Acid films.

#### 3.3.2.1 Vertical PFM imaging

Vertical PFM imaging is carried out by analyzing the vertical component of the tip deflection which is mostly caused due to the out of plane deformation of the sample. Thus, this imaging mode reveals the direction and magnitude of the out of plane component of the polarization vector of the sample. For a sample with available regions of out of plane polarization, PRphase maps result in zones of dark and bright contrast signifying upward and downward direction of the polarization vector, whereas, PRamplitude map results in a continuously varying contrast of the scanned region as the amplitude of piezoresponse can take any value depending on the magnitude of the out of plane component of the polarization vector. In-plane ferroelectric domains in this imaging mode will have contrast intermediate between dark and bright.

#### 3.3.2.2 Lateral PFM imaging

Lateral PFM imaging is carried out by analyzing the lateral component of tip deflection. Due to non-zero off diagonal elements in the strain tensor or due to canted direction of crystallographic axes and polarization vectors with respect to the film plane, lateral displacement of the tip via torsion and buckling of the probe tip is possible. A separate channel in the LiA can be simultaneously used to capture the lateral piezoresponse signal. The lateral signal obtained basically corresponds to the component of polarization along one of the two orthogonal lateral directions. The component along other orthogonal direction is obtained by imaging the same region of the sample after a $90^0$ rotation about the axis perpendicular to the film plane.

#### 3.3.2.3 Vector PFM imaging

Combining the vertical piezoresponse signal with that of the lateral signal along both orthogonal lateral directions, the 3-dimensional orientation of the polarization vector can be mapped. The result of this vector PFM imaging is usually represented as a circular colour plot with concentric bands of coloured circles contain the information of the PRphase and PRamplitude along all three orthogonal directions.

### 3.3.3 PFM Spectroscopy modes

PFM spectroscopy is the technique to obtain the behaviour of ferroelectric properties of a material with respect to a varying external paramter such as the external DC

electric field. Usually local hysteresis loops from ferroelectric materials which can be a hysteresis of PFM phase, PFM amplitude, current etc are measured. From the hysteresis loops, several characteristic properties of the material such as nucleation field, domain dynamics, remanent and saturation polarization etc. can be obtained.

PFM spectroscopy is performed by applying a sweep of DC bias (from positive to negative and the reverse or vice versa) along with an AC modulation signal to the tip in contact with the sample fixed at a particular position. The DC bias polarizes the sample along the direction of the applied electric field and the AC excitation signal is applied to employ the LiA technique working at the frequency of the AC signal to detect the piezoresponse signal at each point of applied DC bias. The PRphase or the complete piezoresponse signal obtained from the LiA is plotted against the applied DC bias which constitutes the hysteresis loop. The PRamplitude signal, when plotted against the applied voltage results in a butterfly type loop shape. Another parameter that is plotted with respect to the applied voltage during a spectroscopy is the cantilever deflection. This gives a direct visualization of the sudden deformation that takes place at the polarization reversal via inverse piezoelectric effect. It must be noted that the presence of the alternating signal is optional. In cases where sensitive parameters such as the piezoelectric oscillations are measured to capture the piezoresponse, the use of alternating probing signal in combination with a LiA helps in improving the signal to noise ration for the detection. A discussion on various other types of imaging modes can be found in the reference [114].

#### 3.3.3.1 Continuous ON-field spectroscopy

When the spectroscopies are carried out in the presence of applied DC electric field, it is called as continuous DC ON-field spectroscopy. In such measurements, the bias voltage is increased in steps of certain voltage bias and the piezoresponse is captured after certain time span of voltage stabilization. During such a spectroscopy, as the piezoresponse signal is acquired during the presence of the DC electric field, the observed signal does not represent the true remanent state. The schematics of the voltage profile of such a mode is shown in figure 3.12 (b).

#### 3.3.3.2 Remanent state OFF-field spectroscopy

Remanent state OFF-field spectroscopy or pulsed DC spectroscopy is carried out by applying a pulse amplitude modulated signal to the tip. Unlike a continuous DC ramp signal as in the case of ON-field spectroscopy, bias is applied in the form of

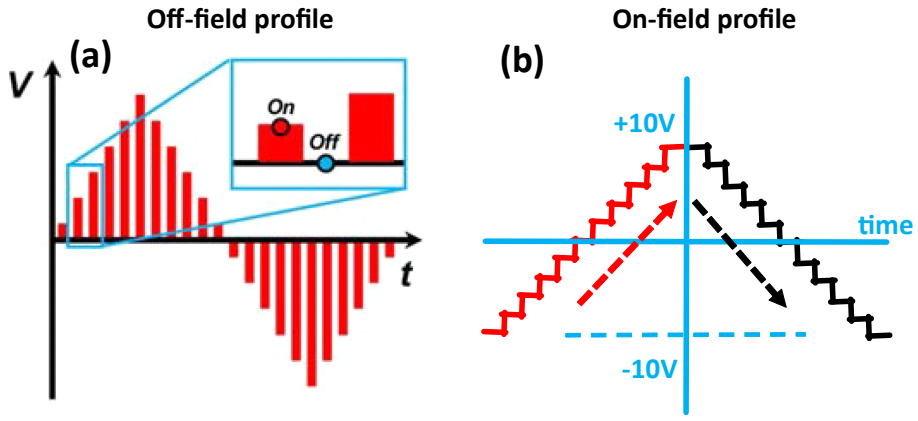


Figure 3.12: Applied voltage profiles for on-field and off-field spectroscopy modes. The off-field profile (a) can be used to acquire signals corresponding to the field-on portions in the profile, however, an entirely on-field spectroscopy is performed with the voltage profile as shown in (b). Figure (a) is taken from the reference [17].

pulses of certain pulsewidth and increasing pulse height. The voltage returns to zero for a certain duration of time after every pulse during which the piezoresponse measurements are carried out with the help of the alternating probing signal which can be applied in superposition with the pulsed signal. The pulse amplitude modulated voltage profile used in this spectroscopic mode is shown in figure 3.12 (a). It must be noted that the same profile can be used to carry out the ON-field measurements if the piezoresponse signal is captured during the ON state (red zones in figure 3.12 (a)) of the applied pulsed DC voltage profile, in which case the spectroscopy mode can be called as pulsed DC ON-field spectroscopy.

As the piezoresponse can be measured in the absence of electric field, in this spectroscopy mode, the effect of tip-sample electrostatic interaction on the spectroscopic results is minimized and the result corresponds to remanent piezoresponse state of the sample revealing retention characteristics of the ferroelectric sample.

In addition to utilizing some of the above spectroscopy methods, we employed a novel spectroscopy method during the work of the thesis which is called as the ferroelectric switching current spectroscopy. This method is based on the simultaneous detection of nanoscopic ferroelectric switching currents and the nanoscopic piezoelectric strain response from a ferroelectric material with standard conducting AFM probes. Ferroelectric switching current is the compensation current that is generated whenever the metal electrodes in contact with the ferroelectric surfaces supply the screening charges in order to screen the electric field from the surface polarization charges upon the reversal of the nanoscopic polarization.

A significant portion of the work in the thesis deals with nanoscopic ferroelectric characterization of organic Croconic Acid films utilizing the above spectroscopy method. A detailed description on this method including the origin of ferroelectric switching current and piezoelectric strain response is presented in chapter 5 along with the results obtained from the method. In chapter 5, we demonstrate how we performed ferroelectric switching current spectroscopy on the organic ferroelectric in an in-situ UHV environment after the growth of the ferroelectric film under UHV conditions. Such ultra clean environment allowed us to perfom very sensitive current detection, thereby, facilitating the above spectroscopy measurements. The application of the switching current spectroscopy can be generalized to any ferroelectric material and it can provide detailed nanoscopic information on the ferroelectric properties of the material.

## 3.4 Polarized Light Microscopy

A polarized microscope is an optical microscope which uses polarized light to image samples possessing optically anisotropic characteristics, for example, anisotropy in refractive index, where anisotropy represents the non-uniform spatial distribution of properties. Such an anisotropy originates due to the anisotropic crystalline orientations within the crystals. Where in optically isotropic solids, the refractive index is isotropic everywhere within the solid, for anisotropic materials, it is dependent on the direction of propagation of light. Thus, for isotropic materials, the interaction with light is independent of the orientation of the sample but it is not so for anisotropic ones.

When light enters an optically anisotropic material, irrespective of the polarization of the incident light, two polarized light rays (wavefronts) are created whose polarizations are mutually orthogonal to each other, travelling in different directions. The directions of polarizations of these two rays are parallel and the normal to the optic axis of the crystal respectively. One of the two rays is called as the ordinary ray and other as extraordinary ray. The refractive indices, thus the optical paths, of the material seen by these two rays are different. After passing through the material, the two rays may interfere with a phase difference to create birefringence pattern.

However, if the incident light is polarized and the direction of polarization is parallel or orthogonal to the that of the optic axis, no birefringence takes place and no changes happen to the polarization direction of the light emerging from the material. Now, if the sample is rotated along the direction of incident light, the

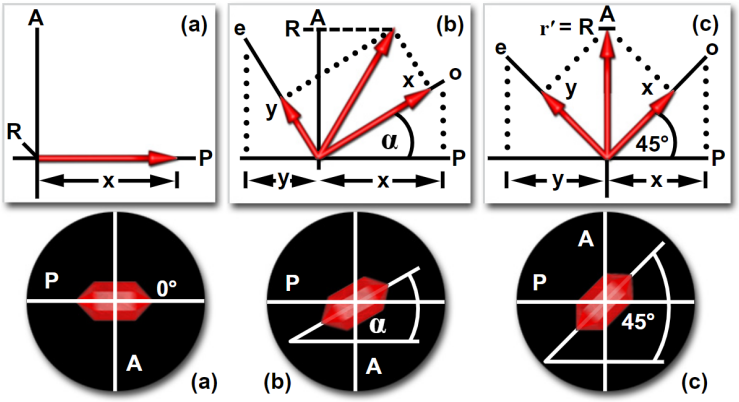


Figure 3.13: Schematics of the birefringence phenomena in a polarized light microscope setup. e and o represent the extra-ordinary and the ordinary directions respectively. P and A represent the polarizer and analyzer axes respectively. x and y denote the components along the ordinary and the extra-ordinary directions respectively. $\alpha$ denotes the angle of rotation of the sample (shown as the red hexagon) with respect to the polarizer axis. R denotes the component of the resultant of the ordinary and extra-ordinary rays along the analyzer axis A. Figure is taken from reference [115].

polarization of the incident light is at an angle to the optic axis and birefringence can take place.

A polarized light microscope (polarimetry setup) utilizes the above concept to capture the optical anisotropy information of a material by using a combination of analyzer-polarizer and the rotation of sample about the axis of light propagation. Normally, the analyzer and polarizer are crossed at $90^0$ with respect to each other. When light passes through the polarizer, without the presence of any optically anisotropic sample, the analyzer blocks the entire light. However, when an optically anisotropic sample is present between the polarizer and analyzer, birefringence may take place modifying the polarization direction of the light passing through the sample and the crossed analyzer may allow some intensity of light to pass through to the camera.

When the sample is oriented in such a way that the optic axis is parallel or orthogonal to the polarizer axis, as no change in polarization of the propagating light takes place, the analyzer blocks the entire light resulting in a dark image of the sample. When the sample is oriented with the optic axis at an angle between $0^0$ to $90^0$ with respect to the polarizer axis, the ordinary and extraordinary rays from the sample recombine via the analyzer and finite intensity is captured in the camera which is maximum for an angle of $45^0$ (figure 3.13). Thus, the maxima and minima

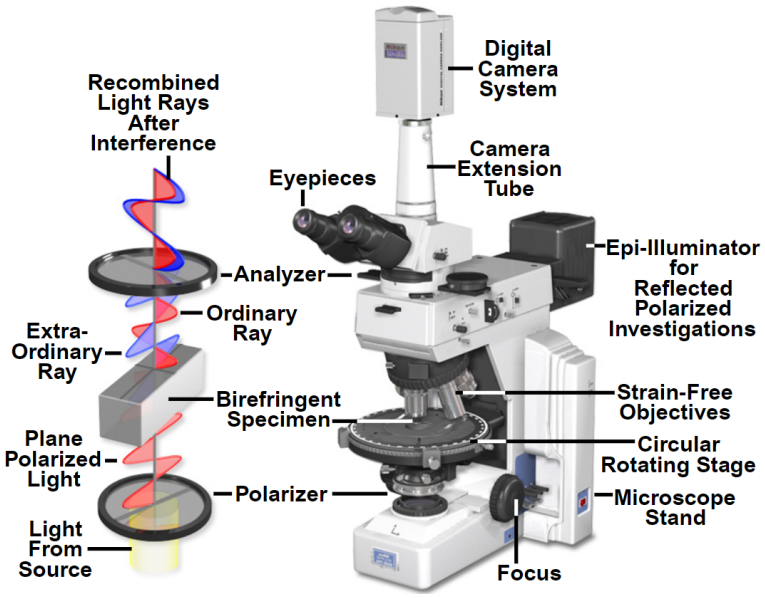


Figure 3.14: Schematics of a commercial transmission type polarized light microscope and the polarization directions of the propagating light. Figure is taken from reference [115].

in the intensity appears at an interval of $45^0$ when the sample is gradually rotated within the crossed analyzer-polarizer arrangement and a complete 360° rotation would result in a total of 2 maxima-minima pairs in the intensity versus rotation angle plot. The above variation in captured intensity signifies the presence of optical anisotropy in the material under study.

Figure 3.14 shows the schematics of polarized light microscopy along with the image of a commercial microscope. The above design of the microscope is based on the transmission of the polarized light through the sample. There are other available designs where the reflected light from the sample is passed through the analyzer before being captured. For the work presented in the thesis, the reflection based polarized light microscope is used.

# Chapter 4

# Ferroelectric properties of Croconic Acid films on metallic substrates

The design of any electronic device involves the crucial step of fabricating the electrodes. The choice of the electrode material depends on the type of applications for which the device is being fabricated. Usually, metal thin films are used as electrodes in most of the electronic devices. Highly conducting metals like gold, silver, copper are common examples of electrode materials. In specialized fields like spintronics, other type of electrodes like ferromagnetic metal electrodes find substantial application.

In a vertically structured nanoelectronic device, the metal electrodes are fabricated in direct proximity to the device. Due to the close proximity of electrode metal films to the device core, the choice of electrode material and the method of its integration with the core system play a very crucial role in defining the overall device characteristics. For example, the electrode resistance, the quality and electronic properties at the electrode-core junction and the properties of electrode materials contribute majorly to the device properties. Therefore, a thorough study on the scrutiny of the choice of right electrode materials in terms of with their fabrication procedure and the study of the real device characteristics in presence of the electrodes are necessary prior to any large scale device fabrication.

In this chapter, we explore the growth and ferroelectric properties of Croconic Acid under ambient conditions on metallic films such as on films of gold and cobalt which are commonly used as electrode materials in the field of nanoelectronics and spintronics. A comparative analysis of the properties on both metal surfaces qualitatively reveals the degree of suitability of both metals as electrodes while harbouring the native properties of CA.

## 4.1 Pertinence of the study

When a thin film of any material is deposited on a substrate surface, there are various properties of the substrate such as crystallinity, roughness, crystalline defects present on the surface and surface reactivity that significantly affect the growth and the properties of the deposited material. Out of these substrate properties, most are tunable, meaning, for example, that the required type of crystallinity, degree of surface roughness etc. can be achieved by appropriate tuning of fabrication and post-fabrication parameters. However, properties like surface reactivity of a substrate surface is intrinsic to the substrate material and cannot be modified without employing drastic measures such as oxygen plasma treatment, surface metallization with metals of different reactivity and so on which often require sophisticated

technical arrangements and a lot of optimization.

Surface reactivity or surface chemical reactivity of a substrate material can be defined as the tendency to chemically interact and form chemical bonds with the depositing materials. Especially, when organic molecules are deposited on metallic substrates, the surface reactivity of the substrate plays an important role in determining the growth and properties of the molecular system. Metals like Au provide relatively inert surfaces on which the molecule-substrate interaction is often governed by Van der Waal forces which are crucial to bring the right molecule-metal distance for a stable growth of molecular layers.[3, 4, 5] This kind of molecular interaction is called as physisorption where the electronic and geometric properties of the depositing molecules are not affected by the inert substrate surface. On the contrary, more reactive surfaces such as that of ferromagnetic materials tend to form strong chemical bonds with the organic molecules. This type of interaction is called chemisorption. Energetically, the strength of the substrate-molecule interaction is determined by the difference between the energy of separate molecules and metals combined and the energy of the substrate-molecule hybrid system. An energy difference beyond 1 eV is generally considered to be the range for chemisorption. However, depending on the surface reactivity and the type of molecules, the range of interface energetics can be quite larger than 1 eV, higher energies corresponding to strong chemisorption happening at the first molecular layer near the interface and lower energies corresponding to weak chemisorption or physisorption for the second molecular layer and onwards. Due to the wide range of the energy scale, intriguing physical properties can emerge at the metal substrate-molecule interface which makes this type of interface different from the all inorganic interfaces.

The chemical environment evolving at the substrate-molecule interface tends to bring modifications to the electronic and geometric properties of the molecule as well as the substrate at the interface, in particular in the case of chemisorption. In the worst case, it is possible that the reactive nature of the substrate can impede the intrinsic properties for which molecules were chosen. For example, it was impossible to switch the spin state of spin crossover molecules directly deposited on metallic Cu (100).[116] This was mainly due to the strong coupling between the molecule and the Cu atoms of the substrate. The switching properties were nevertheless restored upon passivation of the reactive surface by nitrogenation of the metallic copper. The presence of an ultra thin CuN layer reduces the coupling between the molecule and Cu substrate allowing switching of the spin state. However, it brings slight modifications to the topographical features of the deposited molecules. As shown

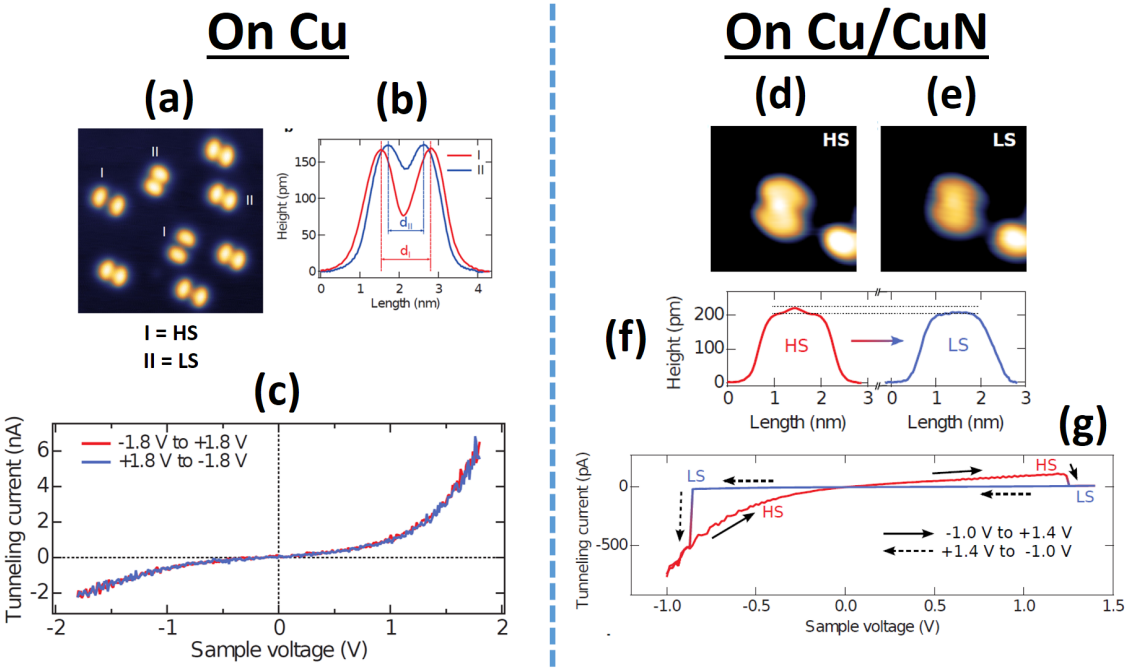


Figure 4.1: Spin state switching studies on a spin crossover molecule on Cu (left column) and CuN surface (right column). (a) and (b) show the molecular structure and surface profile at the indicated positions on the surface for the spin crossover grown on Cu surface. (d), (e) and (f) show the same for the growth on CuN surface. (c) and (g) show the variation of tunneling current through the molecules obtained atop the center of the molecules with respect to the applied bias to the tip for growth on Cu and CuN surface respectively. Figure is taken from reference [116].

in figure 4.1, the topographic features of the high spin and low spin configurations of the molecule on Cu surface, as imaged by STM, are quite different. This is clear from the line profiles across the images of molecules in both spin states (figure 4.1 (a) and (b)). On Cu/CuN surface, the difference in topography between both spin states is reduced but still visible (figure 4.1(d), (e) and (f)). Figure 4.1(c) and (g) show the tunneling current atop the center of the molecules on Cu and Cu/CuN surfaces respectively. As the two spin states of the molecules have different values of conductance, switching of a spin state would be accompanied by a change in the tunnel current. The hysteretic behavior of tunnel current signifies a repeated switching behavior (HS to LS on positive bias side and LS to HS on negative bias side) of the molecule's spin state on Cu/CuN surface upon application of electric field (Figure 4.1(g)), whereas, no such feature is observed in the tunnel current measurements on molecules on Cu surface.

Another example of surface reactivity modulation of substrate surface finds applications in spintronics, where one usually has to use more reactive metallic substrates

like cobalt. In such cases, properties of molecules could be preserved by the intercalation of a thin comparatively less reactive metal spacer like Cu, moderating the metal-molecule interactions without losing the high interface polarization necessary for effects such as magnetoresistance.[117]

Similarly, the stabilization of hydrogen bonded crystalline two dimensional molecular networks of Rhodizonic Acid, another hydrogen bonded molecular member of the CA family, which is believed to be necessary for the appearance ferroelectric ordering, is possible on Au even at elevated temperatures. On the contrary, on a comparatively more reactive Cu surface, it is observed that deprotonation of the molecule and reaction with Cu atoms can happen upon substrate annealing that leads to a different structural arrangement which may in turn influence the expected ferroelectric properties of the molecular layer.[118]

In the field of nanoelectronics and spintronics, the interface between the metal electrode and the device plays a vital role in generating the device's electronic response. Especially, with reduction in size, electronic devices become more and more sensitive to the physical properties that emerge at the interface. Considering the intriguing effects that can occur at the interface of the metal electrode in an organic electronic or spintronic device, it is essential to study the effect of the electrode on the interfacial molecular properties. Further, although the above examples of substrate induced effect on the properties of molecular layer are confined to of a few monolayers apart from the interface, these substrate dependent variations of interface properties may also have substantial impact on the bulk properties of the organic material in thicker films that are commonly employed in commercial electronic devices. Therefore, it is of utmost importance to also study the substrate induced effect on the properties of organic films in the bulk limit.

In view of the above discussion, prior to the realization of electronic or spintronic applications of CA thin films, it becomes necessary to study the ferroelectric properties of CA on relevant metallic substrate surfaces under ambient conditions, especially on substrates with high surface reactivity. With this in mind, we have investigated the stability of the properties of bulk CA films grown on two commonly used spintronic electrodes with similar crystalline nature but with different surface reactivity at room temperature and under atmospheric pressure. We have utilized Au substrates as the electrode material as the less reactive substrate and Co substrates as the one with high surface reactivity.

## 4.2 Fabrication and measurement details

### 4.2.1 Fabrication of Au substrates

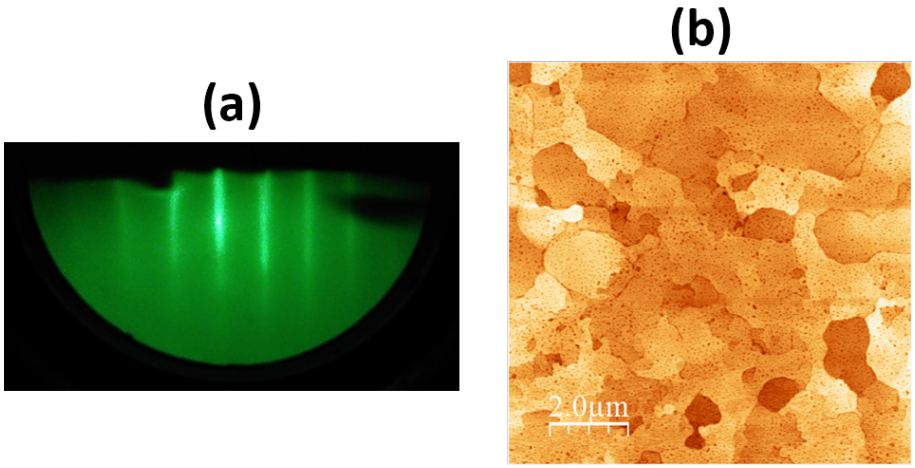


Figure 4.2: Characterization of mica//Au substrate surface. (a) shows the in-situ RHEED patterns obtained after the growth. (b) shows the surface topography as obtained from AFM imaging. Sections of different contrast in (b) represent atomically flat isolated planes of Au surface.

The study of ferroelectric properties of CA on metallic surfaces were conducted using the base substrates of mica//Au which were prepared in the MBE chamber dedicated to metal evaporation. Freshly cleaved mica cut into 10 × 10 $mm^2$ sized substrates were introduced to the chamber at a base pressure of ∼2 × $10^{-10}$ mbar. 150 nm gold was evaporated onto these mica substrates, kept at a temperature of ∼600 °C, using at a rate of ∼1 nm/min under a chamber pressure of maximum 5 × $10^{-9}$ mbar. The surface of Au fabricated in such a way provides large atomically flat terraces which are suitable for generic growth studies. The Reflection High Energy Electron Diffraction (RHEED) images taken during different stages of growth show distinct sharp lines as shown in figure 4.2 (a) which is indicative of high quality growth. Surface topography as obtained by Atomic Force Microscopy (AFM) shows the micrometer sized terraces as shown in figure 4.2 (b). Finally, X-Ray Diffraction (XRD) studies on the gold surface reveal an fcc structure as shown in figure 4.4. These mica//Au samples were ex-situ transferred to the UHV cluster assembly for the deposition of CA samples.

### 4.2.2 Fabrication of Croconic Acid films

CA films of various thicknesses at different flux rates were grown in the OMBE chamber of the UHV cluster assembly from a water cooled Knudsen cell. The substrates were rotated to ensure a uniform flux on the sample and were kept at room temperature during all the sample depositions. Further, the mica//Au substrates were degassed using a resistive heater fixed inside the chamber to remove any moisture before the deposition of CA. The operating temperatures of the Knudsen cell were fixed at 130 °C with the help of a quartz thickness monitor fixed inside the chamber. The quartz thickness monitor was calibrated by employing a Transmission Electron Microscope grid as a shadow mask during the deposition of the molecules and measuring precisely the thickness at the edges or corners of the patterns thus created with the help of an Atomic Force Microscope. This step is crucial as the thickness monitor is highly sensitive to the variation of the room temperature. Figure 4.3 shows one such pattern and the measured thickness profile obtained from AFM.

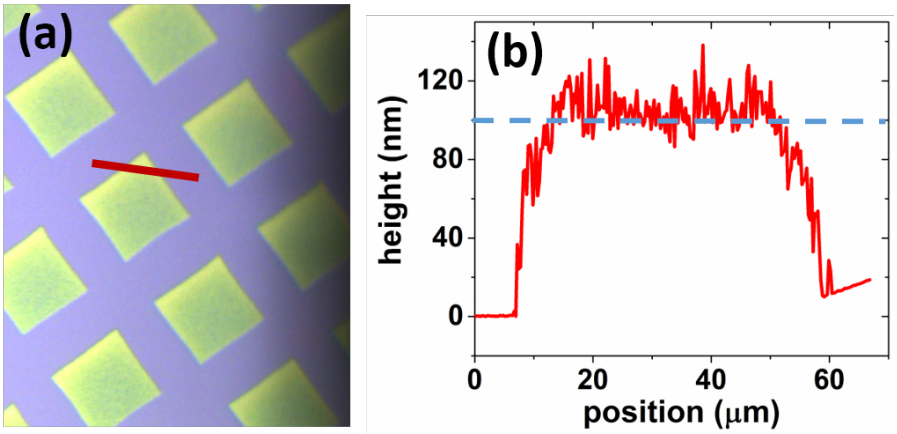


Figure 4.3: Thickness calibration of CA film using AFM imaging. (a) shows the microscope image of CA film of thickness 100 nm patterned using a TEM grid (mesh 300) as a shadow mask during deposition. Green zone corresponds to the deposited molecule and the blue region correspond to the $SiO_2$ substrate underneath. (b) shows the surface height profile of (a) along the solid red line. The height of the plateau in the height profile is close to 100 nm which is approximately the thickness of the sample.

For the growth and ferroelectric property studies of CA films, two types of samples were fabricated. (i) mica//Au/CA and (ii) mica//Au/Co(15 nm)/CA. For the second type of samples, the intermediate Co films were grown by thermal evaporation at room temperature from a water cooled effusion cell in the Evap chamber of

the UHV cluster assembly which was at a base pressure of $\sim 4 \times 10^{-10}$ mbar and a maximum deposition pressure of $4 \times 10^{-9}$ mbar. The XRD studies on these Co surfaces reveal an fcc structure as shown in figure 4.4.

### 4.2.3 X-Ray Diffraction studies on Croconic Acid films

We performed X-Ray Diffraction (XRD) measurements on the films of 100 nm thick CA and compared it with the that on the bare mica substrate. It was observed that the base mica substrate has a lot of peaks populating the whole spectrum of measurement, thereby making it difficult to observe subtler peaks of CA. Figure 4.5 shows the XRD results of a mica//Au/Co/CA sample in a range of incidence angles where the peak of CA is expected to appear. It can be seen that the peaks with huge intensity coming from mica overwhelm the possible peaks of CA.

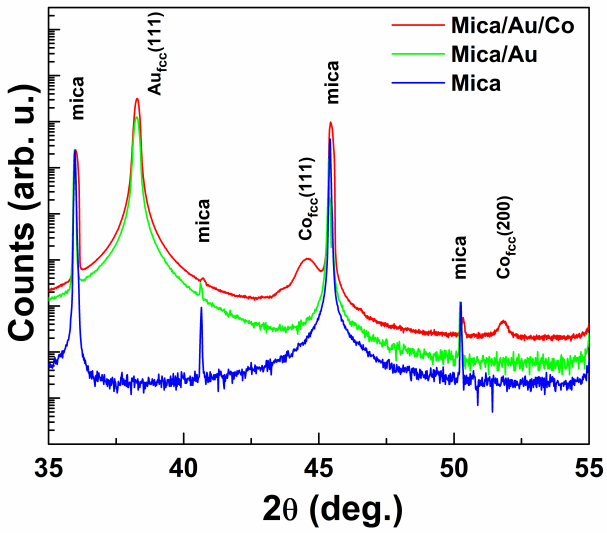


Figure 4.4: X-ray diffraction patterns obtained from the base mica substrates (blue), mica//Au substrates (green) and mica//Au/Co substrate (red) and superimposed on each other. fcc crystalline peaks corresponding to Au and Co surface are evident. Wavelength of X-ray used is 1.5406 Å.

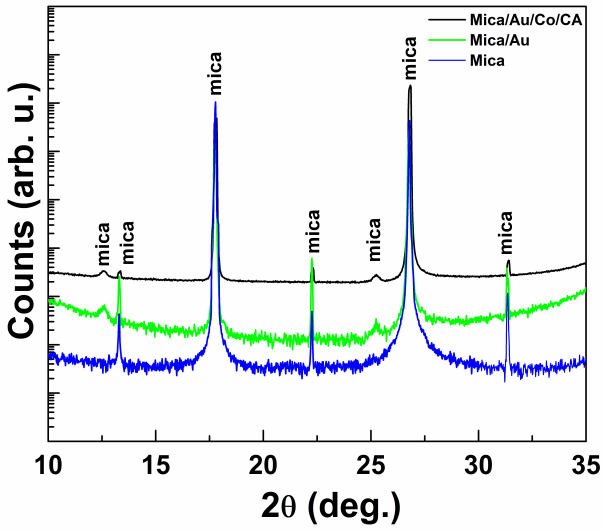


Figure 4.5: X-ray diffraction patterns of 100 nm thick CA sample grown on Co surface (black) superimposed on that of cleaved mica (blue) and mica//Au substrate (green). Large peaks coming from mica populating the entire spectrum of angles hinder the detetion of subtler peaks of the CA layer. Wavelength of X-ray used is 1.5406 Å.

### 4.2.4 Ferroelectric characterization details

The ferroelectric properties of the freshly prepared CA samples were characterized ex-situ at room temperature by a Piezoresponse Force Microscopy (Bruker AFM Dimension Icon) using a conducting tip (Bruker SCM-PIC). The samples were fixed on metallic plates and to provide grounding to the bottom Au surface, contacts with high quality silver paste were made to connect the Au surface to the metal plate which is eventually grounded.

First, certain regions of a few micrometers in width on the sample surface was scanned in contact mode operation while the tip was subjected to an AC electric field of amplitude 4V oscillating at a frequency away from the natural frequency of vibration for the cantilever. With the help of two internal lock-in amplifiers the instrument could separately produce the surface morphology image and the domain images for the particular region. The domain images were essentially the maps of the out-of-plane/vertical and in-plane/lateral phase signals of the outputs from the lock-in amplifier.

Then, to perform the local spectroscopic measurements, a particular grain was chosen and a DC voltage ramp of a minimum of -12 V to a maximum of +12 V was applied while capturing the both the phase signals and the tip deflection signal. The rate of voltage step increment was set at a frequency of 0.1 Hz, i.e. a

voltage increment step of 23 mV. The same region was scanned before and after the spectroscopic measurements to detect any change in the domain patterns within the region under study.

## 4.3 Results of ferroelectric characterization

### 4.3.1 Studies on Au surface

#### 4.3.1.1 Ferroelectric domain imaging

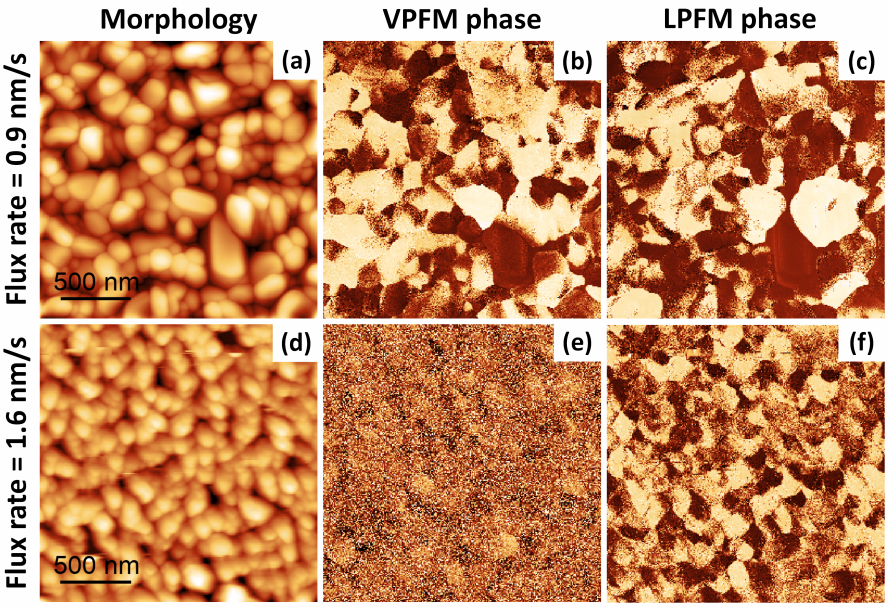


Figure 4.6: Flux rate dependence of morphology and ferroelectric domain structure for mica//Au/CA (50nm). (a, d) Surface morphology, (b, e) out-of-plane PFM phase, and (c, f) in-plane PFM phase of the same 2x2 $\mu m^2$ sample region. The flux rate rates were 0.9 nm/min (panels a-b-c) and 1.6 nm/min (panels d-e-f). Scaling is normalized to minimum and maximum values: (a)=(0 nm,98 nm), (b)=(0°,252°), (c)=(0°,326°), (d)=(0 nm, 61 nm), (e)=(0°,241°), (f)=(0°,249°).

To investigate the effect of growth conditions on the ferroelectric properties of CA films on Au surface, two growth parameters, (i) deposition flux rate and (ii) film thickness, were varied. From the ex-situ ferroelectric characterization by PFM, it was observed that both these parameters have significant effect not only on the growth morphology but also on the ferroelectric domain structures of the CA thin films. As shown in figure 4.6, by increasing the deposition flux rate from 0.9 nm/min (upper panel) to 1.6 nm/min (lower panel), we observe a reduction in grain size

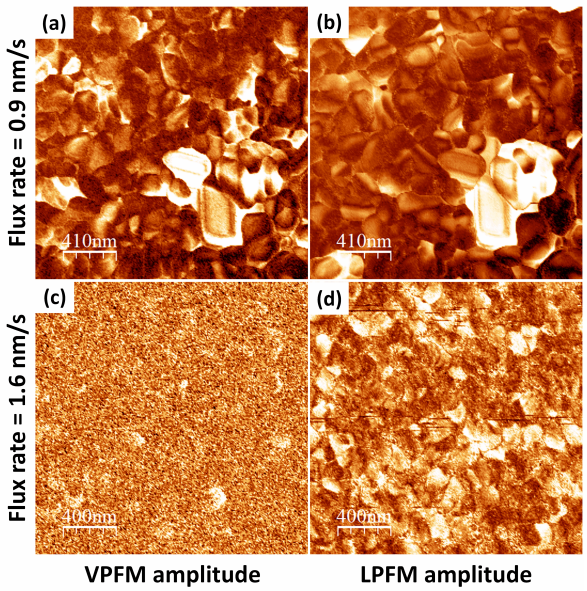


Figure 4.7: Flux rate dependence of PFM amplitudes for mica//Au/CA(50 nm) film, corresponding to figure 4.6.

distribution with the RMS roughness decreasing from 12.8 nm to 8.7 nm. For a rate of 0.9 nm/min, the similar contrast between VPFM and LPFM maps (figure 4.6 (b) and (c) respectively) indicates that the polarization is canted with respect to the substrate surface. However, for a rate of 1.6 nm/min, the LPFM phase contrast is easily visible (figure 4.6 (f)), with the VPFM phase contrast greatly minimized (figure 4.6 (e)), indicating that the polarization is now mainly parallel to the surface. This suggests that the flux rate influences not only the film morphology, but also the structural ordering of these polar molecules.

The fact that the polar ordering depends on the flux rate of deposition can be used to great advantage in device applications to tune the ferroelectric properties of CA layers without varying the layer thickness.The spinterface properties at the interface between Co and CA are expected to be affected by the magnitude and direction of polarization of the CA molecules at the interface. Flux rate based tuning of structural ordering of deposited CA molecules can provide an external way to tune the properties of the spinterface. One of these spinterface properties could be the possible magnetoelectric coupling between the magnetic order of the Co and the electric order of CA. However, detailed optimization would be required before such attempts to explore the interface physics could be made.

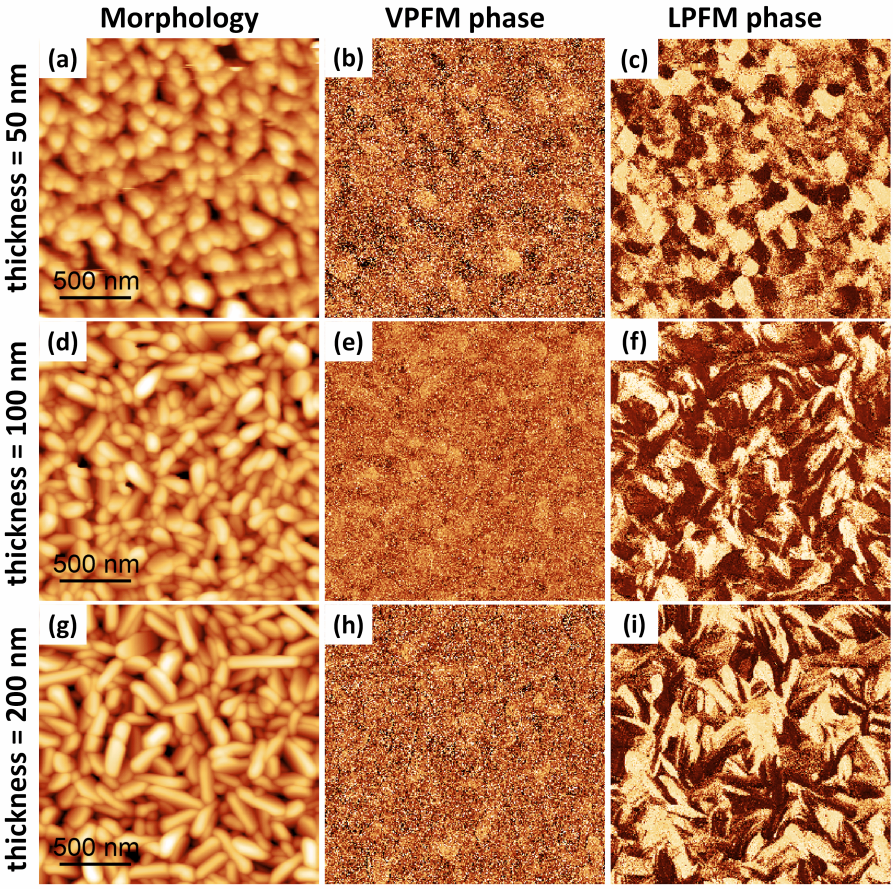


Figure 4.8: Thickness dependence of morphology and ferroelectric domain structure of mica//Au/CA grown at a flux rate of 1.6 nm/min. Upper, middle and lower panels show respectively the topography, out of plane PFM phase and in plane PFM phase for film thickness (t) of 50 nm (upper panels), 100 nm (middle panels), 200 nm (lower panels). For easy comparison, the upper panel is kept the same as the lower panel of figure 4.6. Scaling is normalized to minimum and maximum values: (a)=(0 nm,61 nm), (b)=(0°,240°), (c)=(0°,324°), (d)=(0 nm, 84 nm), (e)=(0°,140°), (f)=(0°,268°), (g)=(0 nm, 79 nm), (h)=(0°,170°), (i)=(0°,217°).

Next, we studied the properties by varying the thickness of the CA film deposited at a fixed flux rate of 1.6 nm/min. For film thicknesses of 50 nm, 100 nm and 200 nm, as shown in figure 4.8 VPFM contrast does not improve indicating that the ferroelectric polarization tends to be in-plane with increase in film thickness for this flux rate of deposition (figure 4.8 (b), (e), (h)). However, grains of CA tend to attain slightly elongated morphology as clear from figure 4.8 (g) which is followed by elongated LPFM domain structures (figure 4.8 (i)). Further, adding to these observations, we also observe coherent contrast variation in the PFM amplitude maps for the above cases thickness and flux variations. In figure 4.7 and figure 4.9, we present the corresponding PFM amplitude maps for figure 4.6 and 4.8 respectively.

It can be seen in both cases that the reduction in contrast in VPFM phase is followed by a drastic suppression of the VPFM amplitude, whereas LPFM amplitude is not suppressed. This observation is consistent with the fact that with the increase in deposition flux rate the polarization axes of the grains tend towards in-plane orientation (figure 4.6).

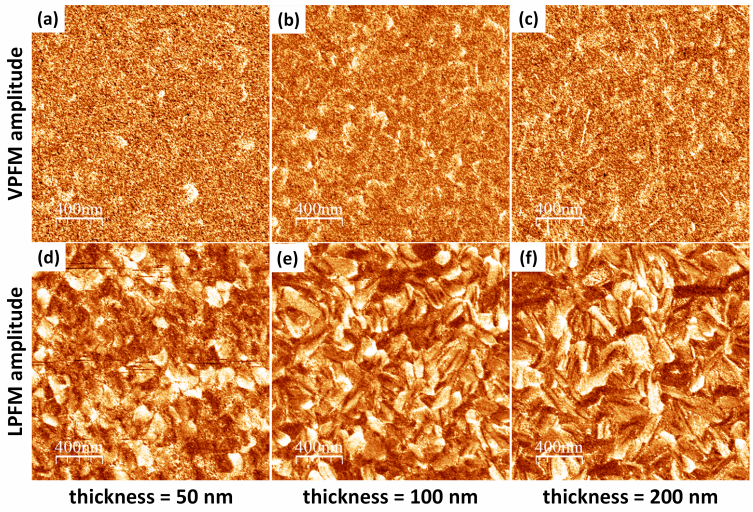


Figure 4.9: Thickness dependence of PFM amplitudes for a growth rate of 1.6 nm/min of mica//Au/CA films, corresponding to figure 4.8.

To better understand the correlation between the grains and the domains, we extracted the contours of the grains from the topographical images (figure 4.8 (a), (d) and (g)) and superposed them on the corresponding LPFM phase images (figure 4.8 (c), (f) and (i)). In this way, the grain boundaries are easily distinguished from domain boundaries. The results are shown in figure 4.10, where grain boundaries are represented by black lines and the LPFM phase contrast by a white-purple contrast. It can be seen that some domains expand over several grains. More often, the domain boundaries coincide with the grain boundaries and in that case it is difficult to identify the domain walls. But there are domains which are formed within single grains and the boundary of such domains can be identified as domain walls. Domains with opposite polarization exist within a single grain to lower the electrostatic energy arising due to polarization charges. Some of these multi-domain grains are marked with red dashed circles in figure 4.10 (c), most of which possess stripe shaped domain patterns. The presence of such stripe domain arrangement indicates, considering the energetics, that probably the polarization is parallel to the domain walls.

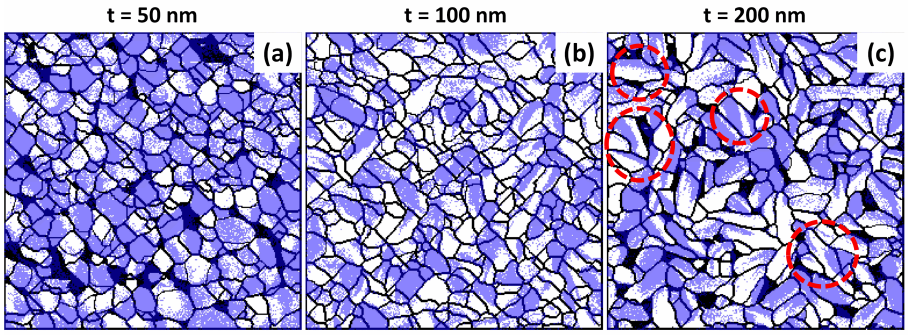


Figure 4.10: Topography contours superimposed on LPFM phase maps. Black lines represent the grain boundaries and the white (minimum)-purple (maximum) shades represent the contrast of LPFM phase response of mica//Au/CA films of thickness, t (a) 50 nm, (b) 100 nm and (c) 200 nm in a region of area 2 × 2 $\mu m^2$. Red dashed circles in panel (c) show some multi-domain grains. Black regions represent morphological voids.

Next, we studied the effect of annealing on the ferroelectric domain structures of a 50 nm CA film grown on Au surface. The atmospheric annealing was performed on the same sample inside an oven consecutively at 3 values of temperature for 30 minutes each followed by the domain imaging in the PFM. It can be seen, in figure 4.11, that with progressive annealing, the ferroelectric domains start to slowly degrade, as characterized by the increase in noise in the phase maps. These noisy regions in (d) and (h) are the result of the destruction of ferroelectric contrast of the particular regions.

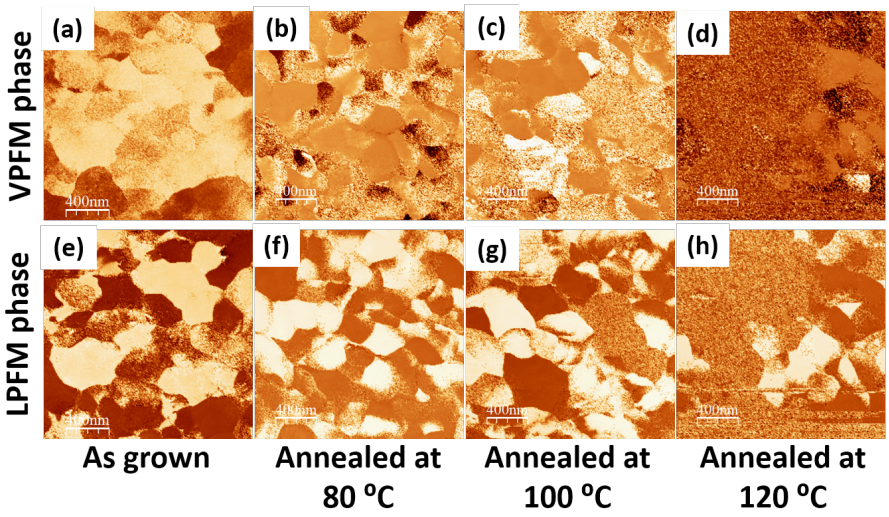


Figure 4.11: Impact of repeated annealing at increasing temperatures on ferroelectric domains of 50 nm CA film grown on Au. The domains can be seen to be badly affected after annealing at 120 $^0$C.

#### 4.3.1.2 Ferroelectric switching spectroscopy

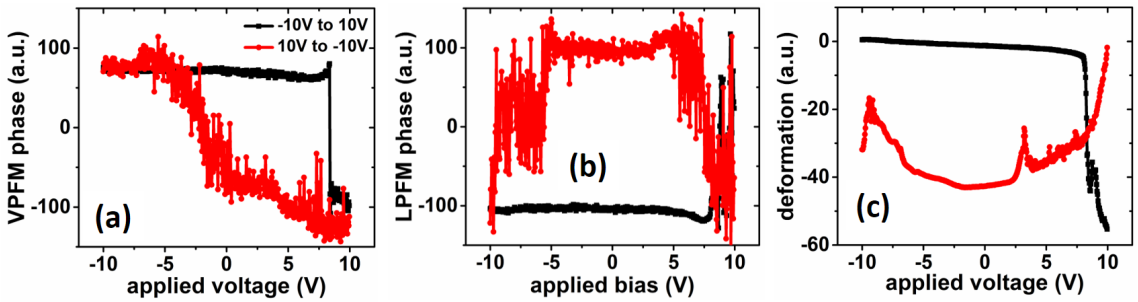


Figure 4.12: Results of a typical switching attempt on mica//Au/CA(50 nm) sample. (a) and (b) show the variation VPFM and LPFM phase with respect to applied voltage during the spectroscopy. (c) shows the tip deflection or grain deformation. Although no robust or clear switching can be observed, (a) seems to have a switching features appearing only on the positive bias side.

The switching spectroscopies on specific granular regions were carried out with a voltage step increment rate of 0.1 Hz, i.e. at a speed of 0.2 V/s. Much to our surprise, none of the samples of CA films on Au surface showed robust polarization reversal. This was confirmed by scanning the region before and after the spectroscopies which showed no change in the domain structures either in VPFM or LPFM phase maps. In one attempt, we obtained a reversal loop which resembled to a ferroelectric reversal occurring only on one direction, as shown in figure 4.12, but such a result was not reproducible. We often observed that with the application of the switching bias, the grains in the region got distorted and morphological voids appeared afterwards. An example of such a distortion and a morphological void is shown in figure 4.13. In certain cases, the distortion was so impactful that it could be captured with the microscope camera of the AFM, as shown in figure 4.14.

Suspecting that a bias of 12 V magnitude could be too much for the grains to bear and the switching could be occurring at smaller bias voltage, we systematically increased the bias maximum from 1 V to 12 V and performed the spectroscopic measurements for each bias maximum followed by a domain imaging of the particular region. We observed no polarization switching until the voltage maximum was ∼10 V and in most cases, 10 V onwards, we observed the morphological distortion.

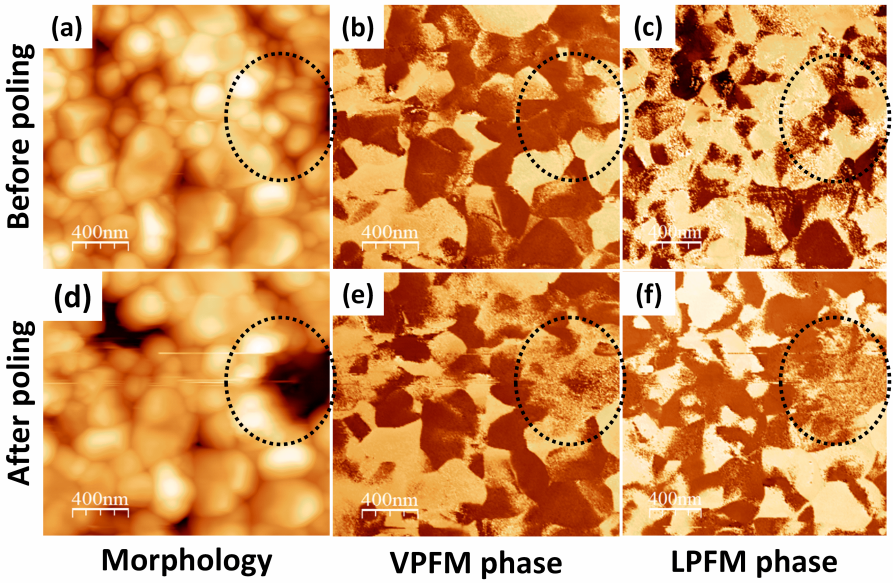


Figure 4.13: Impact of poling bias on the morphology of mica//Au/CA(50 nm) sample. Left, middle and right panels show the morphology, VPFM and LPFM phase respectively before (upper panels) and after (lower) applying the poling bias. The destroyed zone (d) is encircled with black dashed line. The noise in the phase maps in (e) and (f) is indicative of the destruction of ferroelectricity in that zone corresponding to the morphological void created due to the bias.

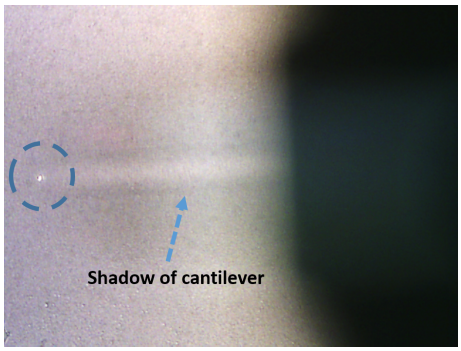


Figure 4.14: Optically visible destruction caused by the spectroscopic bias application on mica//Au/CA(50 nm). The image is captured by the optical microscope of the AFM setup. The destroyed zone is encircled by blue dashed line.

### 4.3.2 Studies on Co surface

#### 4.3.2.1 Ferroelectric domain imaging

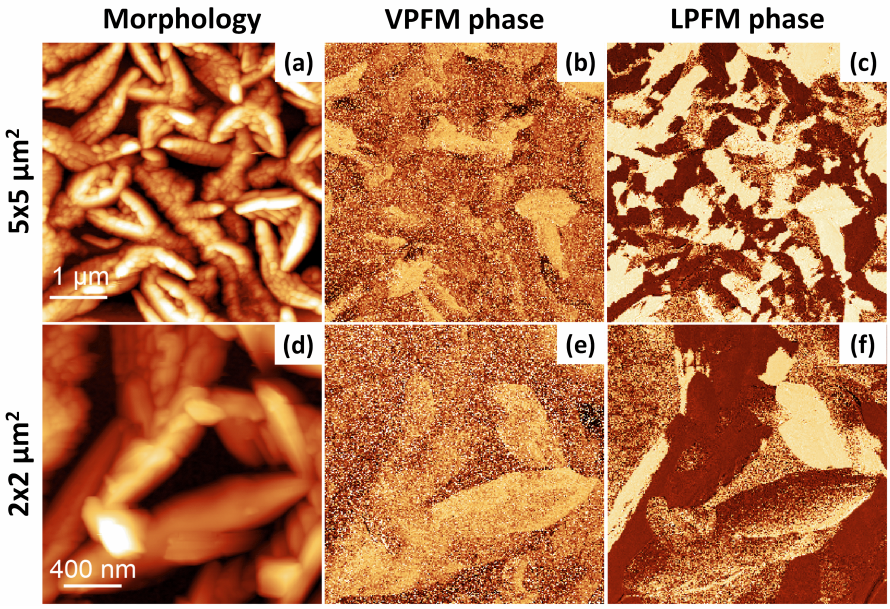


Figure 4.15: Surface morphology and ferroelectric domains of 50 nm of CA grown on mica//Au/Co. Morphology (a, d), VPFM phase (b, e) and LPFM phase (c, f) are shown with large (upper panel) and small (lower panel) scales. The scales for phase images correspond to the scales shown in the morphology in respective panels. Scaling is normalized to minimum and maximum values: (a)=(0 nm,136 nm), (b)=(0°,226°), (c)=(0°,360°), (d)=(0 nm, 216 nm), (e)=(0°,263°), (f)=(0°,331°).

Then, we turned to the films of CA grown on Co surface. As shown in figure 4.15, the grains of a 50 nm film grown at a flux rate of 1.6 nm/min adopt an elongated shape in contrast to spherically shaped grains on Au surface. We also observe a significant decrease in the surface coverage. The ferroelectric domain structure can be seen to follow the morphology. It can further be seen that the LPFM phase contrast is sharper than the VPFM contrast. The presence of non-zero VPFM phase contrast signals a finite out-of-plane component of polarization vector of the grains.

#### 4.3.2.2 Ferroelectric switching spectroscopy

Contrary to the case of lack of polarization switching of CA grains on Au surface, we observed successful and robust polarization switching from single grains on Co surface. We present, in figure 4.17 (a), (b) and (c), hysteresis loops of three different PFM quantities, namely, VPFM, LPFM and relative amplitude of tip deflection. These data show that a polarization switching is possible at a moderate voltage.

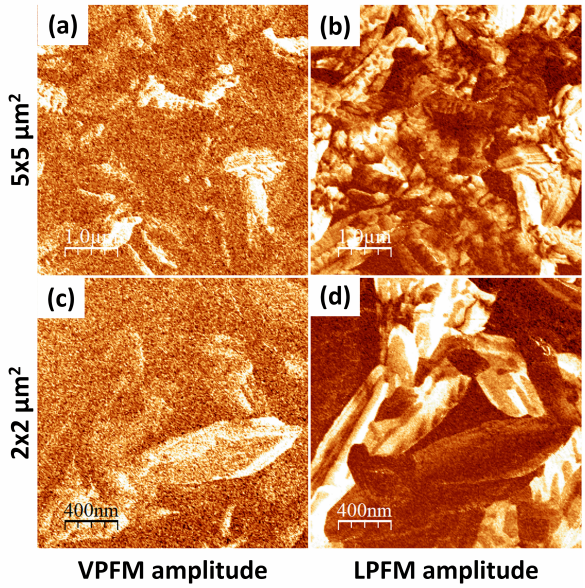


Figure 4.16: PFM amplitude maps corresponding to figure 4.15.

We observe that the reversal curve/hysteresis of the LPFM phase (figure 4.17 (b)) is much sharper than that of VPFM phase (figure 4.17 (a)), as expected since the polarization state is in-plane (figure 4.15 and 4.16). Nevertheless, tiny switching features can also be noticed in the VPFM phase reversal curve (gray arrows of figure 4.17 (a)) that appear at exactly the same voltage values as those for the LPFM phase reversal curve. The successful phase reversal of vertical and lateral phases confirms the ferroelectricity of CA on Co.

The lower panels of figure 4.17 demonstrate a successful polarization reversal process. Figure 4.17 (c) and (g) show the initial ferroelectric state as imaged using VPFM and LPFM, respectively. The phase images after poling the domain with +12 V and -12 V are shown in figure 4.17 (e) and (f), respectively, for the VPFM phase and in figure 4.17 (h) and (i), respectively, for the LPFM phase. A clear change of phase contrast between the two oppositely polarized states is evident in both VPFM and LPFM phases for the grain of interest (dashed circles). The polarization reversal observed in figure 4.17 is happening mainly in the in-plane direction. But the minor switching features in VPFM phase reversal curve and a clear change in VPFM contrast of the domain indicate the presence of a non-zero component of polarization reversal occurring in the out-of-plane direction as well. Furthermore, it can be noted that a field applied perpendicularly to the surface is able to reverse the in-plane polarization which is indicative of coupling between both polarization components. These two facts indicate that the net polarization axis is canted with

respect to the film plane at a small angle. Also, we see in figure 4.17 (b) that the hysteresis loop is not symmetric with respect to the applied voltage and is slightly shifted towards positive bias side. This could be occurring due to some intrinsic field remaining inside the domain.

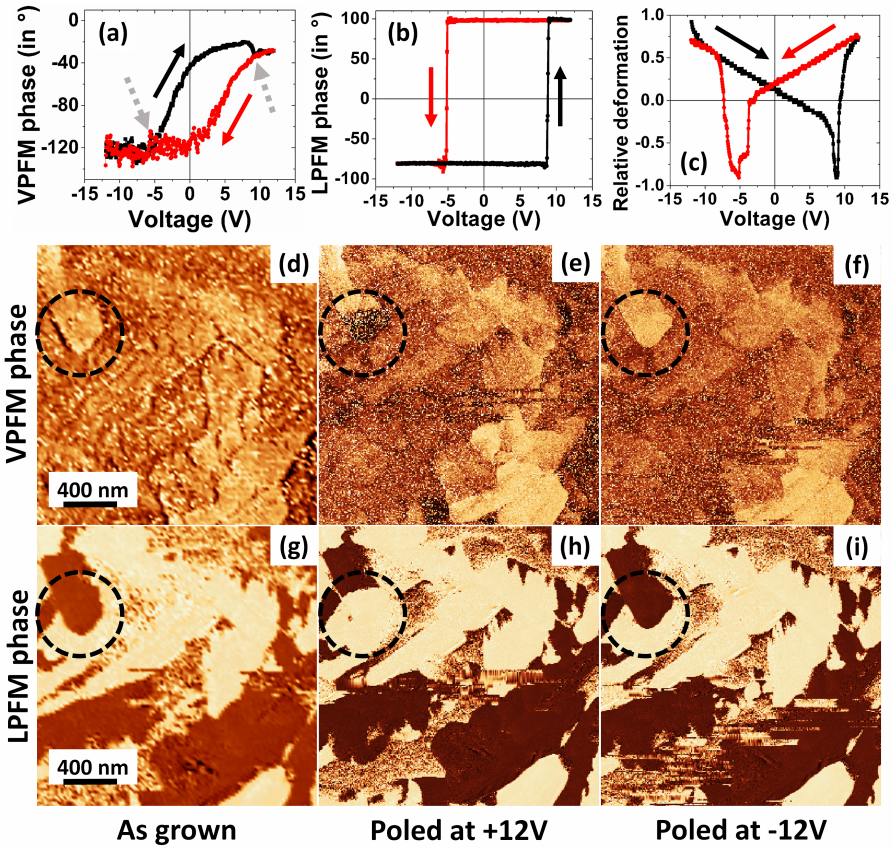


Figure 4.17: Polarization reversal hysteresis loops and phase maps of poled states of a domain in mica//Au/Co/CA(50 nm) film. Upper panel shows polarization reversal curves in terms of VPFM phase (a), LPFM phase (b) and relative grain deformation(c). Dotted arrows in (a) indicate the weakly visible reversal features. Red and black curves represent voltage ramp directions, red for +12 V to -12 V and black for -12 V to +12 V. Middle panel shows the VPFM phase maps in the as grown state (d), after poling with +12 V (e) and after poling with -12 V (f). Lower panels show the LPFM phase maps on the same area as (d), (e) and (f). The as grown states of the domain is shown in (d) and (g) where the dashed circles encircle the grain of interest.

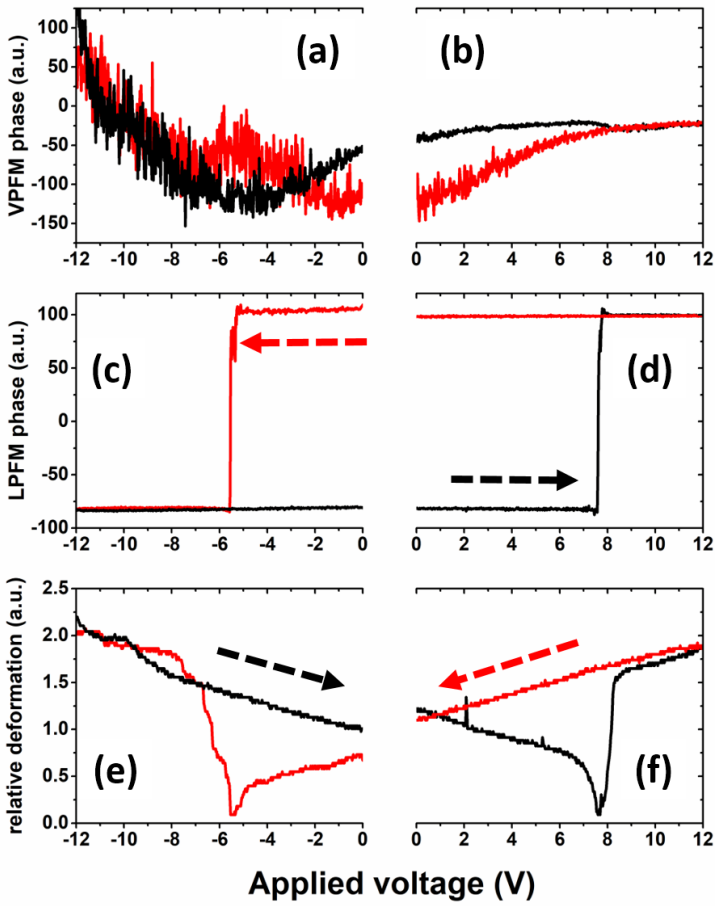


Figure 4.18: Discontinuous writing procedure on a domain in mica//Au/Co/CA(50 nm) film. Upper ((a) and (b)) and middle panels ((c) and (d)) show the VPFM and LPFM phase variation respectively with respect to the applied voltage during spectroscopy. Lower panel ((e) and (f)) shows the grain deformation or tip deflection. Dashed arrows show the direction of voltage increment.

In contrast to the continuous polarization reversal process as shown in figure 4.17, we tried to polarize the domain individually into two polarization states by separately poling the domain from 0 V to +12 V and 0 V to -12 V with a time interval of ∼15 minutes between the two poling attempts. As shown in figure 4.18, the remanent state of the domain at the end of the reversal processes (applied voltage=0 V) along both positive and negative bias directions can be clearly observed. The nice continuity of the curves at the remnant state from one bias side to the other signifies the stability of the retention state of the domain.

Further, to check the robustness of a writing process, we repeatedly write a domain with opposite polarity (+12 V and -12 V) and capture its domain image after each writing process. A spatially detailed LPFM maps acquired after such a consecutive polarization reversal experiment on a 50 nm-thick CA film on Co is

shown in figure 4.19. The grain (white circle) successfully survived repeated poling attempts which resulted in the systematic reversal of the polarization state of a part of the grain, with the voltage polarity determining the resulting polarization state.

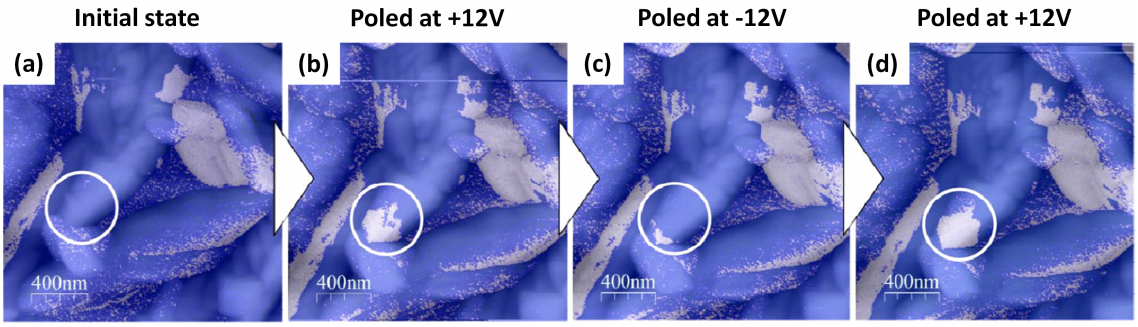


Figure 4.19: Robust polarization reversibility of CA domain on Co surface. Grey-blue contrast shows in-plane domains in the LPFM phase maps of a 2 × 2 $\mu m^2$ region in the initial state (a), after consecutive poling at +12 V (b), -12 V (c) and at +12 V (d).

## 4.4 Discussions

Density Functional Theory and Molecular Dynamics calculations predict that it should be possible to switch the polarization in a 2-dimensional (2D) layer of CA on the surfaces of Au and also on more reactive surface of Ag.[119, 120, 121] However, the experimental confirmation of such switching at a few monolayer level is not easy and has been lacking so far. In 2D layers, the polarization of the CA network is essentially in the plane of the film requiring an in plane electric field for switching, whereas, in a bulk polycrystalline film the polarization axis can be at an angle with respect to the film plane. So even with an out of plane electric field like that emanating from a PFM tip, it is expected that polarization reversal can take place both in and out of the plane directions. Thus it is unclear why on Au surface in bulk films reversible ferroelectric properties of CA are not robust whereas on Co surface they are. In the absence of any structural information of the CA grains on both the surfaces, we attempt to qualitatively explain the anomaly as the following.

Recent STM studies on 2D layer growth of CA on Au and Ag surfaces show that CA molecules form different types of networks depending on the substrate, primarily due to different substrate molecule interactions.[119, 120] Calculations show that the interaction of CA with Au is weaker than that with Ag, for Ag is relatively a more reactive substrate. Further, STM studies reveal high surface mobility and low

diffusion barrier of CA layers on Au surface. Highly unstable networks of CA for less than 1 monolayer thickness coverage have also been observed on Au surface.[122] Similar studies of CA on Co surface have not been reported so far but thanks to higher surface reactivity or Co-molecule interaction on Co surface, stable networks of CA layers can be expected.

This is consistent with our observation of robust properties of CA on Co surface. We believe that the weaker substrate molecule interaction in the initial layers of CA growth on Au surface is at the origin of the observed lack of robustness in the ferroelectric properties on Au surface. This may also account for the observed distortion of the film topography after attempts to switch the polarization in the case of an Au substrate. Thus, we observe that metallic substrates like Co with relatively higher surface reactivity is helping to stabilize the CA ferroelectric properties. This, however, is in contrast to the usually observed scenario where reducing the surface reactivity stabilizes the molecular properties.

## 4.5 Partial conclusions

On Au surface, the presence of multiple domains in a single grain of CA is a sign of ferroelectric order being present but the lack of robust polarization reversal raises doubts on the ease of switchability of CA grains on Au surface. As the proof of ferroelectricity necessarily requires the observation of polarization reversal, it is difficult to conclude on the ferroelectric response of CA on Au surface, however, the piezoelectric response is evident from the presence of sharp contrast in the vertical and lateral phase images. On Co surface, switching is happening predominantly along the film plane with a small component along the normal to it.

In conclusion, it appears that it is possible to fabricate switchable and robust ferroelectric Croconic Acid thin films on Co, whereas, on less reactive substrates like Au it is not so obvious. In contrast to the attempts being made in the field of organic spintronics where the focus is to mitigate the substrate-molecule hybridization strength for stabilizing molecular properties, we observe a positive impact of the substrate-molecule interaction or surface reactivity on the molecular properties. Our observations could work as a guide for the development of multifunctional devices based on ferroelectric Croconic Acid composite films. The stability of ferroelectric properties on Co surface combined with the high polarization charge density of CA should encourage fabrication of devices for spintronics applications; for example, organic (ferroelectric)-inorganic (ferromagnetic) hybrid artificial multiferroic devices,

organic ferroelectric tunnel junctions (O-FTJ) etc. Moreover, our work also hints at possible rich interface phenomena that may be occurring at a ferromagnetic/organic ferroelectric interface and its role in the stabilization of polarization reversal which is not in the scope of the present work. Finally, we believe that further studies on a variety of metal surfaces along with detailed simulations on surface-molecule interfaces and also studies under in-situ conditions are necessary to carefully explore the relationship between the stability of bulk films of CA and the surface reactivity of the metal.

# Chapter 5

# Nanoscopic ferroelectric characterization of organic Croconic Acid films

## 5.1 Pertinence of the study

Ferroelectric materials have found substantial applications in a number of fields ranging from electronic–spintronic devices and sensors–transducers to energy harvesting and heat transfer applications.[123, 124, 125] In the field of electronic devices, the use of ferroelectric materials has contributed to the realization of a plethora of devices, from memory devices to voltage-operated spintronic devices. Most of the commonly used ferroelectric materials till date are inorganic, for which the fabrication and processing are expensive. Besides, inorganic ferroelectrics tend to be formed of elements that may not be environmentally benign. Thus, there is a growing need for alternative ferroelectric materials.

Organic ferroelectric materials are emerging as such possible alternatives as they may provide added advantages due to their flexibility, chemical functionality, non-toxicity, low cost, easy processing and low power consumption. Due to such wide range of such advantages, there is also a growing trend of interest in the device applications of such materials. Organic ferroelectric material based devices such as ferroelectric random access memory (FERAM)[67], ferroelectric field effect transistors (FEFET)[68], ferroelectric tunnel junctions (FTJ)[71, 72], ferroelectric optoelectronic devices[126], ferroelectric resistive switches[127], ferroelectric capacitors[128, 129] and memory diodes[127, 130, 131] have been realized in the recent past. However, the repository of organic ferroelectric materials is relatively smaller and potential applications have been limited mainly to polymer-based materials. Not only do polymeric materials exhibit a small polarization value compared to inorganic materials, but they are not suitable either for low-voltage applications due to the high electric field required to switch the polarization[34, 132] and the presence of leakage current[133, 134] in vertical devices. Thus, there is greatly ongoing research interests and activities to explore the relatively immature field of organic ferroelectrics. Various inherent mechanisms for the origin of ferroelectric order in organic materials such as charge transfer process, hydrogen bonding, chemical tautomerism, supramolecular mechanisms etc.[135] are being studied in order to look for newer organic ferroelectrics.

The recent discovery of stable room temperature ferroelectricity in organic Croconic Acid with polarization values on par with those found in inorganic ferroelectric materials and highest among organic ferroelectric materials[1], has opened up possibilities to realize myriads of organic ferroelectrics based nano-electronic and spintronic devices that combines the advantages of the presence of an organic material

and a high ferroelectric polarization value. Such possibilities require an adequate understanding of the ferroelectric properties of Croconic Acid films grown on surfaces that are commonly employed in device fabrication. Apart from the large polarization value of Croconic Acid, the fact that the polarization can be reversed with small electric fields at frequencies as high as 1 kHz[1] makes it a potential candidate for low-voltage device operations. Further, the observation of a large second-order non-linear susceptibility[136] and the predicted possible photoinduced ferroelectric switching.[9] suggest that Croconic Acid can be potentially useful for non-linear optical or optoelectronic devices.

To explore the potential of this promising ferroelectric candidate from the nanoelectronic device applications stand point, substantial studies of ferroelectric properties in microscopic and nanoscopic devices based on Croconic Acid thin films are required. While several types of macroscopic studies on relatively larger crystals and scanning probe microscopy based growth.[6, 7] studies on ultra-thin films on metallic surfaces have been performed for Croconic Acid, studies such as ferroelectric studies, thin film growth and growth optimization studies are only in their early stages.[10, 137] Consequently, studies on microscopic device application aspect of Croconic Acid are severely limited.

On the other hand, from the commercial device fabrication point of view, the lateral dimensions of the nanoelectronic devices are not microscopic anymore. Whether it is the non-ferroelectric or the ferroelectric based nanoelectronic devices, the need and demand for miniaturization of electronic devices has pushed the boundaries of the lateral dimensions to the nanoscopic range which has been possible thanks to the rapid and concurrent developments in the associated engineering and technological fields over the past few decades. For example, lateral size of the semiconductor based transistors has gone down to the nanoscopic ranges, at present reaching 10 nm in the industrial scale and 5 nm in the research level. Similarly, nanoelectronic devices employing ferroelectric materials are being fabricated at the nanoscopic scales. For example, lateral dimensions in commercially fabricated Ferroelectric Random Access Memory (FERAM) technology has reached a length scale as small as 130 nm.[62]

On a parallel track of scientific research, the corresponding focus has been on the ferroelectric characterizations at the nanoscopic scale, for example, studies on ferroelectric nanodot arrays, among other types of nanostructures, of diameters as small as 100 nm dates back to the late 1990s or early 2000s.[138, 139, 140, 141] Recently, the studies have been intensified even further with the advent of several aspects such as magnetoelectricity and topological domain structures in nanodot

arrays.[142, 143, 144] Even with polymer based ferroelectric materials such as PVDF, such nanoscopic ferroelectric devices are being heavily investigated.[145, 146, 147, 148]

Moreover, it is known that the dimensions of ferroelectric devices greatly influence the ferroelectric properties and characteristics of the devices, which is called as the scaling effect in ferroelectrics. It has been observed that the ferroelectric and piezoelectric properties along with the domain structures get affected with the change in lateral dimension, mainly due to the increase of free surface and surface to volume ratio with decrease in lateral size.[149] A lot of research has gone into experimentally studying the scaling effect on nano patterned ferroelectric devices.[150, 151] In view of the ferroelectric scaling effect, it becomes even more important to probe the ferroelectric materials at the nanoscale, especially for a newly discovered and less studied ferroelectric material. Further, studies on how the scaling effect may behave when it comes to organic ferroelectric materials or materials with prototopic origin of ferroelectricity may be of potential interest for the future applications of organic ferroelectrics.

Furthermore, looking inside a ferroelectric device, a microscopic ferroelectric device may contain several grains of a polycrystalline ferroelectric spacer within each device. But as the lateral dimensions of nanoelectronic devices go down, the typical device approaches the lateral dimensions of the grains, consisting of only a few grains or possibly just a single grain. In a microscopic device, the ferroelectric properties of individual grains may get averaged while defining the overall device response. However, at the nanoscopic scale of devices, due to random crystallographic orientations and, therefore, the ferroelectric properties of individual grains, significant differences among the device performances fabricated from the same ferroelectric layer may arise. In the above context, on one hand, it becomes essential to optimize the growth so as to make the grains as identical as possible and on the other hand, it becomes important to go down with the scale of detailed ferroelectric characterizations to the nanoscopic range.

Thus, at the crossroad of scientific research where future organic ferroelectric devices seem to possess potential for future electronic devices due to several significant advantages over their inorganic counterparts and the lateral size of electronic devices are shrinking to the nano regime, nanoscopic probing of ferroelectric properties of organic materials naturally becomes an essential direction of future explorations. Therefore, to explore the true potentials of CA in future organic ferroelectric nanoscopic electronic devices, it is of crucial importance to investigate its

nanoscopic ferroelectric properties. Owing to the particular type of ferroelectric origin in CA[2, 1], it may be even more interesting to see how its ferroelectric properties evolve as the lateral dimensions will gradually shrink to molecular dimensions. Further, fundamental physics associated with switching kinetics and dynamics, domain walls and their motion etc. can be explored at the nanoscopic scale.[11, 12]

To explore the nanoscopic properties of CA, in this chapter, we present our attempts of study that involves the successful application of a novel nanoscopic probing technique called 'switching current spectroscopy', the details of which are described in the following section. In this study, CA films of thickness of around 50 nm grown on 4 nm Co surface were investigated using the in-situ PFM setup. As we know from the previous chapter, room temperature growth of CA thin films on Co surfaces result in quasi-continuous films with grains typically as large as ∼300 nm in diameter. Usually, the probed nanoscopic region consists of a single grain of the above dimension. Sometimes, it may include of regions of multiple neighboring domains. This understanding of the grain structure helped us align our efforts to measure the nanoscopic ferroelectric properties of CA on Co surface.

## 5.2 Switching current spectroscopy for nanoscopic ferroelectric characterization

The electrical characterization of ferroelectric properties of materials is usually done by studying the electrical response of a capacitor device where the ferroelectric material works as the dielectric of the capacitor. In case of a thin film ferroelectric material, the capacitor device is fabricated by sandwiching the ferroelectric thin film between the top and bottom electrodes. The ferroelectric characterizations are carried out by applying electrical voltage across the capacitor and studying the behavior of circuit current and capacitance of the device with respect to the applied voltage. The measured circuit current measures not only the conduction current through the device but also the compensation currents that are generated due to the compensation charges provided by the electrodes to the ferroelectric film surfaces to neutralize the newly appeared polarization charges after a polarization reversal. This compensation current is commonly called as polarization switching current or, simply, switching current. The detailed description and the schematics of the mechanism is given in figure 5.1.

However, such a method is limited only to macroscopic scales of lateral dimen-

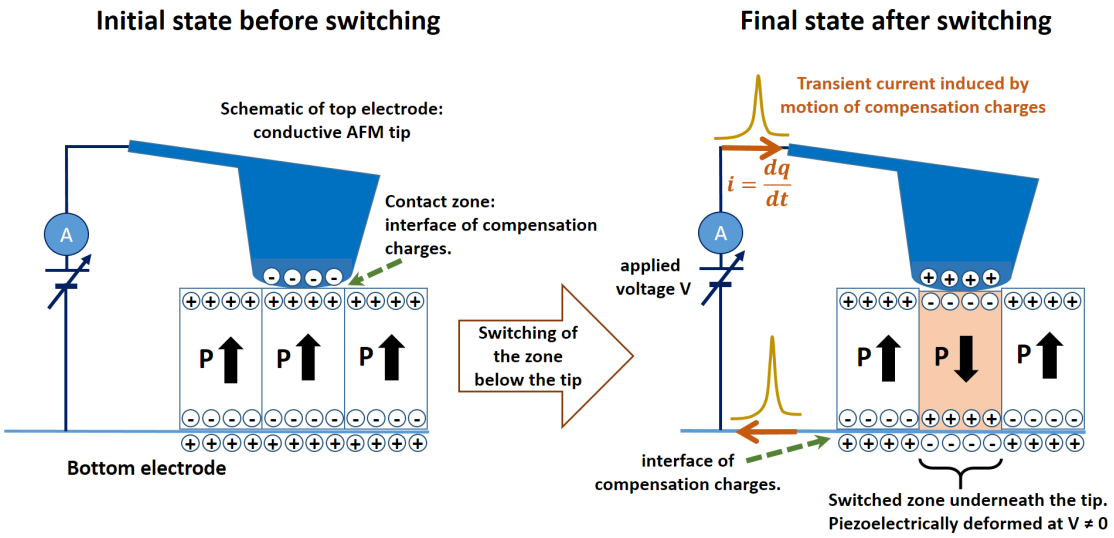


Figure 5.1: Schematics of origin of polarization switching current in ferroelectric materials. At the surface of ferroelectric materials, takes place a sudden spatial variation in electric polarization which gives rise to surface bound charges whose density depends on the magnitude of the polarization in the material and sign depends on the polarization direction of the ferroelectric object or that of a local ferroelectric domain. These charges are called as polarization charges and they are of opposite polarity on opposite surfaces of a film or domain. The electric field that is generated internally due to these opposite polarization charges is called a depolarizing field. Under the influence of this field, charges get induced in a conducting material that comes in contact with the surfaces of the ferroelectric thin film, so as to screen the depolarizing field. These induced charges are called as screening/compensation charges and they are opposite in polarity to the polarization charges of the surface that they form at. This surface can be called as the interface of compensation/screening charges.
When the polarization of a particular domain or a film is reversed by the application of electric field applied via conducting electrodes along the direction opposite to the polarization of the domain or the film, the polarization charges at the ferroelectric surface get reversed in polarity which necessitates in the reversal of the screening charges. This causes a current to flow in the external circuit which is employed to apply the external electric field, called as ferroelectric switching current or polarization switching current, or simply, switching current. The magnitude of this current is directly proportional to the switched area and the polarization strength at the particular area and is inversely proportional to the temporal spread of the switching event. Usually, this current appears as a sharp peak in the I-V measurement, where 'I' is the current measured in the circuit.

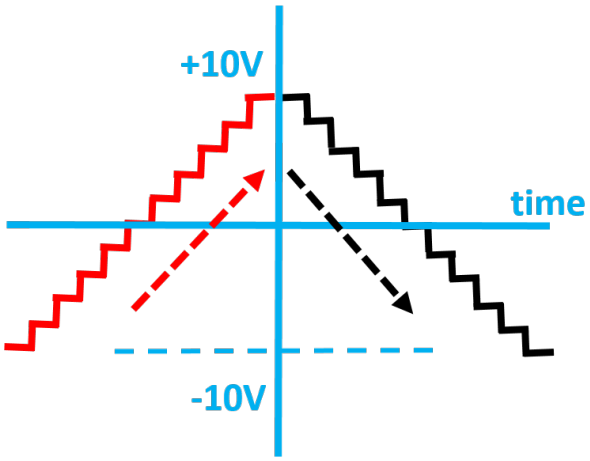


Figure 5.2: Profile of applied DC sweeping voltage for a typical spectroscopic measurement

sions as the circuit design at the nanoscopic scale becomes extremely challenging and expensive and may be done only at the industrial fabrication level. Also, at the nanoscopic scale, the magnitude of switching currents become so small that its accurate detection becomes challenging. Thus, the measured switching currents are purely macroscopic in nature as the lateral dimensions of the capacitor devices are usually in the range of several 10s of micrometers which may include several crystallographically distinct grains in a polycrystalline film. Polarization switching mechanism of such an ensemble of nanoscopic grains within macroscopic geometries is a statistical process, thus, the access to ferroelectric properties at nanoscopic scales, such as individual grains, is hampered in this method of characterization. Moreover, leakage current through capacitor devices due to conduction hotspots, trapped charges and/or impurities interfere with the detection of pure switching current.[13, 152, 14]

On the other hand, nanoscopic ferroelectric characterizations are carried out using PFM, both on microscopic and nanoscopic capacitor devices and on ferroelectric surfaces without any top electrode. Due to the nanoscopic resolution provided by PFM, it has been a standard method for ferroelectric characterization for the last few decades which allows to image ferroelectric domains, manipulate locally the polarization state and record local hysteresis loops. However, the interpretation of PFM in terms of ferroelectricity is vulnerable to artifacts and influences caused by non-ferroelectric effects such as strain and electrostatic effects due to impurities.[153, 154, 155] In the recent past, certain non-ferroelectric processes have been found to contribute to the observed piezoresponse, thereby, leading to poorer

and less accurate interpretation of the investigated properties.

Alternatively, as an extension of PFM, Kwon et al[17] combined the measurement of switching currents and the technique of PFM to perform nanoscopic characterizations. Using a blunted conductive AFM tip as a mobile electrode, they directly measured switching currents from certain nanoscopic ferroelectric nano dot devices and epitaxial ferroelectric film surfaces without any top electrode but such attempts have not received sufficient attention and have been limited only to single crystalline films of some well-known inorganic ferroelectric materials with large polarization values. Further, the observed switching currents suffered from noise due to the conduction leakage currents. Besides, studies on the electro-mechanical behavior of the nanoscopic region, which plays an important role in determining the kinetics of the polarization reversal processes, has been lacking so far.

We introduce the nanoscopic characterization technique called as nanoscopic ferroelectric switching current spectroscopy to investigate the nanoscopic properties of polycrystalline thin films of CA. This method is based on detecting and measuring tiny switching currents originating from the polarization reversal of nanoscopic regions such as a single grain of the ferroelectric material. The origin of nanoscopic ferroelectric switching current is explained in figure 5.1. By simultaneously capturing the electromechanical response (figure 5.3) of the nanoscopic region, we also establish the veracity of obtained switching current measurements. Further, by analyzing this electromechanical response, deeper insights into the kinetics of the polarization reversal processes occurring at the nanoscale are obtained. Furthermore, by taking multiple measurements on the same nanoscopic region, we study the statistical aspect of nanoscopic polarization switching.

The switching current appear as sharp peaks in the I-V spectroscopy. The shape of the switching current peak carries tons of information about not just the switching dynamics and kinetics but also about the underlying switching mechanism in the particular material. For example, studies performed in the 60's show that the symmetry of the switching peak can be associated with the strength of domain-nucleus interaction which determines the speed of domain wall motion.[12] Studies on the shape dependence of switching peak on electric field strength, temperature and film thickness provide even more detailed and more fundamental information such as domain wall motion time, nucleation time and domain-nucleus interaction.[12, 11] These fundamental studies on switching properties were macroscopic in nature involving the switching currents either from large number of individual grains or from macroscopic ferroelectric crystals. Our approach to observe switching currents from

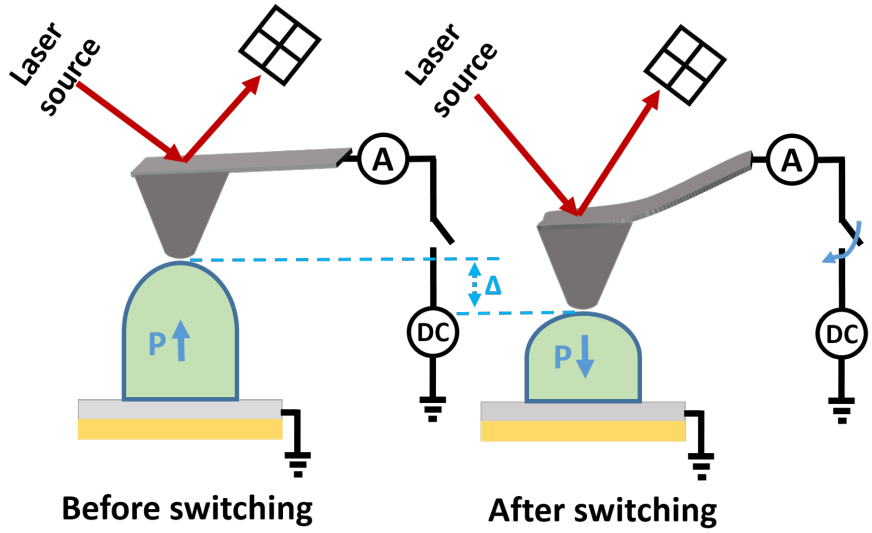


Figure 5.3: Schematics of origin of strain response in a PFM measurement setup. When a polarization of a grain is reversed by applying an electric field, immediately after the reversal process, the electric field is opposite to the direction of the polarization. This results in the sudden contraction of the grain due to the inverse piezoelectric effect. Now if the probe tip is already in contact with the grain, this contraction is sensed by the tip and the cantilever gets deflected momentarily. This tip deflection when captured by the photodetector gives the strain response during a spectroscopic measurement. Here, the tip deflection or the contraction of the grain is denoted by $\Delta$. It must be noted that, along with the grain deformation related deflection, there is a spring force like deflection that is experienced by the cantilever which is due to the capacitive attractive force between the tip-cantilever assembly and the bottom electrode. For the sake of simplicity, this type of cantilever deflection is ignored in the above schematics.

nanoscopic regions will bring deeper and newer insights to our understanding of the above fundamental properties associated to a ferroelectric switching event, especially the stochastic nature of polarization switching occurring at the nanoscale. In addition, detailed studies on switching current peaks supported with appropriate modelling of interfaces may bring about a more vivid picture of metal/ferroelectric interfaces in terms of the nature of screening charges and the electrochemical aspect of the interface.

From applications point of view also, the detection of switching currents from a nanoscopic ferroelectric region can be of significant relevance as almost all the commercial applications utilize polycrystalline ferroelectric thin films. For instance, there have been attempts to employ electronic limitation on ferroelectric switching currents to deterministically control the switched area within a macroscopic switchable region and thereby articulate a multi-step ferroelectric switching mechanism of

the particular region. This provides a controllable way to materialize the concept of multilevel data storage within the same volume of matter with each intermediate ferroelectric states working as one level, hence, multiplying the bit density in ferroelectric-based data storage systems without needing to reduce the physical bit size. Following the above concept, Lee et al[16] could indeed demonstrate the writing of 8 well defined logic states of a FErroelectric Random Access Memory (FERAM) element and improvised a one-bit memory element to form a three-bit system. Understanding switching current properties at the nanoscopic scale or at granular level is at the heart of such ideas and will prove to be helpful in engineering a wide range of electronic devices. Besides, direct extension of such an implementation to nanoscopic regions could open up possibilities to astronomically increase the storage density of commercially available ferroelectrics based memory elements.

## 5.3 Results of switching current spectroscopy

Switching current spectroscopy was performed at the nanoscopic scale on the films of CA of thickness of 50 nm grown on 4 nm Co surface using the in-situ UHV PFM setup. The Co was grown in-situ on the mica//Au substrates as used in the chapter 4. As we know from the previous chapter, room temperature growth of CA thin films on Co surfaces result in quasi-continuous films with grains typically as large as ∼300 nm in diameter. Usually, the probed nanoscopic region consists of a single grain of the above dimension. Sometimes, it may comprise of regions of multiple neighbouring domains.

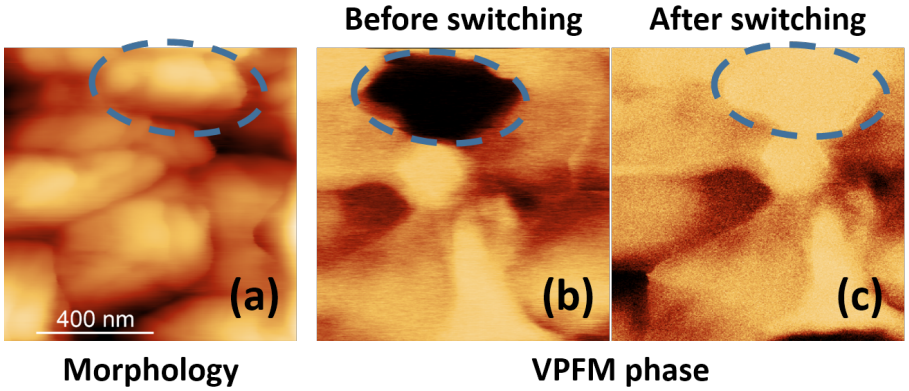


Figure 5.4: PFM Domain imaging of a Co(4 nm)/CA (50 nm) sample. (a) shows the surface morphology of the region where the dashed ellipse encircles the region/grain under study. (b) and (c) show the out of plane or vertical before and after) the switching event respectively.

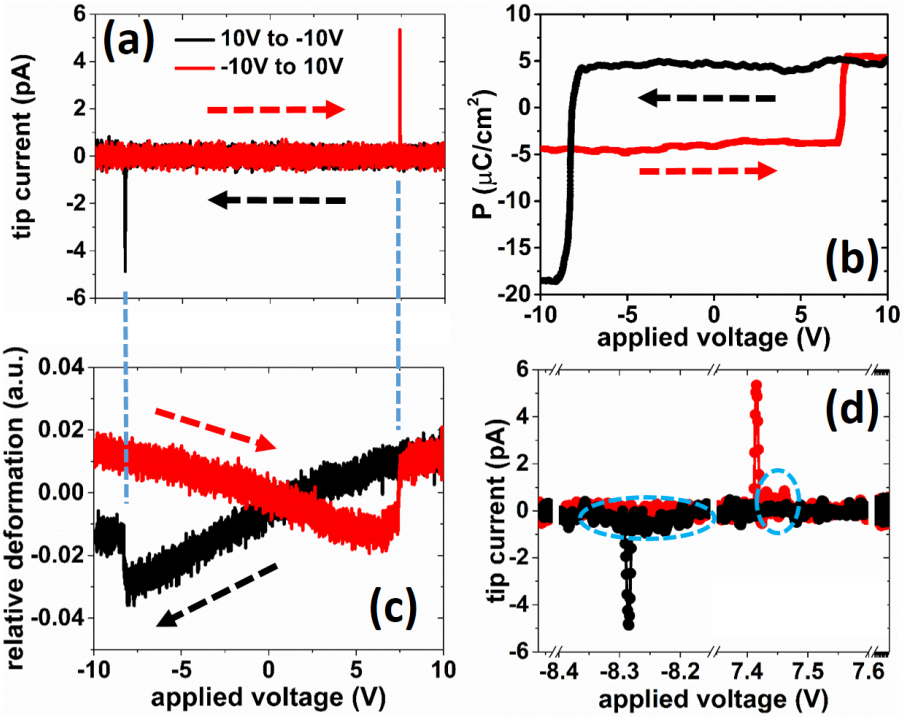


Figure 5.5: Switching current measurements at region indicated in figure 5.4. (a) shows the observed I-V curve with the characteristic current peaks corresponding to polarization switching event. (b) shows the calculated P-V curve, where P is the polarization charge density in $\mu C/cm^2$. The strain response (relative grain deformation) of the grain to the switching event is shown in (c). The sudden jumps in the grain deformation is the characteristics of polarization switching. The synchronization between the currents peaks in (a) and jumps in (c) proves that the current peaks in (a) are indeed due to the switching events. (d) shows a close up view of the I-V plot near the switching current peaks. The dashed circles encircle the regions of tiny but existent current fluctuations near both the current peaks. These fluctuations are signatures of progressive switching of the region due to the continuous nature of the applied voltage ramp. No AC excitation signal was applied during measurement.

The PFM characterizations were performed in the UHV microscopy unit at room temperature in contact mode. The ultra-high vacuum environment and in-situ PFM measurements minimize the presence of impurities that would otherwise spoil the analyses of the measured switching currents. The polarization switching current, and the domain visualization and hysteresis loop measurements were obtained using the standard PFM mode, equipped with a high gain current amplifier stage inside the UHV microscopy unit. The polarization reversal was triggered by applying a voltage ramp to the conductive PFM tip in contact with the nanoscopic region. The switching currents originating from the polarization reversal within the nanoscopic region in the sample were successfully measured as sharp peaks in I-V curves. We

also simultaneously measured the strain response through the deflection of the tip-cantilever assembly caused by the grain deformation upon polarization reversal.

First, to image the ferroelectric domains, an alternating (AC) signal was supplied to the tip from the signal generator and the tip deflection signal from the photodetector was analyzed with the help of a lock-in amplifier to obtain the piezoresponse signal. We scanned the surface to obtain its morphology (figure 5.4 (a)) and the shape of the ferroelectric domains using the PFM phase (figure 5.4 (b), (c)). Then we studied the local ferroelectric switching characteristics of a chosen grain or a nanoscopic region (encircled region in figure 5.4 (a)).

To facilitate the observation of switching currents, we switched off the PFM AC excitation signal to avoid unwanted periodic noise, applied only the DC voltage ramp to the tip and measured the tip current with the help of the current amplifier as a function of applied voltage.

Figure 5.5 (a) shows such an I-V characteristic plot obtained from the aforementioned nanoscopic region after subtracting a linear background (measured I-V curve in the absence of any sample). As it can be seen from the figure, the noise in our I-V measurement lies in the sub-pA range (noise level $\sim 2\times10^{-13}$ A rms). This helped us neatly detect very small values of switching currents originating from nanoscopic regions of the material. Two sharp switching current peaks can be clearly seen as the bias voltage is swept up, then down. Although these peaks are of similar amplitude, their bias position is different. Aside from these switching current peaks, we observed no measurable conduction current of any kind (tunnel, leakage, trapped charges...).

During the I-V measurement, we also simultaneously measured the vertical (normal to the film plane) component of the relative force that is exerted on the tip in contact with the grain. This gave us a direct measure of the grain deformation (strain response) that occurs in synchronization with the polarization reversal process via inverse piezoelectric effect (figure 5.5 (c)). It is evident that the main switch/jump in the grain deformation (figure 5.5 (c)) and the current peaks in figure 5.5 (a) occur at the same voltage, confirming a real polarization reversal.

From figure 5.5 (a) one would conclude that the reversal occurs in one sudden step at the positions given by the peaks in the switching current. However, if we enlarge the scale to focus on the base of the peaks as in figure 5.5 (d), we see that the reversal starts abruptly at $\sim$7.42 V producing a main peak in the switching current, but is complete only at $\sim$7.47 V. Similarly, the peak at $\sim$ -8.28 V is neither an indication for the beginning nor the completion of the reversal. These features are due to the

random character of the reversal, which could be a thermally activated process over energy barriers. As stated in figure 5.1, the switching current is proportional to the rate of polarization changes. A multi-step reversal leads to peaks whose height depends on the reversal rates. This random character is averaged at the macroscopic level but particularly prominent here at the nanoscale.

The switching current can be used to deduce the polarization P of the material. The bias dependence of P is obtained by integrating the current of figure 5.5 (d) over time (each voltage point corresponds to 100µs), divided by the switched area. A switched area of ∼0.103 µm$^2$ was determined from figure 5.4 ((b): before switching and (c): after switching). The as calculated P-V loop is shown in figure 5.5 (b). It can be seen that even though the height of switching current peaks in figure 5.5 (a) are almost the same in both directions of applied voltage, there is a significant difference in the calculated values of polarization for both directions of voltage application.

This discrepancy can be explained by the fact that the value of the measured switching current does not depend only on the area of the switched region but also on the kinetics of the switching process in that region. As the polarization is a time integration of instantaneous current, switching kinetics greatly affects the estimation of its magnitude. On figure 5.5 (d), we see that the peaks are not symmetric: their shapes are different and the peak on the positive bias side spans over a time duration of ∼900 µs whereas the peak on the negative bias side has a larger spread over time with a time duration of ∼1200 µs. (Each data point on the I-V plot corresponds to a time span of 100 $\mu$s which is the time span between two data points for the measurement.)

We believe that a significant portion of the switching current related to the polarization reversal goes undetected because it's below the detection possibilities of our instrument; a gradual reversal can produce a switching current that is buried within the low frequency noise level. In this case, there will be a loss of polarization upon current time integration that will end up with an apparent loss of saturation polarization. Thus, the asymmetry in switching kinetics translates in an asymmetry in the polarization densities in the P-V loops. Kwon et al. also observed a slightly asymmetric polarization charge density that was attributed to the asymmetric junction properties[17]. We show that such asymmetry may also arise from problems related to the current measurements. The maximum value of ∼12 µC/cm$^2$ we obtained for the saturation polarization is thus a lower limit of the real value. This value is 60% less than the reported 30 µC/cm$^2$ value for bulk CA crystals.[2]

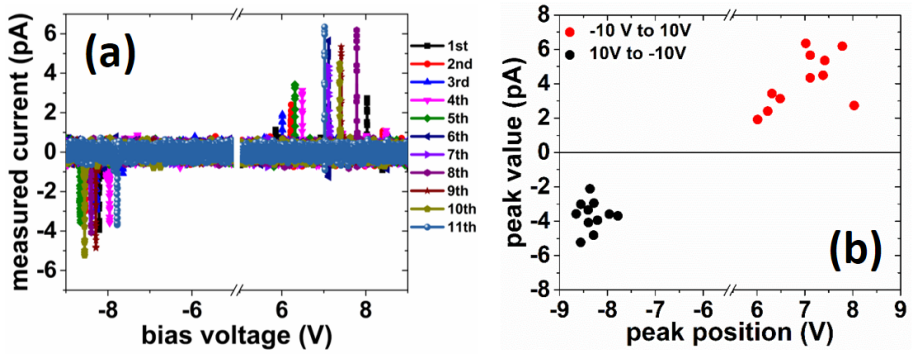


Figure 5.6: Stochastic nature of polarization switching of the region shown in figure 5.4. (a) shows the ensemble of repeated I-V spectroscopies on the same region with experimental parameters unchanged with a time interval of 100 µs between each two successive I-V measurements. Plot labels show the sequence of each measurement. (b) shows a close up view of the plots in (a) near the switching current peaks. (c) shows a scatter plot of the switching current maxima of the I-V curves shown in (a) with respect to applied voltage. The random nature of the distribution depicts the stochastic behavior of the polarization switching process.

If we assume that our grains have the same structure and thus polarization as bulk crystals, the underestimation of the saturation polarization hints at the difficulties to capture the entire switching current at the nanoscale.

To investigate further the stochastic nature of the reversal, we repeated the same measurements eleven times on the same region, keeping all parameters unchanged. The corresponding I-V curves are shown on figure 5.6. We see that the peaks appear at random voltage positions (figure 5.6 (a)). Their height and position are asymmetric with respect to the applied electric field direction for all the reversals (figure 5.6 (a), (b)). It is obvious that a material specific property cannot be deduced from a single measurement; a statistical treatment is necessary. The height and positions of the current peaks visible in figure 5.6 (a) are reported in figure 5.6 (b). Two groups of points are visible, one for negative voltages and one for positive voltages. The corresponding means and standard deviations are (-8.3±0.3 V; -3.7±0.9 pA) and (7.0±0.7 V; 4.2±1.6 pA). There is no significant difference in the mean height of the two groups, but the current peak height has no obvious significance: only the current time integration over the peak expressing the polarization does. The voltage values at which the reversals take place are not symmetric; rather biased towards the negative voltage direction. This shift is probably due to an internal bias field whose magnitude and distribution depend on the composition, microstructure and on the thermal and electrical history of the system.[18] When it concerns the working of a nanoscopic device, the statistical distribution of reversal voltage has to be

considered. For a ferroelectric memory for instance, a high number of experiments must be done to find the required probability to reverse the polarization at a given voltage.

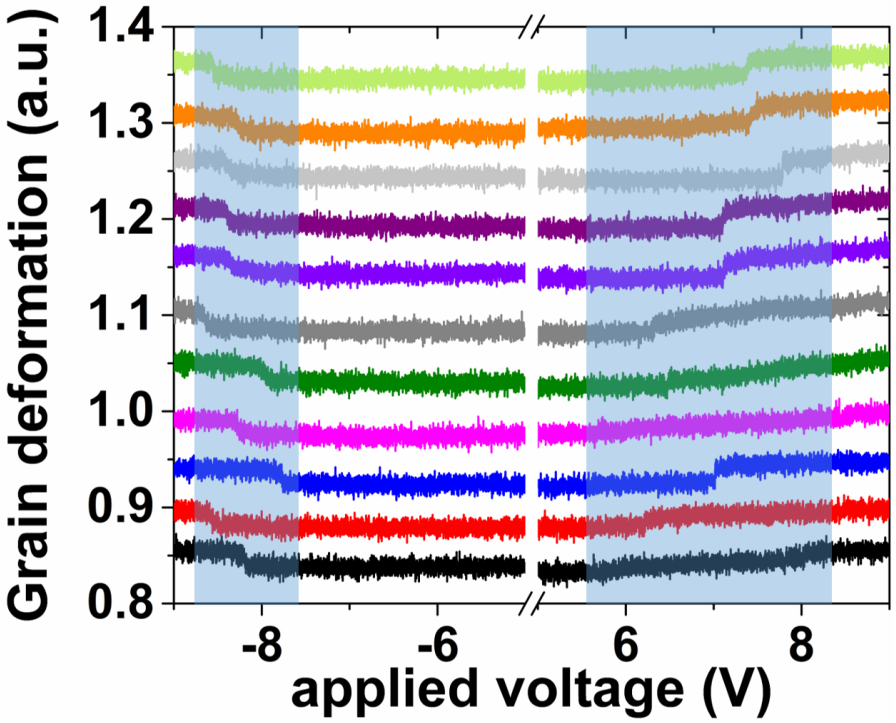


Figure 5.7: Corresponding strain response of switching current spectroscopies as shown in figure 5.6. The sequence of the measurements is from bottom to top. The curves are shifted by an appropriate magnitude for clarity. The blue shades show the ranges of applied voltage over which the grain deformations take place for both directions of applied voltage.

We also looked at the strain response of the ensemble of this spectroscopy measurements. In synchronization with the I-V spectroscopy ensemble (figure 5.6), we see in figure 5.6, that the jumps in the strain response curves occur at the same voltages where the switching current peaks appear, proving that the current peaks are indeed due to the switching events. We also notice that on the negative side of the applied voltage, the spread (blue shade) along the voltage at which a reversal is possible is much narrower than that on the positive side of the applied voltage. This is in agreement to what is observed with the ensemble of switching current peaks. Thus, in terms of the positions of the switching bias, the negative direction seems more deterministic than the positive one. Further, it can be seen that the voltage around which the switching is likely to take place (mean position of the blue shades) is biased towards the negative voltage direction. We also observe that in

some of the spectroscopies, the jumps in the curves corresponding to the reversal events are sharper on the negative side. On the positive side, the jumps are gradual. For example, on the black curve, the jump seems to start at ∼6V and continue till ∼8V, signifying a very gradual switching event and a slower kinetics of reversal.

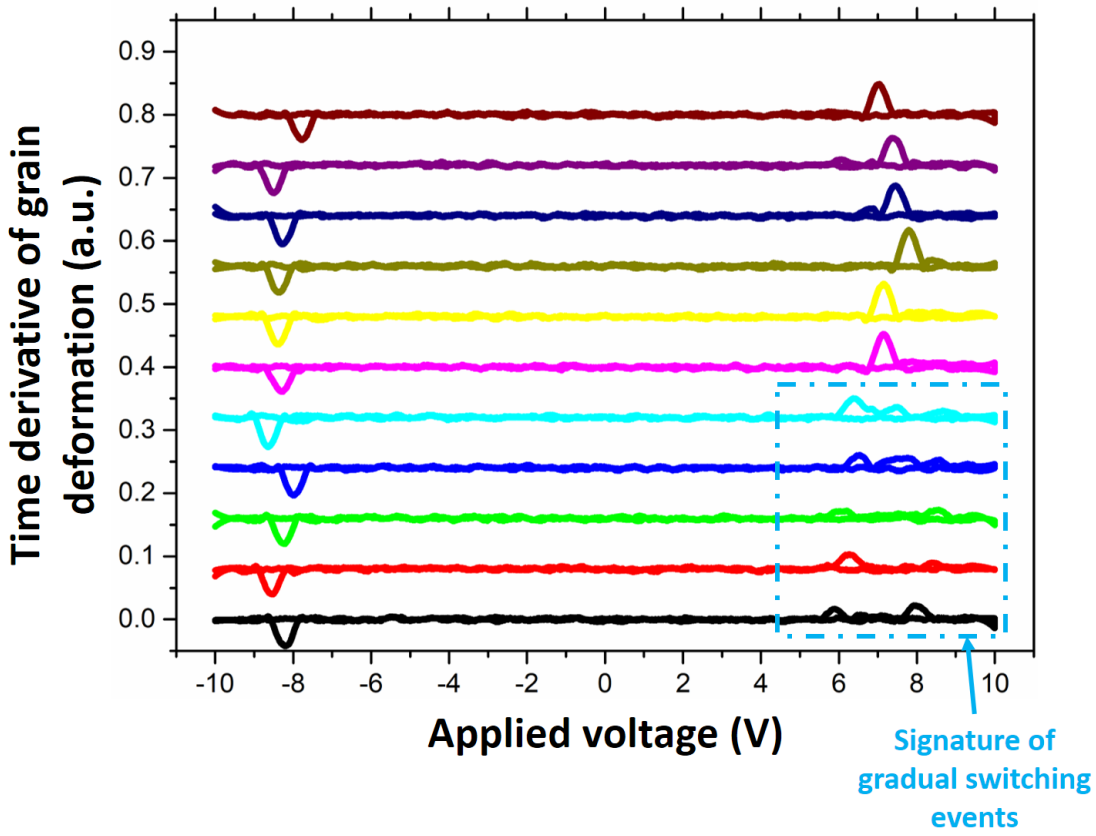


Figure 5.8: First order time derivative of relative grain deformation (strain response) with respect to measurement time for the repetitive spectroscopies ensemble. The derivatives curves are appropriately smoothened. The curves are separated by an appropriate fixed arbitrary value for clarity. The presented curves correspond to a measurement sequence that is from bottom to top. The dashed box indicate the clearly visible broadened peaks due to gradual polarization reversal processes.

To get a clearer view of the effects from the strain response curve ensemble, we plot the time derivatives of these curves, whose backgrounds are smoothened, with respect to the applied voltage. In figure 5.8, the time derivative curves of the corresponding strain response curves in figure 5.7 are shown. It is obvious that a slower or gradual jump in the strain response will result in a broad peak and a sharp jump will result in a relatively narrower peak in the time derivative curves. We clearly observe that on the positive voltage side, there are multiple individual peaks present in one curve (for example on the black curve). Or, it can be said that

the peaks on the positive side are broader. This is consistent with our inference that the reversal kinetics are gradual and slower on the positive voltage direction and there is an asymmetry in the reversal kinetics with respect to the direction of applied electric field.

It is possible that this asymmetry has its origin in the fact that the geometries of the top and bottom junctions, where the top junction is formed by the Pt tip in contact with the grain surface and the bottom junction is formed at the interface of bottom surface of the grain and the Co film underneath, are different. In such a case, it is expected that the asymmetry in reversal kinetics will follow a certain pattern, for example, the slower reversal kinetics should always occur at the positive side of the applied voltage irrespective of the region or grain being studied. However, we have encountered several nanoscopic regions in the same sample where this does not hold true; we observe that the kinetics is slower on the negative side of the applied bias. This suggests that the asymmetry in reversal kinetics could be intrinsic to the nanoscopic region under study and need not necessarily be due to the asymmetry in the geometry of the junctions.

The asymmetry on single measurements can be even more pronounced. On several other grains we have observed, in the switching current spectroscopies, two peaks along one direction of applied electric and a smaller or almost non-existent peak along the other direction (figure 5.9 (a)). But the switching is clearly visible in both directions on the strain response (figure 5.9 (b)). The presence of current peaks corresponds in the strain response to an abrupt jump and their absence to a very gradual jump. Figure 5.9 (c) focuses on the switching mechanism (inside the dashed line in figure 5.9 (b). It is clear that the reversal, when applying a voltage from 10 V to -10 V, is gradual, whereas from -10 V to 10 V it consists mainly of two sharp steps (blue arrows in figure 5.9 (c)) that correspond to the two peaks in the switching current seen figure 5.9 (a). We have a clear evidence that the switching current corresponding to the gradual reversal goes entirely undetected. This is the extreme case of the asymmetric switching kinetics, where, an attempt to deduce the P-V hysteresis loop will result in a complete loss of polarization on one direction (negative voltage side) of applied voltage, making it impossible to obtain a closed hysteresis loop. The reason why there are two switching current peaks on the positive side may have to do with the possibility that the polarization in the entire nanoscopic region is switching in two steps. It is also possible that the region consists of two distinct crystalline grains with distinct coercive field values which switch at separate applied voltages.

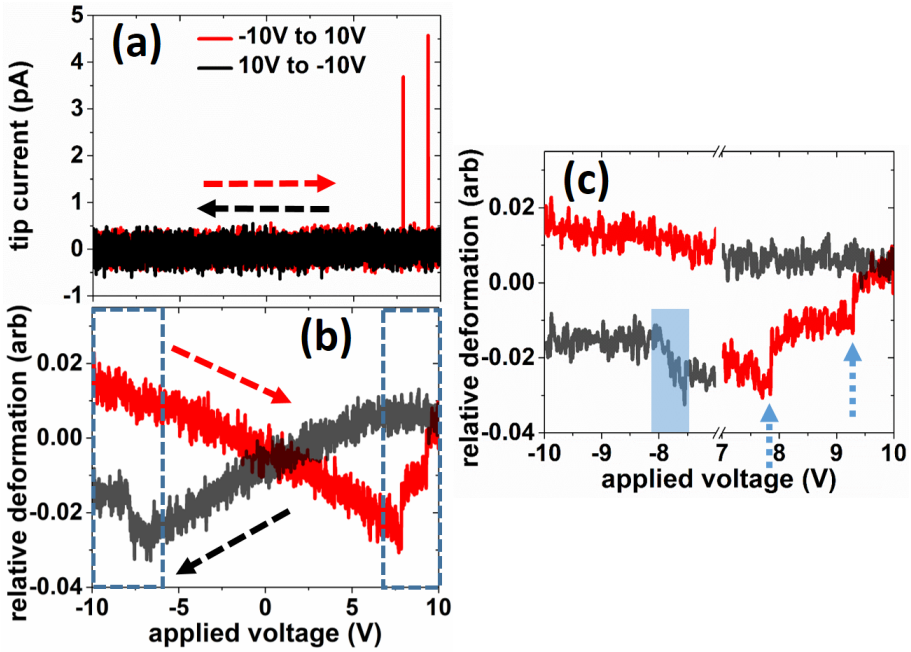


Figure 5.9: Spectroscopic measurements on another typical region/grain. (a) presents the measured I-V curve. Two switching current peaks are present on one side (red), whereas, no peak appears on the other side of applied bias (black). (b) shows the corresponding strain response, i.e. the relative grain deformation during the spectroscopic measurement. Presence of jumps in (b) on both sides of applied bias is an indication of successful polarization switching along both directions of applied field. The absence of switching current peaks on the negative bias side in (a) is attributed to the gradual switching process signified by a smooth jump on the negative side in (b). (c) shows an expanded view of regions marked with dashed rectangles in (b) showing the sharp abrupt jumps on the positive bias side (dashed arrows) and smooth jump on negative bias side (blue rectangular shade).

Further, a hysteresis loop can also be obtained from the PFM signal. To do that, we applied an AC excitation/modulation signal along with DC voltage ramp to the PFM tip in contact with the grain/region and obtained the polarization reversal hysteresis loops (figure 5.10). Note that the loop shown in figure 5.10 is asymmetric; the reversal starts on one side at ∼5 V but at ∼-7 V on the other side and the reversal is more gradual on one side (black curve) than the other (red curve). The fact that the loop is biased towards the negative voltage side is consistent with the switching current spectroscopy results as discussed above. With the PFM signal alone, these features could be attributed to measurements artifacts. This is why, to get more insights into the reversal, we supplemented the PFM hysteresis loop by measuring the switching currents and the grain deformations. It should also be noted that the polarization switching processes take place at different applied biases depending on

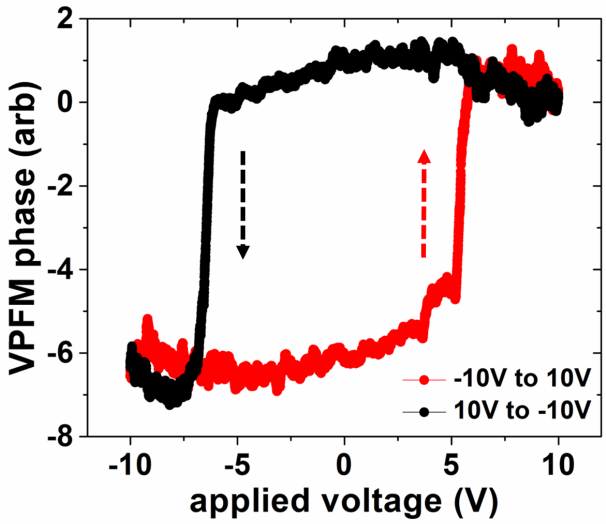


Figure 5.10: PFM characteristic hysteresis loop of the region encircled in figure 5.4. Out of plane/vertical phase (VPFM) data is shown in red/black curves as a function of applied voltage and dashed arrows show the sequence of measurement. The voltage increment step was 0.5 mV with a time lapse of 100 µs between every two voltage measurement points. An AC excitation signal of amplitude 5 V and frequency 5.4 kHz was applied during the spectroscopic measurement.

the presence or absence of the AC excitation signal and its amplitude. This explains the difference in the coercive field values in both cases (∼6 V in the presence and ∼7.5 V in the absence of the excitation signal respectively, compare figure 5.10 and 5.5)[156]. This aspect is discussed in details in the upcoming sections. The voltage position for switching in not symmetric but biased toward negative values, confirming what was observed on the spectroscopy ensemble in figure 5.6.

Nevertheless, it is evident from all the above discussions that polarization switching process along two opposite directions of applied electric field are asymmetric which hints at an asymmetric polarization charge dynamics on the grain surface with respect to the direction of applied electric field. Although the asymmetric contribution to all the above measurements from the asymmetry of top (PFM tip) and bottom (film) interfaces with electrodes should not be ignored, the stochastic behavior and kinetics of the polarization switching, which are more intrinsic to the grain, certainly play a major role in harboring the asymmetry. Keeping in mind all the above points, it is reasonable to say, at the moment, that more detailed experiments are necessary at the nanoscale to understand the surface charge dynamics and the origin of its asymmetry.

Usually, due to poor signal to noise ratio associated with very small values of the switching currents (in femto Ampere range) that originate from nanoscopic ferro-

electric regions such as single nanoscopic grains, it is arduously difficult to measure them with any standard PFM setup but such a measurement could be possible for highly polar materials using standard equipment or by using equipment with ultra-low noise and ultra-high sensitivity. The possibility of measuring switching currents originating from the polarization reversal of nanoscopic ferroelectric regions will certainly pave the way towards understanding of ferroelectric properties at granular level in continuous polycrystalline thin films. More importantly, understanding the associated dynamics and the kinetics of polarization reversal processes at granular level will lead to a better understanding of switching processes in ferroelectric based nanoelectronic devices. Besides, it could emerge as a quantitatively more robust tool for artifact free characterization of ferroelectric materials in the absence of any standard tool for such nanoscopic characterization.

As perspectives, in view of the significance of accessing granular switching currents from small ferroelectric grains, we propose the following method of measurement. Two most important aspects of such a delicate measurement are (i) sharp tip and (ii) low noise high gain current amplifier. A sharp tip reduces the area of effective tip-sample electric field confining to a much smaller region. An atomically sharp conducting tip can be employed to scan the surface morphology in non-contact mode after which the tip can be brought in contact with a specific grain and spectroscopic measurements can be performed. Scanning the surface in non-contact mode will cause minimum damage to the tip before the switching current spectroscopy is carried out. Additionally, the ramp voltage can be replaced by electric voltage pulses with appropriate pulse width and pulse height (pulse amplitude modulated waveform). This will reduce the impact of the electrostatic effects present during the measurements due to the applied DC voltage by facilitating a field-off (no DC voltage) measurement whenever necessary.

## 5.4 Dependence of nanoscopic coercive field on excitation signal amplitude

PFM is a widely used tool and technique to study local ferroelectric properties of materials. However, it is vulnerable to artifacts and influences caused by non-ferroelectric effects. Sometimes non-ferroelectric materials tend to show ferroelectric like hysteresis loops, hampering accurate access to the real ferroelectric nature of newly discovered materials. Therefore, it becomes necessary to test the veracity of

the observed ferroelectric hysteresis phenomena, especially, when the material under study is a less known and a relatively newly discovered ferroelectric. The validation of the observed ferroelectric hysteresis loop measurements can be established by studying the dependence of Coercive field ($E_c$) on the amplitude of the AC excitation or probe signal ($V_{ac}$) which is applied to the sample during a spectroscopic hysteresis loop measurement.[156]

During a spectroscopic hysteresis loop measurement, the role of the DC bias is to initiate the polarization reversal process, whereas, the $V_{ac}$ signal is necessary for the detection of the piezoresponse to obtain the local hysteresis loop of the piezoresponse from the sample. If the amplitude of $V_{ac}$ signal oscillation is faster than the time scales of polarization reversal dynamics, for example, when the reversal dynamics is slow due to pinned domain walls, then it is possible that the polarization reversal dynamics of the ferroelectrics will not get affected by the presence of the excitation signal. However, if the switching dynamics is faster than the $V_{ac}$ frequency then the dynamics responds synchronously to $V_{ac}$ signal and in that case it can be expected that the amplitude of $V_{ac}$ signal will impact the hysteresis loop measurement, as both the DC and the AC signals will contribute equally to the process of polarization dynamics .[156] As the static coercive field (the coercive field without the presence of any AC signal) is specific to the material and does not presumably vary during a spectroscopic measurement, the increase in the $V_{ac}$ amplitude should result in a decrease of the observed coercive field during a spectroscopic hysteresis loop measurement. When the bias is too high, irreversible electrochemical changes might also take place.[157] Usually, a higher $V_{ac}$ amplitude gives a better signal to noise ratio during a spectroscopic measurement. Therefore, for ferroelectric materials with static coercive field values smaller than the minimum $V_{ac}$ amplitude that is required for a decent signal detection, piezoresponse based hysteresis loop measurement procedure may provide misleading information.

The effect of $V_{ac}$ amplitude on the measured nanoscopic coercive fields, more generally, the width of the hysteresis loops as well as on the height of the loops can be clearly seen in figure 5.11 which presents the PFM measurements carried out on PZT based nanocapacitors by Strelcov et al. As it can be seen in figure 5.11, for both the ON-field (non-zero DC bias) and OFF-field (zero DC bias) pulsed DC measurements, the width, thereby, the measured coercive field and the height of the hysteresis loops of total piezoresponse go down with increase in the $V_{ac}$ amplitude. (Details on the above type of applied voltage profile is provided in chapter 3) It can also be noted that for the highest value of signal amplitude, that is 4 V, the

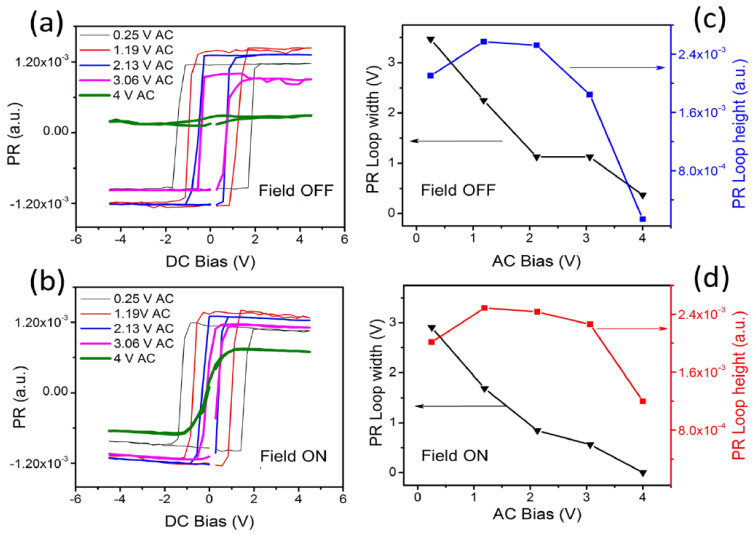


Figure 5.11: Probing signal amplitude dependence of PFM hysteresis loop shape for PZT nanocapacitors. 'PR' represents the entire piezoresponse signal. Figure is taken from reference [156].

hysteresis loop in the ON-field case approaches the super-paraelectric type loop and in the OFF-field case it collapses down to minimum polarization values. This can be explained with the arguments that during the former case, the average polarization state is maintained at some finite value due to the presence of the DC signal, whereas, in the latter case, the polarization reverses repeatedly during the entire measurement and the average polarization becomes zero in the absence of any DC field. Thus, the estimation of the coercive field for a material from the piezoresponse based hysteresis loop measurement is sensitive to the presence of the excitation signal during the measurement.

From figure 5.11, it seems that the only way to detect the most accurate/precise static coercive field with a piezoresponse based hysteresis loop measurment would ideally require switching off the $V_{ac}$ signal, in which case the hysteresis loop measurement itself will not be possible in the first place. On the other hand, the use of a very small amplitude of the $V_{ac}$ signal may result in noisy signal detection due to poor signal to noise ratio, making it difficult to determine the correct coercive field. One way to circumvent the issue is to extrapolate the observed behavior of increase of coercive field with decrease in $V_{ac}$ amplitude to the case of zero $V_{ac}$ amplitude. This may provide some estimation of the accurate $E_c$ value corresponding to the the case of zero $V_{ac}$ amplitude and is called as the static $E_c$ value. However, the extrapolation procedure may not always be linear and accurate without modelling the underlying mechanism of this phenomenon. Adding to the issue, it can also be

seen in the reference [156] that there may not be any global, unique and material independent trend for the excitation signal amplitude dependence of the measured coercive field. The above issue may become even more prominent when the measurement is nanoscopic where the polarization reversal is usually sharper and the hysteresis loops are more rectangular.

In an innovatively smart way, we employed our technique of switching current spectroscopy technique as discussed in the previous section to accurately determine the nanoscopic static coercive fields from the positions of the switching current peaks or from that of the jumps in the strain response curves. As our method of switching current spectroscopy does not require the application of any $V_{ac}$ signal, its effect on the hysteresis loop mesurement is avoided and static coercive field can be obtained. In this section of the chapter, we present the $V_{ac}$ amplitude dependence of the width of the hysteresis loop during the continuous DC ON-field spectroscopic measurements on a nanoscopic region of CA along with our attempt to determine the accurate nanoscopic static coercive field. In our case, as the obtained hysteresis loops are usually biased, the coercive field values are different on the positive ($E_c^+$) and negative ($E_c^-$) directions of the x-axis. Although, the study could focus separately on both these coercive fields, for the sake of simplicity, we studied the width of the hysteresis loop which may be defined as the the difference between the two coercive field values. Further, we report the coercive field values in the units of Volt which simply represents the value of applied DC voltage (not the electric field) at which the polarization reversal takes place.

First, we attempt to measure the accurate static coercive fields of a nanoscopic region of the sample of 50 nm of CA grown on Co (the same sample as studied in the previous section) using our switching current spectroscopy technique with the applied DC voltage profile as shown in figure 5.2 and without applying any AC probing signal. In an ideal case, when the switching kinetics of the nanoscopic region are sharper on both directions of applied voltage, it is expected that there will be sharp switching current peaks on both sides of the applied voltage during a switching current spectroscopy measurement. The precise voltage positions of these current peaks will help determine the accurate values for both the static coercive fields ($E_c^+$ and $E_c^-$). However, in some of the cases, due to asymmetric switching kinetics of the nanoscopic region or due to very small magnitudes of switching currents, it may be difficult to obtain sharp switching current peaks on one or both sides of the applied voltage direction. This makes it difficult to determine the exact voltages at which the polarization switching takes place. In such cases, it is difficult to determine the

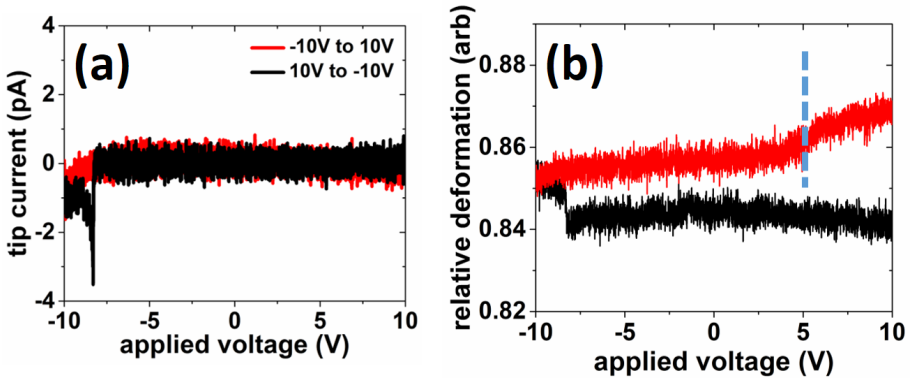


Figure 5.12: Switching current spectroscopy results on the concerned nanoscopic region. No AC excitation signal is applied during the measurement. Gradual reversal kinetics results in the disappearance of switching current peak on the positive voltage side. Dashed line in (b) indicates the approximate voltage position from where the grain deformation starts to take place as visible on the red curve.

exact static coercive field values. Alternatively, the corresponding strain response curve may reveal the exact reversal voltage positions which can be used to estimate more accurate values for both the static coercive fields.

The static measurements that is the switching current measurements on a certain nanoscopic region of the CA film are presented in figure 5.12, where it can be seen that the switching current peak on negative direction of applied voltage appears at -8.3 V and is absent on the positive direction of applied voltage. However, an approximate voltage position on the positive side at which the polarization switching may be occurring is inferred from the jump in the strain response curve (red curve in figure 5.12 (b)) to be 5.1 V. Thus, the nanoscopic static loop width, where loop width = ($E_c^+$ - $E_c^-$), for the probed region as measured directly in the absence of any AC signal can be estimated to be 13.4 V.

Now, for the standard AC spectroscopic hysteresis loop measurements, along with the sweeping DC bias, an AC signal ($V_{ac}$) was also applied whose frequency was kept fixed at 5.4 kHz and hysteresis loops of both the vertical PFM and lateral PFM phase signals were obtained for different values of $V_{ac}$ amplitude. It must be noted that the applied DC sweeping bias profile for this spectroscopy is similar to that illustrated in 5.2 and is different from that used by Strelcov et al.[156] To calculate the width of a loop, we first determine the numerical average of the x co-ordinates of all the data points on the positive (right) ($E_{c,avg}^+$) and negative (left) ($E_{c,avg}^-$) sides or branches of the loop separately. The difference between the averaged x co-ordinate values for the two sides gives the width of the loop, loop width = $E_{c,avg}^+$ - $E_{c,avg}^-$. Similarly, the difference for the averaged y co-ordinate values (arbitrary

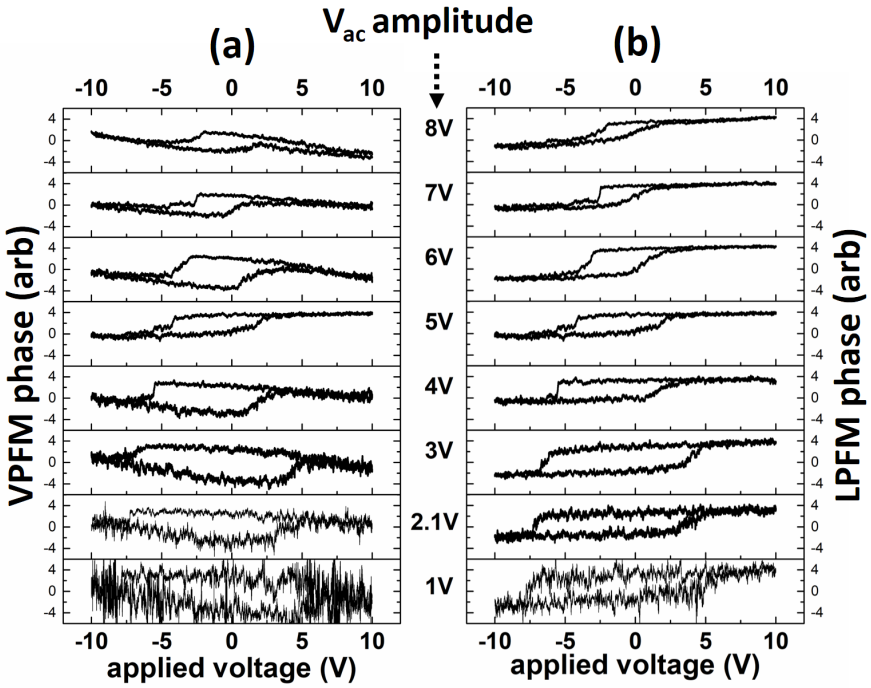


Figure 5.13: PFM phase loops for varying amplitudes of the probing AC signal. (a) and (b) represent the hysteresis loops of VPFM and LPFM phases respectively.

values) of the top and bottom sides or branches of the loop gives the height of the loop. The slopes present in the hysteresis loops are likely to be coming from the DC electrostatic interaction between the cantilever and the bottom conducting surface originating due to the presence of the DC voltage during the measurement.

As presented in figure 5.13 (a) and 5.13 (b), the effect of the probing signal amplitude on the shapes of the hysteresis loops of both VPFM and LPFM is evident. With the increase in the amplitude of $V_{ac}$, we observe a decreasing width for both VPFM and LPFM phase loops. However, the heights of these loops seem to be unaffected by the increment in $V_{ac}$ amplitude unlike in the case decribed in reference [156]. This is expected as our piezoresponse signal consists of only the phase part of the lock-in output and the entire piezoresponse signal consisting of the piezoresponse amplitude is not captured. The amplitude component of the lock-in output signal represents the amplitude of piezoelectric oscillation of the region upon application of an AC voltage which determines the height of a hysteresis loop. If the measured hysteresis loops consisted of the entire piezoresponse signal, the height of the loops would also go down with the increase of the $V_{ac}$ signal amplitude.[156]

The static loop width value from the standard AC spectroscopy mesurements is obtained by extrapolating the straight line fit curve of the hysteresis loop widths

(blue dashed curve) in figure 5.14. The y-intercept of this extrapolation gives the static loop width value. It must be noted that such a procedure can be followed for individual coercive field values and the static $E_c^+$ and $E_c^-$ values can be obtained from the standard AC spectroscopy measurements.

By the above extrapolation method, we obtain a static loop width value of 12.6 V from the LPFM phase loops and 14.04 V from the VPFM phase loops. These values are very close to the static loop width value of 13.4 V measured directly from the switching current spectroscopy method in the absence of any AC excitation signal. The excellent agreement between the directly measured and extrapolated static loop width values is evident in figure 5.14, where the directly measured static loop value is represented as cyan open circles.

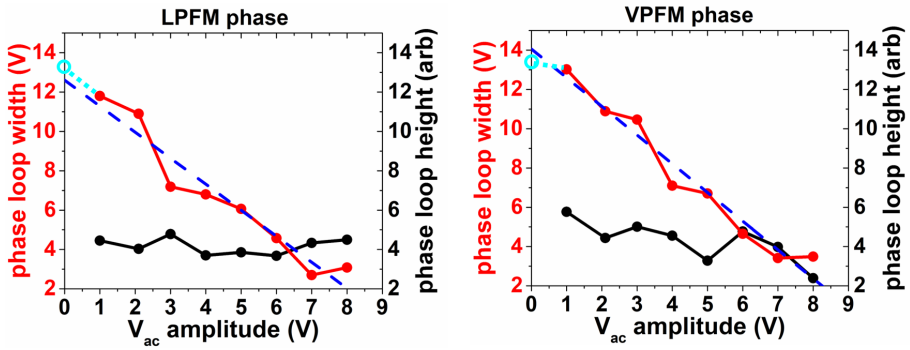


Figure 5.14: Width and height dependence of phase loops on the amplitude of excitation signal ($V_{ac}$). Blue lines are the linear fits to the phase loop widths. The y-axis intercept of the dashed blue line gives the extrapolated value for the twice of the static coercive field value. The cyan coloured open circles represent static loop width value as obtained from the switching current spectroscopy.

Thus, it can be concluded that the variation of the PFM phase loop width and the measured coercive fields with respect to the amplitude of the applied AC probing signal is linear for the nanoscopic regions of CA. This is consistent with what was observed by Strelcov et al[156] for PZT nanocapacitors. Similar observations in the case of CA hints at the fact that the polarization reversal processes at the nanoscale in CA could be of simple 180° type which is consistent with the observed 180° domain walls in chapter 4 and the uniaxial nature of ferroelectric polarization in CA. The dependence of coercive field on AC excitation signal amplitude also establishes the veracity of our PFM hysteresis loop measurements. Moreover, the successful implementation of the switching current spectroscopy to directly measure the static loop width or coercive field without the influence of the presence of any AC excitation signal suggests that it can be a robust method for accurate estimation

of nanoscopic static coercive field.

## 5.5 Semi 3-dimensional mapping of polarization vector at the nanoscale

Commercial applications of ferroelectric thin films usually employ polycrystalline films due to the ease in fabrication and processing. These films consist of polycrystalline grains of certain shape and sizes that depend on the growth parameters. The typical dimensions of such grains may fall in the nanoscopic range of 30-100 nm. However, the crystallographic axes and, thereby, the polarization axes in the grains may be randomly oriented. As the lateral dimensions of ferroelectric devices approach the nanoscopic scale, ferroelectric properties of individual grains or nanoscopic regions play dominant role in determining the overall nanoscopic device response. In this context, it becomes essential to determine the direction of remanent polarizations of nanoscopic regions such as individual grains in a polycrystalline ferroelectric thin film.

The polarization vector of a nanoscopic ferroelectric region is a 3-D vector which can be oriented along any of the eight 3-dimensional quadrants or along any of the three orthogonal axes. During regular PFM imaging, piezoresponse of the region under the tip contain information on the component of polarization vector along only two orthogonal axes directions, essentially, imaging a 2-D map of the polarization vector. To get accurate information on the direction of polarization, it is important to image complete the 3-D map which consists of the information on the polarization vector components along all three orthogonal axes directions. There are certain ways in which PFM can be employed to perform such a mapping and it is called as 3-D vector PFM mapping.

There are two ways in which the 3-D vector mapping of a nanoscopic region and, then eventually, that of the entire ferroelectric surface can be obtained, (a) by obtaining piezoresponse information along the remaining axis direction and (b) by creating a domain wall within a single grain of the film[158]. Method (a) can be carried out by physically rotating the sample under study followed by PFM domain imaging in the same nanoscopic region. However, it may be difficult to perform such a measurement as the measurement setup must allow for such a procedure. Also, it becomes a difficult and time consuming affair to find back the region of interest after a sample rotation. Nevertheless, if PFM domain imaging can be performed

along all three orthogonal directions, the piezoresponse phase and amplitude signals can be used to create an accurate 3-D mapping of the polarization vector.[159]

In method (b), the PFM tip can be used to apply DC voltage locally on a portion of a larger grain to switch a portion of the grain and create a domain wall in a single crystalline grain unit. By analyzing the direction of the created domain wall combined with the PFM hysteresis loops obtained on that particular region of the grain, it is possible to map the polarization vector of that region in the grain accurately.[158]

As a part of nanoscopic probing of CA thin films, we attempt to obtain information on the polarization directions of the nanoscopic regions and, in some cases, of the individual grains. As our measurement setup does not allow for the rotation of the sample, we opt for method (b). However, we were unable to partially reverse the polarization of any grain and, hence, were not successful in creating a domain wall within a single grain. Further, due to the availability of limited number of BNC ports in our setup, we could only capture the piezoresponse phase signals during the PFM hysteresis loop measurements. Thus, the entire piezoresponse could not be captured. Therefore, it was not possible to perform a 3-D vector imaging to accurately determine the polarization directions of the nanoscopic regions. Nevertheless, with the help of accurate imaging of both vertical and lateral phase maps of the region before and after the PFM hysteresis loop measurements, in correlation with the obtained hysteresis loops of the piezoresponse phase, we could successfully determine the direction of that component of the polarization vector which is confined in one of the vertical planes, say x-z plane. This may be called as semi 3-dimensional polarization vector imaging. As no information could be obtained on the component along the remaining axis direction, the exact 3-dimensional mapping of the polarization vector was not possible. However, with the above semi 3-dimensional mapping, we could prove that the polarization vectors of nanoscopic grains of CA are indeed canted with respect to the film plane which is consistent with our observations on the CA films measured ex-situ and as described in chapter 4.

### 5.5.1 Schematics of polarization vector orientation

Before we proceed to the discussion of the schematics of the polarization vector orientation, some assumptions and conventions must be mentioned. Hysteresis loop measurements were carried out with the applied voltage starting from -10V and ramping up to +10V and then ramping back down to -10V. Thus, the -10V and

+10V states of the concerned region are considered as 'unswitched' and 'switched' states respectively of the polarization vector of that region. The -10V to +10V cycle is coloured red and the +10V to -10V cycle is coloured black. 'L' denotes Lateral for LPFM and 'V' denotes Vertical for VPFM. The net polarization vector is denoted by $\wp$ and the its component in a plane is denoted by P. Positive or higher values of VPFM phase and LPFM phase are associated with the orientation along positive z and x axes respectively. Similarly, negative or lower values of these phase signals are associated with orientations along the negative direction of the corresponding axes.

Let us further assume that in the laboratory frame of reference, the vertical direction corresponds to the z-axis and the orthogonal lateral direction along which information is obtained in the PFM experiments corresponds to the x-axis. If no component of the polarization vector $\wp$ lies in the x-z plane, that is the $\wp$ vector is oriented entirely along the y-axis, it would be impossible to obtain any information on the orientation of $\wp$ in the above measurement arrangement. However, in a set of randomly oriented $\wp$ vectors, such a situation would occur very rarely and we never came across such a situation during our experiments on several grains and regions of CA. In all other cases of orientation of $\wp$ in the 3-dimensional space, there will be a component lying in the x-z plane in which case, the above measurement arrangements can be used to obtain partial information on the orientation of $\wp$.

In the x-z plane, the component of $\wp$ vector, P can (i) entirely lie along either the x or z axis or (ii) it can be oriented at an angle with respect to either or the x and z axis.

#### 5.5.1.1 P lies entirely along an axis in the x-z plane

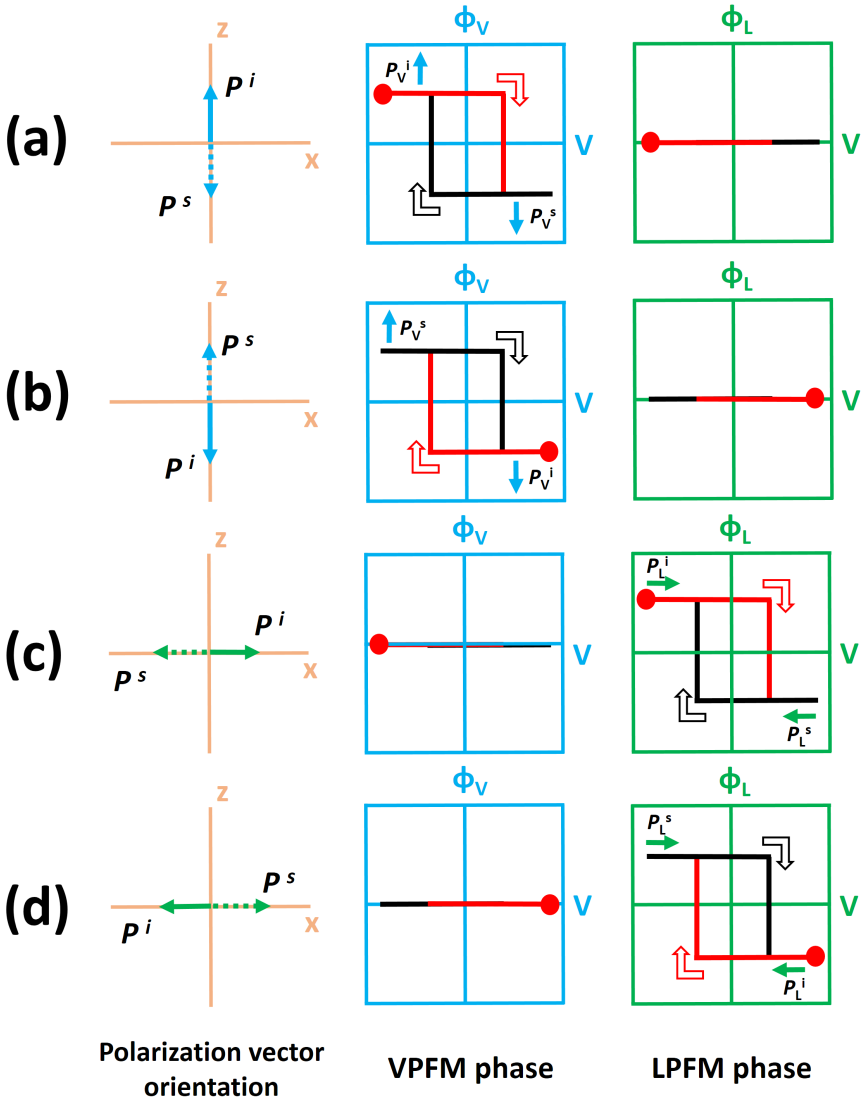


Figure 5.15: Schematics of polarization orientation along one of the axes in the x-z plane and the corresponding hysteresis loop schematics for PFM phase signals. Colours blue and green correspond to VPFM and LPFM components respectively. 'i' and 's' stand for initial and switched states respectively. The red dot in the hysteresis loops signify the beginning of the measurement with the red (switching) and black (back switching) open arrows showing the sequence of applied voltage.

The above two cases are demonstrated in the schematics as shown in figure 5.15 (a) and 5.15 (c) respectively. The reason for the existence of two forms of hysteresis loops for the VPFM phase (figure 5.15 (b)) in the former case and for the LPFM phase (figure 5.15 (d)) in the latter case is the difference between the orientation of the polarization vectors in the initial state . For example, in case of figure 5.15 (a),

the initial polarization direction is along positive z-axis; VPFM phase values traverse from positive to negative values in the first cycle (switching) of -10V to +10V (red curve) and from negative to positive in the next cycle (backswitching) of +10V to -10V (black curve) of the hysteresis loop. In the case of figure 5.15 (b), as the initial direction of polarization vector is along the negative z-axis. Now the applied voltage during the polarization hysteresis must begin from +10V and not from -10V (as indicated by the red dot on the hysteresis loops). Then, the VPFM phase traverses in a way opposite to that described above, thereby, forming a hysteresis loop which looks inverted in the colour scheme. The LPFM phase in both cases do not show any hysteresis loop as there is no component of the polarization vector lying in the x-axis. Similarly, in the cases of figure 5.15 (c) and (d), two colour inverted hysteresis loops are formed for the LPFM phase and no loops for the VPFM phase corresponding to the polarization vector lying entirely along the x-axis.

#### 5.5.1.2 P lies at an angle with respect to an axis in the x-z plane

When the P vector lies in the x-z plane at an angle with respect to one of the axes, say x-axis, there is a component of it that lies along the z-axis and another that lies along the x-axis. Thus, upon polarization reversal, both the VPFM and LPFM phase undergo reversal and give rise to hysteresis loops for both phase signals, unlike in case (i). Again, depending on the direction of the P vector in the x-z plane in the initial state, a total of 4 different forms of hysteresis loops may arise. All these cases are shown in the schematics figure 5.16. For the sake of completion, only two of the cases are described as below.

In the case of figure 5.16 (a), the initial polarization direction (-10V state) is such that its components both along the z and x axes lie along the positive direction and upon polarization reversal, during the first cycle of the hysteresis loop, both the components reverse to the negative directions along the z and the x-axis respectively. Thus, the black curve of the hysteresis loop goes from positive (higher) to negative (lower) values for both the VPFM and LPFM phase loops.

For figure 5.16 (c), the situation is different. The component of initial polarization vector along z-axis is along +ve direction but the component along x-axis is along –ve direction. Thus, upon polarization reversal, the components along z-axis goes from +ve to –ve direction, whereas, that along the x-axis goes from –ve to +ve direction during the first cycle of the hysteresis loop (-10 V to +10V). But in the next cycle (+10 V to -10 V), the reversal of the components takes the inverted paths.

This results in phase hysteresis loops for VPFM and LPFM phases to be opposite to each other in terms of their paths along both the cycles of the hysteresis loop (switching and backswitching). Figures 5.16 (b) and (d) represent an inverse situation to that of figure 5.16 (a) and (c) respectively in terms of the initial orientation of the polarization vector.

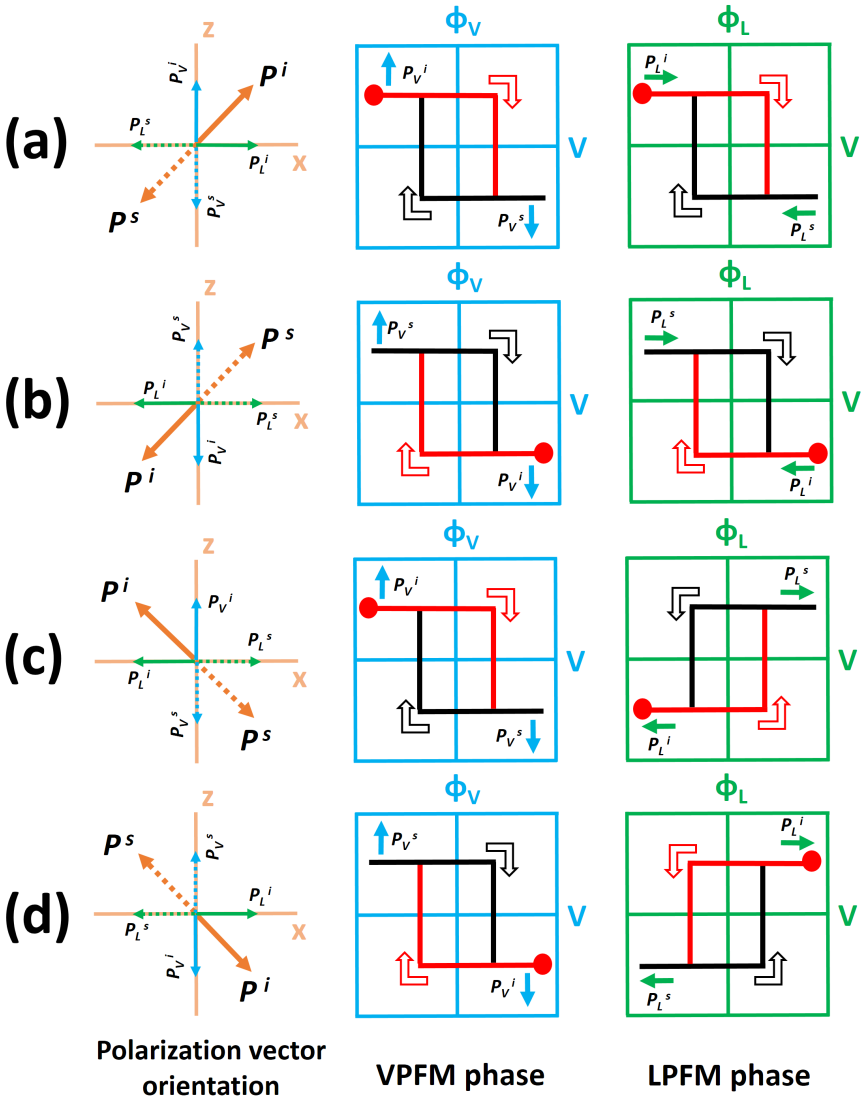


Figure 5.16: Schematics of polarization vector orientated at some angle to one of the axes in the x-z plane and the corresponding hysteresis loop schematics for PFM phase signals. Colours blue and green correspond to VPFM and LPFM components respectively. 'i' and 's' stand for initial and switched states respectively. The red dot in the hysteresis loops signify the beginning of the measurement with the red (switching) and black (back switching) open arrows showing the sequence of applied voltage.

### 5.5.2 Results of semi 3-dimensional polarization mapping

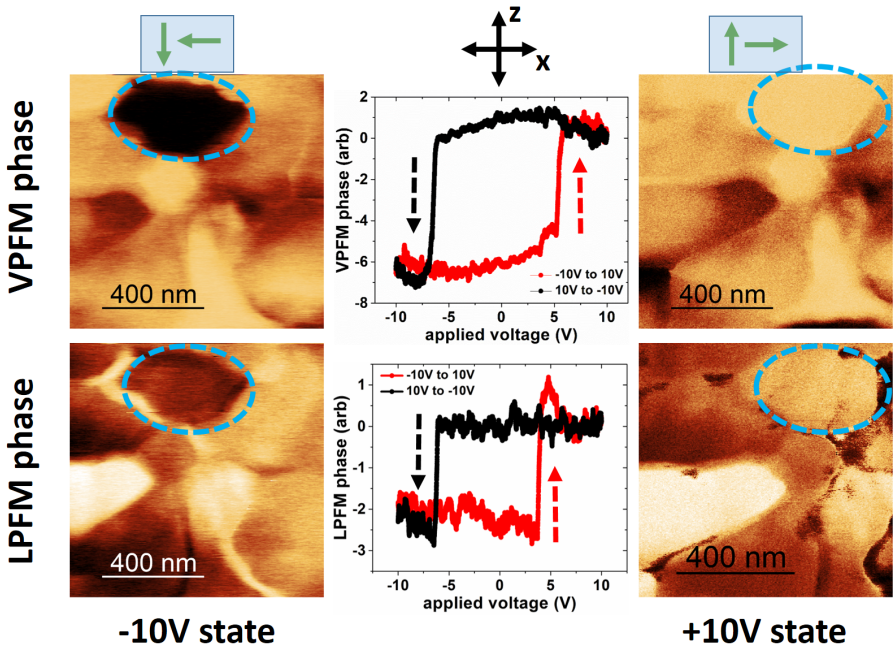


Figure 5.17: Domain maps and PFM phase hysteresis loops of a nanoscopic region with the polarization vector orientation following the schematics of (a)-(b) of figure 5.16. The region of study is represented by the dashed circles. The green arrows on top represent the orientations of vertical and lateral component of the polarization vector in the x-z plane. The PFM hysteresis loops begin from -10 V of applied voltage.

During our PFM measurements on several different grains or nanoscopic regions of CA, we never came across a scenario that resembled case (i) and all the scenarios resembled the case (ii). This is because our PFM signals consist of only piezoresponse phase and not the amplitude. The piezoresponse amplitude signal and the entire piezoresponse signal are sensitive to the angle of inclination of the polarization vector with respect to an axis. The inclination angle influences the amplitude of the piezoelectric oscillation of the grain, thereby, influences the amplitude part of the output from the lock-in amplifier which is proportional to the amplitude of piezoelectric oscillation. Therefore, obtaining hysteresis loops of the amplitude components along with the phase components of the vertical and lateral piezoresponse signals would bring up a more quantitative picture of the polarization vector orientation in the particular plane of concern. If the piezoresponse amplitude signal can be calibrated against some known polarization vector, for example, against a fully out of plane polarization vector, then the exact angle of inclination of any polar-

ization vector in the x-z plane may be determined from the combine information of piezoresponse phase and amplitude signals.

In some cases, we observed nanoscopic regions for which the domain polarization orientation corresponds to (a) and (b) schematics in figure 5.16. The PFM domain maps and hysteresis loops obtained on such a region is demonstrated in figure 5.17. The initial (-10 V state) orientation of the polarization vector in figure 5.17, is along –ve x-axis and –ve z-axis in the x-z plane. This is signified by the dark domains both in the VPFM and LPFM phase maps for the '-10V state'. After the polarization switching of the particular region, in the +10 V state, both the VPFM and LPFM phase maps show bright contrast for the region of study. This corresponds to the direction of polarization vector orienting along +ve z-axis and +ve x-axis in the x-z plane. Correspondingly, the PFM hysteresis loops for a complete switching-backswitching procedure for both VPFM and LPFM phase reveal that the phase changes from lower (-ve) to higher (+ve) phase value during switching (-10 V to +10 V) and vice versa during the backswitching (+10 V to -10 V) of the polarization.

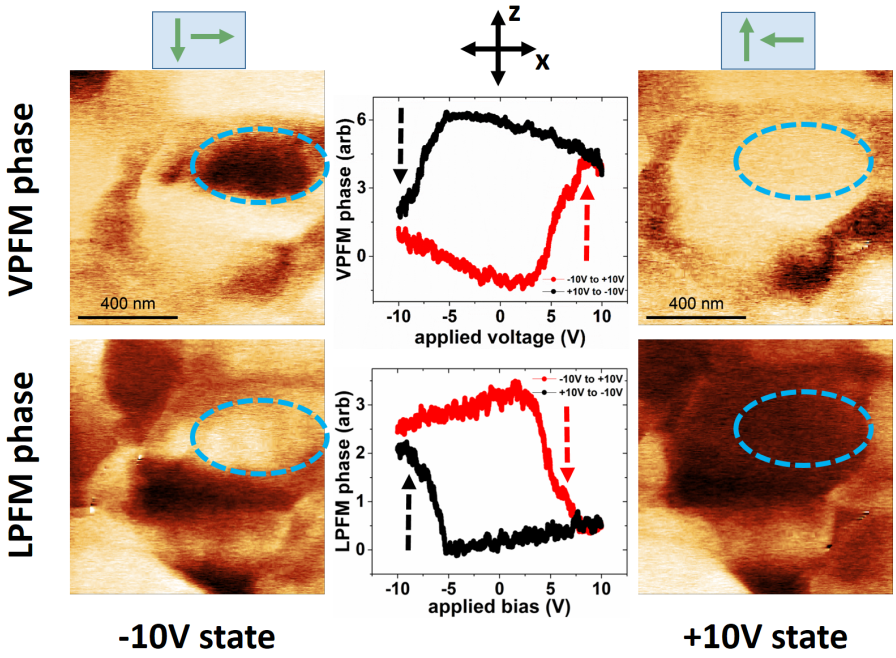


Figure 5.18: Domain maps and PFM phase hysteresis loops of a nanoscopic region with the polarization vector orientation following the schematics of (c)-(d) of figure 5.16. The region of study is represented by the dashed circles. The green arrows on top represent the orientations of vertical and lateral component of the polarization vector in the x-z plane. The PFM hysteresis loops begin from +10 V of applied voltage.

Similarly, for some other nanoscopic regions, we observed that the domain polarization orientation corresponds to the (c) and (d) schematics in figure 5.16. The PFM domain maps and hysteresis loops obtained on such a region is demonstrated in figure 5.18. The initial (-10 V state) orientation of the polarization vector in figure 5.18, is along +ve x-axis and −ve z-axis in the x-z plane. This is signified by the dark domains in the VPFM and bright in the LPFM phase maps for the '-10V state'. After the polarization switching of the particular region, in the +10 V state, the VPFM and LPFM phase maps show bright and dark contrast respectively for the region of study. This corresponds to the direction of polarization vector orienting along +ve z-axis and -ve x-axis in the x-z plane. Correspondingly, the PFM hysteresis loops for a complete switching-backswitching procedure for VPFM phase reveal that the phase changes from lower (-ve) to higher (+ve) phase value during switching (-10 V to +10 V) and vice versa during the backswitching (+10 V to -10 V) of the polarization. However, unlike in the case shown in figure 5.17, the LPFM phase reversal is opposite in manner to that of the VPFM phase. LPFM phase goes from higher (+ve) to lower (-ve) value during switching (-10 V to +10 V) and vice versa during backswitching (-10 V to +10 V).

From the above figures, it may be possible to determine the type of polarization reversal, 90-degree or 180-degree reversal. Without a detailed look, it seems that the polarization reversal is of 180-degree type. However, such an inference is erroneous without the information on the amplitude component of the piezoresponse signal. It is possible that the above PFM phase reversals can take place for certain other 90-degree type of polarization reversal. Nevertheless, as we have observed in chapter 4, that the grains of CA tend to form 180-degree domain walls, we can assume that the observed polarization reversal processes are of 180-degree reversal type.

## 5.6 Partial Conclusions

We probed the nanoscopic ferroelectric properties of the novel organic ferroelectric, Croconic Acid in its thin film form under ultra-high vacuum and in-situ measurement conditions using PFM and switching current spectroscopy methods. We were able to detect the tiny nanoscopic polarization switching currents, in the range of a few pico Amperes, from the surface of Croconic Acid film directly with the probe tip and without the use of any capping electrode. This work is the very first demonstration of detecting nanoscopic switching currents from the surface of any organic ferroelectric material. From the measured switching currents, we could estimate the nanoscopic

polarization values in a Croconic Acid thin film. The polarization value for Croconic Acid was previously known only in its bulk crystal form and our work revealed that the polarization value remains in the same order of magnitude in nanoscopic regions of a thin film as that in the crystals. Although our observed value of polarization of 12 $\mu C/cm^2$ is almost 60% smaller than that reported for CA crystals which is 30 $\mu C/cm^2$, this led us to realize the asymmetric polarization reversal kinetics at the nanoscale which may be partly at the origin of this loss of estimated polarization.

The estimation of polarization value at the nanoscopic scale is a very important step towards establishing the robustness of the observed ferroelectricity in Croconic Acid, considering that scaling effects may have a very negative effect on the ferroelectric properties at smaller dimensions. We demonstrated that the polarization retains the order of magnitude of its value in the nanoscopic region of Croconic Acid films as compared to that observed in macroscopic crystal structures. Further, with the help of switching current spectroscopy, we could estimate the static nanoscopic coercive field for Croconic Acid. Performing the PFM spectroscopic measurements, we could also infer that the polarization vector in a nanoscopic region of a Croconic Acid polycrystalline thin film could be tilted at an angle with respect to the film plane.

# Chapter 6

# Exotic domain-like structures in macroscopic crystals of Croconic Acid

Studies on ferroelectric domain structures, their formation, modification and propagation date back to the 1950s when various optical and electrical characterizations were performed to understand the above ferroelectric features in a number of ferroelectric materials, for example, in single crystals of Barium Titanate (BTO) [15] and Triglycine Sulfate (TGS) [160]. With the advances in engineering and technology in the last several decades, there are numerous sophisticated techniques presently available to characterize ferroelectric domains in much detailed manner. These developments have made it possible to explore varieties of interesting aspects related to ferroelectric domains. Motivation for such explorations is also fueled by the possibilities of future applications that the understanding of ferroelectric domains can lead to.

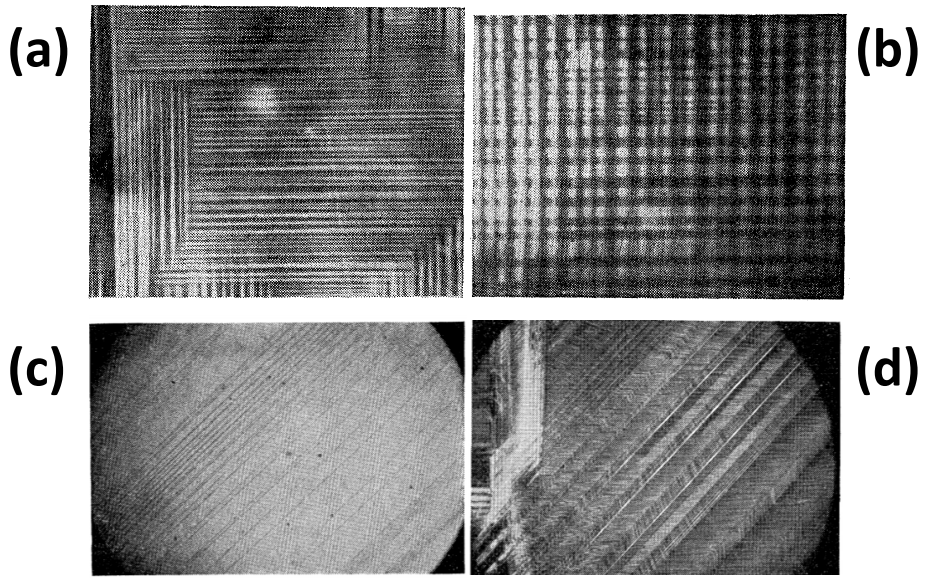


Figure 6.1: Ferroelectric domains in Rochelle salt (a)-(c) and in $KH_2PO_4$ (d) observed optically by polarization microscopy. Figure is taken from reference [161].

There are two interesting aspects related to ferroelectric domains, (i) the polar or domain structure and (ii) the domain wall. In the recent times, both these aspects have gained ever growing attention and have showcased ever expanding repository of interesting phenomena. On one hand, complicated and exotic polar structures in various ferroelectric materials are being discovered and on the other hand, ferroelectric domain walls are emerging as potential feature for applications in future nanoelectronic devices.

The complex interplay of charge and lattice degrees of freedom in low dimensional ferroelectrics have been shown to lead to exotic polar topological structures such as vortex structures[162, 163, 164, 165] and polar skyrmions.[166, 167, 143] Other type

of domain structures that also seem to have promising future device applications are the flux closure and twin domain structures that have been observed in ferroelectric films.[168, 169, 170, 171, 172] Interestingly, such complicated domain structures are also being discovered in organic and organometallic ferroelectric materials.[173, 174] However, as organic ferroelectrics have not been abundant, such observations are not abundant either.

Similarly, due to their significantly different electrical properties in comparison to the bulk properties[175], domain walls have been a fascinating topic of exploration giving rise to the field of domain wall electronics for newer nanoelectronic devices.[176, 177, 178, 179] Further, efforts to dive into the internal structure of domain walls have revealed the existence of unconventional type of ferroelectric domain walls[180], such as Bloch and Neel type and chiral domain walls, in contrast to the traditionally expected Ising type walls.[181]

Croconic Acid seems to be an interesting organic ferroelectric with promising future applications. After it was first synthesized in 2001 by Braga et al[90] and after the discovery of room temperature ferroelectricity in its crystal form in 2010 by Horiuchi et al[1], its macroscopic crystal structure has received significant attention with studies focusing on the origin of ferroelectricity and non-linear and optical properties of the crystals. We have been able to observe some exotic domain-like structures such as twin domain stripes and flux closure type domains on the as-grown macroscopic crystals of Croconic Acid. This chapter focuses on our attempts to characterize and study these domain-like structures using optical and scanning probe methods of characterization towards understanding the origin of the observed domain-like structures. Detailed understanding of the properties and nature of the observed domains and the extension of the approach towards understanding the domain walls may open up paths to explore the so far undiscovered phenomena in organic ferroelectric materials, especially in Croconic Acid.

The experimental method of imaging domains ranges from optical and electrical methods to scanning probe microscopy and x-ray based techniques. Especially for crystals, several different techniques such as electron imaging[182], X-ray topography[183], second harmonic generation[184] have been employed in the past. However, the use of optical polarization microscopy (polarimetry) for ferroelectric domain imaging is relatively a simpler technique, has been in use from the early days and is still in extensive use in spite of the diffraction limit associated with the optical light. For example, the domains patterns in Barium Titanate[185, 15], Rochelle salt and $KH_2PO_4$[161] were observed in the early days using polarization

microscopy and are shown in figure 6.1. It is interesting to see that in figure 6.1two mutually perpendicular sets of parallel stripe domain patterns can be observed to co-exist in Rochelle salt crystals. These two types of domains run along two different crystallographic and optical axes directions but co-exist at the same region.[15]

## 6.1 Growth of Croconic Acid crystals

The macroscopic crystals of Croconic Acid were grown from commercially available Croconic Acid powder (98% pure) from Tokyo Chemical Industries by slowly evaporating the CA powder dissolved in 1N Hydrochloric acid solution at room temperature under atmospheric pressure. By varying the concentration of the solution, different varieties of crystals were obtained. As shown in figure 6.2, these structure of crystals depends on the concentration of the solution. Usually, the crystals are coagulated to form a big lump of crystals stuck around each other. However, at the particular solution concentration of 75 mg/ml, crystallization becomes interesting in terms of the shape of the formed crystals. A lot of well separated smaller sharp crystals appear at this solution concentration. A portion of our studies deal with this type of crystals, thus, we categorize these as type-I crystals. By reducing the concentration to 50 mg/ml, beautifully shaped domain-like patterns arise on the crystal coagulates. We categorize these type of crystals as type-II crystals. With further decrease of the concentration of the solution to 25 mg/ml, it becomes difficult for large crystals to form and a lot of small crystals appear that do not show any intriguing feature.

A white light optical image of type-I crystals are shown in figure 6.3 and figure 6.4. Type-I crystals are almost rectangular and elongated with a typical dimension of 800 µm in length, 200 µm in width and 40-60 µm in thickness and usually have a triangularly shaped domain-like shade within them. In an optical image, such triangular shades appear as green regions. The rest of the regions appear brown. Along with the triangular shade, we also observe two parallel stripe like green shades near the two long edges of the crystals. Some crystals, however, have only one of the two shades, either green or brown.

Further, it should be noted that the type-I crystals resemble partly to the crystals obtained by Horiuchi et al, the comparative view of which is presented in figure 6.5. However, the main difference is the shape of the crystals. Our crystals were always rectangular for both type-I and type-II, in comparison to their hexagonally grown crystals. This indicates that our growth procedure results in crystallographically

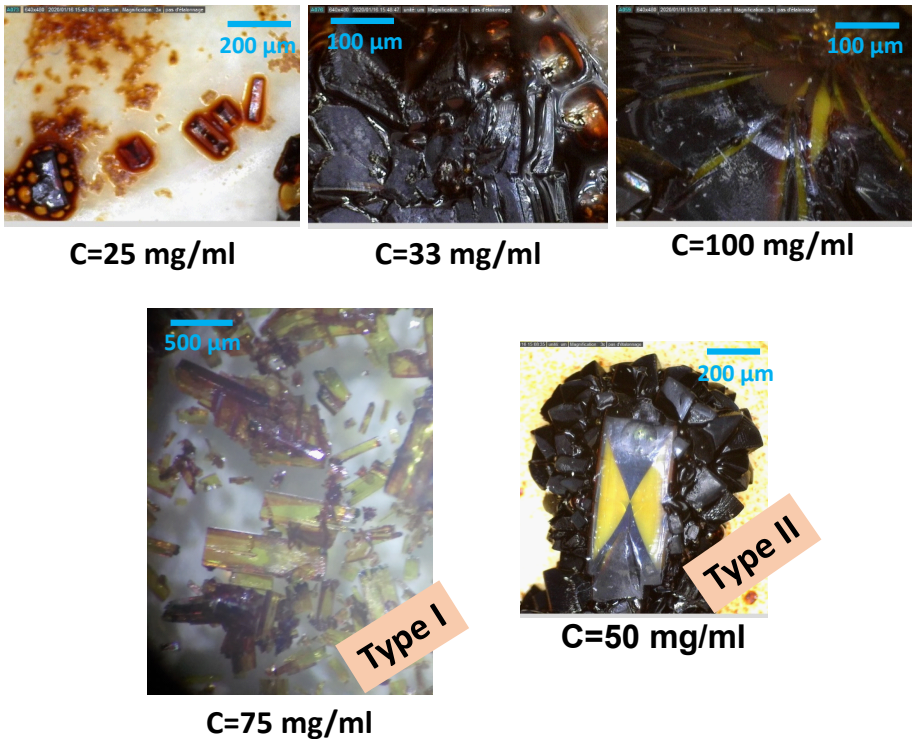


Figure 6.2: Optical images of crystals formed from various solution concentrations. Crystals forming from solution concentration of 75 mg/l and 50 mg/l are categorized as type-I and type-II crystals respectively.


Figure 6.3: Optical image of as grown type-I crystals. Images were taken under white light.

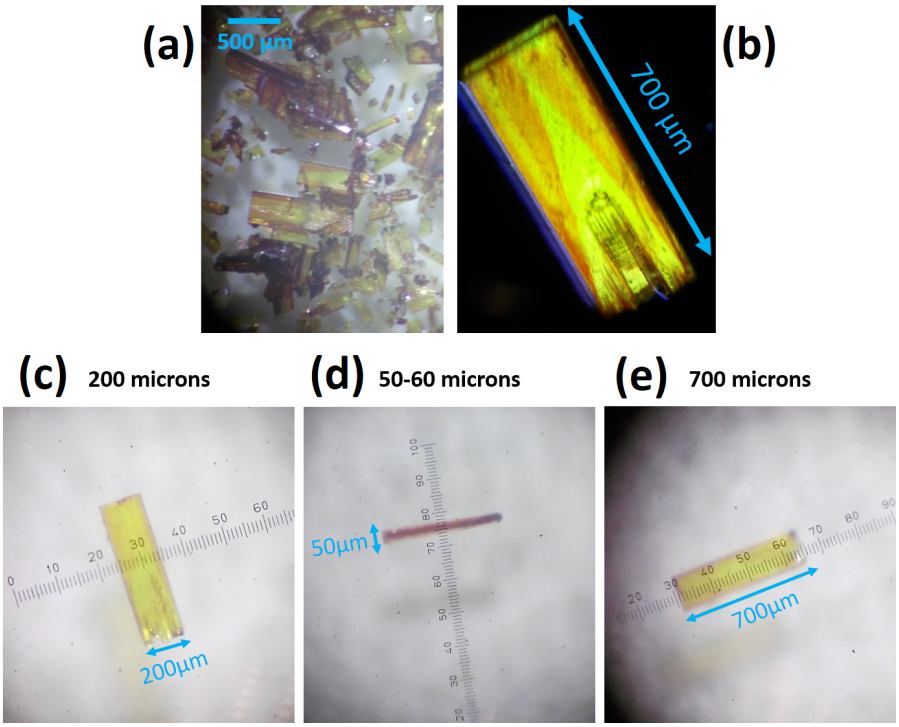


Figure 6.4: Optical images of as grown crystals of type-I with dimensions. The images were taken under white light. (c)-(e) show the dimensions of a typical crystal. The least count of the superposed scale is 20 µm.

different crystals. This may also be the reason for the fact that we observe the domain-like shades in our crystals, whereas, they did not observe any such shades in their crystals.[1]

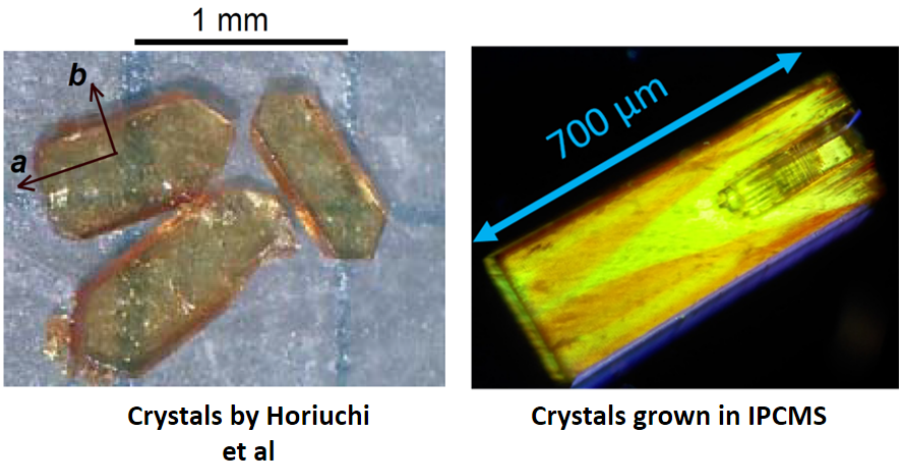


Figure 6.5: A comparative view of optical images of the crystals grown by Horiuchi et al and the type-I crystals grown by us at IPCMS.

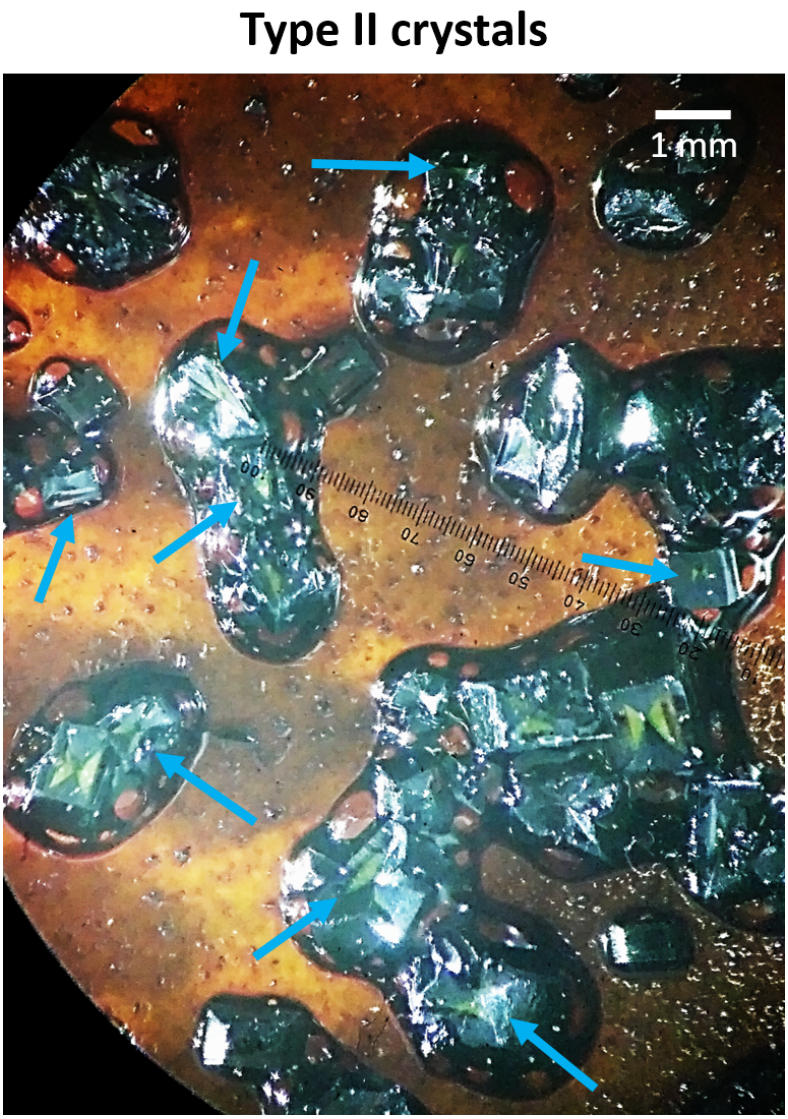


Figure 6.6: Optical image of type-II crystals under white light. The blue arrows point to the hidden crystals which are difficult to see due to their small size or optical shadows from incident light

Similarly, type-II crystals also showed triangularly shaped domain-like patterns, however, these patterns were more exotic. As shown in figure 6.2, two triangular shades (yellow) are connected at the vertices to form a flux closure domain pattern like structure (or butterfly like structure) which has a yellow-black shade under white light. The type-II crystals were more often found to be embedded in the large lump of smaller crystals and were not easily available separately. Thus, it was not easy to measure the dimensions of the type-II crystals. The typical lateral dimension, nevertheless, are approximately $1000 \times 200$ µm$^2$, as seen on figure 6.2.

It must be noted that for both the type-I and type-II crystals, the domain-like

shapes are visible under simpler optical microscope with white light illumination. To make sure that these shades are not due, for example, to some optical effects, we observed the crystals optically at varying angles of incident light. We believe that the shades or the green and brown regions for type-I and yellow-black for type-II may represent as-grown ferroelectric domains formed within the crystal and their shapes depend on the geometry of the particular crystals and also on the growth process. However, to establish that these domain-like shades are indeed ferroelectric domains, sincere detailed characterizations are required, for it is possible that these optically different domain-like structures are merely some chemical features coming up due to certain environmental reasons during the crystal growth, not necessarily having to do with the ferroelectricity in the Croconic Acid crystals.

## 6.2 Characterization of Croconic Acid crystals

### 6.2.1 X-ray Diffraction

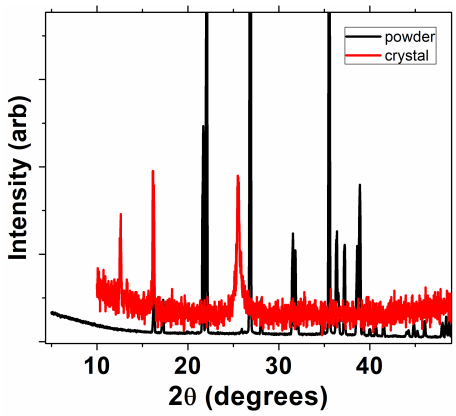


Figure 6.7: Comparison of XRD peaks of type-I crystal to that of the source powder. Wavelength of X-ray used is 1.5406 Å.

First, we carried out X-ray diffraction measurements on type-I crystals to test if the crystals have any particular crystallographic signature. A comparison of the crystal structure obtained from a crystal such as the one shown in figure 6.3 (b) to that obtained from the source Croconic Acid powder reveals the specific crystallographic planes that the crystals possess, as shown in figure 6.7. On several other crystals of this type, we obtained very similar crystallographic results. The important point to note here is that, in figure 6.7, the crystal peak close to $26^0$ is shifted with respect to that in the powder and the peak at $12.5^0$ which is present in the crystal is absent in

the powder. This indicates that the crystallization procedure may have resulted in a new crystalline phase within the crystals which was absent in the source crystalline powder.

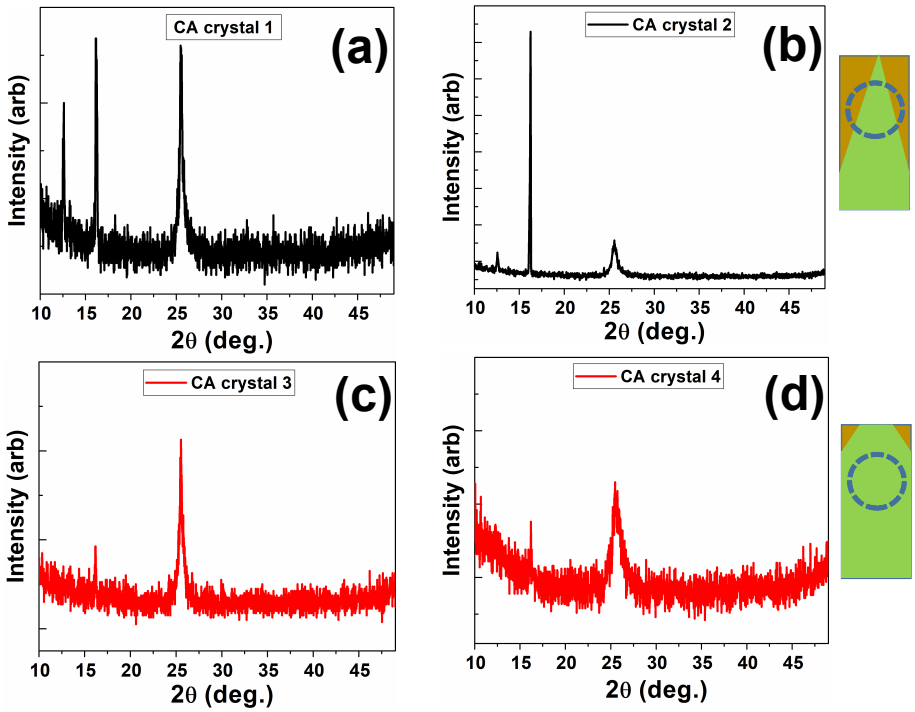


Figure 6.8: XRD studies on type-I crystals. (a) and (b) correspond to two different crystals with triangular domain like shades with x-ray beam focused at a region consisting of both these regions (two domain like crystal). (c) and (d) correspond to two different crystals without any triangular domain like shade (monodomain like crystal). The two schematics on the right demonstrate the difference in the shade patterns of the two classes of type-I crystals used for the XRD measurement with the dashed circle representing the position of the incident x-ray beam on the crystal. Wavelength of X-ray used is 1.5406 Å.

Further, to understand if the domain-like shades in the crystals have any crystallographic features associated with them, we performed XRD measurements on two different classes of crystals of type-I. One of the classes had these triangularly shaped green-brown domain like shades as shown in figure 6.8 and the other didn't have this shade, rather it was entirely green. The difference between the crystallographic behavior is evident in figure 6.8, where we see that the crystalline peaks occurring at $\sim 12.5^0$ ((a) and (b)) in crystals with the two domain-like shades are absent ((c) and (d)) in the crystals which do not have this triangular shade within the region of the incident x-ray beam. This is indicative of the fact that the green and brown zones have distinct crystallographic features associated with them. How-

ever, it is necessary to perform further detailed characterizations to understand the correlation between the difference in the crystallographic features and the difference between the ferroelectric ordering in the two shaded regions.

### 6.2.2 Polarized optical microscopy

We then performed polarized optical microscopy or optical polarimetry measurements in the electromag laboratory of IPCMS on the type-I crystals using the optical polarization microscope. As presented in figure 6.9, optical polarimetry with crossed analyzer-polarizer arrangement clearly shows the triangular domain pattern of the crystals via the image contrast for two separate crystals. Also, profile scans along the line cuts across these domain-like shades show clear jumps in intensity for both crystals (figure 6.10).

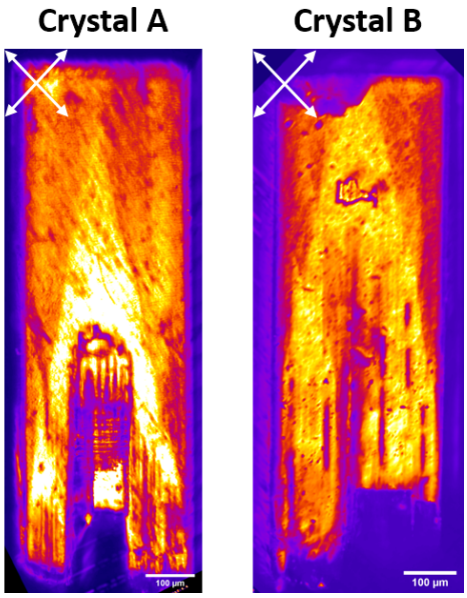


Figure 6.9: Optical polarimetry on two crystals of type-I. The triangular shade can be clearly distinguished due to the variation in the contrast. The crossed analyzer-polarizer schematics is shown in the insets.

Next, we captured the polarimetry images while we rotated the crystals under the polarimetry microscope. The captured images at diffeent angles of sample rotation are shown together in figures 6.11 and 6.12 for both the type-I crystals considered. It can be seen that with the rotation of the crystals, the intensities of the same regions on the crystals vary, starting from almost no intensity at an angle of $0^0$ to reaching a peak of intensity at around $45^0$ and then reaching a minimum at $90^0$ and so on. This variation of intensity of the entire captured frame containing a crystal

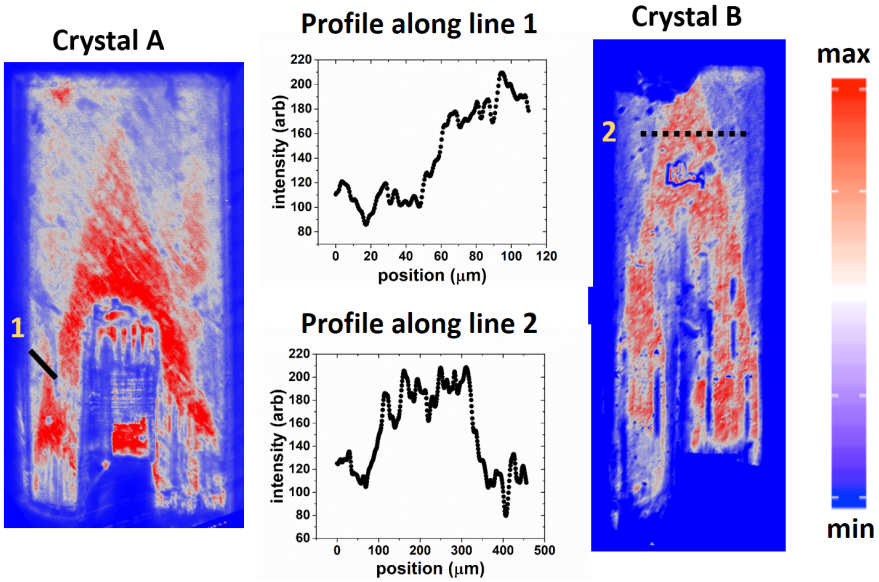


Figure 6.10: Line scans along cuts across domain like shades in optical polarimetry images of two different crystals of type-I.

with respect to the captured frame number is shown in figure 6.11 (b) and 6.12 (b) for crystal A and crystal B respectively. The oscillatory behavior of the intensities as we rotated the crystal samples under the microscope ($\phi$=angle of rotation) is evident for both crystals. Further, it can be seen that, the spread of intensity within one crystal is non uniform at all angles of rotation; intensity from the triangular domain like patterns is clearly more than the remaining areas of the crystals.

The fact that the intensity of the whole crystal varies upon sample rotation under a crossed analyzer-polarizer arrangement suggests that there is some optical activity or anisotropy present in the crystal. As discussed in chapter 3, the appearance of periodic maxima-minima cycles of intensity in a polarized light microscope signifies the presence of an optically anisotropic material. However, the reduction in the maximum intensity at rotation angles of $135^0$ for both the crystals in comparison to that at angles $45^0$ for the respective crystals reduces the height of the second peaks in the intensity variation plots. But this is simply due to the problem of focusing of the camera and has nothing to do with the samples. As the crystal samples could not be placed in such a way that their centers lied exactly on the path of the light being captured by the camera, their rotation resulted in the expulsion of portions of the crystal from the view of the captured frames at certain angles of rotation and as the intensity captured was from the entire frame, this resulted in the difference in the maxima of intensities (at angles of $45^0$ and $135^0$).

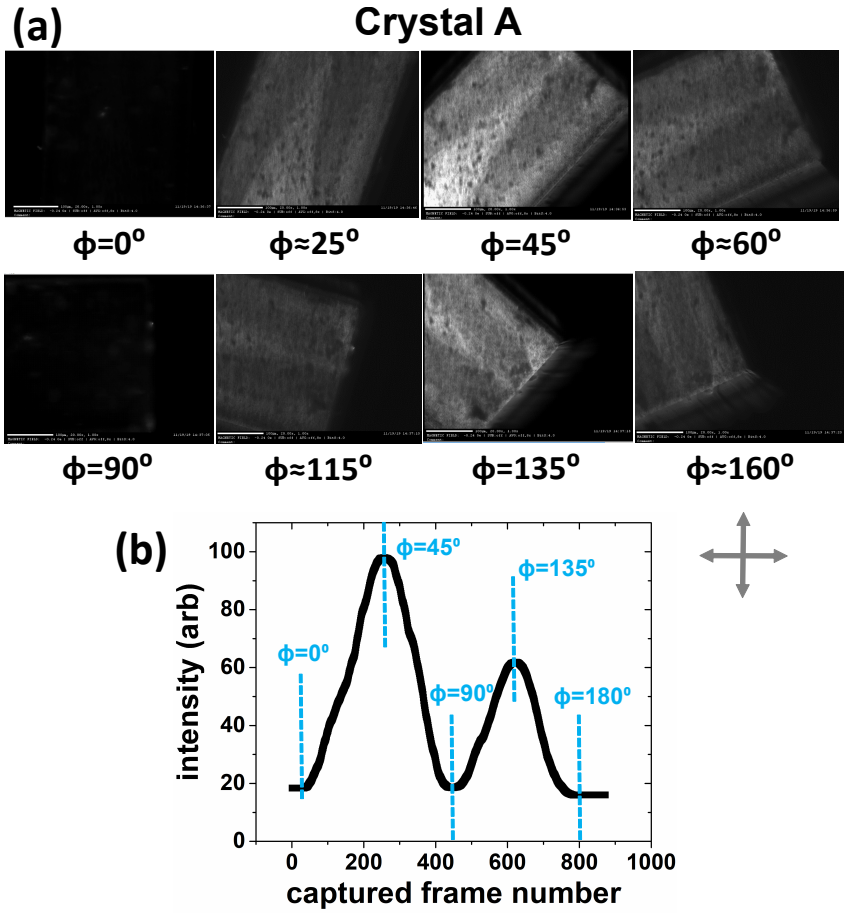


Figure 6.11: Optical polarimetry under crystal rotation for a type-I crystal (crystal A). (a) presents the grey scale snapshots of crystal polarimetric image at different angles of crystal rotation. (b) shows the intensity variation of the images in (a) with respect to the rotation angle. The crossed analyzer-polarizer schematics is shown in the inset. Rotation of the crystal is clockwise about the axis along the thickness of the crystal.

Next, we performed polarimetry studies on a crystal of type-II. As shown in figure 6.13, we observe a flux-closure type domain-like shade represented as orange-purple shade as shown in (a). Figure 6.13 (b)-(e) show the contrast variation of the image for the same crystal at different angles of crystal rotation. Further, we also observe horizontal and vertical stripes in the polarimetry image of figure 6.13 (a). To get a better view into these stripe like patterns, we focus on two regions in the image as enclosed by the dashed boxes and capture images while rotating the crystal, similar to what was done for type-I crystals. These results are presented in figure 6.14 for region 1 and figure 6.15 for region 2. Clear parallel stripes along mutually perpendicular directions (tweed domain structure) can be easily observed for both regions on the sample. Both types of stripes are visible on a single captured

frame only when the sample is rotated at some angle with respect to the analyzer or polarizer, for example, when $\phi$=45$^0$ or 135$^0$. The fact that the visible intensity of the stripes is dependent on the rotation angle of the sample may have to do with the optically active nature of the stripes.

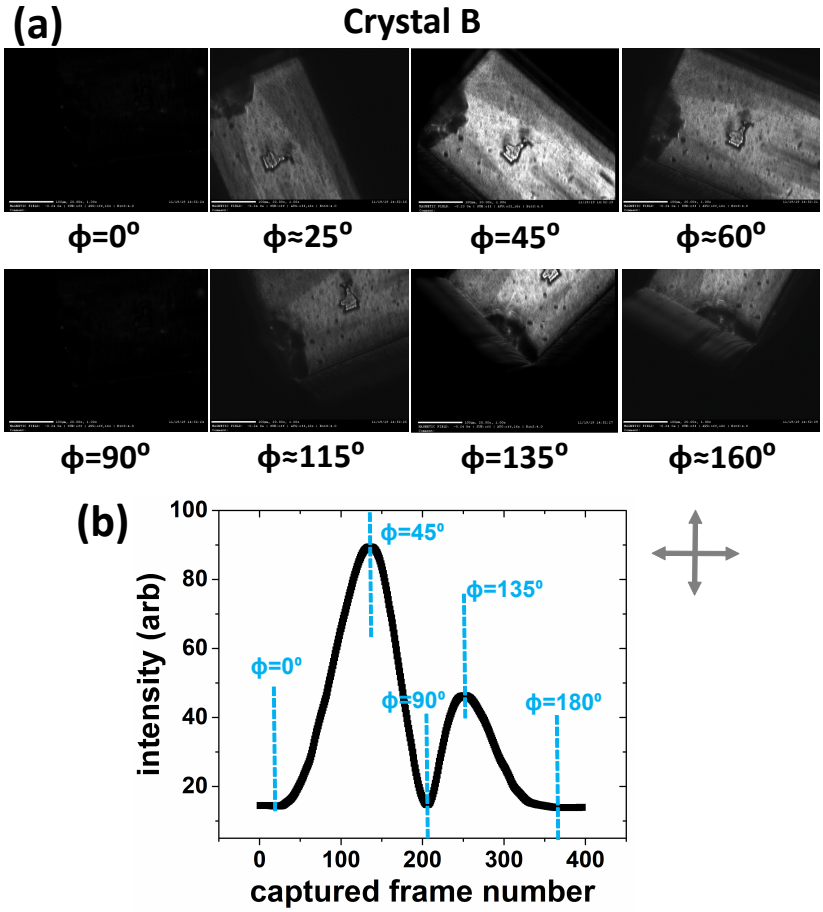


Figure 6.12: Optical polarimetry under crystal rotation a type-I crystal (crystal B). (a) presents the grey scale snapshots of crystal polarimetric image at different angles of crystal rotation. (b) shows the intensity variation of the images in (a) with respect to the rotation angle. The crossed analyzer-polarizer schematics is shown in the inset. Rotation of the crystal is anti-clockwise about the axis along the thickness of the crystal.

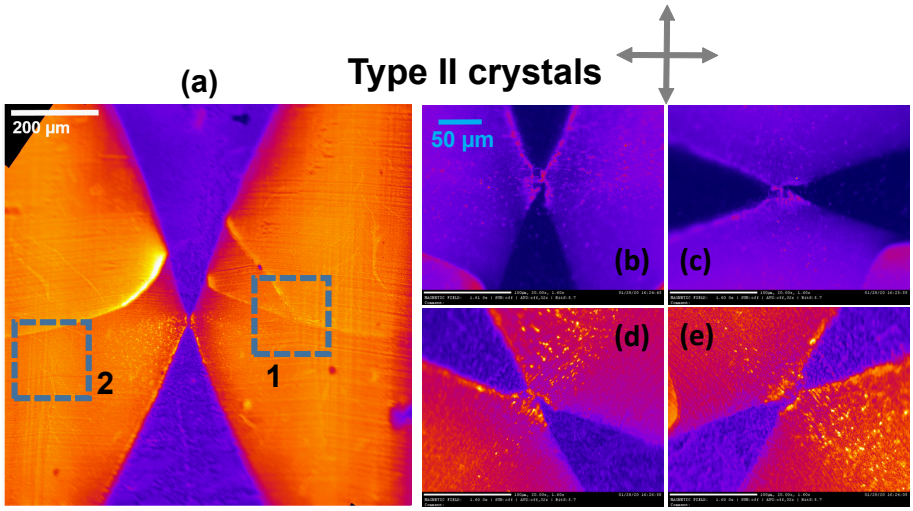


Figure 6.13: Optical polarimetry on a type-II crystal. (a) shows a large scale image and (b)-(e) show images of the same crystal at different rotation angles of the crystal. Dashed boxes represent regions of interest for expanded views shown in upcoming figures.

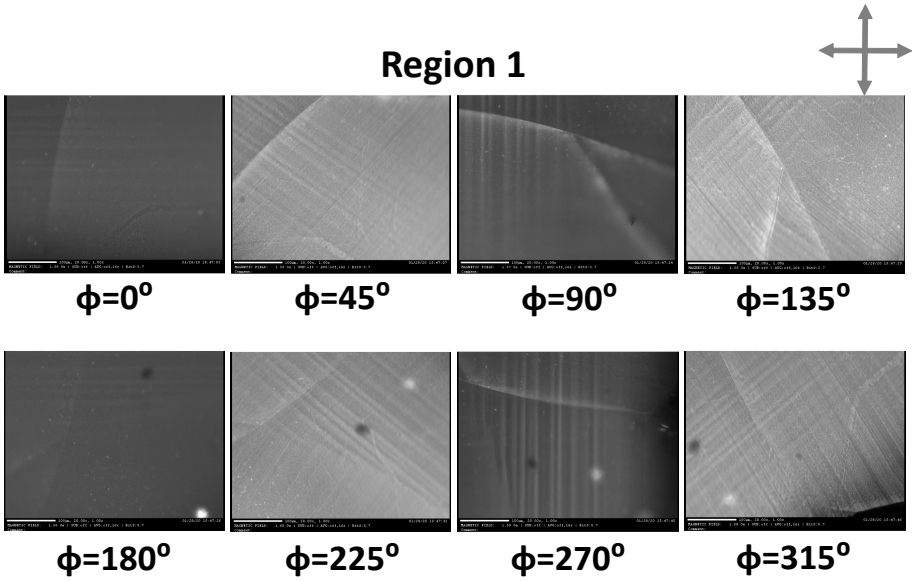


Figure 6.14: Optical polarimetry images of a type-II crystal at region 1 as specified in figure 6.13 (a) for different angles of rotation of the crystal sample. The crossed analyzer-polarizer schematics is shown in the top inset.

We attempted to carry out standard PFM measurements on both types of crystals by performing PFM domain imaging and applying electric poling voltage to specific regions of the crystals, however, due to the large thickness of the crystals, the effective electric field was poor and no contrast was visible, nor was any electric-field induced possible domain reaarangement could be observed. Further,

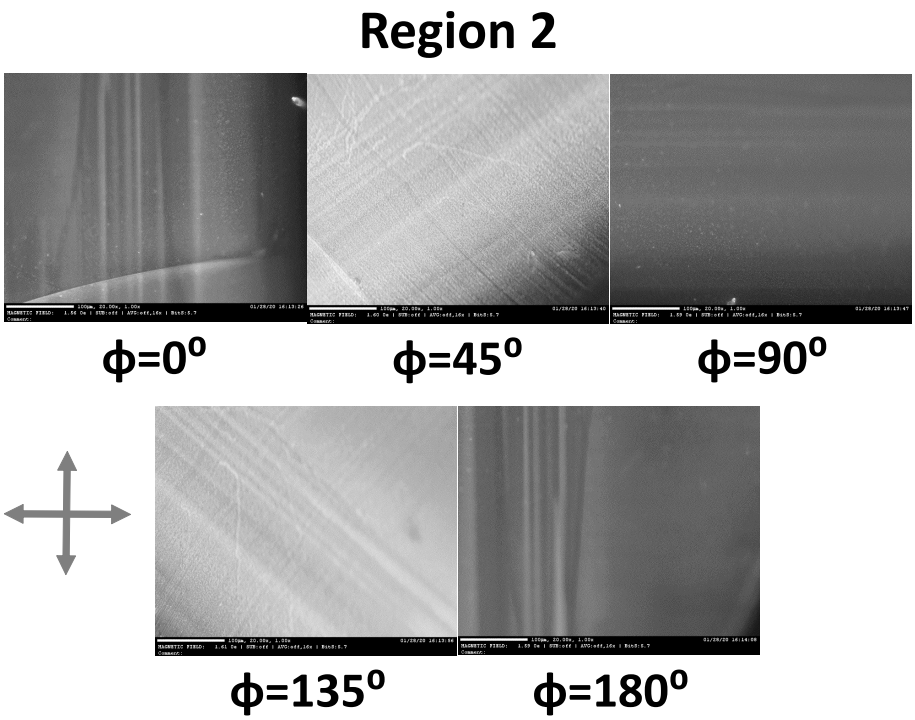


Figure 6.15: Optical polarimetry images of a type-II crystal at region 2 as specified in figure 6.13(a) for different angles of rotation of the crystal sample. The crossed analyzer-polarizer schematics is shown in the top inset.

the impurities and defects present on the crystal surface added to the problems. We inferred that high voltage PFM is necessary to image the domains or electrically probe the domains.

We also carried out surface morphology measurements with Atomic Force Microscopy to investigate the surface structure of these crystals. On type-I crystals, we did not see any morphological features at the boundaries of the optically observed triangular shapes. Similarly, on type-II crystals, we did not observe any features at the boundaries of the butterfly shaped domains. Nevertheless, in region 2 of type-II crystals (as shown in figure 6.13 (a)), we could obtain the surface morphological information. Results of such an attempt is shown in figure 6.16 where we see that the surface morphology consists of intersecting horizontal and vertical stripe like patterns (similar to the tweed domain like structures). Although these patterns should not be compared to what was observed optically, as the regions of study on the samples were not exactly the same and the patterns on the crystal are not uniform at all regions. Also, the optical images may not provide precise details on the dimensions of the observed patterns due to the optical smoothening of captured information. Nevertheless, it is easy to notice the shape correlation between the patterns obtained in AFM morphological scans and the optically obtained images

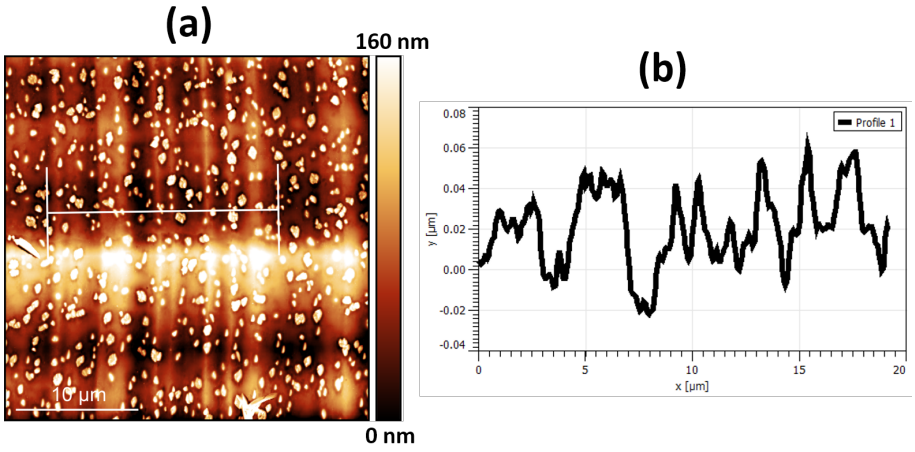


Figure 6.16: AFM imaging on crystal of type-II at region 2 of figure 6.13. (a) shows the surface morphology and (b) is the line profile of the topography along the indicated white straight line in (a).

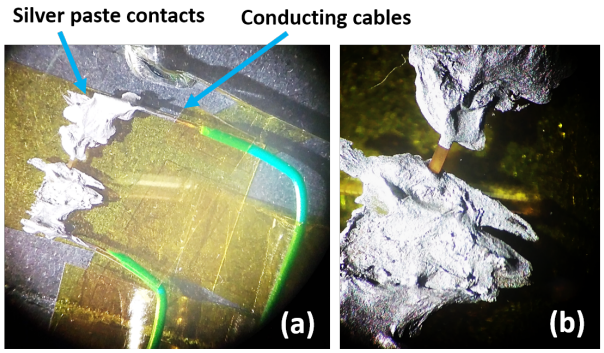


Figure 6.17: Arrangements to electrically pole along the length of the crystal of type-I.

(figure 6.15).

Although the polarization in the crystal is expected to orient along the c-axis, lack of detailed XRD measurement and analysis could not convince us that this axis is necessarily along the thickness of the crystal, thus we attempted to apply high voltage along the length (along b-axis) of a crystal using a high voltage power supply. The arrangements to make contacts with the crystals using silver paste is shown in figure 6.17, where we applied a maximum of 1000 V across the crystal while the crystal was being observed under a polarized microscope. Unfortunately, as we could not go beyond 1000 V with our power supply unit, the length of the crystal was longer for sufficient electric field to be generated along the length. We also attempted to pole the crystals along the c-axis of type-I crystals by applying a maximum of 250 V in the ferroelectric tester setup housed in the electromag laboratory of IPCMS.

This attempt again failed to produce any results as the crystals were too thick along the c-axis and 250 V was not sufficient to generate electric field large enough to reach the coercive field of CA.

## 6.3 Partial conclusions

We have optically observed domain-like patterns on macroscopic crystals of Croconic Acid. These patterns mainly have triangular (type- I), butterfly shapes (type-II) or tweed domain-like structures (type-II). The morphological observation of the tweed patterns with AFM imaging proves the presence of such patterns in type-II crystals and it proves that these patterns are not merely some optical effects. The presence of optical contrast and its dependence on the sample rotation observed under the crossed analyzer-polarizer arrangements of optical polarimetry setup signifies optical activity in both types of crystals.

These optical contrasts may have originated from the ferroelastic nature of the observed patterned structures, meaning that the observed domains may be ferroelastic. As the optical refractive indices of two different ferroelastic domains may be different, the optical intensities of the two domains become different, hence the contrast appears via birefringence. Polarized light microscopy commonly employs this fact to image ferroelastic domains. However, as Croconic Acid is known to be ferroelectric, it is expected that these domain-like structures are ferroelectric as well. This inference on the ferroelectricity of the observed domains cannot directly be drawn from optical observations as it may be possible that this particular phase and the patterns in the crystals are indeed non-ferroelectric but ferroelastic. Although for non-ferroelastic ferroelectric domains the refractive indices could be homogeneous and thereby, generating no optical contrast, observation of such contrast should not be inferred as a consequence of ferroelectricity. Other optical techniques such as Second Harmonic Generation (SHG) imaging or electro-optic imaging microscopy should be employed to directly probe and verify the ferroelectric nature of the domains.[186, 187]

Alternatively, a simpler way to prove the ferroelectric nature of these domain patterns would be to modulate them by applying local electric field. As our methods to electrically probe the crystals and the domain structures remained incomplete due to lack of sufficiently strong electric field, it would not be possible to direct infer on the ferroelectric nature of the observed exotic domain patterns. Thus, we conclude that the observed domains are more likely ferroelastic and as perspective, we plan

to carry our detailed measurements to explore the nature and origin of such domain structures in Croconic Acid crystals. Additionally, applying external strain may also bring changes to these domain patterns which can be another direction of attempts to understand the nature of the patterns.

# Chapter 7

# Conclusions and perspective

Ferroelectricity is one of the most intriguing phenomena in condensed matter science. Even after several decades of discovery of the phenomena in the early 20th century, it continues to intrigue researchers with the regularly unraveling new aspects of the phenomena and their prospects for applications towards solutions of real world problems. With the continuous development in the material synthesis and characterization technologies, it has been possible to explore this phenomenon at its fundamental level of existence. In parallel, it has also been possible to envisage and fabricate many different type of ferroelectric based devices. The area of applications of ferroelectric materials is widespread, spanning various fields such as sensors and actuators, memory devices, nanoelectronics and spintronics, flexible electronics, bio-compatible electronics, energy harvesting and so on.[125, 188, 189, 190, 191, 192] Recently, future directions of applications such as negative capacitance devices, domain wall memory devices and diodes, skyrmionic memory devices, topologically exotic structures, memristor like devices based on ferroelectric materials are also being explored.[193]

Owing to the substantial applications that ferroelectrics already find and the possible future applications, it is imperative to address the issues and limitations that exist with the currently available repository of ferroelectric materials and work towards designing novel ferroelectric materials to counter the challenges. This has motivated researchers to look beyond the existing repository and explore newer ferroelectric materials. A significant portion of this effort is dedicated towards the search and explorations of ferroelectricity in organic materials. As almost all the applications of ferroelectric materials are based on inorganic materials, the research on organic systems is expanding the boundaries of the repository of ferroelectric materials. More importantly, the advantages over inorganic materials that the organic ones bring with them is the most encouraging factor for researchers to study organic ferroelectric systems and for industries to look for their possible applications.

The major concern with the use of inorganic ferroelectrics is related to the presence of toxic elements, for example Pb, Bi etc. Ferroelectrics such as PZT and $PbTiO_3$ are the most commonly used inorganic ferroelectrics and a significant percentage of Pb is a part of their compositions. The excessive use of such Pb-based ferroelectric materials may have negative toxic impact on the environment. With the increase of global environmental awareness, governments of some countries are focusing on the limited use of such materials. This has led to the search for lead-free alternatives not only for ferroelectric materials but also other materials such as photovoltaic ones even within the regime of inorganic elements[194, 195, 196, 197].

Alternatives such as alkaline niobates and barium-titanate-based compositions are being explored in this direction. Similarly, hybrid organic-inorganic structures with ferroelectricity are also being investigated.[198, 199] Pure organic materials, on the other hand, clearly race ahead of all other inorganic materials when it comes to the issue of environmental suitability. This is one of the reasons why organic ferroelectric materials deserve significant attention from the scientific research and industrial community.

Other advantages that organic ferroelectric materials provide over the inorganic ones are their light weight and flexibility. At a time when miniaturization of electronic devices has become the central motive of all type of device fabrication and the world is going towards the usage of 'internet of things' and wearable electronic devices, the above two features are going to play essential roles in the design of practical devices in the near future. Organic ferroelectric materials would prove crucial for the design of such light eight flexible electronic devices. On-going efforts to design new organic materials that possess a combination of properties such as ferroelectricity, piezoelectricity and flexibility are already proving to be fruitful.[200]

Also, the feature that electronic components based on organic materials when integrated into devices provide lower heat generation in comparison to traditional electronic components is a very welcoming one from the device applications point of view.[201, 202] This also implies that the power consumption by the electronic devices is lowered with the usage of organic components, providing us with an efficient usage of energy. Further, the decrease in the heat produced allows for the electronic components and assemblies to adopt complicated designs and structures which would otherwise necessitate challenging cooling mechanisms for the proper functioning of the components and devices.

Further, the fabrication and processing of organic materials in the making of electronic devices is simpler and more cost effective than the inorganic materials. Simpler and inexpensive fabrication methods such as dry casting, spin coating etc. can be employed to fabricate organic ferroelectric devices whereas inorganic ferroelectric devices may need expensive fabrication setups.

Another interesting aspect of organic materials is their bio-compatibility. Organic ferroelectrics may find bio-compatible applications by the virtue of this feature. For example, a very commonly found biological unit named imidazole unit has been shown to be ferroelectric via proton tautomerism mechanism between its proton donor and acceptor sections with a spontaneous polarization value reaching a few $\mu C/cm^2$. Similarly, other biological tissues such as gamma-glycine, which is a

common component of proteins, and aortic walls also are ferroelectric.[203, 204, 205] Further, piezoelectricity and pyroelectricity have been found to exist in several biological systems.[206, 207, 208, 209] Ferroelectricity along with the aforementioned properties found in biological systems, on one hand, can provide an efficient way of early diagnosis of diseases provided the detailed understanding of the biological ferroelectricity is achieved. On the other hand, it provides the exciting future prospective of active bio-electronic human interface devices.

Lastly, organic ferroelectric systems are open to chemical functionalization. The possibility to functionalize an organic ferroelectric system to improve its already existing properties and/or bring out possibly the newer ones, while retaining the original ferroelectric properties, offers the freedom to design organic ferroelectric materials responding to the needs and challenges of different sectors of applications. Supramolecular engineering based approaches are already in progress resulting in the design of new various types of organic ferroelectric complexes which combine more than one possible types of mechanisms that ferroelectricity is originated from.[135] The other major methods of chemical functionalization are the co-crystallization and metal organic framework structures. Co-crystals are defined as crystalline solid units with two or more molecular components present in the same crystal lattice.[210] Co-crystal engineering makes it possible to create novel multifunctional organic materials with targeted properties such as ferroelectricity and ferromagnetic properties or combinations of various properties.[211, 212, 213] Although most of the co-crystal engineering focuses on inorganic systems, organic co-crystals such as that based on H-bonded systems and 2D co-crystals are also being explored recently.[214, 215, 216] Similarly, metal-organic frameworks which utilize metal-organic ligand co-ordination bonds bringing together the advantages of organic ligands and the freedom of inorganic element in tailoring the overall electronic, optical and magnetic properties of the complex is an innovative way to design new organic or molecular ferroelectrics.[217]

Despite all the above advantages, the bottleneck issues with organic ferroelectrics have been the scarcity of stable organic systems with high enough room temperature spontaneous ferroelectric polarization. For a long time, the maximum polarization in any organic systems was stagnant at a value of $\sim$13 $\mu C/cm^2$, the polarization value shown by PVDF-TrFE co-polymer. This is the reason why most of the applications has so far been limited to this polymer based ferroelectric. However, the need for alternative organic ferroelectrics with higher spontaneous polarization is leading to the synthesis and discovery of new organic systems whose polarization

values are at par with some of the inorganic ferroelectric systems. Although pure organic single component molecular Croconic Acid, being one such material whose polarization value exceeds that of some of the inorganic ones, has received a lot of attention in the last one decade after the discovery of its above room temperature ferroelectricity, studies towards the applications of this novel organic ferroelectric material are still in a nascent stage. Further, being one of the few available organic ferroelectric candidates whose vacuum evaporation onto thin film forms is possible which then offers great possibilities to fabricate and study more sensitive interface based device structures and integrate into the UHV fabrication assemblies in commercial fabrication systems, Croconic Acid possesses astounding future prospects for applications in a wide range of fields.

In this thesis, we worked towards realizing the idea that the large spontaneous polarization of Croconic Acid molecules can be capitalized on to create novel efficient multifunctional devices. As such a realization requires adequate understanding of the growth and ferroelectric properties of thin films of the organic ferroelectric, we have focused our attention on certain aspects of these properties, whose understandings are crucial for its future applications in the fields of nanoelectronics and spintronics.

In chapter 4, we show the work towards the room temperature growth optimization of UHV-grown thin films of Croconic Acid with thickness in the range of a few 10s of nanometers. With the help of ex-situ piezoresponse force microscopy, we demonstrated the robust ferroelectric behavior of such films on Co surface and with the help of similar studies on Au surface, we established that ferroelectric properties of Croconic Acid films may be dependent on the substrate material. We also showed that the polarization vector orientation (in-plane and out of plane) in polycrystalline films on Au surface can be modulated by varying the deposition flux rate which can be utilized to the advantage of tuning device properties. The robust ferroelectricity observed on Co surface opens up possible directions of explorations of intriguing spinterface phenomena that could be present at the interface between thin films of an organic ferroelectric and an inorganic ferromagnetic material.[218] Further, our work points along the direction of realizing an organic-inorganic hybrid multiferroic system which can utilize the magnetoelectric effect possibly present at the Co and Croconic Acid interface to allow for the electric control of the magnetic properties of ferromagnetic Co.

As perspectives to these results, the following directions for future research are expected to be pursued. The growth of the thin films can be optimized with the help of electric field guidance during the growth.[106] Low substrate temperature growth

can be performed to increase the surface smoothness and coverage of deposited layers of Croconic Acid. Further, ultra-thin films on Co surfaces can be investigated with scanning probe techniques to understand the influence of the molecular networks on the stability of the observed bulk ferroelectricity in thicker films.

After successful growth optimization for smooth and continuous thin films with ferroelectric properties unhampered, advanced processing methods such as nano-bead processing [219] as developed at the hybrid spintronics laboratory of IPCMS can be adopted to prepare nanojunction based tunnel devices with Croconic Acid layers working as the spacer. Combining this approach with growth of trilayer devices having ferromagnetic electrodes and performing magneto-transport measurements across the tunnel junctions, Croconic Acid based organic MTJ devices can also be realized. On the other hand, to realize the magnetoelectric phenomenon possibly existing at the Co/molecule interface, macroscopic regions of Croconic Acid films grown on Co thin films can be electrically written, following which local magnetic characterizations can be performed to study the impact of ferroelectric polarization on the properties of ferromagnetic substrate films.

In chapter 5, we explored the room temperature in-situ ferroelectric properties of Croconic Acid continuous polycrystalline thin films at the nanoscopic scale. With the help of our novel technique, switching current spectroscopy, we characterized the local nanoscopic regions by directly detecting the ferroelectric switching currents and the piezoelectric strain response originating from the particular nanoscopic regions via a conducting probe tip. We also measured the local thin film polarization value demonstrating, for the first time, that it is in the order of that reported for bulk crystals. By detecting clear switching current peaks on both directions of applied DC voltage, we demonstrated an accurate way of measuring the static nanoscopic coercive field of a ferroelectric material. Further, by performing a semi-3 dimensional mapping of the nanoscopic polarization vectors, we could prove that the polarization vectors are canted at some angles with respect to the plane of the film.

More importantly, our results show that direct detection of tiny polarization switching currents from nanoscopic regions in organic ferroelectric systems is possible with the use of standard probe tips, thereby, paving the way to perform detailed studies on the kinetics and dynamics of the reversal mechanisms in organic ferroelectrics. This is an important step towards ferroelectric characterization at the nanoscale as PFM based characterization may be crowded with artefacts and cross talks and the conventional method of switching current measurement is macroscopic.

As perspectives to the results of this chapter, the shapes of the switching current

peaks can be investigated which can lead to the understanding of reversal kinetics in Croconic Acid. Also, switching current spectroscopy can be performed on isolated grains or nanoscopic regions where the ferroelectric properties will not be influenced by the presence of surrounding grains. Further, advanced probe tips can be employed to probe even smaller nanoscopic areas for the ferroelectric characterization. Similarly, attempts to detect switching currents from atomically thin films of Croconic Acid may reveal 2-dimensional ferroelectric properties of this organic ferroelectric. Moreover, a big ensemble of statistical measurements of the switching currents from a specific region can be obtained to better understand the stochastic reversal behavior of a nanoscopic ferroelectric regions.

In chapter 6, we presented the studies performed on the macroscopic crystals of Croconic Acid where the newly observed domain like patterns in these crystals were characterized by optical means. Although our attempts to characterize the patterns to prove their ferroelectric nature remained incomplete and inconclusive, we nevertheless believe that the observed domain like patterns have some type of ferroelectric character associated with them. This can be investigated by modulating the domain like patterns by electrical (for ferroelectricity) or mechanical means (for ferroelasticity). Besides, advanced characterization methods such as SHG imaging, micro-Raman microscopy and Microwave Imaging Microscopy (MIM) can be employed to characterize the observed domain like patterns in the macroscopic crystals of Croconic Acid. If the domain like patterns indeed turn out to be ferroelectric, the macroscopic crystals can be smartly used to explore the magnetoelectric aspect of the work which can be done, for example, by depositing Co thin films on the flat surfaces of the crystals and performing local magnetic characterizations on them.

To conclude, this thesis is being prepared at a time when, on one side, due to the increasing demand for organic ferroelectric systems, research is intensifying on the quest for newer all organic ferroelectric materials and on the other side, studies on already available candidates with high spontaneous polarization like Croconic Acid are not abundant. We believe that this work will bring insight into the possibility of considering this novel organic system for possible future applications and encourage researchers working on topics related to ferroelectric thin films to drive their attention towards the prospects of Croconic Acid and organic ferroelectrics in general as well. Furthermore, with the expertise of our group in organic spintronics, interface science and surface supported molecular systems, we expect to explore the multifunctional aspect of this organic ferroelectric to realize electrically controllable active molecular spinterfaces.[220]

# Bibliography


[1] S. Horiuchi, Y. Tokunaga, G. Giovannetti, S. Picozzi, H. Itoh, R. Shimano, R. Kumai, and Y. Tokura, "Above-room-temperature ferroelectricity in a single-component molecular crystal," *Nature*, vol. 463, pp. 789–792, Feb. 2010.

[2] S. Horiuchi, K. Kobayashi, R. Kumai, and S. Ishibashi, "Proton tautomerism for strong polarization switching," *Nat Commun*, vol. 8, p. 14426, Apr. 2017.

[3] M. Mura, A. Gulans, T. Thonhauser, and L. Kantorovich, "Role of van der Waals interaction in forming molecule-metal junctions: flat organic molecules on the Au(111) surface," *Phys. Chem. Chem. Phys.*, vol. 12, pp. 4759–4767, Apr. 2010. Publisher: The Royal Society of Chemistry.

[4] J. R. Reimers, M. J. Ford, S. M. Marcuccio, J. Ulstrup, and N. S. Hush, "Competition of van der Waals and chemical forces on gold–sulfur surfaces and nanoparticles," *Nat Rev Chem*, vol. 1, pp. 1–13, Feb. 2017. Number: 2 Publisher: Nature Publishing Group.

[5] N. Sändig and F. Zerbetto, "Molecules on gold," *Chem. Commun.*, vol. 46, pp. 667–676, Jan. 2010. Publisher: The Royal Society of Chemistry.

[6] D. A. Kunkel, J. Hooper, S. Simpson, G. A. Rojas, S. Ducharme, T. Usher, E. Zurek, and A. Enders, "Proton transfer in surface-stabilized chiral motifs of croconic acid," *Phys. Rev. B*, vol. 87, p. 041402, Jan. 2013.

[7] J. Hooper, D. A. Kunkel, E. Zurek, and A. Enders, "Interplay between Hydrogen Bonding, Epitaxy, and Charge Transfer in the Self-Assembly of Croconic Acid on Au(111) and Ag(111)," *J. Phys. Chem. C*, vol. 119, pp. 26429–26437, Nov. 2015.

[8] R. Sawada, H. Uemura, M. Sotome, H. Yada, N. Kida, K. Iwano, Y. Shimoi, S. Horiuchi, and H. Okamoto, "Large second-order optical nonlinearity

in a ferroelectric molecular crystal of croconic acid with strong intermolecular hydrogen bonds," *Appl. Phys. Lett.*, vol. 102, p. 162901, Apr. 2013.

[9] K. Iwano, Y. Shimoi, T. Miyamoto, D. Hata, M. Sotome, N. Kida, S. Horiuchi, and H. Okamoto, "Ultrafast photoinduced electric-polarization switching in a hydrogen-bonded ferroelectric crystal," *Physical review letters*, vol. 118, no. 10, p. 107404, 2017.

[10] X. Jiang, H. Lu, Y. Yin, X. Zhang, X. Wang, L. Yu, Z. Ahmadi, P. S. Costa, A. D. DiChiara, X. Cheng, A. Gruverman, A. Enders, and X. Xu, "Room temperature ferroelectricity in continuous croconic acid thin films," *Appl. Phys. Lett.*, vol. 109, p. 102902, Sept. 2016.

[11] E. Fatuzzo and W. J. Merz, "Switching Mechanism in Triglycine Sulfate and Other Ferroelectrics," *Phys. Rev.*, vol. 116, pp. 61–68, Oct. 1959.

[12] E. Fatuzzo, "Theoretical Considerations on the Switching Transient in Ferroelectrics," *Phys. Rev.*, vol. 127, pp. 1999–2005, Sept. 1962.

[13] L. Pintilie, I. Vrejoiu, D. Hesse, G. LeRhun, and M. Alexe, "Ferroelectric polarization-leakage current relation in high quality epitaxial Pb(Zr,Ti)$O_3$ films," *Phys. Rev. B*, vol. 75, p. 104103, Mar. 2007.

[14] B. Nagaraj, S. Aggarwal, T. K. Song, T. Sawhney, and R. Ramesh, "Leakage current mechanisms in lead-based thin-film ferroelectric capacitors," *Phys. Rev. B*, vol. 59, pp. 16022–16027, June 1999.

[15] W. J. Merz, "Domain Formation and Domain Wall Motions in Ferroelectric $BaTiO_3$ Single Crystals," *Phys. Rev.*, vol. 95, pp. 690–698, Aug. 1954. Publisher: American Physical Society.

[16] D. Lee, S. M. Yang, T. H. Kim, B. C. Jeon, Y. S. Kim, J.-G. Yoon, H. N. Lee, S. H. Baek, C. B. Eom, and T. W. Noh, "Multilevel Data Storage Memory Using Deterministic Polarization Control," *Advanced Materials*, vol. 24, no. 3, pp. 402–406, 2012.

[17] O. Kwon, D. Seol, D. Lee, H. Han, I. Lindfors-Vrejoiu, W. Lee, S. Jesse, H. N. Lee, S. V. Kalinin, M. Alexe, and Y. Kim, "Direct Probing of Polarization Charge at Nanoscale Level," *Advanced Materials*, vol. 30, no. 1, p. 1703675, 2018.

[18] V. Koval, G. Viola, and Y. Tan, "Biasing Effects in Ferroic Materials," *Ferroelectric Materials - Synthesis and Characterization*, July 2015.

[19] J. Li, Y. Liu, Y. Zhang, H.-L. Cai, and R.-G. Xiong, "Molecular ferroelectrics: where electronics meet biology," *Phys. Chem. Chem. Phys.*, vol. 15, pp. 20786–20796, Nov. 2013. Publisher: The Royal Society of Chemistry.

[20] S. Mishra, L. Unnikrishnan, S. K. Nayak, and S. Mohanty, "Advances in Piezoelectric Polymer Composites for Energy Harvesting Applications: A Systematic Review," *Macromolecular Materials and Engineering*, vol. 304, no. 1, p. 1800463, 2019.

[21] M. Ichikawa, T. Gustafsson, and I. Olovsson, "Is NaNO2 a pure order–disorder type ferroelectric?," *Solid State Communications*, vol. 123, pp. 135–139, July 2002.

[22] J. Valasek, "Piezo-Electric and Allied Phenomena in Rochelle Salt," *Phys. Rev.*, vol. 17, pp. 475–481, Apr. 1921. Publisher: American Physical Society.

[23] J. Valasek, "Piezo-Electric Activity of Rochelle Salt under Various Conditions," *Phys. Rev.*, vol. 19, pp. 478–491, May 1922. Publisher: American Physical Society.

[24] H.-Y. Ye, Y.-Y. Tang, P.-F. Li, W.-Q. Liao, J.-X. Gao, X.-N. Hua, H. Cai, P.-P. Shi, Y.-M. You, and R.-G. Xiong, "Metal-free three-dimensional perovskite ferroelectrics," *Science*, vol. 361, pp. 151–155, July 2018. Publisher: American Association for the Advancement of Science Section: Research Article.

[25] Y. Murata, K. Tsunashima, N. Koizumi, K. Ogami, F. Hosokawa, and K. Yokoyama, "Ferroelectric properties in polyamides of m-xylylenediamine and dicarboxylic acids," *Japanese journal of applied physics*, vol. 32, no. 6B, p. L849, 1993. Publisher: IOP Publishing.

[26] J. W. Lee, Y. Takase, B. A. Newman, and J. I. Scheinbeim, "Ferroelectric polarization switching in nylon-11," *Journal of Polymer Science Part B: Polymer Physics*, vol. 29, no. 3, pp. 273–277, 1991. Publisher: Wiley Online Library.

[27] A. C. Jayasuriya, S. Tasaka, T. Shouko, and N. Inagaki, "Ferroelectric behavior in fluorinated aliphatic polyurethanes," *Polymer journal*, vol. 27, no. 2, pp. 122–126, 1995. Publisher: Nature Publishing Group.

[28] M. Khatun, E. Kabir, and M. Rahman, "A review on polymer and organic ferroelectrics for flexible high energy storage material," in *AIP Conference Proceedings*, vol. 2142, p. 040014, AIP Publishing LLC, 2019. Issue: 1.

[29] V. K. Thakur and R. K. Gupta, "Recent progress on ferroelectric polymer-based nanocomposites for high energy density capacitors: synthesis, dielectric properties, and future aspects," *Chemical reviews*, vol. 116, no. 7, pp. 4260–4317, 2016. Publisher: ACS Publications.

[30] L. Ruan, X. Yao, Y. Chang, L. Zhou, G. Qin, and X. Zhang, "Properties and Applications of the $\beta$ Phase Poly(vinylidene fluoride)," *Polymers*, vol. 10, p. 228, Mar. 2018. Number: 3 Publisher: Multidisciplinary Digital Publishing Institute.

[31] S. Kasap, *Springer handbook of electronic and photonic materials*. Springer Science & Business Media, 2006.

[32] A. J. Lovinger, "Ferroelectric Polymers," *Science*, vol. 220, pp. 1115–1121, June 1983. Publisher: American Association for the Advancement of Science Section: Articles.

[33] A. J. Lovinger, "Recent developments in the structure, properties, and applications of ferroelectric polymers," *Japanese Journal of Applied Physics*, vol. 24, no. S2, p. 18, 1985. Publisher: IOP Publishing.

[34] W. J. Hu, D.-M. Juo, L. You, J. Wang, Y.-C. Chen, Y.-H. Chu, and T. Wu, "Universal ferroelectric switching dynamics of vinylidene fluoride-trifluoroethylene copolymer films," *Scientific reports*, vol. 4, p. 4772, 2014.

[35] X. Chen, X. Han, and Q.-D. Shen, "PVDF-Based Ferroelectric Polymers in Modern Flexible Electronics," *Advanced Electronic Materials*, vol. 3, no. 5, p. 1600460, 2017.

[36] J.-H. Bae and S.-H. Chang, "PVDF-based ferroelectric polymers and dielectric elastomers for sensor and actuator applications: a review," *Funct. Compos. Struct.*, vol. 1, p. 012003, Mar. 2019.

[37] Y. Tokura, S. Koshihara, Y. Iwasa, H. Okamoto, T. Komatsu, T. Koda, N. Iwasawa, and G. Saito, "Domain-wall dynamics in organic charge-transfer compounds with one-dimensional ferroelectricity," *Phys. Rev. Lett.*, vol. 63, pp. 2405–2408, Nov. 1989. Publisher: American Physical Society.

[38] P. García, S. Dahaoui, P. Fertey, E. Wenger, and C. Lecomte, "Crystallographic investigation of temperature-induced phase transition of the tetrathiafulvalene-p-bromanil, TTF-BA charge transfer complex," *Phys. Rev. B*, vol. 72, p. 104115, Sept. 2005. Publisher: American Physical Society.

[39] S. Horiuchi and Y. Tokura, "Organic ferroelectrics," *Nature Materials*, vol. 7, pp. 357–366, May 2008. Number: 5 Publisher: Nature Publishing Group.

[40] K. Kobayashi, S. Horiuchi, R. Kumai, F. Kagawa, Y. Murakami, and Y. Tokura, "Electronic Ferroelectricity in a Molecular Crystal with Large Polarization Directing Antiparallel to Ionic Displacement," *Phys. Rev. Lett.*, vol. 108, p. 237601, June 2012. Publisher: American Physical Society.

[41] S. Horiuchi, K. Kobayashi, R. Kumai, N. Minami, F. Kagawa, and Y. Tokura, "Quantum ferroelectricity in charge-transfer complex crystals," *Nature Communications*, vol. 6, p. 7469, June 2015. Number: 1 Publisher: Nature Publishing Group.

[42] F. Kagawa, S. Horiuchi, H. Matsui, R. Kumai, Y. Onose, T. Hasegawa, and Y. Tokura, "Electric-Field Control of Solitons in a Ferroelectric Organic Charge-Transfer Salt," *Phys. Rev. Lett.*, vol. 104, p. 227602, June 2010. Publisher: American Physical Society.

[43] J.-i. Kishine, T. Luty, and K. Yonemitsu, "Ferroelectric phase transition, ionicity condensation, and multicriticality in charge-transfer organic complexes," *Phys. Rev. B*, vol. 69, p. 075115, Feb. 2004. Publisher: American Physical Society.

[44] A. Moreac, A. Girard, Y. Delugeard, and Y. Marqueton, "The neutral-to-ionic phase transition of TTF-CA: a Raman and infrared study versus temperature at atmospheric pressure," *J. Phys.: Condens. Matter*, vol. 8, pp. 3553–3567, May 1996. Publisher: IOP Publishing.

[45] E. Collet, M.-H. Lemée-Cailleau, M. B.-L. Cointe, H. Cailleau, M. Wulff, T. Luty, S.-Y. Koshihara, M. Meyer, L. Toupet, P. Rabiller, and S. Techert, "Laser-Induced Ferroelectric Structural Order in an Organic Charge-Transfer Crystal," *Science*, vol. 300, pp. 612–615, Apr. 2003. Publisher: American Association for the Advancement of Science Section: Report.

[46] Z. G. Soos, "Identification of dimerization phase transitions driven by Peierls and other mechanisms," *Chemical Physics Letters*, vol. 440, pp. 87–91, May 2007.

[47] S. Horiuchi, F. Ishii, R. Kumai, Y. Okimoto, H. Tachibana, N. Nagaosa, and Y. Tokura, "Ferroelectricity near room temperature in co-crystals of nonpolar organic molecules," *Nature Materials*, vol. 4, pp. 163–166, Feb. 2005. Number: 2 Publisher: Nature Publishing Group.

[48] R. Kumai, S. Horiuchi, H. Sagayama, T.-h. Arima, M. Watanabe, Y. Noda, and Y. Tokura, "Structural Assignment of Polarization in Hydrogen-Bonded Supramolecular Ferroelectrics," *J. Am. Chem. Soc.*, vol. 129, pp. 12920–12921, Oct. 2007. Publisher: American Chemical Society.

[49] S. Horiuchi, R. Kumai, and Y. Tokura, "Hydrogen-bonded donor–acceptor compounds for organic ferroelectric materials," *Chem. Commun.*, pp. 2321–2329, June 2007. Publisher: The Royal Society of Chemistry.

[50] S. Horiuchi, R. Kumai, and Y. Tokura, "Room-Temperature Ferroelectricity and Gigantic Dielectric Susceptibility on a Supramolecular Architecture of Phenazine and Deuterated Chloranilic Acid," *J. Am. Chem. Soc.*, vol. 127, pp. 5010–5011, Apr. 2005. Publisher: American Chemical Society.

[51] S. Horiuchi, R. Kumai, and Y. Tokura, "A Supramolecular Ferroelectric Realized by Collective Proton Transfer," *Angewandte Chemie International Edition*, vol. 46, no. 19, pp. 3497–3501, 2007.

[52] R. Kumai, S. Horiuchi, Y. Okimoto, and Y. Tokura, "Large dielectric susceptibility associated with proton transfer in a supramolecular structure of chloranilic acid and 5,5'-dimethyl-2,2'-bipyridine," *J. Chem. Phys.*, vol. 125, p. 084715, Aug. 2006. Publisher: American Institute of Physics.

[53] S. Horiuchi, F. Kagawa, K. Hatahara, K. Kobayashi, R. Kumai, Y. Murakami, and Y. Tokura, "Above-room-temperature ferroelectricity and antiferroelectricity in benzimidazoles," *Nature Communications*, vol. 3, p. 1308, Dec. 2012. Number: 1 Publisher: Nature Publishing Group.

[54] S. Horiuchi, R. Kumai, and Y. Tokura, "Hydrogen-Bonding Molecular Chains for High-Temperature Ferroelectricity," *Advanced Materials*, vol. 23, no. 18, pp. 2098–2103, 2011.

[55] K. Yoshino and Y. Inuishi, "Ferroelectric Liquid Crystal and Its Application," *Jpn. J. Appl. Phys.*, vol. 20, p. 3, Jan. 1981. Publisher: IOP Publishing.

[56] R. B. Meyer, "Ferroelectric Liquid Crystals; A Review," *Molecular Crystals and Liquid Crystals*, vol. 40, pp. 33–48, Jan. 1977. Publisher: Taylor & Francis.

[57] S. Pirkl and M. Glogarova, "Ferroelectric Liquid Crystals with High Spontaneous Polarization," *Ferroelectrics - Physical Effects*, Aug. 2011. Publisher: IntechOpen.

[58] Q. Guo, K. Yan, V. Chigrinov, H. Zhao, and M. Tribelsky, "Ferroelectric Liquid Crystals: Physics and Applications," *Crystals*, vol. 9, p. 470, Sept. 2019. Number: 9 Publisher: Multidisciplinary Digital Publishing Institute.

[59] A. S. Tayi, A. K. Shveyd, A. C.-H. Sue, J. M. Szarko, B. S. Rolczynski, D. Cao, T. J. Kennedy, A. A. Sarjeant, C. L. Stern, W. F. Paxton, W. Wu, S. K. Dey, A. C. Fahrenbach, J. R. Guest, H. Mohseni, L. X. Chen, K. L. Wang, J. F. Stoddart, and S. I. Stupp, "Room-temperature ferroelectricity in supramolecular networks of charge-transfer complexes," *Nature*, vol. 488, pp. 485–489, Aug. 2012. Number: 7412 Publisher: Nature Publishing Group.

[60] P. Heremans, G. H. Gelinck, R. Müller, K.-J. Baeg, D.-Y. Kim, and Y.-Y. Noh, "Polymer and Organic Nonvolatile Memory Devices," *Chem. Mater.*, vol. 23, pp. 341–358, Feb. 2011. Publisher: American Chemical Society.

[61] A. Laudari, J. Barron, A. Pickett, and S. Guha, "Tuning Charge Transport in PVDF-Based Organic Ferroelectric Transistors: Status and Outlook," *ACS Appl. Mater. Interfaces*, vol. 12, pp. 26757–26775, June 2020. Publisher: American Chemical Society.

[62] T. Mikolajick, U. Schroeder, and S. Slesazeck, "The Past, the Present, and the Future of Ferroelectric Memories," *IEEE Transactions on Electron Devices*, vol. 67, pp. 1434–1443, Apr. 2020. Conference Name: IEEE Transactions on Electron Devices.

[63] T. Lenz, D. Zhao, G. Richardson, I. Katsouras, K. Asadi, G. Glaßer, S. T. Zimmerman, N. Stingeling, C. Roelofs, M. Kemerink, P. W. M. Blom, and D. M. d. Leeuw, "Microstructured organic ferroelectric thin film capacitors by solution micromolding," *Physica Status Solidi A : Applications and material science*, vol. 212, pp. 2124–2132, Oct. 2015. Publisher: Wiley-VCH Verlag.

[64] D. Zhao, I. Katsouras, M. Li, K. Asadi, J. Tsurumi, G. Glasser, J. Takeya, P. W. M. Blom, and D. M. de Leeuw, "Polarization fatigue of organic ferroelectric capacitors," *Scientific Reports*, vol. 4, p. 5075, May 2014. Number: 1 Publisher: Nature Publishing Group.

[65] J. Jo, W. Y. Choi, J.-D. Park, J. W. Shim, H.-Y. Yu, and C. Shin, "Negative Capacitance in Organic/Ferroelectric Capacitor to Implement Steep Switching MOS Devices," *Nano Lett.*, vol. 15, pp. 4553–4556, July 2015. Publisher: American Chemical Society.

[66] Y. Noda, T. Yamada, K. Kobayashi, R. Kumai, S. Horiuchi, F. Kagawa, and T. Hasegawa, "Few-Volt Operation of Printed Organic Ferroelectric Capacitor," *Advanced Materials*, vol. 27, no. 41, pp. 6475–6481, 2015.

[67] M. Guo, J. Jiang, J. Qian, C. Liu, J. Ma, C.-W. Nan, and Y. Shen, "Flexible Robust and High-Density FeRAM from Array of Organic Ferroelectric Nano-Lamellae by Self-Assembly," *Advanced Science*, vol. 6, no. 6, p. 1801931, 2019.

[68] K. N. Narayanan Unni, R. de Bettignies, S. Dabos-Seignon, and J.-M. Nunzi, "A nonvolatile memory element based on an organic field-effect transistor," *Applied physics letters*, vol. 85, no. 10, pp. 1823–1825, 2004.

[69] H. Sun, Q. Wang, Y. Li, Y.-F. Lin, Y. Wang, Y. Yin, Y. Xu, C. Liu, K. Tsukagoshi, L. Pan, X. Wang, Z. Hu, and Y. Shi, "Boost Up Carrier Mobility for Ferroelectric Organic Transistor Memory via Buffering Interfacial Polarization Fluctuation," *Sci Rep*, vol. 4, Nov. 2014.

[70] J. J. Brondijk, K. Asadi, P. W. M. Blom, and D. M. d. Leeuw, "Physics of organic ferroelectric field-effect transistors," *Journal of Polymer Science Part B: Polymer Physics*, vol. 50, no. 1, pp. 47–54, 2012.

[71] S. Majumdar, B. Chen, Q. H. Qin, H. S. Majumdar, and S. van Dijken, "Electrode Dependence of Tunneling Electroresistance and Switching Stability in Organic Ferroelectric P (VDF-TrFE)-Based Tunnel Junctions," *Advanced Functional Materials*, vol. 28, no. 15, p. 1703273, 2018.

[72] B. B. Tian, J. L. Wang, S. Fusil, Y. Liu, X. L. Zhao, S. Sun, H. Shen, T. Lin, J. L. Sun, and C. G. Duan, "Tunnel electroresistance through organic ferroelectrics," *Nature communications*, vol. 7, p. 11502, 2016.

[73] B. B. Tian, Y. Liu, L. F. Chen, J. L. Wang, S. Sun, H. Shen, J. L. Sun, G. L. Yuan, S. Fusil, V. Garcia, B. Dkhil, X. J. Meng, and J. H. Chu, "Space-charge Effect on Electroresistance in Metal-Ferroelectric-Metal capacitors," *Scientific Reports*, vol. 5, p. 18297, Dec. 2015. Number: 1 Publisher: Nature Publishing Group.

[74] R. Ramesh and N. A. Spaldin, "Multiferroics: progress and prospects in thin films," *Nature Materials*, vol. 6, pp. 21–29, Jan. 2007. Number: 1 Publisher: Nature Publishing Group.

[75] W. Eerenstein, N. D. Mathur, and J. F. Scott, "Multiferroic and magnetoelectric materials," *Nature*, vol. 442, pp. 759–765, Aug. 2006. Number: 7104 Publisher: Nature Publishing Group.

[76] N. A. Spaldin and R. Ramesh, "Advances in magnetoelectric multiferroics," *Nature Materials*, vol. 18, pp. 203–212, Mar. 2019. Number: 3 Publisher: Nature Publishing Group.

[77] A. Mardana, S. Ducharme, and S. Adenwalla, "Ferroelectric Control of Magnetic Anisotropy," *Nano Lett.*, vol. 11, pp. 3862–3867, Sept. 2011. Publisher: American Chemical Society.

[78] F. Kagawa, S. Horiuchi, M. Tokunaga, J. Fujioka, and Y. Tokura, "Ferroelectricity in a one-dimensional organic quantum magnet," *Nature Physics*, vol. 6, pp. 169–172, Mar. 2010. Number: 3 Publisher: Nature Publishing Group.

[79] R. C. Subedi, R. Geng, H. M. Luong, W. Huang, X. Li, L. A. Hornak, and T. D. Nguyen, "Large magnetoelectric effect in organic ferroelectric copolymer-based multiferroic tunnel junctions," *Appl. Phys. Lett.*, vol. 110, p. 053302, Jan. 2017. Publisher: American Institute of Physics.

[80] P. Lunkenheimer, J. Müller, S. Krohns, F. Schrettle, A. Loidl, B. Hartmann, R. Rommel, M. de Souza, C. Hotta, J. A. Schlueter, and M. Lang, "Multiferroicity in an organic charge-transfer salt that is suggestive of electric-dipole-driven magnetism," *Nature Materials*, vol. 11, pp. 755–758, Sept. 2012. Number: 9 Publisher: Nature Publishing Group.

[81] W. Qin, D. Jasion, X. Chen, M. Wuttig, and S. Ren, "Charge-Transfer Magnetoelectrics of Polymeric Multiferroics," *ACS Nano*, vol. 8, pp. 3671–3677, Apr. 2014. Publisher: American Chemical Society.

[82] S. Ren and M. Wuttig, "Organic Exciton Multiferroics," *Advanced Materials*, vol. 24, no. 6, pp. 724–727, 2012.

[83] G.-C. Xu, W. Zhang, X.-M. Ma, Y.-H. Chen, L. Zhang, H.-L. Cai, Z.-M. Wang, R.-G. Xiong, and S. Gao, "Coexistence of Magnetic and Electric Orderings in the Metal–Formate Frameworks of $[NH_4][M(HCOO)_3]$," *J. Am. Chem. Soc.*, vol. 133, pp. 14948–14951, Sept. 2011. Publisher: American Chemical Society.

[84] D.-W. Fu, W. Zhang, H.-L. Cai, Y. Zhang, J.-Z. Ge, R.-G. Xiong, S. D. Huang, and T. Nakamura, "A Multiferroic Perdeutero Metal–Organic Framework," *Angewandte Chemie International Edition*, vol. 50, no. 50, pp. 11947–11951, 2011.

[85] Y. Tian, J. Cong, S. Shen, Y. Chai, L. Yan, S. Wang, and Y. Sun, "Electric control of magnetism in a multiferroic metal–organic framework," *physica status solidi (RRL) – Rapid Research Letters*, vol. 8, no. 1, pp. 91–94, 2014.

[86] Y. Tian, A. Stroppa, Y. Chai, L. Yan, S. Wang, P. Barone, S. Picozzi, and Y. Sun, "Cross coupling between electric and magnetic orders in a multiferroic metal-organic framework," *Scientific Reports*, vol. 4, p. 6062, Aug. 2014. Number: 1 Publisher: Nature Publishing Group.

[87] Y. Cai, S. Luo, Z. Zhu, and H. Gu, "Ferroelectric mechanism of croconic acid: A first-principles and Monte Carlo study," *The Journal of Chemical Physics*, vol. 139, p. 044702, July 2013.

[88] T. Kolev, B. Koleva, and M. Spiteller, "Solid-state linear polarized IR-spectroscopy of croconic and rhodizonic acids," *Open Chemistry*, vol. 6, no. 3, pp. 393–399, 2008. Publisher: De Gruyter.

[89] M. Washino, K. Yamada, and Y. Kurita, "The Dipole Moments and Molecular Structures of Croconic Acid and Dimethyl Croconate," *BCSJ*, vol. 31, pp. 552–555, May 1958. Publisher: The Chemical Society of Japan.

[90] D. Braga, L. Maini, and F. Grepioni, "Crystallization from hydrochloric acid affords the solid-state structure of croconic acid (175 years after its discovery) and a novel hydrogen-bonded network," *CrystEngComm*, vol. 3, no. 6, pp. 27–29, 2001. Publisher: Royal Society of Chemistry.

[91] F. Bisti, A. Stroppa, S. Picozzi, and L. Ottaviano, "Fingerprints of the hydrogen bond in the photoemission spectra of croconic acid condensed phase: An x-ray photoelectron spectroscopy and ab-initio study," *J. Chem. Phys.*, vol. 134, p. 174505, May 2011. Publisher: American Institute of Physics.

[92] J. Seliger, J. Plavec, P. Šket, V. Žagar, and R. Blinc, "$^{17}$O NQR and $^{13}$C NMR study of hydrogen-bonded organic ferroelectric croconic acid," *physica status solidi (b)*, vol. 248, no. 9, pp. 2091–2096, 2011. Publisher: Wiley Online Library.

[93] T. Kolev, B. B. Koleva, and M. Spiteller, "Solid-state linear polarized IR-spectroscopy of croconic and rhodizonic acids," *cent.eur.j.chem.*, vol. 6, pp. 393–399, Sept. 2008.

[94] F. Fernandez-Alonso, M. J. Gutmann, S. Mukhopadhyay, D. B. Jochym, K. Refson, M. Jura, M. Krzystyniak, M. Jiménez-Ruiz, and A. Wagner, "Hydrogen Bonding in the Organic Ferroelectric Croconic Acid: Insights from Experiment and First-Principles Modelling," *Journal of the Physical Society of Japan*, vol. 82, no. Suppl. A, p. SA001, 2013. Publisher: The Physical Society of Japan.

[95] S. Mukhopadhyay, M. J. Gutmann, M. Jura, D. B. Jochym, M. Jimenez-Ruiz, S. Sturniolo, K. Refson, and F. Fernandez-Alonso, "Ferroelectric behaviour in solid croconic acid using neutron scattering and first-principles density functional theory," *Chemical Physics*, vol. 427, pp. 95–100, 2013. Publisher: Elsevier.

[96] S. Mukhopadhyay, M. Gutmann, and F. Fernandez-Alonso, "Hydrogen-bond structure and anharmonicity in croconic acid," *Phys. Chem. Chem. Phys.*, vol. 16, no. 47, pp. 26234–26239, 2014.

[97] V. V. Zhurov and A. A. Pinkerton, "Charge Density Analysis of an Organic Ferroelectric. Croconic Acid: an Experimental and Theoretical Study," *Zeitschrift für anorganische und allgemeine Chemie*, vol. 639, no. 11, pp. 1969–1978, 2013. Publisher: Wiley Online Library.

[98] D. Di Sante, A. Stroppa, and S. Picozzi, "Structural, electronic and ferroelectric properties of croconic acid crystal: a DFT study," *Phys. Chem. Chem. Phys.*, vol. 14, no. 42, p. 14673, 2012.

[99] T. Miyamoto, D. Hata, T. Morimoto, H. Yamakawa, N. Kida, T. Terashige, K. Iwano, H. Kishida, S. Horiuchi, and H. Okamoto, "Ultrafast polarization control by terahertz fields via $\pi$-electron wavefunction changes in hydrogen-bonded molecular ferroelectrics," *Sci Rep*, vol. 8, p. 15014, Dec. 2018.

[100] F. Kagawa, S. Horiuchi, N. Minami, S. Ishibashi, K. Kobayashi, R. Kumai, Y. Murakami, and Y. Tokura, "Polarization switching ability dependent on multidomain topology in a uniaxial organic ferroelectric," *Nano letters*, vol. 14, no. 1, pp. 239–243, 2014. Publisher: ACS Publications.

[101] M. Sotome, N. Kida, S. Horiuchi, and H. Okamoto, "Visualization of ferroelectric domains in a hydrogen-bonded molecular crystal using emission of terahertz radiation," *Appl. Phys. Lett.*, vol. 105, p. 041101, July 2014.

[102] S. Chen, A. Enders, and X. C. Zeng, "Influence of Structural Fluctuations, Proton Transfer, and Electric Field on Polarization Switching of Supported Two-Dimensional Hydrogen-Bonded Oxocarbon Monolayers," *Chem. Mater.*, vol. 27, pp. 4839–4847, July 2015.

[103] K. Chang, J. Liu, H. Lin, N. Wang, K. Zhao, A. Zhang, F. Jin, Y. Zhong, X. Hu, W. Duan, Q. Zhang, L. Fu, Q.-K. Xue, X. Chen, and S.-H. Ji, "Discovery of robust in-plane ferroelectricity in atomic-thick SnTe," *Science*, vol. 353, pp. 274–278, July 2016. Publisher: American Association for the Advancement of Science Section: Report.

[104] D. Peterson, J. Liu, F. Guzman, J. Etzweiler, G. Santoyo, S. Murphy, S. J. Callori, K. Cousins, T. Usher, R. Zhang, and F. Selim, "Studying the interface between croconic acid thin films and substrates using a slow positron beam," *AIP Conference Proceedings*, vol. 2182, p. 050022, Dec. 2019. Publisher: American Institute of Physics.

[105] P. S. Costa, F. Guzman, K. Cousins, S. J. Callori, E. Sanchez, P. K. Dixon, D. Smith, T. Usher, and R. Zhang, "Fabricating high-quality ultra-thin croconic acid film using electric field guidance," *Applied Surface Science*, vol. 427, pp. 541–546, 2018. Publisher: Elsevier.

[106] Y. Yuan, X. Jiang, S. Poddar, and X. Xu, "Electric-field assisted nucleation processes of croconic acid films," *CrystEngComm*, vol. 21, pp. 7460–7467, Dec. 2019.

[107] vacuum science, "fundamentals of vacuum science, https://www.vacuumscienceworld.com/," 2020.

[108] M. Studniarek, *Interface and multifunctional device spintronics : studies with synchrotron radiation.* These de doctorat, Strasbourg, Nov. 2016.

[109] S. Maghsoudy-Louyeh, M. Kropf, and B. R. Tittmann, "Review of Progress in Atomic Force Microscopy," *The Open Neuroimaging Journal*, vol. 12, Dec. 2018.

[110] A. Nano, "NT-MDT Spectrum Instruments. Principles and Instrumental Aspects of Piezoresponse Force Microscopy. https://www.azonano.com/article.aspx?articleid=2682," 2020.

[111] A. L. Kholkin, S. V. Kalinin, A. Roelofs, and A. Gruverman, "Review of ferroelectric domain imaging by piezoresponse force microscopy," in *Scanning probe microscopy*, pp. 173–214, Springer, 2007.

[112] E. Soergel, "Piezoresponse force microscopy (PFM)," *Journal of Physics D: Applied Physics*, vol. 44, no. 46, p. 464003, 2011. Publisher: IOP Publishing.

[113] S. Hong, J. Woo, H. Shin, J. U. Jeon, Y. E. Pak, E. L. Colla, N. Setter, E. Kim, and K. No, "Principle of ferroelectric domain imaging using atomic force microscope," *Journal of Applied Physics*, vol. 89, pp. 1377–1386, Dec. 2000. Publisher: American Institute of Physics.

[114] A. Gruverman, M. Alexe, and D. Meier, "Piezoresponse force microscopy and nanoferroic phenomena," *Nature Communications*, vol. 10, p. 1661, Apr. 2019. Number: 1 Publisher: Nature Publishing Group.

[115] P. C. Robinson and M. W. Davidson, "Polarized Light Microscopy, https://www.microscopyu.com/techniques/polarized-light/polarized-light-microscopy," 2020.

[116] T. Miyamachi, M. Gruber, V. Davesne, M. Bowen, S. Boukari, L. Joly, F. Scheurer, G. Rogez, T. K. Yamada, P. Ohresser, E. Beaurepaire, and W. Wulfhekel, "Robust spin crossover and memristance across a single molecule," *Nature Communications*, vol. 3, pp. 1–6, July 2012.

[117] M. Gruber, F. Ibrahim, S. Boukari, L. Joly, V. Da Costa, M. Studniarek, M. Peter, H. Isshiki, H. Jabbar, V. Davesne, J. Arabski, E. Otero,

F. Choueikani, K. Chen, P. Ohresser, W. Wulfhekel, F. Scheurer, E. Beaurepaire, M. Alouani, W. Weber, and M. Bowen, "Spin-Dependent Hybridization between Molecule and Metal at Room Temperature through Interlayer Exchange Coupling," *Nano Lett.*, vol. 15, pp. 7921–7926, Dec. 2015.

[118] D. A. Kunkel, J. Hooper, S. Simpson, S. Beniwal, K. L. Morrow, D. C. Smith, K. Cousins, S. Ducharme, E. Zurek, and A. Enders, "Rhodizonic Acid on Noble Metals: Surface Reactivity and Coordination Chemistry," *J. Phys. Chem. Lett.*, vol. 4, pp. 3413–3419, Oct. 2013. Publisher: American Chemical Society.

[119] D. A. Kunkel, J. Hooper, S. Simpson, G. A. Rojas, S. Ducharme, T. Usher, E. Zurek, and A. Enders, "Proton transfer in surface-stabilized chiral motifs of croconic acid," *Physical Review B*, vol. 87, no. 4, p. 041402, 2013.

[120] J. Hooper, D. A. Kunkel, E. Zurek, and A. Enders, "Interplay between Hydrogen Bonding, Epitaxy, and Charge Transfer in the Self-Assembly of Croconic Acid on Au (111) and Ag (111)," *The Journal of Physical Chemistry C*, vol. 119, no. 47, pp. 26429–26437, 2015.

[121] S. Chen, A. Enders, and X. C. Zeng, "Influence of Structural Fluctuations, Proton Transfer, and Electric Field on Polarization Switching of Supported Two-Dimensional Hydrogen-Bonded Oxocarbon Monolayers," *Chemistry of Materials*, vol. 27, no. 13, pp. 4839–4847, 2015.

[122] J. Hooper, D. A. Kunkel, E. Zurek, and A. Enders, "Interplay between Hydrogen Bonding, Epitaxy, and Charge Transfer in the Self-Assembly of Croconic Acid on Au (111) and Ag (111)," *The Journal of Physical Chemistry C*, vol. 119, no. 47, pp. 26429–26437, 2015. Publisher: ACS Publications.

[123] L. W. Martin and A. M. Rappe, "Thin-film ferroelectric materials and their applications," *Nature Reviews Materials*, vol. 2, no. 2, p. 16087, 2017.

[124] N. Fujimura, Y. Kuroiwa, A. Ando, Y. Cho, M. Iwata, K.-i. Kakimoto, K. Kato, H. Nagata, M. Shimizu, and T. Tsurumi, *Ferroelectric Materials and Their Applications FOREWORD*. IOP PUBLISHING LTD TEMPLE CIRCUS, TEMPLE WAY, BRISTOL BS1 6BE, ENGLAND, 2018.

[125] J. F. Scott, "Applications of modern ferroelectrics," *science*, vol. 315, no. 5814, pp. 954–959, 2007.

[126] L. Hu, S. Dalgleish, M. M. Matsushita, H. Yoshikawa, and K. Awaga, "Storage of an electric field for photocurrent generation in ferroelectric-functionalized organic devices," *Nature communications*, vol. 5, p. 3279, 2014.

[127] V. Khikhlovskyi, R. Wang, A. J. van Breemen, G. H. Gelinck, R. A. Janssen, and M. Kemerink, "Nanoscale organic ferroelectric resistive switches," *The Journal of Physical Chemistry C*, vol. 118, no. 6, pp. 3305–3312, 2014.

[128] A. Islam Khan, D. Bhowmik, P. Yu, S. Joo Kim, X. Pan, R. Ramesh, and S. Salahuddin, "Experimental evidence of ferroelectric negative capacitance in nanoscale heterostructures," *Applied Physics Letters*, vol. 99, no. 11, p. 113501, 2011.

[129] A. Islam Khan, K. Chatterjee, B. Wang, S. Drapcho, L. You, C. Serrao, S. Rahman Bakaul, R. Ramesh, and S. Salahuddin, "Negative Capacitance in a Ferroelectric Capacitor," *arXiv preprint arXiv:1409.3273*, 2014.

[130] K. Asadi, M. Li, N. Stingelin, P. W. Blom, and D. M. de Leeuw, "Cross-bar memory array of organic bistable rectifying diodes for nonvolatile data storage," *Applied Physics Letters*, vol. 97, no. 19, p. 242, 2010.

[131] J. Lee, A. J. Van Breemen, V. Khikhlovskyi, M. Kemerink, R. A. Janssen, and G. H. Gelinck, "Pulse-modulated multilevel data storage in an organic ferroelectric resistive memory diode," *Scientific reports*, vol. 6, p. 24407, 2016.

[132] J. Schütrumpf, S. Zhukov, Y. A. Genenko, and H. Von Seggern, "Polarization switching dynamics by inhomogeneous field mechanism in ferroelectric polymers," *Journal of Physics D: Applied Physics*, vol. 45, no. 16, p. 165301, 2012.

[133] S. Fabiano, X. Crispin, and M. Berggren, "Ferroelectric polarization induces electric double layer bistability in electrolyte-gated field-effect transistors," *ACS applied materials & interfaces*, vol. 6, no. 1, pp. 438–442, 2013.

[134] S. K. Hwang, I. Bae, S. M. Cho, R. H. Kim, H. J. Jung, and C. Park, "High Performance Multi-Level Non-Volatile Polymer Memory with Solution-Blended Ferroelectric Polymer/High-k Insulators for Low Voltage Operation," *Advanced Functional Materials*, vol. 23, no. 44, pp. 5484–5493, 2013.

[135] A. S. Tayi, A. Kaeser, M. Matsumoto, T. Aida, and S. I. Stupp, "Supramolecular ferroelectrics," *Nature Chemistry*, vol. 7, pp. 281–294, Apr. 2015. Number: 4 Publisher: Nature Publishing Group.

[136] R. Sawada, H. Uemura, M. Sotome, H. Yada, N. Kida, K. Iwano, Y. Shimoi, S. Horiuchi, and H. Okamoto, "Large second-order optical nonlinearity in a ferroelectric molecular crystal of croconic acid with strong intermolecular hydrogen bonds," *Appl. Phys. Lett.*, vol. 102, p. 162901, Apr. 2013.

[137] S. Mohapatra, V. D. Costa, G. Avedissian, J. Arabski, W. Weber, M. Bowen, and S. Boukari, "Robust ferroelectric properties of organic croconic acid films grown on spintronically relevant substrates," *Mater. Adv.*, vol. 1, pp. 415–420, June 2020.

[138] A. Schilling, D. Byrne, G. Catalan, K. G. Webber, Y. A. Genenko, G. S. Wu, J. F. Scott, and J. M. Gregg, "Domains in Ferroelectric Nanodots," *Nano Lett.*, vol. 9, pp. 3359–3364, Sept. 2009. Publisher: American Chemical Society.

[139] B. A. Hernandez, K.-S. Chang, E. R. Fisher, and P. K. Dorhout, "Sol-Gel Template Synthesis and Characterization of $BaTiO_3$ and $PbTiO_3$ Nanotubes," *Chem. Mater.*, vol. 14, pp. 480–482, Feb. 2002. Publisher: American Chemical Society.

[140] H.-J. Shin, J. H. Choi, H. J. Yang, Y. D. Park, Y. Kuk, and C.-J. Kang, "Patterning of ferroelectric nanodot arrays using a silicon nitride shadow mask," *Appl. Phys. Lett.*, vol. 87, p. 113114, Sept. 2005. Publisher: American Institute of Physics.

[141] S. Prosandeev and L. Bellaiche, "Characteristics and signatures of dipole vortices in ferroelectric nanodots: First-principles-based simulations and analytical expressions," *Phys. Rev. B*, vol. 75, p. 094102, Mar. 2007. Publisher: American Physical Society.

[142] Z. Li, Y. Wang, G. Tian, P. Li, L. Zhao, F. Zhang, J. Yao, H. Fan, X. Song, D. Chen, Z. Fan, M. Qin, M. Zeng, Z. Zhang, X. Lu, S. Hu, C. Lei, Q. Zhu, J. Li, X. Gao, and J.-M. Liu, "High-density array of ferroelectric nanodots with robust and reversibly switchable topological domain states," *Science Advances*, vol. 3, p. e1700919, Aug. 2017. Publisher: American Association for the Advancement of Science Section: Research Article.

[143] Y. Tikhonov, S. Kondovych, J. Mangeri, M. Pavlenko, L. Baudry, A. Sené, A. Galda, S. Nakhmanson, O. Heinonen, A. Razumnaya, I. Luk'yanchuk, and V. M. Vinokur, "Controllable skyrmion chirality in ferroelectrics," *Scientific Reports*, vol. 10, p. 8657, May 2020. Number: 1 Publisher: Nature Publishing Group.

[144] X. Lu, Y. Kim, S. Goetze, X. Li, S. Dong, P. Werner, M. Alexe, and D. Hesse, "Magnetoelectric Coupling in Ordered Arrays of Multilayered Heteroepitaxial $BaTiO_3/CoFe_2O_4$ Nanodots," *Nano Lett.*, vol. 11, pp. 3202–3206, Aug. 2011. Publisher: American Chemical Society.

[145] Y. Ahn, Y.-H. Shin, and J. Y. Son, "Ferroelectric switching response of P(VDF-TrFE) nanodots with and without nanomolds," *Appl. Phys. A*, vol. 122, p. 882, Sept. 2016.

[146] J. Ryu, K. No, Y. Kim, E. Park, and S. Hong, "Synthesis and Application of Ferroelectric Poly(Vinylidene Fluoride-co-Trifluoroethylene) Films using Electrophoretic Deposition," *Scientific Reports*, vol. 6, p. 36176, Nov. 2016. Number: 1 Publisher: Nature Publishing Group.

[147] X.-Z. Chen, Q. Li, X. Chen, X. Guo, H.-X. Ge, Y. Liu, and Q.-D. Shen, "Nano-Imprinted Ferroelectric Polymer Nanodot Arrays for High Density Data Storage," *Advanced Functional Materials*, vol. 23, no. 24, pp. 3124–3129, 2013.

[148] Y. Ahn and J. Y. Son, "Size effect on polarization switching kinetics of P(VDF-TrFE) copolymer nanodots," *Organic Electronics*, vol. 41, pp. 205–208, Feb. 2017.

[149] T. M. Shaw, S. Trolier-McKinstry, and P. C. McIntyre, "The Properties of Ferroelectric Films at Small Dimensions," *Annual Review of Materials Science*, vol. 30, no. 1, pp. 263–298, 2000.

[150] V. Nagarajan, A. Roytburd, A. Stanishevsky, S. Prasertchoung, T. Zhao, L. Chen, J. Melngailis, O. Auciello, and R. Ramesh, "Dynamics of ferroelastic domains in ferroelectric thin films," *Nature Materials*, vol. 2, pp. 43–47, Jan. 2003. Number: 1 Publisher: Nature Publishing Group.

[151] S. Bühlmann, B. Dwir, J. Baborowski, and P. Muralt, "Size effect in mesoscopic epitaxial ferroelectric structures: Increase of piezoelectric response with

decreasing feature size," *Appl. Phys. Lett.*, vol. 80, pp. 3195–3197, Apr. 2002. Publisher: American Institute of Physics.

[152] T. J. Zhang, R. K. Pan, Z. J. Ma, M. G. Duan, D. F. Wang, and M. He, "Large rectifying leakage current in $Pt/BaTiO_3/Nb:SrTiO_3/Pt$ structure," *Appl. Phys. Lett.*, vol. 99, p. 182106, Oct. 2011.

[153] S. M. Yang, A. N. Morozovska, R. Kumar, E. A. Eliseev, Y. Cao, L. Mazet, N. Balke, S. Jesse, R. K. Vasudevan, C. Dubourdieu, and S. V. Kalinin, "Mixed electrochemical–ferroelectric states in nanoscale ferroelectrics," *Nature Physics*, vol. 13, pp. 812–818, Aug. 2017.

[154] R. K. Vasudevan, N. Balke, P. Maksymovych, S. Jesse, and S. V. Kalinin, "Ferroelectric or non-ferroelectric: Why so many materials exhibit "ferroelectricity" on the nanoscale," *Applied Physics Reviews*, vol. 4, p. 021302, May 2017.

[155] D. Seol, S. Park, O. V. Varenyk, S. Lee, H. N. Lee, A. N. Morozovska, and Y. Kim, "Determination of ferroelectric contributions to electromechanical response by frequency dependent piezoresponse force microscopy," *Scientific Reports*, vol. 6, pp. 1–10, July 2016.

[156] E. Strelcov, Y. Kim, J. C. Yang, Y. H. Chu, P. Yu, X. Lu, S. Jesse, and S. V. Kalinin, "Role of measurement voltage on hysteresis loop shape in Piezoresponse Force Microscopy," *Appl. Phys. Lett.*, vol. 101, p. 192902, Nov. 2012.

[157] S. V. Kalinin, S. Jesse, A. Tselev, A. P. Baddorf, and N. Balke, "The Role of Electrochemical Phenomena in Scanning Probe Microscopy of Ferroelectric Thin Films," *ACS Nano*, vol. 5, pp. 5683–5691, July 2011. Publisher: American Chemical Society.

[158] A. Roelofs, U. Böttger, R. Waser, F. Schlaphof, S. Trogisch, and L. M. Eng, "Differentiating 180° and 90° switching of ferroelectric domains with three-dimensional piezoresponse force microscopy," *Appl. Phys. Lett.*, vol. 77, pp. 3444–3446, Nov. 2000. Publisher: American Institute of Physics.

[159] M. Kratzer, M. Lasnik, S. Röhrig, C. Teichert, and M. Deluca, "Reconstruction of the domain orientation distribution function of polycrystalline PZT ceramics using vector piezoresponse force microscopy," *Scientific Reports*, vol. 8, p. 422, Jan. 2018. Number: 1 Publisher: Nature Publishing Group.

[160] S. M. Shapiro, R. W. Gammon, and H. Z. Cummins, "Visual observation of ferroelectric domains in TGS," *Applied Physics Letters*, vol. 10, no. 4, pp. 113–115, 1967. Publisher: American Institute of Physics.

[161] T. Mitsui and J. Furuichi, "Domain Structure of Rochelle Salt and $KH_2PO_4$," *Phys. Rev.*, vol. 90, pp. 193–202, Apr. 1953.

[162] S.-L. Hsu, M. R. McCarter, C. Dai, Z. Hong, L.-Q. Chen, C. T. Nelson, L. W. Martin, and R. Ramesh, "Emergence of the Vortex State in Confined Ferroelectric Heterostructures," *Adv. Mater.*, vol. 31, p. 1901014, Sept. 2019.

[163] A. Gruverman, D. Wu, H.-J. Fan, I. Vrejoiu, M. Alexe, R. J. Harrison, and J. F. Scott, "Vortex ferroelectric domains," *J. Phys.: Condens. Matter*, vol. 20, p. 342201, Aug. 2008.

[164] H.-Y. Zhang, X.-J. Song, X.-G. Chen, Z.-X. Zhang, Y.-M. You, Y.-Y. Tang, and R.-G. Xiong, "Observation of Vortex Domains in a Two-Dimensional Lead Iodide Perovskite Ferroelectric," *J. Am. Chem. Soc.*, vol. 142, pp. 4925–4931, Mar. 2020.

[165] D. Karpov, Z. Liu, A. Kumar, B. Kiefer, R. Harder, T. Lookman, and E. Fohtung, "Nanoscale topological defects and improper ferroelectric domains in multiferroic barium hexaferrite nanocrystals," *Phys. Rev. B*, vol. 100, p. 054432, Aug. 2019.

[166] S. Das, Y. L. Tang, Z. Hong, M. a. P. Gonçalves, M. R. McCarter, C. Klewe, K. X. Nguyen, F. Gómez-Ortiz, P. Shafer, E. Arenholz, V. A. Stoica, S.-L. Hsu, B. Wang, C. Ophus, J. F. Liu, C. T. Nelson, S. Saremi, B. Prasad, A. B. Mei, D. G. Schlom, J. Íñiguez, P. García-Fernández, D. A. Muller, L. Q. Chen, J. Junquera, L. W. Martin, and R. Ramesh, "Observation of room-temperature polar skyrmions," *Nature*, vol. 568, pp. 368–372, Apr. 2019. Number: 7752 Publisher: Nature Publishing Group.

[167] M. A. P. Gonçalves, C. Escorihuela-Sayalero, P. Garca-Fernández, J. Junquera, and J. Íñiguez, "Theoretical guidelines to create and tune electric skyrmion bubbles," *Science Advances*, vol. 5, p. eaau7023, Feb. 2019. Publisher: American Association for the Advancement of Science Section: Research Article.

[168] R. McQuaid, L. McGilly, P. Sharma, A. Gruverman, and J. Gregg, "Mesoscale flux-closure domain formation in single-crystal $BaTiO_3$," *Nat Commun*, vol. 2, p. 404, Sept. 2011.

[169] R. G. P. McQuaid, A. Gruverman, J. F. Scott, and J. M. Gregg, "Exploring Vertex Interactions in Ferroelectric Flux-Closure Domains," *Nano Lett.*, vol. 14, pp. 4230–4237, Aug. 2014.

[170] Y. Ivry, D. P. Chu, J. F. Scott, and C. Durkan, "Flux Closure Vortexlike Domain Structures in Ferroelectric Thin Films," *Phys. Rev. Lett.*, vol. 104, p. 207602, May 2010.

[171] G. Catalan, A. Lubk, A. H. G. Vlooswijk, E. Snoeck, C. Magen, A. Janssens, G. Rispens, G. Rijnders, D. H. A. Blank, and B. Noheda, "Flexoelectric rotation of polarization in ferroelectric thin films," *Nature Materials*, vol. 10, pp. 963–967, Dec. 2011. Number: 12 Publisher: Nature Publishing Group.

[172] S. Li, Y. L. Zhu, Y. J. Wang, Y. L. Tang, Y. Liu, S. R. Zhang, J. Y. Ma, and X. L. Ma, "Periodic arrays of flux-closure domains in ferroelectric thin films with oxide electrodes," *Appl. Phys. Lett.*, vol. 111, p. 052901, July 2017.

[173] Y. Ai, Y.-L. Zeng, W.-H. He, X.-Q. Huang, and Y.-Y. Tang, "Six-Fold Vertices in a Single-Component Organic Ferroelectric with Most Equivalent Polarization Directions," *J. Am. Chem. Soc.*, vol. 142, pp. 13989–13995, Aug. 2020. Publisher: American Chemical Society.

[174] W. Liu, Y. Liu, J. Wang, C. Wu, C. Liu, L. Xiao, Z. Chen, S. Wang, and Q. Gong, "Twin Domains in Organometallic Halide Perovskite Thin-Films," *Crystals*, vol. 8, p. 216, May 2018.

[175] P. S. Bednyakov, B. I. Sturman, T. Sluka, A. K. Tagantsev, and P. V. Yudin, "Physics and applications of charged domain walls," *npj Comput Mater*, vol. 4, p. 65, Dec. 2018.

[176] J. Jiang, Z. L. Bai, Z. H. Chen, L. He, D. W. Zhang, Q. H. Zhang, J. A. Shi, M. H. Park, J. F. Scott, C. S. Hwang, and A. Q. Jiang, "Temporary formation of highly conducting domain walls for non-destructive read-out of ferroelectric domain-wall resistance switching memories," *Nat Mater*, vol. 17, no. 1, pp. 49–56, 2018.

[177] G. Sanchez-Santolino, J. Tornos, D. Hernandez-Martin, J. I. Beltran, C. Munuera, M. Cabero, A. Perez-Muñoz, J. Ricote, F. Mompean, M. Garcia-Hernandez, Z. Sefrioui, C. Leon, S. J. Pennycook, M. C. Muñoz, M. Varela, and J. Santamaria, "Resonant electron tunnelling assisted by charged domain walls in multiferroic tunnel junctions," *Nat Nanotechnol*, vol. 12, no. 7, pp. 655–662, 2017.

[178] J. R. Whyte and J. M. Gregg, "A diode for ferroelectric domain-wall motion," *Nature Communications*, vol. 6, p. 7361, June 2015. Number: 1 Publisher: Nature Publishing Group.

[179] J. Schaab, S. H. Skjærvø, S. Krohns, X. Dai, M. E. Holtz, A. Cano, M. Lilienblum, Z. Yan, E. Bourret, D. A. Muller, M. Fiebig, S. M. Selbach, and D. Meier, "Electrical half-wave rectification at ferroelectric domain walls," *Nature Nanotechnology*, vol. 13, pp. 1028–1034, Nov. 2018. Number: 11 Publisher: Nature Publishing Group.

[180] L. Li, P. Gao, C. T. Nelson, J. R. Jokisaari, Y. Zhang, S.-J. Kim, A. Melville, C. Adamo, D. G. Schlom, and X. Pan, "Atomic Scale Structure Changes Induced by Charged Domain Walls in Ferroelectric Materials," *Nano Lett.*, vol. 13, pp. 5218–5223, Nov. 2013. Publisher: American Chemical Society.

[181] S. Cherifi-Hertel, H. Bulou, R. Hertel, G. Taupier, K. D. Dorkenoo, C. Andreas, J. Guyonnet, I. Gaponenko, K. Gallo, and P. Paruch, "Non-Ising and chiral ferroelectric domain walls revealed by nonlinear optical microscopy," *Nat Commun*, vol. 8, p. 15768, Aug. 2017.

[182] M. Tanaka and G. Honjo, "Electron Optical Studies of Barium Titanate Single Crystal Films," *J. Phys. Soc. Jpn.*, vol. 19, pp. 954–970, June 1964. Publisher: The Physical Society of Japan.

[183] N. Niizeki and M. Hasegawa, "Direct Observation of Antiparallel 180° Domains in $BaTiO_3$ by X-Ray Anomalous Dispersion Method," *J. Phys. Soc. Jpn.*, vol. 19, pp. 550–554, Apr. 1964. Publisher: The Physical Society of Japan.

[184] H. Yokota, R. Haumont, S. Kawado, J.-M. Kiat, C. Malibert, and Y. Uesu, "SHG Microscope Observations of Domain Structures in Multiferroic $BiFeO_3$," *Ferroelectrics*, vol. 379, pp. 177–182, May 2009. Publisher: Taylor & Francis.

[185] P. W. Forsbergh, "Domain Structures and Phase Transitions in Barium Titanate," *Phys. Rev.*, vol. 76, pp. 1187–1201, Oct. 1949.

[186] G. F. Nataf and M. Guennou, "Optical studies of ferroelectric and ferroelastic domain walls," *J. Phys.: Condens. Matter*, vol. 32, p. 183001, Feb. 2020. Publisher: IOP Publishing.

[187] N. Setter and E. L. Colla, *Ferroelectric ceramics: tutorial reviews, theory, processing, and applications*. Springer, 1993.

[188] C. R. Bowen, H. A. Kim, P. M. Weaver, and S. Dunn, "Piezoelectric and ferroelectric materials and structures for energy harvesting applications," *Energy & Environmental Science*, vol. 7, no. 1, pp. 25–44, 2014. Publisher: Royal Society of Chemistry.

[189] A. Blázquez-Castro, A. García-Cabañes, and M. Carrascosa, "Biological applications of ferroelectric materials," *Applied Physics Reviews*, vol. 5, no. 4, p. 041101, 2018. Publisher: AIP Publishing LLC.

[190] N. Setter, D. Damjanovic, L. Eng, G. Fox, S. Gevorgian, S. Hong, A. Kingon, H. Kohlstedt, N. Y. Park, and G. B. Stephenson, "Ferroelectric thin films: Review of materials, properties, and applications," *Journal of applied physics*, vol. 100, no. 5, p. 051606, 2006. Publisher: American Institute of Physics.

[191] A. K. Tagantsev, V. O. Sherman, K. F. Astafiev, J. Venkatesh, and N. Setter, "Ferroelectric materials for microwave tunable applications," *Journal of electroceramics*, vol. 11, no. 1-2, pp. 5–66, 2003. Publisher: Springer.

[192] Y. Yuan, Z. Xiao, B. Yang, and J. Huang, "Arising applications of ferroelectric materials in photovoltaic devices," *Journal of Materials chemistry A*, vol. 2, no. 17, pp. 6027–6041, 2014. Publisher: Royal Society of Chemistry.

[193] L. W. Martin and A. M. Rappe, "Thin-film ferroelectric materials and their applications," *Nature Reviews Materials*, vol. 2, pp. 1–14, Nov. 2016. Number: 2 Publisher: Nature Publishing Group.

[194] R. López-Juárez, F. González, and M.-E. Villafuerte-Castrejón, "Lead-Free Ferroelectric Ceramics with Perovskite Structure," *Ferroelectrics - Material Aspects*, Aug. 2011. Publisher: IntechOpen.

[195] S. F, S. S, L. Hn, and M. Ao, "Advancement on Lead-Free Organic-Inorganic Halide Perovskite Solar Cells: A Review.," *Materials (Basel)*, vol. 11, June 2018.

[196] R.-A. Eichel and H. Kungl, "Recent developments and future perspectives of lead-free ferroelectrics," *Functional Materials Letters*, vol. 3, no. 01, pp. 1–4, 2010. Publisher: World Scientific.

[197] V. V. Shvartsman and D. C. Lupascu, "Lead-free relaxor ferroelectrics," *Journal of the American Ceramic Society*, vol. 95, no. 1, pp. 1–26, 2012. Publisher: Wiley Online Library.

[198] Y. Hou, C. Wu, D. Yang, T. Ye, V. G. Honavar, A. C. T. van Duin, K. Wang, and S. Priya, "Two-dimensional hybrid organic–inorganic perovskites as emergent ferroelectric materials," *Journal of Applied Physics*, vol. 128, p. 060906, Aug. 2020. Publisher: American Institute of Physics.

[199] D. Yang, L. Luo, Y. Gao, S. Chen, and X. C. Zeng, "Rational design of one-dimensional hybrid organic–inorganic perovskites with room-temperature ferroelectricity and strong piezoelectricity," *Mater. Horiz.*, vol. 6, pp. 1463–1473, Aug. 2019. Publisher: The Royal Society of Chemistry.

[200] M. Owczarek, K. A. Hujsak, D. P. Ferris, A. Prokofjevs, I. Majerz, P. Szklarz, H. Zhang, A. A. Sarjeant, C. L. Stern, R. Jakubas, S. Hong, V. P. Dravid, and J. F. Stoddart, "Flexible ferroelectric organic crystals," *Nature Communications*, vol. 7, p. 13108, Oct. 2016. Number: 1 Publisher: Nature Publishing Group.

[201] Y. Duan, B. Zhang, S. Zou, C. Fang, Q. Wang, Y. Shi, and Y. Li, "Low-power-consumption organic field-effect transistors," *J. Phys. Mater.*, vol. 3, p. 014009, Jan. 2020. Publisher: IOP Publishing.

[202] X. Ren, F. Yang, X. Gao, S. Cheng, X. Zhang, H. Dong, and W. Hu, "Organic Field-Effect Transistor for Energy-Related Applications: Low-Power-Consumption Devices, Near-Infrared Phototransistors, and Organic Thermoelectric Devices," *Advanced Energy Materials*, vol. 8, no. 24, p. 1801003, 2018.

[203] Y. Liu, Y. Wang, M.-J. Chow, N. Q. Chen, F. Ma, Y. Zhang, and J. Li, "Glucose Suppresses Biological Ferroelectricity in Aortic Elastin," *Phys. Rev. Lett.*, vol. 110, p. 168101, Apr. 2013. Publisher: American Physical Society.

[204] Y. Liu, Y. Zhang, M.-J. Chow, Q. N. Chen, and J. Li, "Biological Ferroelectricity Uncovered in Aortic Walls by Piezoresponse Force Microscopy," *Phys. Rev. Lett.*, vol. 108, p. 078103, Feb. 2012. Publisher: American Physical Society.

[205] A. Heredia, V. Meunier, I. K. Bdikin, J. Gracio, N. Balke, S. Jesse, A. Tselev, P. K. Agarwal, B. G. Sumpter, S. V. Kalinin, and A. L. Kholkin, "Nanoscale Ferroelectricity in Crystalline $\gamma$-Glycine," *Advanced Functional Materials*, vol. 22, no. 14, pp. 2996–3003, 2012.

[206] S. B. Lang, "Pyroelectric Effect in Bone and Tendon," *Nature*, vol. 212, pp. 704–705, Nov. 1966. Number: 5063 Publisher: Nature Publishing Group.

[207] H. Athenstaedt, "Pyroelectric and Piezoelectric Properties of Vertebrates," *Annals of the New York Academy of Sciences*, vol. 238, no. 1, pp. 68–94, 1974.

[208] E. Fukada and H. Ueda, "Piezoelectric Effect in Muscle," *Jpn. J. Appl. Phys.*, vol. 9, p. 844, July 1970. Publisher: IOP Publishing.

[209] R. M. Zilberstein, "Piezoelectric activity in invertebrate exoskeletons," *Nature*, vol. 235, no. 5334, pp. 174–175, 1972. Publisher: Springer.

[210] S. Aitipamula, R. Banerjee, A. K. Bansal, K. Biradha, M. L. Cheney, A. R. Choudhury, G. R. Desiraju, A. G. Dikundwar, R. Dubey, N. Duggirala, P. P. Ghogale, S. Ghosh, P. K. Goswami, N. R. Goud, R. R. K. R. Jetti, P. Karpinski, P. Kaushik, D. Kumar, V. Kumar, B. Moulton, A. Mukherjee, G. Mukherjee, A. S. Myerson, V. Puri, A. Ramanan, T. Rajamannar, C. M. Reddy, N. Rodriguez-Hornedo, R. D. Rogers, T. N. G. Row, P. Sanphui, N. Shan, G. Shete, A. Singh, C. C. Sun, J. A. Swift, R. Thaimattam, T. S. Thakur, R. Kumar Thaper, S. P. Thomas, S. Tothadi, V. R. Vangala, N. Variankaval, P. Vishweshwar, D. R. Weyna, and M. J. Zaworotko, "Polymorphs, Salts, and Cocrystals: What's in a Name?," *Crystal Growth & Design*, vol. 12, pp. 2147–2152, May 2012. Publisher: American Chemical Society.

[211] R. A. Wiscons, N. R. Goud, J. T. Damron, and A. J. Matzger, "Room-Temperature Ferroelectricity in an Organic Cocrystal," *Angewandte Chemie International Edition*, vol. 57, no. 29, pp. 9044–9047, 2018.

[212] V. Jornet-Mollá, Y. Duan, C. Giménez-Saiz, Y.-Y. Tang, P.-F. Li, F. M. Romero, and R.-G. Xiong, "A ferroelectric iron (II) spin crossover material,"

*Angewandte Chemie*, vol. 129, no. 45, pp. 14240–14244, 2017. Publisher: Wiley Online Library.

[213] W.-K. Han, L.-F. Qin, C.-Y. Pang, C.-K. Cheng, W. Zhu, Z.-H. Li, Z. Li, X. Ren, and Z.-G. Gu, "Polymorphism of a chiral iron(II) complex: spin-crossover and ferroelectric properties," *Dalton Trans.*, vol. 46, pp. 8004–8008, June 2017. Publisher: The Royal Society of Chemistry.

[214] Y. Wang, W. Zhu, H. Dong, X. Zhang, R. Li, and W. Hu, "Organic Cocrystals: New Strategy for Molecular Collaborative Innovation," *Top Curr Chem (Z)*, vol. 374, p. 83, Nov. 2016.

[215] G. Bolla, H. Dong, Y. Zhen, Z. Wang, and W. Hu, "Organic cocrystals: the development of ferroelectric properties," *Sci. China Mater.*, vol. 59, pp. 523–530, July 2016.

[216] D. A. Kunkel, J. Hooper, B. Bradley, L. Schlueter, T. Rasmussen, P. Costa, S. Beniwal, S. Ducharme, E. Zurek, and A. Enders, "2D Cocrystallization from H-Bonded Organic Ferroelectrics," *J. Phys. Chem. Lett.*, vol. 7, pp. 435–440, Feb. 2016.

[217] W. Zhang and R.-G. Xiong, "Ferroelectric metal–organic frameworks," *Chemical reviews*, vol. 112, no. 2, pp. 1163–1195, 2012. Publisher: ACS Publications.

[218] S. Liang, H. Yang, H. Yang, B. Tao, A. Djeffal, M. Chshiev, W. Huang, X. Li, A. Ferri, R. Desfeux, S. Mangin, D. Lacour, M. Hehn, O. Copie, K. Dumesnil, and Y. Lu, "Ferroelectric Control of Organic/Ferromagnetic Spinterface," *Advanced Materials*, vol. 28, no. 46, pp. 10204–10210, 2016.

[219] E. Urbain, *Utilisation de semi-conducteurs organiques comme barrière tunnel pour l'électronique de spin.* These de doctorat, Strasbourg, Dec. 2017.

[220] M. Cinchetti, V. A. Dediu, and L. E. Hueso, "Activating the molecular spinterface," *Nature Materials*, vol. 16, pp. 507–515, May 2017. Number: 5 Publisher: Nature Publishing Group.